

# **A HANDBOOK FOR THE APPLICATION OF SEISMIC METHODS FOR QUANTIFYING NATURALLY FRACTURED GAS RESERVOIRS IN THE SAN JUAN BASIN, NEW MEXICO**

## **Project Report**

**Submitted to:**

**National Energy Technology Laboratory**

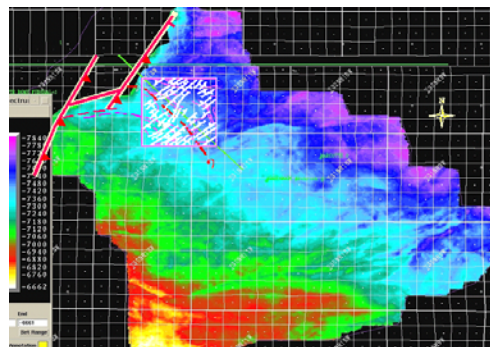
Ernest Majer, John Queen, Tom Daley, Mark Fortuna, Dale Cox, Peter D'Onfro, Rusty Goetz, Richard Coates, Kurt Nihei, Seiji Nakagawa, Larry Myer, Jim Murphy, Charles Emmons, Heloise Lynn, John Lorenz, David LaClair, Mathias Imhoff, Jerry Harris, Chunling Wu, Jame Urban, Sonja Maultzsch, Enru Liu, Mark Chapman, and Xiang-Yang Li

**September 30, 2004**

**For U.S. Department of Energy**

**Contract No. DE-AC03-76SF00098**

**Lawrence Berkeley National Laboratory, ConocoPhillips, Hi-Q Geophysics, Stanford University, Schlumberger Inc., Lynn Inc., Virginia Tech University, Edinburgh University Anisotropy Project, Sandia National laboratory.**



## EXECUTIVE SUMMARY

To meet the future needs of domestic gas exploration and production in naturally fractured gas reservoirs one must have reliable and cost effective methods for not only locating faults and fractures in the subsurface but for quantifying the nature of the fractures to determine the maximum potential for gas production. The overall objective of this work is to extend current seismic technology to progress beyond just locating fractures to characterizing and quantifying fractures controlling production in the reservoir. In essence the primary question posed was how does one use the right combination, scale and timing/sequence of seismic methods to identify the fractures controlling the productivity of a gas resource?

In order to meet the above objectives a four year (2000-2004) comprehensive program between DOE National Laboratories, universities and industry was formed to carryout an integrated field-testing and analysis effort aimed at improving the fundamental understanding of seismic wave propagation in naturally fractured gas reservoirs. The field site was in the San Juan basin in New Mexico. This cooperative research program was organized between Lawrence Berkeley National Laboratory (LBNL), Conoco Inc. (now ConocoPhillips), Lynn Inc., Schlumberger Inc., Stanford University, and Virginia Technology University. In addition to these primary organizations the Edinburgh Anisotropy Project in the U.K., HI-Q Geophysics and Sandia National Laboratory also participated.

A primary hypothesis of this work was that that in order to advance beyond simple anisotropy mapping it was necessary to have seismic measurements at greater resolution that conventional surface seismic could provide. Therefore, the basic premise of this work was that seismic data collected at the right scale and proper quantity contains the information necessary to derive the fracture properties of interest. It was anticipated that this could be accomplished by not only using the more advanced methods but also by revisiting current seismic techniques and reprocessing/reanalyzing the results to use data that was once thought to be noise. In other words determining if certain parts of the “noise” in seismic data is due to the target of interest, i.e. fractures affecting gas production causing scattering or other artifacts in the seismic data . Last but not least the project was also meant to form the fundamental basis of implementing this technology on a cost effective basis.

The project was organized into tasks that focused on field tests sites for experimental field work and model validation. The work plan was divided into three broad tasks: 1.Modeling, 2.Field Measurements and 3.Processing and Interpretation. To that end a 20 square mile study area was selected in the San Juan basin to carry out the work. LBNL and university personnel worked cooperatively with both the exploration and production departments of the petroleum companies to design integrated geophysical methods and analysis techniques. Industry provided access to the field sites, data collected at the test and production sites, validation wells, participation in the planning and execution of the experiments, processing and modeling of the data as well as participation in every analysis step of the project. LBNL and the universities provided basic theory and modeling support to aid in the design of the investigations, and perform some of the characterization experiments. The analysis of the data was done by all of the participants.

Past and ongoing theoretical efforts in scattering theory formed the basis for the modeling. An important component was developing the capability to model discrete fractures and faults versus equivalent medium materials. The purpose of the modeling was not only to understand the data collected, but also to aid in the design of the field experiments. The modeling and analysis effort consisted of a series of parametric studies of the effects of finite length fractures embedded in sand-shale lithologies. The fracture spacing, dimensions, and stiffness was varied to include a full range of possible values that may exist in situ. The partitioning of an incident body wave into the various fracture-related waves and the subsequent radiation off the fracture back into body waves was examined for both P- and S-wave sources. These simulations were performed using existing finite difference, boundary element, and global matrix (two-dimensional, elastic) codes developed at LBNL. The second effort utilized the synthetic data to develop new methods for extracting fracture properties such as fracture orientation, spacing, and stiffness from the fracture-generated waves.

Finite difference modeling based on the displacement discontinuity formalism was found to be valuable in a number of applications. Fundamental insight into the nature of discrete fracture response has been gained. Of particular interest are the mode converted events generated by discrete fractures and the need for finer scale sampling. In order to image these events with surface reflection seismic data, advanced imaging algorithms needed to be developed and applied. The limit of specific fracture stiffness detectable in surface reflection measurements has been estimated at  $10^{10}$  Pa/m. Realistic earth models have revealed the complex interaction between fracture scattered seismic events and detailed layering. Finally, the use of full 3-D modeling to design, process and interpret 3-D 9-C VSP data was illustrated. Overall, sophisticated modeling capability was found to be a critical component in quantifying fractures through seismic data.

In terms of field testing, controlled field experiments was an integral part of the program in an iterative fashion. The overall goal of the fieldwork was to provide data and testing of methods that could be used to determine if one can “pick out” the significant (permeable) fracture(s) from non-permeable and from natural heterogeneity. The fieldwork was carried out in a producing gas field at scales from the well logging to the surface seismic, (1 m to 1 km scale). Several data sets already existed within the San Juan basin (3-D P-wave surface seismic, production data, geologic data, well logs and limited core data) to provide validation as well as complementary information. The objective of the field tests was to augment these data as well as collect new data at both the borehole scale and surface seismic scale. Field-testing involved performing multi-component/multi-azimuth VSP and single well seismic in an area where surface 3-D seismic had been performed. This allowed a range of resolution of data in the same site where well data exist. This also provided a fundamental data set upon which to base the work. Well logging included both conventional logging as well logs for fracture mapping. The field components had the following elements:

1. Surface studies
  - (a) 3-D P-wave Reflection seismic. AVO, AVA, vs. frequency content with P wave,
  - (b) P-wave anisotropy

2. 3-D VSP (9-C)
  - (a) Multicomponent sources to 3-components receivers in fractured media for same contribution as 1(a and b) in addition to S-wave effects
3. Single well studies using both P&S wave for imaging fracture to derive fracture properties
  - (a) CDP imaging
  - (b) Guided wave
4. Well Logging
  - (a) Acoustic (monopole compressional and shear wave)
  - (b) Four arm caliper
  - (c) Gamma- Ray
  - (d) Resistivity
  - (e) Neutron Density
  - (f) FMI

The objective of the processing and interpretation was to derive images that are indicative of the fracture characteristics. Each method (surface seismic, VSP, single well, well logs) results in a different image at different scales. Processing was performed on all scales of data types, surface, VSP, logging and single well. The sequence was as follows: The existing 3-d data from the target area was reprocessed at Conoco with current state-of-the-art processing methodologies of Conoco. Lynn Inc. also had specific processing requirements in order to enhance the azimuthal P-wave analysis that Conoco also performed. The VSP and single well data was processed for fracture anisotropy and fracture reflectivity using codes at LBNL, Conoco and Schlumberger. Stanford performed analysis of the VSP data. Modeling was done at Stanford and LBNL for the single well data. LBNL, ConocoPhillips, and Hi-Q performed discrete fracture modeling. Sandia performed the core analysis. Geomechanical modeling was also performed by Hi-Q and LBNL. In terms of interpretation, modeling played a key role in the interpretation to separate matrix effects, lithologic effects (layering) and heterogeneity (i.e. lenses, channel sands, etc.) from fracture effects.

The overall work flow in the project was as follows: A 20 square mile study area was selected within a newly acquired (1998) 500 square mile 3D P-wave survey in the San Juan based on Conoco's future drilling sites. The plan was to compare the surface seismic results to well bore studies (VSP, single well and well logging), in the new wells and compare the results to geologic and production data. Once the 20 square mile study area was selected the first step was to select and reprocess the 3-D P-wave surface seismic data so that it was suitable for studies such as identifying discrete scatterers and P-wave anisotropy studies. Analysis of the surface seismic was

carried out using P-wave anisotropy analysis in time and complemented with limited amplitude studies. Finite element 2-D and 3-D modeling of the geologic model derived from the surface seismic and available well logs was carried out to design the VSP work within the 20 square mile study area. The geologic model was derived by using well logs and a statistical approach to defining heterogeneity in the lithology. Models with and without fractures using the discrete-continuity approach were used in the modeling. Modeling was used through out the project to refine our understanding of fractures as well as in aiding our interpretation of the data. The next step was to collect additional field data using VSP (3-D 9-C), multicomponent single well and well logging data. Combined with the single well and well logging data a unique seismic data set that scales from the sub-meter to the kilometer scale was collected. The processed data were interpreted with the geologic data (analysis of core outcrop and well logging results) and modeling results from 2-D and 3-D geomechanical modeling. These results were then compared with production data.

The overall results support the initial hypothesis that surface seismic, while useful, provides information at scales that mainly provide general fracture trends and gross structural information. Surface seismic as deployed in the San Juan Basin does not appear to have the resolution to detect subtle complexity in fracture properties that may be controlling gas production. The VSP data were only collected at one well and provided limited information over a relatively small volume compared to the surface seismic, however, VSP and higher resolution methods such as single well seismic have the capability to characterize complex fracture patterns associated with higher production. It was also shown that although the San Juan basin is overall structurally simple, however, at the reservoir scale it is very complex and a multi-scale approach is necessary. In summary, combining the seismic data from multiple scales has yielded a picture consistent with the production data and known geology of the study area, thus leading to the conclusion that a multiscale approach is the most useful.

## **ACKNOWLEDGMENTS**

This work was supported by the Assistant Secretary for Fossil Energy, National Energy Technology Laboratory (NETL) of the U.S. Department of Energy under contract No. DE-AC03-76SF000098. We would also like to acknowledge the support of Frances Toro, Tom Mroz, Jim Ammer, Hugh Guthrie and Brad Tomer at NETL. We would also like to thank all of the personnel at LBNL, ConocoPhillips, IVI, I/O, Pelton, Mertz, Schlumberger, and P/GSI for making the data collection possible as well as for general project support. In particular John Sinton, Allan Huffman, Rob Habiger and Peter Eike at ConocoPhillips. Last but not least we would like to thank Royal Watts for his vision initiating this project and unwavering support.

## TABLE OF CONTENTS

EXECUTIVE SUMMARY .....	1
ACKNOWLEDGMENTS .....	5
TABLE OF CONTENTS.....	6
LIST OF FIGURES .....	9
LIST OF TABLES .....	21
ABSTRACT.....	22
1. INTRODUCTION AND BACKGROUND .....	22
1.1 PROJECT MOTIVATION AND OBJECTIVES.....	23
1.2 RATIONAL FOR SELECTING SEISMIC METHODS .....	25
1.3 GEOLOGIC SETTING AND STUDY AREA.....	26
1.3.1 Core Studies .....	35
1.3.2 Evidence of Faulting and Fracturing from 3-D P-wave Surface Seismic .....	39
2. PROJECT ORGANIZATION AND TASKS.....	44
2.1 SPECIFIC TASKS.....	44
2.1.1 Task 1. Modeling.....	44
2.1.2 Task 2. Field Testing.....	45
2.1.3 Task 3. Processing and Interpretation .....	46
3. DATA ACQUISITION.....	49
3.1 SURFACE SEISMIC.....	49
3.1.1 Reprocessing of the 3-D P-wave Surface Seismic in the 20 Square Mile Study Area.....	49
3.1.2 Geometry, Trace Edit, First Break Picking, Refraction Statics.....	50
3.1.3 Gain .....	51
3.1.4 Noise Attenuation.....	53
3.1.5 Deconvolution .....	54
3.1.6 Multiples.....	54
3.1.7 Surface Consistent Amplitude Balance.....	55
3.1.8 Velocity Analysis .....	57
3.1.9 Fold of Stack Plots .....	58
3.1.10 QC Stack and KASTM.....	59
3.1.11 Pre-Stack Kirchhoff Migration.....	61
3.1.12 Data Acquisition Parameters .....	66
3.1.13 San Juan Processing Sequence .....	67
3.2 VERTICAL SEISMIC PROFILING DATA ACQUISITION .....	68

## TABLE OF CONTENTS (CONTINUED)

3.3	SINGLE WELL SEISMIC DATA ACQUISITION.....	74
3.3.1	Orbital Vibrator Source Data: .....	74
3.3.2	Piezoelectric Source Data:.....	75
3.4	WELL LOGGING ACQUISITION .....	76
4.	PROCESSING AND INTERPRETATION OF THE DATA .....	78
4.1	3-D SURFACE SEISMIC FOR FAULT STRUCTURE .....	78
4.2	ANALYSIS OF P-WAVE ANISOTROPY FROM SURFACE SEISMIC.....	91
4.2.1	Background .....	91
4.2.2	Analysis of the P-wave data .....	94
4.2.3	Results .....	96
4.2.4	Conclusions of P-wave Anisotropy Analysis of the 3-D Surface Seismic Data .....	101
4.3	VSP DATA ANALYSIS .....	102
4.3.1	Shear Wave Analysis.....	102
4.3.2	Interpretation of the shear wave splitting results.....	109
4.3.5	Tomographic Analysis .....	114
4.3.5.1	Traveltime tomography of 3-D VSP data .....	114
4.3.5.2	Travel time picking.....	115
4.3.5.3	Inversion .....	115
4.3.4	CDP Processing.....	122
4.4	SINGLE WELL ANALYSIS .....	128
4.4.1	High Amplitude Zone Analysis.....	135
4.4.2	Modeling study of Single Well Data.....	137
4.5	WELL LOG ANALYSIS .....	139
4.5.1	Lithology Analysis .....	140
4.5.2	Geology & Geomechanics Analysis.....	146
4.5.3	Conclusion of well log analysis.....	160
5.	MODELING THE EFFECT OF DISCRETE FRACTURES.....	161
5.1	THEORETICAL AND LABORATORY BASIS FOR DISPLACEMENT DISCONTINUITY MODELING .....	162
5.1.1	Conceptual Model of Displacement Discontinuity .....	167
5.1.2	Development of Finite Difference Modeling for Geoscience Application ..	168
5.1.3	Development of Matrix Geologic Model .....	169
5.1.4	Basic Features of Seismic Fracture Response. ....	172
5.1.5	Discrete Fracture Example in 2-D.....	179
5.1.6	VSP Modeling in 3-D.....	185
6.	SYNTHESIS OF THE RESULTS .....	191
6.1	CORRELATION OF SEISMIC DATA WITH HISTORICAL PRODUCTION DATA .....	191
6.2	INFORMATION ON FRACTURING FROM GEOLOGIC AND GEOMECHANICAL ANALYSIS.....	197

**TABLE OF CONTENTS (CONTINUED)**

7. CONCLUSIONS AND RECOMMENDATIONS..... 220

APPENDIX I—CORE FROM PICTURES FROM 28-7 #225E AND THE MERIDIAN  
SUNRAY H COMM 6 WELLS ..... 1

    A.1 CORE FROM THE 28-7 #225E WELL, DAKOTA SECTION ..... 1

    A-2 CORE FROM THE MERIDIAN SUNRAY H COMM 6 WELLS, MESAVERDE  
        SECTION..... 5

REFERENCES ..... 1

## LIST OF FIGURES

	<b>Page</b>
1.1. A schematic showing the different scales and resolutions of the seismic methods used in this study. As can be seen the scale of resolution range from the centimeter to the 10's of meters while the image volume ranged from the sub-meter to 100's of kilometers .....	24
1-2. The general location of the San Juan Basin in the U.S.....	28
1-3. Index map showing the structural elements of the San Juan Basin. Also shown is the approximate location of the 20 square mile study area used in this work (red box). Areas of steep dip (monoclines) are shown as patterned areas with the direction of dip indicated by strike and dip tic marks; long dashed line separates the Chaco Slope from the Central Basin and is drawn approximately where the Pictured Cliffs Sandstone is subaerially exposed (modified from Lorenz and Cooper 2003). .....	29
1-4. A SW-NE crosssection through the San Juan Basin showing the general lithology and dips of the formations of interest, i.e the Mesaverde and the Dakota formations. ....	30
1-5. The Tectonic elements in the southwest U.S. affecting the underlying structure of the San Juan Basin (modified after Woodward and Callender, 1977).....	31
1-6. Conceptual diagrams of the size and effect of different styles of faulting on the surrounding material. ....	34
1-7. Some examples of fracturing in the San Juan basin in the Mesaverde. ....	39
1-8. The location of the seismic study area (20 square mile red square) superimposed upon the location of the “large 3-D” P-wave seismic reflection. The structural horizon shown is the top of the Mississippian carbonates.....	40
1-9. An expanded view of the 20 square mile study area in Figure 1-8.....	40
1-10. The fault structure derived from a compilation of 2-D and 3-D seismic data. ....	41
1-11. An expanded view of the seismic interpretation of the faults in the San Juan Basin. The red box shows the area selected for the 20 square mile study area in which the 3-D surface seismic was reprocessed. ....	41
1-12. An expanded view of the 20 square mile study area in the San Juan basin as it was understood from surface seismic data at the beginning of this study. ....	42
1-13. A map of the first year gas production out of the Mesaverde, note the inconsistency across the area. ....	43
3-1. The dark blue rectangle shows the outline of the output prestack time migration. The area covered by the input data is indicated by the pink rectangle. Source positions are shown in green. Receiver positions are shown in blue.....	49
3-2. Example of a shot gather sorted with increasing offset to the right. The colored lines highlight the three refractions.....	51
3-3. This is part of one shot gather. Each trace was recorded at a different receiver location. Notice the rapid variation in moveout, discontinuous moveout trends, and significant changes in waveform character. ....	51

## LIST OF FIGURES (CONTINUED)

		<b>Page</b>
3-4.	Example of two shot gathers after geometrical divergence correction and muting, but before statics were applied. Cultural noise, airwave and ground roll are noted. Left side is has no noise attenuation. Right side shows the same gathers after noise attenuation.....	53
3-5.	Example of auto correlations.....	54
3-6.	Example of multiple reflections in a stacked section.....	54
3-7.	Scale factor as a function of offset that was multiplicatively applied to the seismic data prior to migration. ....	55
3-8.	Scale factors as a function of source and receiver position that was multiplicatively applied to the seismic data prior to migration. The top map shows the factors for the source positions. The bottom map shows the factors for the receiver positions. ....	56
3-9.	Velocity analysis before (left) and after (right) Radon demultiple.....	57
3-10.	Shown is a map of the fold-of-stack for azimuth range $N45W \pm 45^\circ$ and for offset range 0 to 3,000 ft. The color indicates the total number of traces at each CMP location. The small open circles indicate well locations.....	58
3-11.	Shown is a map of matrix population for 10 by 10 CMP super bins. The color indicates the total number of populated bins in the matrix. The matrix has 48 bins representing eight azimuth and six offset ranges. The small open circles indicate well locations.....	59
3-12.	Example time slices (top sections) , cross lines (left side sections) and in lines (right side sections).....	60
3-13a.	Crossline section extracted from the original processed volume.....	62
3-13b.	Crossline section extracted from the new processed volume. ....	63
3-14a.	Inline section extracted from the original processed volume. ....	64
3-14b.	Inline section extracted from the new processed volume. ....	65
3-15.	The location of the VSP well (blue star) in the 20 square mile study area. It is plotted with respect to an attribute derived from the P-wave anisotropy analysis, the travelttime between two reflectors as a function of azimuth (SE far offset). ....	68
3-16.	Shot locations of the VSP work. The double stars are where we duplicated the two different vibrators used. The color contours are the surface elevations. The lack of symmetry was due to land access issues.....	69
3-17a.	A comparison of the I/O and IVI traces, at each level the traces are plotted next to one another. The data have been bandpassed filtered from 10 to 90 hertz.....	70
3-17b.	The difference between the I/O and IVI Transfer Function filtered to 10-90 hz., note the lack of a difference between the two different data sets. ....	70
3-18a.	An example of the raw data quality at a near offset (475 feet from the well head) for the 9-C VSP. The depth of interest is approximately from 3500 to 5000 feet.....	71
3-18b.	An example of the raw data quality at a intermediate offset (817 feet from the well head) for the 9-C VSP. The depth of interest is from 3500 to 5000 feet. ....	72

## LIST OF FIGURES (CONTINUED)

		<b>Page</b>
3-19.	Six-component single well common offset gather. The data is all shots for one 3-component sensor at an offset of 87 ft. below the source. Source depth is shown on the top horizontal axis. All components have similar arrivals, which are dominated by tube waves, including direct, reflected and multiple arrivals. ....	75
3-20.	Shot gather of piezoelectric source single well data. The source is at 4822 ft. depth with the 24 sensors offset from 32 to 262 ft. below the source. The red line indicates the moveout velocity of the dominant event (4598 ft/s which is the tube-wave).....	76
4-1.	Two different examples of shooting patterns for 3-D seismic. The conventional example on the left is used in areas of good access. The pattern on the right was implemented in the San Juan due to access and cost issues. ....	78
4-2.	The fold of stack display for this area. The blue is 80 and red is 120 fold. The red lines are the locations of the seismic cross sections to follow. ....	79
4-3.	Fault picks using method A. This cross section is the southern most line in Figure 4-2.....	80
4-4.	Fault picks using method B along same line (1340) as Figure 4-3.....	81
4-5.	North - South line through the VSP well, note lack of picked faults.....	81
4-6.	East-West line in the vicinity of the VSP well. ....	82
4-7.	East-West seismic line (1366) through the VSP well.....	82
4-8.	East-West cross line (1368), just north of the VSP well.....	83
4-9.	A seismic line 440 feet north of the line in Figure 4-8. ....	83
4-10.	Seismic crossline located in the northern most part of the study area. ....	84
4-11.	Seismic cross line just 440' south of the line in Figure 4-10 towards the VSP well. ....	84
4-12.	Seismic line 440 feet south of the line shown in Figure 4-11.....	85
4-13.	A final crossline, another 440 feet south of the line in Figure 4-12 towards the VSP well. Note how the placement, orientation and even number of faults vary significantly from line to line while separated by only 440 feet in horizontal distance. ....	85
4-14.	Fault picks derived from Method A overlain on the Menefee time horizon for the 20 square mile study area re-processed data. Ticks indicate down dip direction. ....	86
4-15.	Fault interpretation overlaying the Menefee horizon showing the “smoothed/aliased” results of Method B. ....	87
4-16.	Mississippian sub sea depth map with basement fault interpretation (pink faults). ....	88
4-17.	The Mesaverde combination fault interpretation (white faults), superimposed on the previous fault (pink) and Mississippian structure map. ....	89
4-18.	A cross section across the NW part of the San Juan basin as shown on the green line in Figure 4-16.....	89
4-19.	Azimuth attribute display created from the Menefee time structure map with overlay of the summary combined A&B methods fault interpretation (triangles point to the downthrown hangingwall side of the normal faults). ....	90

## LIST OF FIGURES (CONTINUED)

		<b>Page</b>
4-20.	The SE Greenhorn-Entrada isochron. The reds turn out to also correlate to the shale rich material and the greens to the sand rich formations. Blue star is the location of the VSP Well. ....	97
4-21.	The SE far Greenhorn-Entrada isochron correlated with first year production of the wells. ....	98
4-22.	An analysis of the P-wave anisotropy in the Greenhorn-Entrada (Dakota section) in the 20 square mile study area. ....	99
4-23.	The results of analyzing the interval velocity data in the Mesaverde for frequency content. ....	100
4-24.	The result of analyzing the data around LS2C for average frequency content. Compare to Figure 4-21. ....	101
4-25.	Four-component shear-wave data from a near-offset source location, a) before Alford rotation, b) after Alford rotation. The components are labeled according to source and receiver orientation (first and second letter, respectively). After Alford rotation the energy in the cross-diagonal components is minimized, and the data are separated into fast and slow shear wave arrivals, respectively. ....	103
4-26.	Equal area projection of measured S1-polarization and time delay in the reservoir (below 4000 ft). The orientation of the lines is the azimuth of the S1-polarization, whereas the length of the lines is proportional to the time delay between the split shear waves. For instance, the time delay for source 238 is 2 ms, while for source 48 it is 10 ms. Near-offset data (incidence angles < 30°) show a consistent polarization of the leading shear wave with an average of N55°E and small time delays. For far offsets the S1-polarization is nearly radial, and time delays are large. At far-offset locations 5 and 463 NW and SE of the well the S1-polarization is still radial, but the time delay does hardly increase in the reservoir. ....	104
4-27.	Sketches that summarize the measured shear-wave splitting patterns as a function of depth for groups of source locations, in which the shear-wave behaviour is similar. Near-offset data show an HTI effect above 2500 ft and below 4000 ft, while far-offset data indicate VTI anisotropy with clear evidence of a shear-wave singularity at offset/depth $\approx 1$ . ....	106
4-28.	Shear-wave splitting data from near-offset source 178 in comparison with the synthetic modelling results. Dashed lines indicate mean values of the measured polarization data. The main features of constant S1-polarization with depth around N55°E, constant time delay in the Lewis shale (2500 ft - 4000 ft), and increase in time delay above and below are well matched. In the real data, there is great variability in time delay with source location at the shallow receivers, which cannot be explained by a single model. ....	107

## LIST OF FIGURES (CONTINUED)

		<b>Page</b>
4-29.	Far-offset data and modelling example from source location 159. Both real and synthetic data clearly show the effect of a shear-wave singularity, where the S1-polarization flips by 90° from normal to parallel to the source-well azimuth, and the time delay reaches zero. The magnitude of decrease in time delay above and increase below the singularity are well matched by the model. ....	108
4-30.	Results of shear-wave splitting analysis from real and synthetic data for far-offset source 5 NW of the well. The shear-wave singularity is still clearly observable in data and model. However, below the singularity the time delay reaches a constant level, which is reproduced by the synthetic model. ....	109
4-31.	Shear-wave splitting data from synthetic VSPs for source 159, where the layer above the shallowest receiver is isotropic (left), or the second layer has only HTI and no VTI anisotropy (right). The graphs demonstrate that the steep continuous decrease in time delay measured in the real data cannot be explained without VTI anisotropy in the overburden, especially above 1200 ft. ....	112
4-32.	Equal area projections of S1-polarization and time delay for models of the reservoir layer. a) one fracture set striking N55°E, fracture density 0.15; b) two fracture sets striking N35°E and S85°E, fracture densities 0.2 and 0.1. The data, which are overlain on the graphs, do not provide sufficient constraints to distinguish between the two models. ....	113
4-33.	3-D VSP source locations plotted with the elevation map. ....	115
4-34.	(a) Shot gather recorded with vertical vibrator positioned at 4,144 ft from the well (source IO 187) with P-wave travel time picks; (b) detailed view of the sections indicated on (a). Note the change in the direction of the slope of the first arrival and inversion of polarity in component 3 (vertical). ....	116
4-35.	P-wave travel time picks organized sorted according to the distance from the source to the well. Note that the travel times obtained from the source located at 8000 ft from the well don't follow the same pattern of the previous data, indicating possible error on the source location coordinates. ....	117
4-36.	1-D P-wave velocity tomograms displayed in three dimensions. (a) planes located at 0 and 90 degrees; (b) 20 and 110 degrees; (c) 60 and 150 degrees; (d) 80 and 170 degrees from the X direction. ....	118
4-37.	Results from 1-D tomography applied to twenty shots from the San Juan 3-D VSP dataset. Estimated layer velocities for long offset and near offset shots are different. Pattern of heterogeneity indicates need for consistent 3-D inversion. ....	119
4-38.	S-wave travel time picks organized sorted according to the distance from the source to the well. ....	120
4-39.	P-wave travel time picks. Source IO 238 – Vertical vibrator with P-wave first arrival picks (source-receiver offset = 2732.5 ft). ....	121
4-40.	Source IO 238 - horizontal vibrator (radial) and shear-wave first arrival picks. ....	122
4-41.	Corridor stacks from shot points near the VSP well. Note the difference between FFID 7 and 41, 7 had a “good” lock on the tool and 41 had a bad lock on the VSP tool. ....	124

## LIST OF FIGURES (CONTINUED)

		<b>Page</b>
4-42.	A corridor stack from the VSP data inserted into an inline surface seismic line.....	125
4-43.	A corridor stack from the VSP data inserted into a crossline surface seismic line .....	125
4-44	Example of VSP CDP data from a short, intermediate and far off set. ....	126
4-45.	The ray tracing model used in the processing of the VSP data. ....	127
4-45a.	Single well model with single layer, no borehole is include in this initial model. ....	129
4-45b.	Model seismograms for a shot gather (one shot, 24 sensors) using the model shown in Figure 4-45a for three components of sensors, horizontal, vertical and pressure (left to right). The large arrival from 1 to 11 ms is the direct P-wave while the two events intersecting the direct arrival are reflections from the top and bottom of the layer. The pressure response (right) is modeling the hydrophone response. ....	129
4-46.	True amplitude 6-component single well common offset gather showing data in the anomalous zone (arrows, approximately 4350 to 4400 ft.) and nearby traces. Traces outside the zone, that appear blank, do have data, but are much lower in amplitude than arrivals in the anomalous zone.....	130
4-47.	Relation between interpreted well logs and single well amplitude. Logs, left to right, are gas porosity (green), stratigraphy, hydrocarbon porosity (red), permeability (gas=green, water=blue, hydrocarbon=red). Single well amplitude (far right) is r.m.s. amplitude for x and y source (solid and dashed line respectively) for 3-component sensor. Arrows indicate correspondence between high gas shows and high single well amplitude.....	131
4-48.	One component (source H2, receiver V) of the common-offset gather of channel1 (offset 87 ft) with AGC. ....	132
4-49	(a) Generally visible events in the field data; (b) Sonic logs (P- and fast S-waves) and the estimated low frequency tube-wave velocity from logs. Velocities are used to predict the arrival times to identify the events in the data: 1 - direct tube-wave; 2u/2d - up/down-going interface reflections; 3d - down-going multiple reflections; 4 - reflected tube-wave from the well plug.....	133
4-50.	Schematic diagram of tube-waves in the single-well survey: (a) Wave paths; (b) Arrivals on the seismogram. ....	134
4-51.	The apparent velocity ( $c'$ ) and true velocity $\textcircled{c}$ of the direct, reflected, and multiple tube-waves in the field data with AGC. ....	134
4-52.	True amplitude display of the data: the anomalous zone (4387-4442 ft) with low velocity and high amplitude.....	135
4-53.	Polarization diagram for receiver H2 and V of the source H2. The anomalous zone (in the red box) has horizontal polarization but the rest has vertical polarization. ....	136
4-54.	Dispersion of flexural waves (Paillet et al. 1991): (a) Sandstone (fast, hard formations $V_p > V_s > V_f$ ); (b) Shale (slow, soft formations $V_p > V_f > V_s$ ). $V_{ph}$ and $V_g$ are phase and group velocities, respectively.....	136
4-55.	(a) Model; (b) Blocked logs.....	138

## LIST OF FIGURES (CONTINUED)

		<b>Page</b>
4-56.	(a) Synthetic common-shot gather (vertical component of channel1): marked events are the same as those in the field data (Figure 4-49(a)); (b) Blocked fast $V_s$ log.....	139
4-57.	Cliff House Formation Evaluation Summary: Track 1, Gamma ray and caliper, Track 2 resistivity arrays and rw value. Track 3, Resistivity Image, Track 4, Density & Neutron Porosity and PEF. Track 5 Lithology and hydrocarbon volumes. Track 6 Relative Permeability and estimated production, Track 7 thickness and average permeability .....	143
4-58.	Menafee Formation Evaluation Summary: Track 1, Gamma ray and caliper, Track 2 resistivity arrays and rw value. Track 3 Resistivity Image, Track 4, Density & Neutron Porosity and PEF. Track 5 Lithology and hydrocarbon volumes. Track 6 Relative Permeability and estimated production, Track 7 thickness and average permeability .....	144
4-59.	Point Lookout Formation Evaluation: Track 1, Gamma ray and caliper, Track 2 resistivity arrays and rw value. Track 3 Resistivity Image, Track 4, Density & Neutron Porosity and PEF. Track 5 Lithology and hydrocarbon volumes. Track 6 Relative Permeability and estimated production, Track 7 thickness and average permeability .....	145
4-60.	Combined FMI and formation evaluation logs for the Newberry well for a segment of the middle Menefee between 4730 and 4780 feet. Bedding is clearly visible on the FMI (left) as lighter (more resistive sands) and darker (less resistive shales and coals). This is reflected in the quartz fraction (yellow) on the lithology log (right). Note the drilling induced fractures running vertically through the in the lower sand .....	146
4-61.	An FMI image displayed using static (left) and dynamic scaling (right) of the Dakota sands. An isolated fracture with a dip of approximately 50 degrees and a strike of NNE is visible at 7435 feet as a sinusoid crossing the right image. ....	147
4-62.	An FMI image displayed using static (left) and dynamic scaling (right) of the Menefee sands. Some isolated events, such as the one at 4647 feet may be fractures but are more likely to be depositional features and cross-bedding. ....	148

## LIST OF FIGURES (CONTINUED)

		<b>Page</b>
4-63.	A segment of DSI dipole data from the middle Menefee in the Newberry well. The right-most track shows selected waveforms generated as if the dipole source was oriented along the fast axis of the formation anisotropy (red) and slow axis (blue). Above 4900 ft these waveforms overlay well indicating little anisotropy. Between 4900 and 4930 feet there is a significant phase difference indicating the presence of anisotropy. The yellow band indicates the time window used for anisotropy processing. The next track to the right indicates the Stoneley (purple dash), fast and slow flexural (red and blue respectively) and compressional (green dash) slownesses. The center track indicates the azimuth of the fast direction of anisotropy (red line) together with an estimate of its uncertainty (orange shade). The next track to the left shows the gamma ray (green), hole diameter (orange), the azimuthal orientation of the tool (dark blue) and the deviation of the tool from vertical (light blue). Finally the left most track shows the maximum and minimum cross-line energy as the data is rotated. If acquisition and processing has been done correctly the left edge of the green band should always be close to zero. Where no significant apparent anisotropy is present the green band is narrow. Where significant anisotropy is present the green band is wide. ....	150
4-64.	The result of the DSI processed for anisotropy over the Cliff House section of the Newberry well. Some anisotropy is present indicating some aligned microcracks are present with a dominant orientation around N40degE.....	151
4-65.	The result of the DSI processed for anisotropy over the Menefee section of the Newberry well. Very little anisotropy is present indicating weak or poorly aligned microcracks. ....	152
4-66.	The result of the DSI processed for anisotropy over the Point Lookout section of the Newberry well. Significant anisotropy is present with a fast direction around N30degE. This indicating significant well aligned microcracks with a maximum regional stress in the N30degE direction. ....	153
4-67.	Breakout and ovality logs for the Cliff House formation. Track 1 shows the gamma ray. Track 2 shows the two orthogonal caliper measurements together with a red bar where significant breakouts occur. Track 3 shows the borehole ovalization. Track 4 shows individual breakouts in black and summed breakouts over ten foot intervals in green. ....	154
4-68.	Breakout and ovality logs for the Menefee formation. Track 1 shows the gamma ray. Track 2 shows the two orthogonal caliper measurements together with a red bar where significant breakouts occur. Track 3 shows the borehole ovalization. Track 4 shows individual breakouts in black and summed breakouts over ten foot intervals in green.....	155

## LIST OF FIGURES (CONTINUED)

		<b>Page</b>
4-69.	Breakout and ovality logs for the Point Lookout formation. Track 1 shows the gamma ray. Track 2 shows the two orthogonal caliper measurements together with a red bar where significant breakouts occur. Track 3 shows the borehole ovalization. Track 4 shows individual breakouts in black and summed breakouts over ten foot intervals in green. ....	156
4-70.	Stoneley permeability and fracture aperture logs for the Cliff House formation. Track 1 shows the depth and bulk density. Track 2 shows the gamma ray, Stoneley slowness and two orthogonal caliper measurements. Track 3 shows the up, down and average (red) Stoneley transmission coefficients from the data together with that computed theoretically from the inversion results. Track 4 and 5 show the actual and computed Stoneley reflection coefficients for up and down-going waves respectively. Track 6 shows assumed fracture density, fracture dip and fracture apertures needed for the model. Track 7 shows the computed Stoneley permeability and Track 8 shows the input Stoneley waveforms. ....	157
4-71.	Stoneley permeability and fracture aperture logs for the Menefee formation. Track 1 shows the depth and bulk density. Track 2 shows the gamma ray, Stoneley slowness and two orthogonal caliper measurements. Track 3 shows the up, down and average (red) Stoneley transmission coefficients from the data together with that computed theoretically from the inversion results. Track 4 and 5 show the actual and computed Stoneley reflection coefficients for up and down-going waves respectively. Track 6 shows assumed fracture density, fracture dip and fracture apertures needed for the model. Track 7 shows the computed Stoneley permeability and Track 8 shows the input Stoneley waveforms. ....	158
4-72.	Stoneley permeability and fracture aperture logs for the Point Lookout formation. Track 1 shows the depth and bulk density. Track 2 shows the gamma ray, Stoneley slowness and two orthogonal caliper measurements. Track 3 shows the up, down and average (red) Stoneley transmission coefficients from the data together with that computed theoretically from the inversion results. Track 4 and 5 show the actual and computed Stoneley reflection coefficients for up and down-going waves respectively. Track 6 shows assumed fracture density, fracture dip and fracture apertures needed for the model. Track 7 shows the computed Stoneley permeability and Track 8 shows the input Stoneley waveforms. ....	159
5-1.	Concept of fracture stiffness, the fracture represents a discontinuity in the displacement of the seismic wave across the interface, the more the displacement the less stiff and more attenuative the wave. ....	163
5-2.	Effect of fracture stiffness on the travel time and amplitude of seismic wave was a function of frequency. ....	164
5-3.	Conceptual fracture model of displacement discontinuity stiffness. ....	168

## LIST OF FIGURES (CONTINUED)

		<b>Page</b>
5-4.	Model surfaces. The purple to green surfaces bound transgressive intervals, while the pink to blue surfaces bound regressive sequences. The thicker interval between the green and pink surfaces is the central Mesaverde. The white dots mark the location of the 40 wells used to construct these surfaces. Also shown are the blocked Newberry and Moore wells. ....	170
5-5.	Geostatistical facies model. The facies range from marine, offshore, foreshore, barrier, to floodplane with channels. ....	171
5-6.	Geostatistical lithology model (sand and shale). Each facies in Figure 5-5 was modeled as shale with a facies-dependent amount of sand. The blocked sand-shale pseudologs derived from the gamma logs at the Newberry and Moore wells was used to condition the simulation. ....	172
5-7.	Simple 5 layer model with small fractures in the Cliffhouse Sand, and larger scale fractures extending through the Mesa Verde section. ....	173
5-8.	Details of the simple model showing details of small scale fracturing in the Cliffhouse Sand. ....	174
5-9.	Wave field snapshot for the model without any fractures. ....	175
5-10.	Wave field snapshot for model including small scale fractures. ....	175
5-11.	Snapshot of the wave field with both large and small scale fractures. ....	176
5-12.	Synthetic shot gather seismograms for simulated receivers deployed along the surface of the model. Seismograms on the left are for a model with no fractures, while seismograms on the right are for a model with both sets of fractures. ....	177
5-13.	Effect of spatial sampling. Events arising from discrete fractures are aliased at typical receiver spacings. ....	178
5-14.	Effects of varying the fracture stiffness on the visibility of fracture generated scattered events. ....	179
5-15.	Snapshot of the horizontal component of the wave field overlaid on the P-wave velocity model. ....	180
5-16.	Wave field shortly after crossing the Lewis shale boundary. ....	181
5-17.	Wave field shortly after the wave front crosses the cluster of fractures and the fault nearest to the source. ....	182
5-18.	Wave field shortly after the wave front crosses the cluster of fractures and the fault farthest from the source. ....	183
5-19.	Propagation with time of major fracture event from far offset fractures to the surface. ....	184
5-20.	Shot gather for a source located at -1250 m. The fracture event tracked in Figure 5-19 is arrowed. ....	185
5-21.	X-Z plane snapshot from the 3-D model at 0.550 s. The blue lines show the locations of intermediate and far offset VSP wells where seismic traces were generated. ....	186
5-22.	Simulated VSP vertical geophone traces for the intermediate offset well. ....	187
5-23.	Simulated VSP vertical and horizontal geophone traces for the far offset well. ....	187

## LIST OF FIGURES (CONTINUED)

		<b>Page</b>
5-24.	Newberry LS 2C P-wave velocity model overlain by a vertical motion snapshot at 0.520 s .....	189
5-25.	Synthetic vertical traces from the Newberry LS 2C 3-D velocity model .....	190
6-1.	The first year production from each well contoured over the 20 square mile study area. ....	192
6-2.	The faults picked using method A and using the azimuth direction in the Point Lookout plotted on top of the contoured production. ....	193
6-3.	The faults picked using method A on the Menefee azimuth directions.....	194
6-4.	The results of taking the summary of fault picking using methods A and B and overlying the production data. ....	195
6-5.	The result of over laying the final result of the method “A” fault picking.....	196
6-6.	The maximum horizontal stress orientation derived from several different analysis and the natural fracture directions. The box shows the 20 square mile study area. ....	197
6-7.	Sketch of fractures on a bedding surface of Mesaverde sandstones on the Hogback north of Waterflow, New Mexico (location “a” on Figure 6-6).....	199
6-8.	Rose diagram showing the strikes of 259 fractures measured on Ute Dome. ....	199
6-9.	Strike curvature anomalies on the 3D seismic survey at location “i”. The green linears mark probable fault zones that have created fracture-enhanced permeability connecting three wells. Courtesy Bruce Hart, McGill University (see Hart et al., 2000.).....	202
6-10.	The results of the boundary element stress analysis compared to the production and fault map derived from the surface seismic data analysis. The green square is the zone of the VSP sources and the blue star is the well used for the VSP. The red zones on the left figure are the zones where the critical stress is 0.8 of failure. These are the zones in the model where the factures may either may initiate or start to open.....	204
6-11.	The maximum tensile principle stress model as calculated from Poly 3D for the 15 faults mapped from the surface seismic in the vicinity of the VSP well . The objective was to determine if one could anticipate subseismic faulting from the observed fault and stress directions. ....	205
6-12.	The maximum Coulomb stress model as calculated from Poly 3D for the 15 faults mapped from the surface seismic in the vicinity of the VSP well . The objective was to determine if one could anticipate sub-seismic faulting from the observed fault and stress directions. ....	206
6-13.	Example of data processed to show scattered energy, left side shows data before the down going and up going data are removed .....	207
6-14.	The sites where the scattering analysis was performed. ....	208
6-15.	Sites where scattering was observed.....	209
6-16.	An example of the reflection observed in the VSP data at sites close to the VSP well. ....	210

## LIST OF FIGURES (CONTINUED)

	<b>Page</b>
6-17. Sites where the VSP data showed a reflection from the zone where the single well data showed the high amplitude data. ....	211
6-18. Location of the VSP shots with respect to the faults mapped with the surface seismic. The black boxes show the CDP VSP shot locations of the CDP results shown in Figure 6-20 and 6-21. ....	212
6-19. The Production data plotted with the VSP shot locations and the faults inferred from the surface seismic. The black box shows the CDP VSP shot locations of the CDP results shown in Figure 6-20 and 6-21. ....	213
6-20. CDP images from shots from 159, 48, 210, and 692, the shots in the top black box in Figures 6-18 and 6-19. The data have been interpreted for faults. ....	214
6-21a. CDP images from the lower black box in Figures 6-18 and 6-19, interpreted for faults. ....	215
6-21b. CDP images from the lower black box in Figures 6-18 and 6-19, interpreted for faults. ....	215
6-22. The tensile stress model from 15 faults in the vicinity of the VSP well. ....	216
6-23. The tensile stress model from 15 faults plotted with the production data in the vicinity of the VSP well. ....	217
6-24. First month's gas production from the Newberry LS 2C well. ....	218
6-25. The last part of a full year's production from the Newberry LS 2C well. ....	219

**LIST OF TABLES**

Table 1. Formation Evaluation Parameters.....140  
Table 2. Permeability Model Parameters  $K^{1/2}=C*\phi^{4*((\text{Phit-BVI})/\text{BVI})^2}$  .....141  
Table 3. Production Rate Prediction Parameters (assumes skin=-3 at 168 hours) .....141  
Table 4. Cliff House Formation .....141  
Table 5. Menefee Formation.....142  
Table 6. Point Lookout Formation.....142

## ABSTRACT

A four year (2000 - 2004) comprehensive joint industry, University and National Lab project was carried out in a 20 square mile area in a producing gas field in the Northwest part of the San Juan Basin in New Mexico to develop and apply multi-scale seismic methods for detecting and quantifying fractures in a naturally fractured gas reservoirs. 3-D surface seismic, multi-offset 9-C VSP, 3-C single well seismic, and well logging data were complemented by geologic/core studies to model, process and interpret the data. The overall objective was to determine the seismic methods most useful in mapping productive gas zones.

Data from nearby outcrops, cores, and well bore image logs suggest that natural fractures are probably numerous in the subsurface reservoirs at the site selected and trend north-northeast/south-southwest despite the apparent dearth of fracturing observed in the wells logged at the site (Newberry and Moore wells). Estimated fracture spacing is on the order of one to five meters in Mesaverde sandstones, less in Dakota sandstones. Fractures are also more frequent along fault zones, which in nearby areas trend between north-northeast/south-southwest and northeast-southwest and are probably spaced a mile or two apart. The maximum, in situ, horizontal, compressive stress in the vicinity of the seismic test site trends approximately north-northeast/south-southwest. The data are few but they are consistent.

The seismic data present a much more complicated picture of the subsurface structure. Faulting inferred from surface seismic had a general trend of SW – NE but with varying dip, strike and spacing. Studies of P-wave anisotropy from surface seismic showed some evidence that the data did have indications of anisotropy in time and amplitude, however, compared to the production patterns there is little correlation with P-wave anisotropy. One conclusion is that the surface seismic reflection data are not detecting the complexity of fracturing controlling the production. Conclusions from the P-wave VSP studies showed a definite 3-D heterogeneity in both P- and S-wave characteristics. The analysis of shear-wave splitting from 3D VSP data gave insight into the anisotropy structure with depth around the borehole. In the reservoir, the VSP shear-wave splitting data do not provide sufficient constraints against a model of lower symmetry than orthorhombic, so that the existence of more than one fracture set must be considered. It was also demonstrated that a VTI and orthorhombic symmetry could be well defined from the field data by analyzing shear-wave splitting patterns. The detection of shear-wave singularities provides clear constraints to distinguish between different symmetry systems. The P-wave VSP CDP data showed evidence of fault detection at a smaller scale than the surface seismic showed, and in directions consistent with a complicated stress and fracture pattern. The single well data indicated zones of anomalous wave amplitude that correlated well with high gas shows. The high amplitude single well seismic data could not be explained by well bore artifacts, nor could it be explained by known seismic behavior in fractured zones. Geomechanical and full wave elastic modeling in 2- and 3-D provided results consistent with a complicated stress distribution induced by the interaction of the known regional stress and faults mapped with seismic methods. Sophisticated modeling capability was found to be a critical component in quantifying fractures through seismic data. Combining the results with the historical production data showed that the surface seismic provided a broad picture consistent with production, but not detailed enough to consistently map complex structuring which would allow accurate well placement. VSP and borehole methods show considerable promise in mapping the scale of fracturing necessary for more successful well placement. Specific recommendations are given at which scale each method and fracture complexity is appropriate.

## **1. INTRODUCTION AND BACKGROUND**

### **1.1 PROJECT MOTIVATION AND OBJECTIVES**

Over the past ten years there has been an increased awareness that natural fractures can have a significant impact on fluid flow in the subsurface (Majer et al 1997). In particular, in naturally fractured gas reservoirs such as the San Juan basin in New Mexico fractures are thought to play a significant role in the productivity of the natural gas resource (Lorenz and Cooper 2003). Locating and characterizing the fractures that control the production of the gas reservoirs in the San Juan Basin, however, has not been an easy task. In some instances operators have resorted to drilling on a grid and/or been guided by surface access rather than on reliable information on the location of “sweet” spots in the subsurface. Fractures can be mapped using outcrops, core and well logs but as is the case with almost all surface and point measurements it is difficult to accurately extrapolate and/or interpolate these data to the subsurface and/or wider volumes. In terms of geophysical measurements seismic methods have been used extensively to image the subsurface. The most widely used and commercialized method is surface reflection. Data and a variety of analysis methods derived from both 2-d and 3-d P-wave methods have been used in the San Juan to map structure and lithology to varying degrees of success. Current methods rely on gross definition of fracture properties such as P-wave anisotropy or other seismic attributes such as amplitude versus offset (AVO) or amplitude versus azimuth (AVA). While these are useful for gross fracture detection these do not define “THE” fracture or fracture sets which control the permeability. Less used have been vertical seismic profiling (VSP), well logs such as Formation Micro-Imager (FMI), full wave form sonic, cross dipole shear wave and Stoneley wave logging, single well seismic imaging and the use of multi-component methods (both surface seismic and VSP methods). This is mainly due to the cost of the more “specialized methods” and the lack of a full understanding of the use of the data derived from the more advanced methods. Figure 1-1 is a schematic of the different methods we employed to span the possible scale of seismic measurements. As will be seen one of the main objectives was to define the appropriate scale of measurements necessary to successfully define the fractures controlling flow.

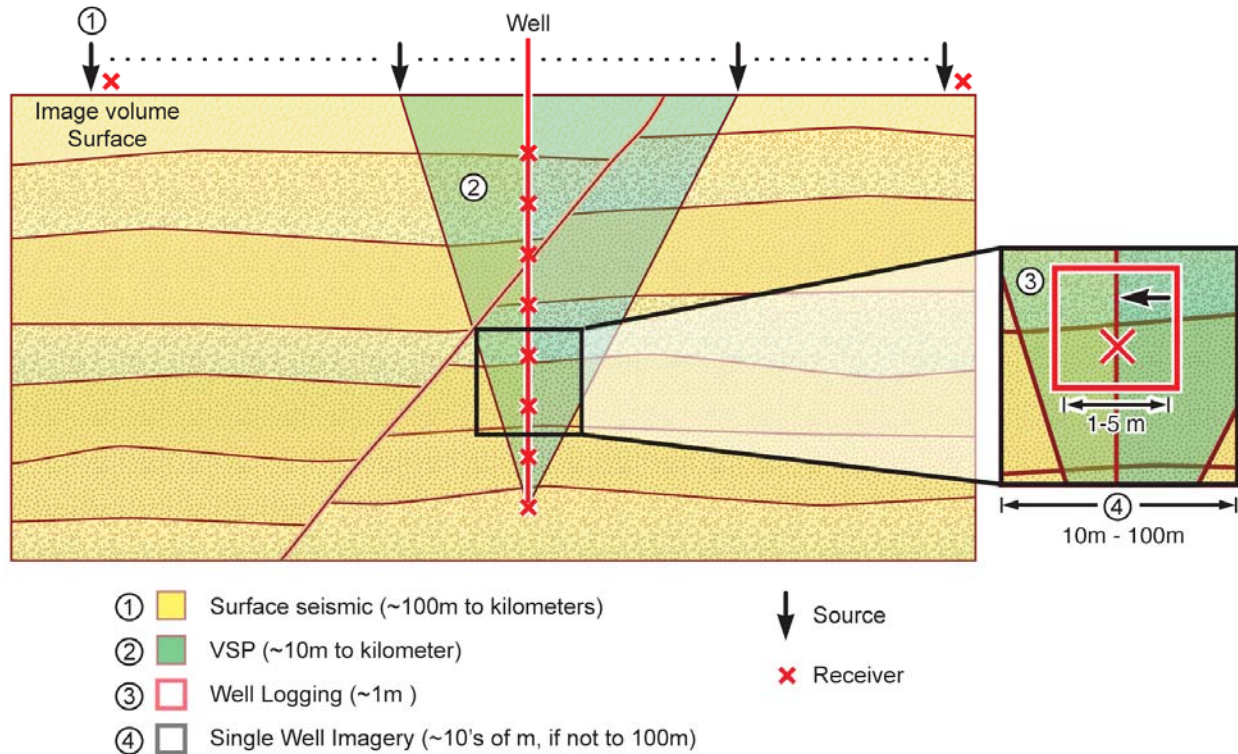


Figure 1.1. A schematic showing the different scales and resolutions of the seismic methods used in this study. As can be seen the scale of resolution range from the centimeter to the 10's of meters while the image volume ranged from the sub-meter to 100's of kilometers

Therefore, due to an ever increasing need to produce more and more domestic gas reserves in an efficient manner there is a need to develop reliable and cost effective methods for not only locating faults and fractures in the subsurface but for quantifying the nature of the fractures to determine the potential for being a productive gas zone. The subject project focused on seismic methods. In addition to the obvious advantage of seismic methods to map large volumes of the subsurface it was also due to the wide use of the seismic methods as well as the potential of expanding the current commercial methodologies to collect data for advanced analysis to successfully map the fracture properties of interest.

Therefore, the overall objective of the work was to extend current seismic technology to characterize and quantify naturally fractured gas reservoirs. **In essence the primary question posed was how does one use the right combination, scale and timing/sequence of seismic methods to locate and quantify the fractures controlling the productivity of a gas resource in naturally fractured reservoirs?**

At the beginning of this project in 2000 anisotropy was (and still is) widely used as an indicator of fracture content. P-wave AVO had been used to some success (it was also tried in this effort to compare to the other methods), however, one of the goals of this project was to go beyond simple anisotropy mapping. It is generally true that fractures affect seismic P- and S- wave anisotropy, but bedding, matrix velocity differences, micro-fabric and other geologic features also produce seismic anisotropy which must be separated from the features of interest. One of the

basic premises of this work was that seismic data collected at the right scale and proper quantity contains the information necessary to derive the fracture properties of interest. That is, one needs to go beyond anisotropy (see section below on rational of using seismic methods). It was anticipated that this could be accomplished by not only by using the more advanced methods but also revisiting current seismic techniques and reprocessing/reanalyzing the results to use data that was once thought to be noise. In other words determining if certain parts of the “noise” in seismic data is due to the target of interest, i.e. fractures affecting gas production.

As stated above a large segment of this work is based upon the hypothesis that to obtain the required resolution it is necessary to gather data at higher frequencies and with greater spatial sampling than surface based methods can provide. This implies that seismic information must be recorded by using sources and/or receivers placed in the subsurface to either supplement or replace information gathered with conventional surface seismic methods. Technology is currently being jointly being developed in the public and commercial sector that will enable emplacement of subsurface sources and receivers in the future in either semi-permanent or on a permanent basis in a cost effective fashion (for examples of technology development see <http://www.fe.doe.gov/programs/oilgas/index.html>). This is a leap in technology that we anticipate will be routinely implemented five to ten years in the future. This project was also meant to form the fundamental basis of implementing this technology on a cost effective basis.

In order to meet the above objectives LBNL became the lead institution of a comprehensive program between DOE, universities and industry for an integrated field-testing and analysis effort aimed at improving the fundamental understanding of seismic wave propagation in naturally fractured gas reservoirs. A cooperative research program was organized between LBNL and Conoco Inc. (now ConocoPhillips), Lynn Inc., Schlumberger Inc., Stanford University, and Virginia Technology University. In addition to the organizations above we have also been cooperating with the Edinburgh Anisotropy Project in the U.K. Two recent additions in the last year of the project have been HI-Q Geophysics and Sandia National Labs. The project was organized into tasks, which focused on field tests sites for experimental fieldwork and model validation. To that end a 20 square mile study area was selected in the San Juan basin to focus the work. LBNL and university personnel worked cooperatively with both the exploration and production departments of the petroleum companies to design integrated geophysical procedures and analysis techniques. Industry provided access to the field sites; data collected at the test and production sites, validation wells, participation in the planning and execution of the experiments, processing and modeling of the data as well as participation every step of the project. LBNL and the universities provided basic theory and modeling support to aid in the design of the investigations, and perform some of the characterization experiments. The analysis of the data was done by all of the participants.

## **1.2 RATIONAL FOR SELECTING SEISMIC METHODS**

The great majority of work in seismic imaging has been based upon the assumption that seismic waves are limited to detection of features, which are a significant percentage of the wavelength, i.e. resolution is normally assumed to be  $\frac{1}{4}$  of a wavelength and detection on the order of  $\frac{1}{10}$  of a wavelength. However, many seismic data sets were definitely observed to be affected by fractures, i.e. features much thinner than conventional theory would predict to be detectable. Over the last 10 to 15 years there has evolved two different approaches to considering the effect

of fractures on seismic wave propagation. 1. Considering the effect as an overall volume effect (continuum approach or effective moduli) and 2. considering the effect to be a function of discrete fractures.

The effective moduli theories (e.g., see Zimmerman, 1991) approach employs a static (i.e., zero frequency) approximation to develop analytic expressions for the anisotropic elastic moduli of an aligned population of microcracks (Nur, 1971; Hudson, 1981; Crampin, 1984) or planar fractures (Moreland, 1974; White, 1983; Shoenberg and Douma, 1988). Because this approach employs a zero frequency approximation, it does not predict attenuation that may result from reflection and scattering losses. Intrinsic attenuation can be included in these models by assuming that the cracks or void spaces of the fractures are filled with a viscous fluid producing viscous shear losses (O'Connell and Budiansky, 1977). Another disadvantage is that cannot be used to look at individual effects of fractures.

Prior to our work it was long suspected that static effective moduli theories for fractured rock may have a limited range of applicability, particularly at reservoir and engineering field scales where frequencies may be well into the kilohertz range. For example, frequency-dependent transmission losses have been observed in field and laboratory seismic measurements in crystalline and clastic rocks containing natural and artificial fractures (e.g., Morris et al, 1964; Kleinberg et al., 1982; Medlin and Marsi, 1984; King et al., 1986; Pyrak-Nolte et at, 1990a). The laboratory measurements of Pyrak-Nolte et at (1990a) clearly illustrate that a fracture behaves like a low pass filter which attenuates the wave by removing the high frequency part of the signal and introduces a frequency-dependent phase delay. In addition, static effective moduli theories do not predict the existence of guided waves such as the large amplitude interface waves observed by Harris (1988) in his 1 - 5 khz crosswell measurements across thin beds of sedimentary rock.

An alternative to the continuum approach for modeling seismic wave propagation in fractured rock is to treat each fracture separately and to examine the velocities and amplitudes of the transmitted and reflected P-and S-waves. A new theoretical development, displacement discontinuity, predicts a number of effects from discrete fractures beyond what the equivalent media theories give us. These include scattering effects, guided waves, and frequency dependent transmission and reflection effects. Extensive theoretical and laboratory work (Meyer et al 1985) established that the key parameter characterizing a discrete fracture in this new approach is the specific stiffness across the fracture. The additional effects predicted by this theory beyond the usual anisotropy are usually treated as "noise" in typical seismic processing schemes, and much work is expended to eliminate them from the final processed data. However, if processing methods that enhance rather than eliminate these effects can be developed, such effects could be identified in the various seismic data sets. Once identified, sophisticated modeling could then be applied to interpret these effects in terms of the specific stiffness' of fractures, which can then ultimately be related to characteristics of the fractures affecting fluid flow such as aperture.

### **1.3 GEOLOGIC SETTING AND STUDY AREA**

In order to properly design and interpret seismic surveys for fracture detection in the San Juan Basin (or any other site) it is necessary to have geologic information on the fracture characteristics expected in the subsurface as well as information on the general lithology in

which the resource is expected to occur. This discussion is not intended to be a detailed description of the entire geologic and stress conditions in the San Juan, but a general overview of the significant properties possibly affecting the fracture properties and how they may relate to the seismic imaging of fractures and faults. A detailed overview can be found in Lorenz and Cooper (2003), and a more complete description can be found in Lorenz and Cooper (2001). Much of the discussion that follows is derived from these two sources.

The San Juan Basin of northwest New Mexico and southwest Colorado is the second-largest gas field in the conterminous U.S., second only to the giant Hugoton field of Texas, Oklahoma, and Kansas. Figure 1-2 shows the general location of the field. The relatively recent (since the 1970's) development of the Fruitland coal-bed methane (CBM) reservoir has doubled previous estimates of ultimate recoverable gas reserves for the basin from 25 TCFG (for the fractured sandstone reservoirs) to more than 50 TCFG for all gas reservoirs in the basin. To date the basin has produced in excess of 31 TCFG; CBM from Fruitland coals accounts for 9 TCFG. Cumulative oil production is more than 300 million barrels. The basin contains more than 300 oil and gas fields that produce from Paleozoic, Jurassic, Cretaceous, and Tertiary reservoirs, but more than 93% of the oil and 99% of the gas in the basin has come from Upper Cretaceous rocks. Nearly all of the non-CBM gas in the basin has been produced from three fractured-sandstone reservoirs in the Dakota Sandstone, Mesaverde Group, and Pictured Cliffs Sandstone. These reservoirs have produced nearly 21 TCFG. Down-spacing and infill drilling has occurred in the fractured-sandstone reservoirs resulting in the production of "new" gas and reversing the decline in gas production from these reservoirs (Fassett, 2002).

The basin overall is structurally simple, a broad syncline stretching over about a 100 miles, however, different tectonic events have combined to create complicated fault patterns in the basin when one looks in detail. Production currently takes place from a self-sourcing shale/sand bar sequences called the Mesaverde formation (Mississippian) and to a lesser extent from a deeper (Pennsylvanian) Dakota sands. Permeability in both cases is controlled by fractures.

The Mesaverde Formation, which was the primary target of this work, producing primarily from the Blanco Field in New Mexico and the Ignacio Blanco Field in Colorado, has produced over 10 Tcf of gas from over 6600 wells in an area covering over 2500 square miles. An analysis of the production decline trends show that in many areas of the reservoir, down spacing of the field from 320 acre to 160 acre units in during the 1970's and 1980's yielded significant incremental reserves. The historical relationship between parent wells and infill wells shows that in most cases, the infill wells have reduced rates and reserves when compared to the parent wells. However, the infill wells do not appear to significantly impact the decline trends of the parent wells because of their incremental reserves. In some areas, infill wells have resulted in modest rate increases in offset wells. Preliminary results from over 1000 wells drilled since the 80 acre spacing was approved indicate that a similar trend will be expected as more of the reservoir is drilled on 80 acre spacing. Some infill well pressure tests show higher than expected reservoir pressures in what was believed to be highly depleted parts of the reservoir. These observed pressures are related to the low permeability and fracturing of the reservoir. They show that there is significant future production potential for this aging gas field (Hale et al., 2002).



Figure 1-2. The general location of the San Juan Basin in the U.S.

The basin is asymmetric and has strata dipping gently to the northeast toward an off center synclinal hinge located near the Colorado-New Mexico state line. The general shape and structure are shown in Figure 1-3. Also shown in figure 1-3 is the 20 square mile study area that was selected for this work. In this area there were existing wells, a newly acquired 3-D P-wave surface seismic data set, and the location where two new wells were to be drilled by ConocoPhillips to serve as validation and study wells.

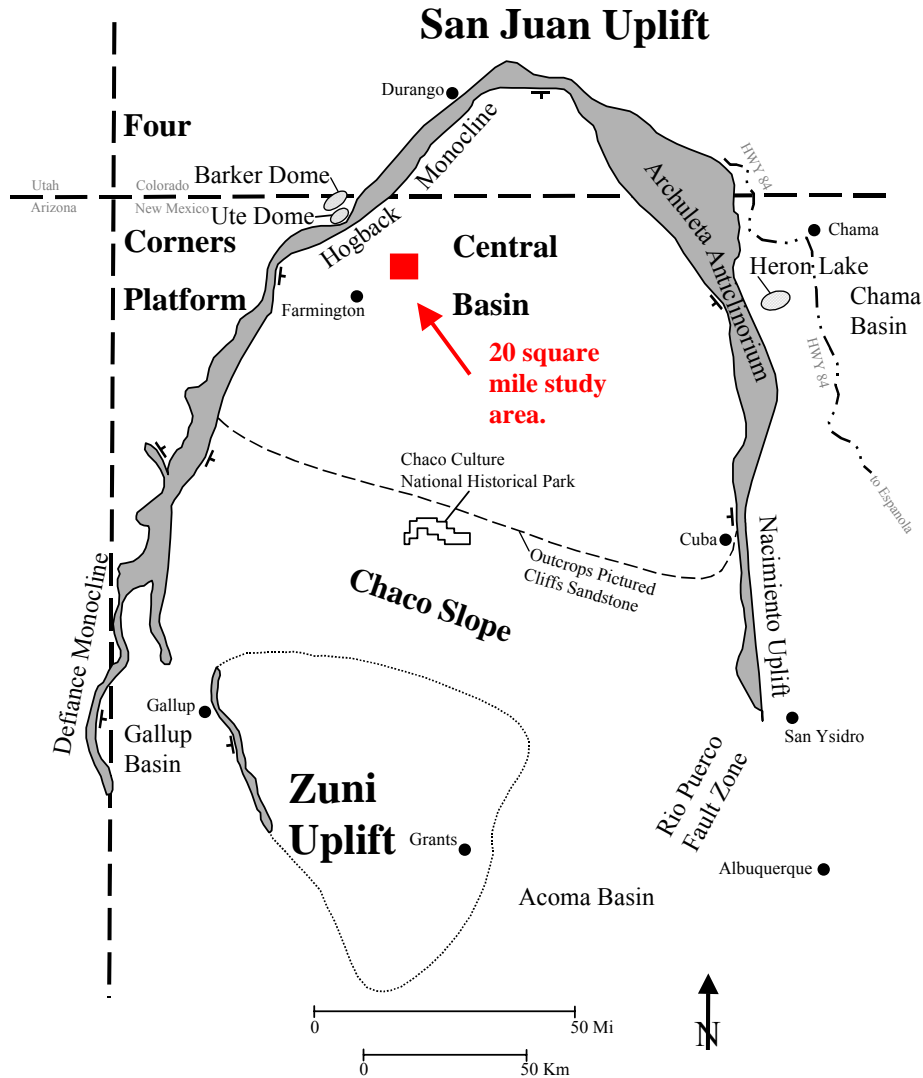


Figure 1-3. Index map showing the structural elements of the San Juan Basin. Also shown is the approximate location of the 20 square mile study area used in this work (red box). Areas of steep dip (monoclines) are shown as patterned areas with the direction of dip indicated by strike and dip tic marks; long dashed line separates the Chaco Slope from the Central Basin and is drawn approximately where the Pictured Cliffs Sandstone is subaerially exposed (modified from Lorenz and Cooper 2003).

Figure 1-4 shows a SW-NE cross section through the basin and the units of interest to this study, i.e. the Mesaverde and the Dakota sand stones. These are interlaced with shale beds and overlain by more extensive shale formations.

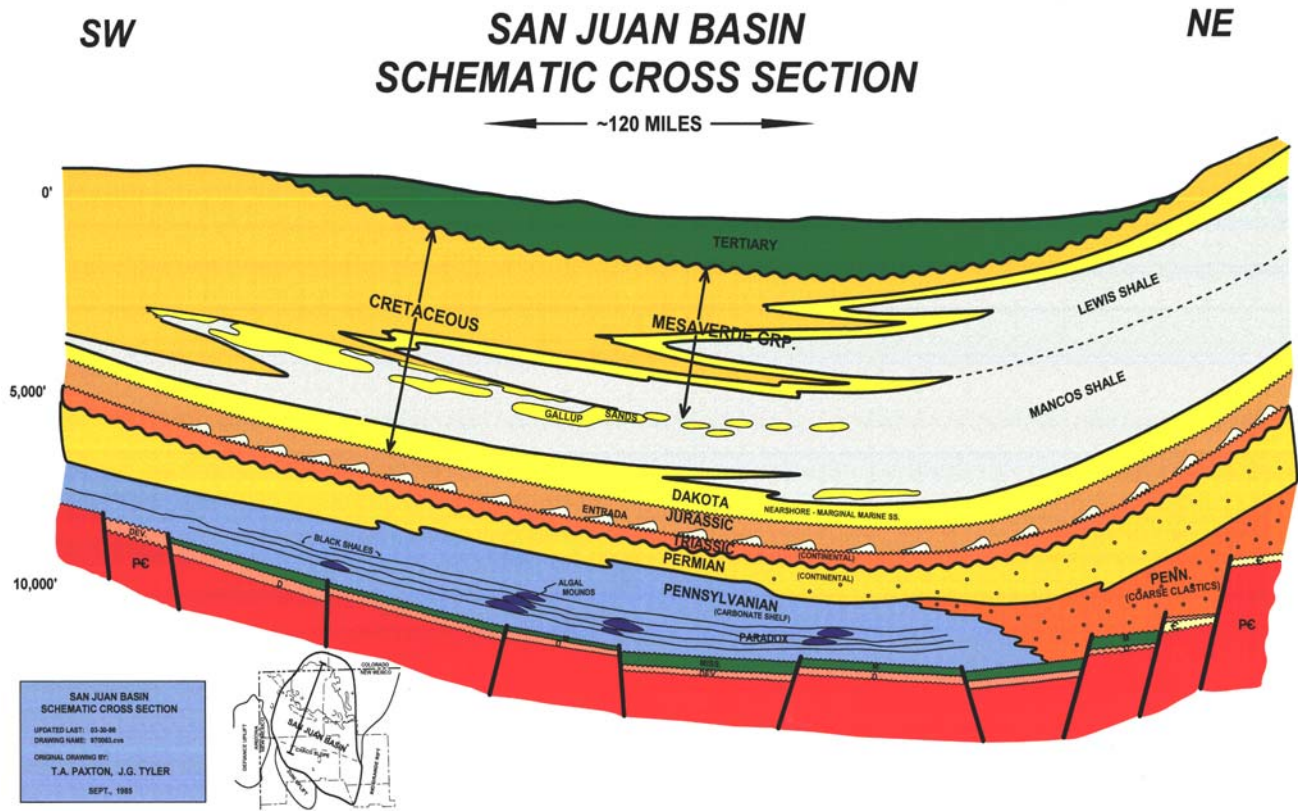


Figure 1-4. A SW-NE cross-section through the San Juan Basin showing the general lithology and dips of the formations of interest, i.e. the Mesaverde and the Dakota formations.

The San Juan Basin is a product of several different events, which have combined to form the present day structure and lithology. This is important to remember when one is trying to image the fracture content because the seismic methods essentially integrate all of the history of the volume it is imaging. The main features bounding the basin are the San Juan uplift to the north, the Hogback and Defiance uplift to the west, the Zuni uplift to the south, the Nacimientto uplift to the southeast, and the Archuleta antiformal structure to the northeast (see Figure 1-3). One of the primary events affecting the structure and fracturing was the Laramide orogeny that extended from the Cretaceous through the Eocene periods. This event translated the Colorado Plateau northeastward with respect to the Rocky Mountain foreland, thus rotating the area (and the San Juan Basin which lies in the southeast corner) several degrees clockwise.

Also of major importance are the lithology and structure of the Precambrian tectonic elements underlying the San Juan basin (Figure 1-5). It is important to point out in the context of this work, that information from geologic mapping may provide useful clues about the present day fractures that may be controlling the hydrocarbon production. In an area such as this where there have been many different geologic and tectonic events occurring throughout the eons, there are many separate events which have the potential to cause faulting and fracturing. As time progresses the prior event will to some extent control the later fracturing, even if the stress distributions have changed over time.

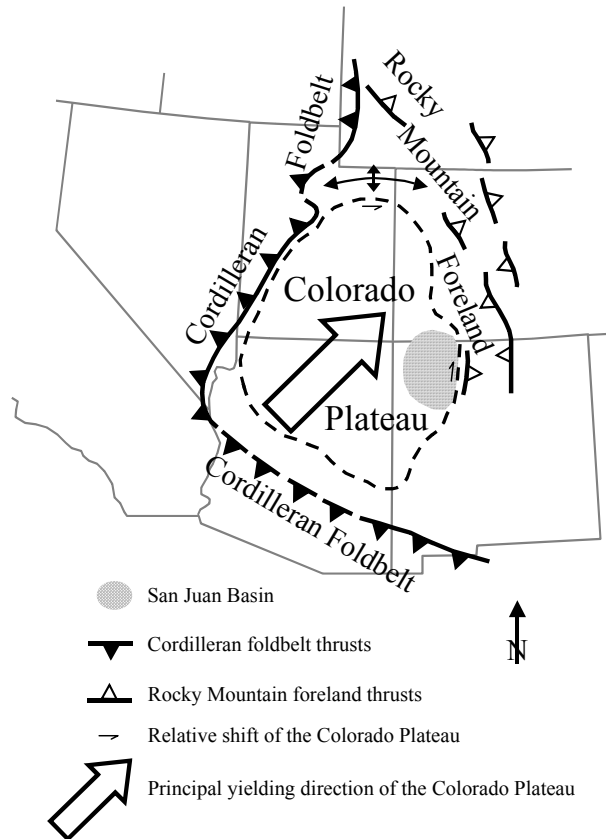


Figure 1-5. The Tectonic elements in the southwest U.S. affecting the underlying structure of the San Juan Basin (modified after Woodward and Callender, 1977).

The observed fracture and structure characteristics in the northwestern part of the San Juan basin can be explained as the superposition of two Laramide fabrics, both related to the reactivation of basement faults in different ways.

1. The floor of the San Juan Basin, which superficially appears to be relatively structure-less, is underlain by a Paleozoic and Precambrian basement cut by numerous ancient faults trending NE-SW and NW-SE (Taylor and Huffman, 1998). Reactivation of these faults created and controlled localized local fracture patterns in the overlying strata. The ConocoPhillips structure maps show common small-scale offsets within the Cretaceous strata, faults that were propagated upward from the basement when subjected to Laramide continental-scale stresses. The northeast-trending basement faults seem to have been preferentially reactivated.

2. The more widespread, regional, north-south striking, background/regional fracture patterns owe their existence and orientation to southward indentation into the basin of the San Juan dome from the north which imposed strong horizontal compressive stresses onto the basin-filling strata, which fractured them. The basement-cored San Juan dome was uplifted along reactivated basement faults in response to the same Laramide stresses, but in this case they accommodated considerably larger offsets.

The Laramide orogeny, extending from latest Cretaceous through Eocene time, was the first tectonic event to influence the San Juan Basin following deposition of the Dakota and Mesaverde strata under study. Reconstructions suggest that the Colorado Plateau, which encompasses the San Juan Basin within its southeastern corner, was translated northeastward with respect to the Rocky Mountain foreland during the Laramide orogeny (Figure 1-5) (Kelley, 1957; Woodward and Callender, 1977; Chapin and Cather, 1981; Woodward et al., 1992). In the process, it may have been rotated several degrees clockwise about a pole in northern Texas (Hamilton, 1981; 1988). Numerous northeast-facing Laramide folds within the Cordilleran foldbelt of southwestern New Mexico (Corbitt and Woodward, 1973) document related northeastward yielding.

Most of the strain recorded by the pervasive fracturing of Cretaceous strata within the San Juan basin, however, was caused by the displacement of the San Juan and Zuni uplifts toward each other, with the San Juan basin caught between them. The local kinematics were secondary effects of the larger-scale plate tectonics, which jostled the basement blocks in the crust below the San Juan basin along ancient faults. Jostling at the lithospheric level raised some basement blocks, such as the San Juan and Zuni uplifts, into block-faulted units which were also thrust laterally into the adjacent basin, affecting stresses and creating fractures in the shallower, sedimentary strata. The stress orientations within the sedimentary units filling the basin were the result of the frontal configuration and indentation vectors of these uplifts, and were only indirectly related to the more regional plate motions and geometries. Orientations of the pre-existing faults, more than the orientation of the deep crustal stresses or directions of plate motion, dictated the geometry of the resulting structures. In general the resultant stress trajectory was N-S to NNE-SSW within the San Juan basin, as recorded by the fracture sets within the Dakota Sandstone and Mesaverde Group.

Concurrent with indentation from the north and south, basement blocks on either side of the Hogback monocline were transpressively wrench-faulted against each other with a right-lateral sense of motion. Deep-seated Laramide strain was accommodated by basement thrusting at the northern and southern basin margins, and by basement wrenching at the eastern and western margins.

The resulting compressional and shear strains in the strata of the basin are recorded by N-S to NNE-SSW striking vertical extension fractures within the Mesaverde Group and Dakota Sandstone along with conjugate fractures in the Dakota. High horizontal stresses, coupled with overpressuring in Eocene to Oligocene time, would have produced stress conditions and mechanical properties favorable to fracturing. Most of the observed fracture characteristics and orientations are compatible with this N-S to NNE-SSW shortening within the San Juan Basin.

Support for this interpretation lies in the two pairs of conjugate shear fractures that are present locally in Dakota strata at the northern edge of the basin (Lorenz and Cooper, 2001), and in a recently discovered, east-west striking vertical stylolite in the Dakota section east of Durango. The formation of these structures requires an exceptionally strong N-S compressive stress. One conjugate pair has a bed-parallel axis of intersection and the other has a bed-normal axis of intersection, but both have bed-parallel, acute-angle bisectors that strike approximately N-S. These conjugate, strike-slip and thrust-oriented fracture pairs are consistent with a southward-

directed horizontal compressive force, one that exceeded the magnitude of the overburden stress at the time of formation at these locations.

Other conjugate shear fractures suggest that locally, specifically on the eastern margin and in the southeastern corner of the San Juan basin, the maximum horizontal compressive stress was oriented NE-SW (Lorenz and Cooper, 2001). These conjugate geometries may be related to a late-Laramide stress superimposed locally onto strata in the corners of the basin. The most likely source of NE-SW compression in these parts of the basin is a change from wrench faulting to overthrusting along the Nacimiento front (Woodward et al., 1972), resulting in compression of the strata between that front and northeastward indentation of the Zuni Uplift.

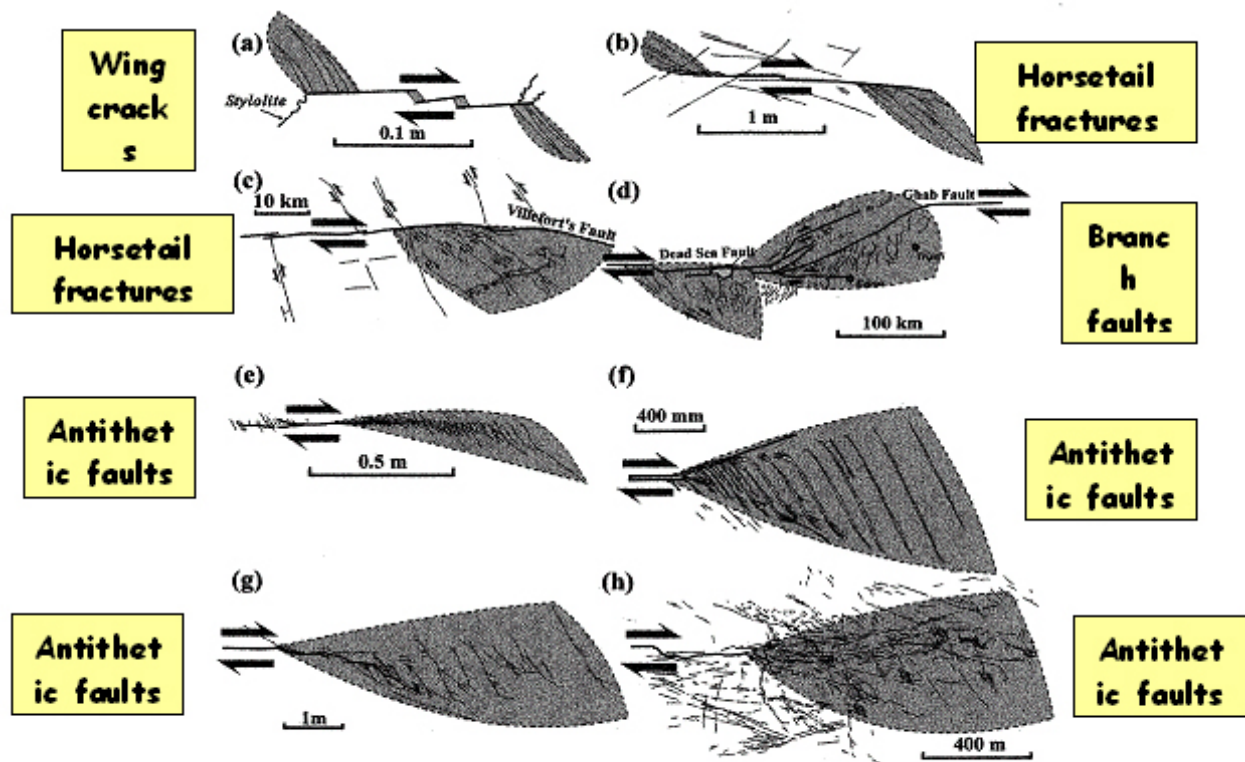
It is often assumed that the N-S striking extension fractures in the San Juan basin formed under conditions of Miocene and younger, E-W Rio Grande extension. However, extension would not produce the observed strike-slip or reverse-dip-slip conjugate fracture patterns. Only significant compression is capable of forming such conjugate geometries, and only the Laramide orogeny produced high horizontal compressive forces, let alone compression of any sort, in the region of the San Juan basin during post-Jurassic time. It is unlikely that the strata hosting N-S extension fractures would have remained unfractured during the high-stress, N-S Laramide compressive conditions that formed the observed conjugate fracture systems. It is plausible, and more likely, that the extension and conjugate fracture systems are genetically related to the Laramide N-S thrust events, a correlation that is strongly supported by the common symmetry axes of the two fracture systems.

Laramide shortening was replaced by incipient Basin and Range extension in west-central New Mexico approximately 36 million years ago (Cather, 1989), and extensional structures related to the Rio Grande Rift have overprinted parts of the San Juan basin. The E-W, Basin and Range extensional tectonic system has axes of symmetry that are, coincidentally, nearly parallel to the shallow Laramide stress axes. However, whereas Laramide tectonics were derived from an increase in the N-S horizontal compressive stress, the later, extensile regime involved a decrease in the E-W horizontal compressive stress. Some large-scale paleostress indicators, such as the Miocene, N-S trending, Archuleta dike swarm in the northeastern corner of the basin, represent a response to Rio Grande rift extension.

Post-Laramide extension fractures with N-S strikes could have formed in the Cretaceous strata in this extensional setting. However, earlier fracturing is the preferred interpretation because extension can not account for the conjugate fracture pairs, numerous examples of shear, or for the north-south thrusting seen in the outcrop and subsurface at several scales. Baltz (1967, 1978) in fact suggested that there is little or no evidence for Late Tertiary E-W extension across northern New Mexico, other than the normal faults which accommodate the rift itself and the N-S striking igneous dikes.

An important concept in this work is not only the faulting, but also the type of faulting and the implications it has on the fracturing or “damage” associated with the faulting. For example, Figure 1-6 shows a conceptual diagram of different types of damage or fracturing that may occur with different types of faulting or failure. It is important to note that depending upon which type of failure occurs different zones are affected as well as the resulting “damage” or fracturing. It is

easy to imagine that the fracturing will become more complex as different tectonic events occur and the latest faulting interacts with past faulting.



Kim, Peacock & Sanderson, 2004

Figure 1-6. Conceptual diagrams of the size and effect of different styles of faulting on the surrounding material.

In terms of fracturing that has been inferred from mapped surface features, Lorenz and Cooper (2003) state that “The Cretaceous strata that fill the San Juan Basin of northwestern New Mexico and southwestern Colorado were shortened in a generally N-S to NNE-SSW direction during the Laramide orogeny. This shortening was the result of compression of the strata between southward indentation of the San Juan Uplift at the north edge of the basin and northward to northeastward indentation of the Zuni Uplift from the south. Right-lateral strike-slip motion was concentrated at the eastern and western basin margins of the basin to form the Hogback Monocline and the Nacimiento Uplift at the same time, and small amounts of shear may have been pervasive within the basin as well. Vertical extension fractures, striking N-S to NNE-SSW with local variations (parallel to the Laramide maximum horizontal compressive stress), formed in both Mesaverde and Dakota sandstones under this system, and are found in outcrops and in the subsurface of the San Juan Basin. The immature Mesaverde sandstones typically contain relatively long, irregular, vertical extension fractures, whereas the quartzitic Dakota sandstones contain more numerous, shorter, sub-parallel, closely spaced, extension fractures. Conjugate

shear planes in several orientations are also present locally in the Dakota strata.” In any case the structure and complexity of the basin varies from somewhat simple to highly complex.

### 1.3.1 Core Studies

Core studies were undertaken by this project during the last six months of this project to provide validation and geologic input to the interpretation. Core was examined which was derived from the Mesaverde and Dakota formations from three different wells near the study area to examine the nature of the fracturing in the subsurface. It should be pointed out that most of the well bore studies (VSP, single well and well logging) was done in the Mesaverde with the well logging the only method done in the Dakota. Thus our prime interest was in the Mesaverde, but the data was also relevant in order to derive an overall model of the fracture system in the area. One set of core from the Meridian Sunray H Comm 6 well, located in section 11, T 30 N., R. 10 W came from a location approximately ten miles southeast of the study area, which was the closest Mesaverde core that was available. Cores from two other wells, the San Juan 28-7 #238R and the San Juan 28-7 #225E were also examined. These cores were from a field approximately 35 miles southeast of the 20 square mile study site, but they were worth examining because conventional knowledge was that fracture orientations and characteristics have been relatively consistent across the San Juan basin (e.g., Lorenz and Cooper, 2002). Appendix I has photographs of the core examined.

The #225E core consisted of 110 ft of the unoriented slabs and butts of a four-inch diameter core; core from the #238R well is 143 ft long, but only the slab faces of a smaller (2 5/8ths-inch) core were available. Scribe lines on the 238R core surface suggested that it was originally oriented, but we did not have the orientation survey and without the butts one could not tell which was the orientation scribe line, thus the fractures in this core could not be oriented. Both cores were taken in the Dakota Sandstone, somewhat deeper than the Mesaverde interval that is of primary interest at the test site. However, fractures indicate that the entire section was stressed and that the Mesaverde sandstones are likely to be fractured as well.

In the San Juan 28-7 #225E core twenty-nine coring-induced petal and petal-centerline fractures visually dominated this core (see Appendix I). However, 16 natural fractures were also present, ranging from 0.2 to 1.0 ft in vertical extent along the core axis. The fractures terminated vertically at clay partings, at stylolites, at changes in lithology, and sometimes within homogeneous lithologies. A few fractures were less than vertical and exit the core before terminating. Few natural fractures were present in the dark, highly bioturbated sandstones that dominate the upper parts of the core. This is probably due to the ductile mechanical properties of such strata created by the inclusion of clays and organic materials into the sand during burrowing. Most of the natural fractures occurred within the cleaner, more tightly cemented sandstones. Examination of the core butts showed that fracturing can be intense in the thinner (one-foot thick) beds of clean sandstone, with parallel fractures a few inches apart (i.e., at a depth of 7108 ft). Average fracture vertical height is about half a foot, and total cumulative fracture height is 8.1 ft, thus about 7% of the total core length contains vertical natural fractures.

Five of the natural fractures were poorly mineralized with patchy calcite. Calcite is more common near the narrow vertical terminations of fractures, the wider mid parts of many fractures being apparently unmineralized. Six of the natural fractures display no mineralization within the limited confines of the rock sampled by the core. One fracture contained patches of stellate,

iron-rich dolomite (Mike Dixon at Omni Labs X-rayed it for composition). Fracture apertures ranged from about 0.1 mm to about 0.5 mm: these are remnant, open apertures, not the widths of the occluding mineralization.

Absolute fracture orientations could not be determined in this well. However, fractures can be related to petal fractures in three instances in this core, where they have parallel strikes. Since petal fractures usually record a consistent regional stress field (Lorenz et al 2001) they can be taken as a constant, probably with a NNE strike, and most of the natural fractures thus are also probably parallel to one another, and probably strike close to NNE. However, one example was noted where a fracture strikes 50 degrees counter-clockwise to a petal fracture. This particular fracture is also anomalously mineralized as noted above. No crosscutting relationships were cored so the relative age of this fracture with the others cannot be determined. However, this fracture suggests that there is a subordinate fracture set in this reservoir, probably striking NE to ENE.

In the San Juan 28-1 #238R well eight vertical natural fractures and five inclined natural fractures were found in this core. Since the slab faces of the small diameter core represent an extremely small sampling of the reservoir, the total, cumulative fracture height of the inclined and vertical fractures (6.3 ft) is significant. Fractures are confined to the well-sorted, well cemented sandstones: the high-porosity, poorly sorted, coarse grained sandstones and conglomerates in this core are not fractured. This coarse-grained facies accounts for approximately 80 of the 143 ft of core from this well and an additional 12 ft of core is from unfractured black shale lithologies, thus over 10% of the remaining 51 ft of fracture-prone, clean sandstone lithologies contains natural fractures.

The eight vertical fractures, ranging from 0.1 to 1.5 ft in vertical extent, terminate most commonly at partings, stylolites, and lithology changes. The five inclined natural fractures are 0.2 to 1.0 ft in minimum vertical extent along the core, typically exiting the core before terminating. They have an en echelon character, suggesting that they represent a conjugate fracture set with a vertical bisector to the acute conjugate angle. This fracture set was not noted in the #225E core.

Two other fracture sets were found in this core but not in the #225E core. Nine short (<0.1 ft high) gashes extend from the teeth of the larger stylolites. As seen in other cores across the basin, these can locally form horizons of interlocking fractures in stylolite-bearing zones. The other fracture set consists of horizontal shear planes, over 25 logged, that locally break the white, well-cemented sandstone intervals into poker-chips (as many as 14 shear planes in the interval between 7194 ft and 7197 ft). These fractures indicate horizontal shear with movement in the same direction as the strike of the natural fractures, but their origin is poorly understood.

Only three petal and petal-centerline fractures were noted in this core, but three other artificial fractures, created by the wedging action of the scribe knives are present. These scribe-knife fractures split the core and can be mistaken for unmineralized natural fractures, especially where the induced fracture joined a pre-existing mineralized natural-fracture plane (i.e., at depth 7173 ft).

As with the #225E core, the natural fractures strike parallel to petal and petal-centerline fractures where such a relationship can be pieced together. However, one piece of core (at 7275 ft) displays the intersection of two vertical natural fractures at an angle of 35 degrees. This is similar to the 50-degree angle noted for the intersection between an anomalous fracture and a petal fracture in the #225E well, supporting the inference that a minor secondary fracture set exists at depth.

In terms of the core from the Mesa Verde (our formation of interest) one hundred and eighty-seven feet of core were available, but not all of it was the optimum full-diameter, four-inch core. See appendix I for pictures of the core examined. Twenty-six of this 187 ft consisted of only the slab faces of small-diameter (1.5-inch) core. Of the remaining 161 ft of 4-inch core, only the slab faces were available for all but 60 ft: slabs and butts both are available for the remaining 60 ft. Because this is such a small lateral sampling of the reservoir, the presence of numerous fractures in this core suggests that the reservoir is significantly fractured.

The main findings were that natural fractures are present in the sandstones and siltstones in this core but no fractures or faults were encountered in the shales and mudstones, so natural fracture distribution is possibly controlled by lithology. Some of the sandstones are highly bioturbated marine sandstones, and these do not contain fractures: presumably the introduction of muddy and organic materials during burrowing altered the mechanical properties, and this facies is not susceptible to fracturing (consistent with observations made from outcrop and other cores around the basin).

Numerous fractures were found to be present. If the multiple associated strands of fracture families are counted individually, at least 40 vertical extension fractures are present in the core. If they are lumped, the fracture count drops to around 30, still a significant number. The heights of individual natural fractures ranged from 0.1 ft to 5.0 feet. One remarkable natural fracture system consisting of 5-7 fracture segments extended for 16.7 ft along the core axis, starting at the top of a 24.6 ft thick sandstone and exiting the core downward. The lower termination is somewhere outside of the core: presumably the fracture extends downward through the remaining eight of sandstone and terminates at the underlying shale. A total of approximately 28.6 ft of cumulative fracture height is present in the 187 ft of core, so 15% of the total core height contains fractures. However, only 108 ft of core length consists of fracturable sandstones and siltstones, and 26% of these lithologies contain fractures. This can be further subdivided: 68% of the thickest sandstone is fractured, and 14% of the remaining sandstone and siltstone beds contain fractures.

Mineralization was found only locally along the fractures being more common in the siltstones and where the fractures start to narrow near a shale boundary. Where present, mineralization consists of scattered patches of calcite one to four millimeters in diameter. None of the early, crystalline quartz fracture mineralization phase that is common in other Rocky Mountain basins was observed. Open fracture apertures ranged from 0.1 to 1.0 mm. Two instances were cored where natural fractures trend parallel to the maximum horizontal compressive stress as indicated by the strikes of associated petal fractures. Four examples were cored where natural fractures strike parallel to each other. No examples were cored where natural fractures strike oblique to each other or to associated petal fractures, and no fractures with anomalous mineralizations or characteristics were cored. Therefore the evidence suggests that a single, sub-parallel fracture

set is present in the subsurface, unlike the Dakota examples reported on earlier where a secondary fracture set is present in the subsurface.

The main conclusions of the core studies was that the cores from the Dakota Sandstones contain a significant number of fractures, with approximately 10% of the fracture-prone clean sandstone facies containing vertical and/or inclined fractures. However, the high porosity, poorly cemented, coarse-grained lithologies appear to contain few if any fractures. Most of the fractures have parallel strikes, probably about NNE, although a minor oblique population (probably striking ENE) is also present in the subsurface. These fractures have the potential to affect seismic signals.

Observations in the Mesaverde core suggest that a single set of parallel-striking, vertical extension fractures is present in the subsurface, and that they strike parallel to the present-day maximum horizontal compressive in situ stress. Fifteen percent of the total core length contains fractures, and 26% of the fracture-prone sandstones and siltstones are fractured. A fracture family is present in 68% of the thickest (25-ft thick) sandstone. Fractures in this principle reservoir consist of multi-stranded fracture families that extend top to base of the reservoirs. These observations suggest that the reservoir strata contain significant numbers of sub-parallel fractures. Last but not least, for comparison to the core observations Figure 1-7 shows the fracturing that occurs in out crops. As can be seen there is significant jointing and fracturing observed in the outcrops at scales of sub-meters to 10's of meters over the scales of the outcrop. Several obvious questions are, can one extrapolate these observations to the subsurface, which fractures are controlling the gas flow, and can seismic methods be used to quantify the fracture patterns?

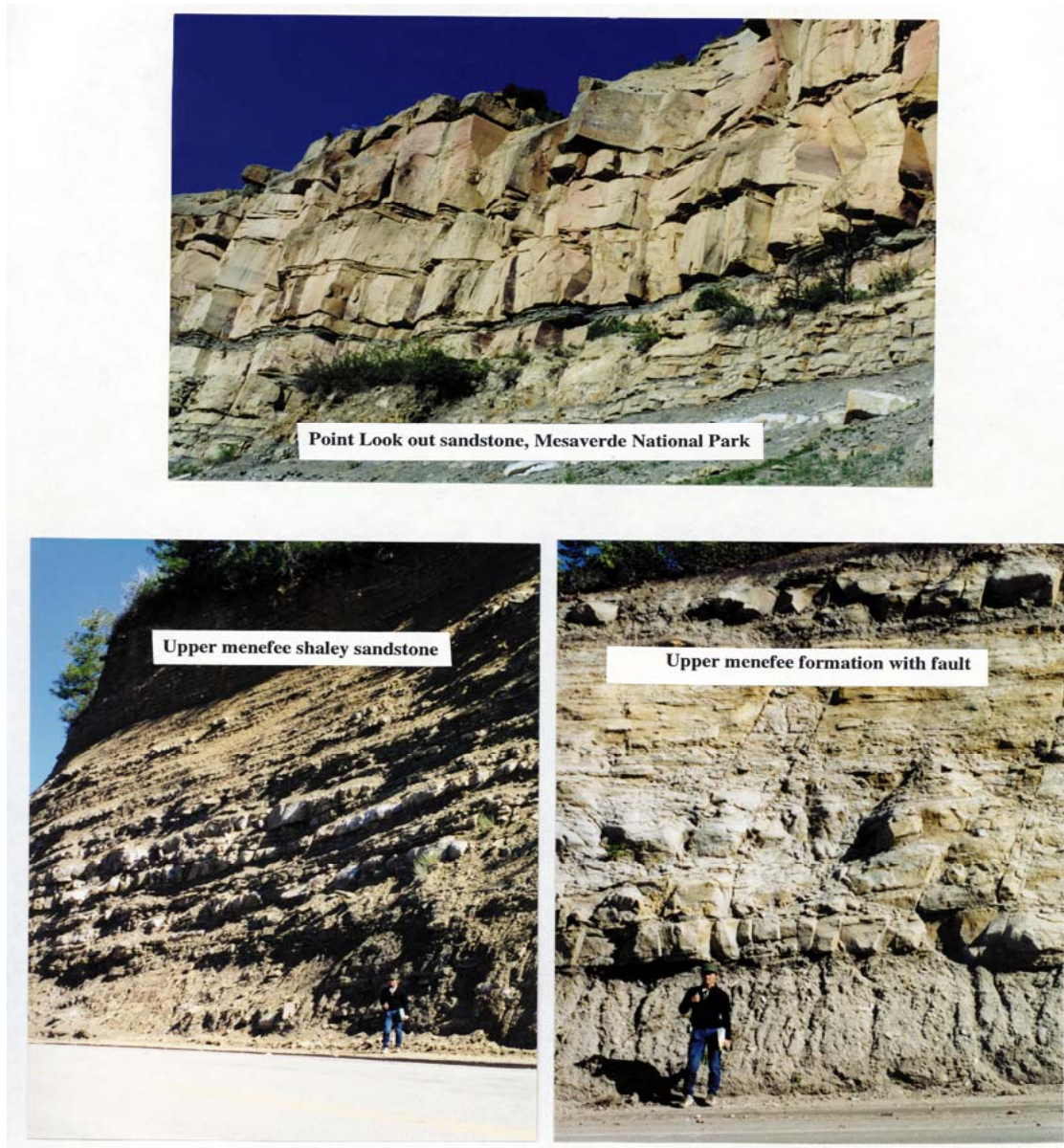


Figure 1-7. Some examples of fracturing in the San Juan basin in the Mesaverde.

### 1.3.2 Evidence of Faulting and Fracturing from 3-D P-wave Surface Seismic

Prior to the initiation of this study, a large amount of seismic data, both 2-D and 3-D, had been recently acquired in the San Juan Basin. Figure 1-8 displays the location of the 20 square mile study area relative to the much larger ~ 500 square mile P-wave survey assembled in 1998. Also shown in Figure 1-8 is the Mississippian seismic depth structure map. For reference the Hogback fault is depicted in yellow. The generally gentle regional NE dip is interrupted in areas by major basement faulting, a characteristic of this region (sub-sea depth scale at lower left side, reds are structurally higher, the blues are deeper).

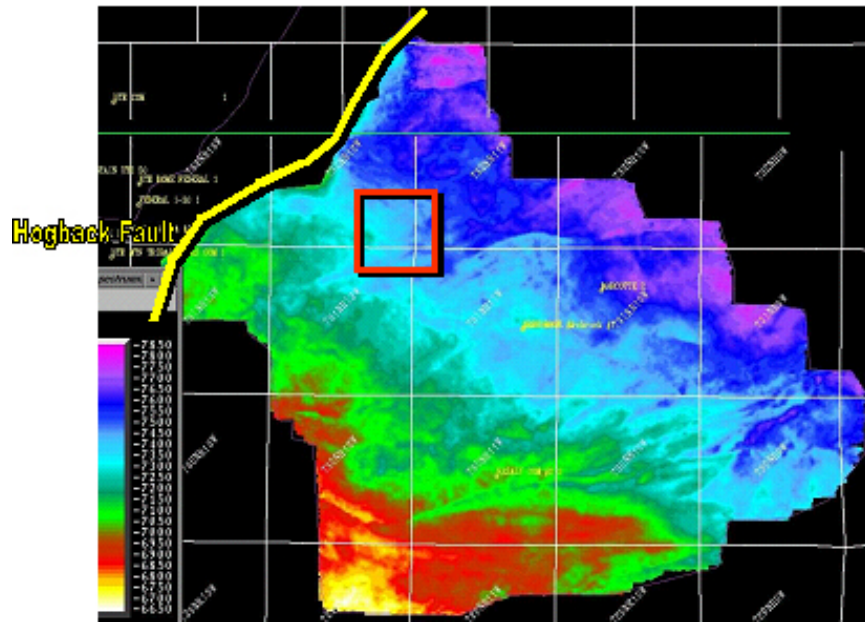


Figure 1-8. The location of the seismic study area (20 square mile red square) superimposed upon the location of the “large 3-D” P-wave seismic reflection. The structural horizon shown is the top of the Mississippian carbonates

An expanded view is shown in Figure 1-9.

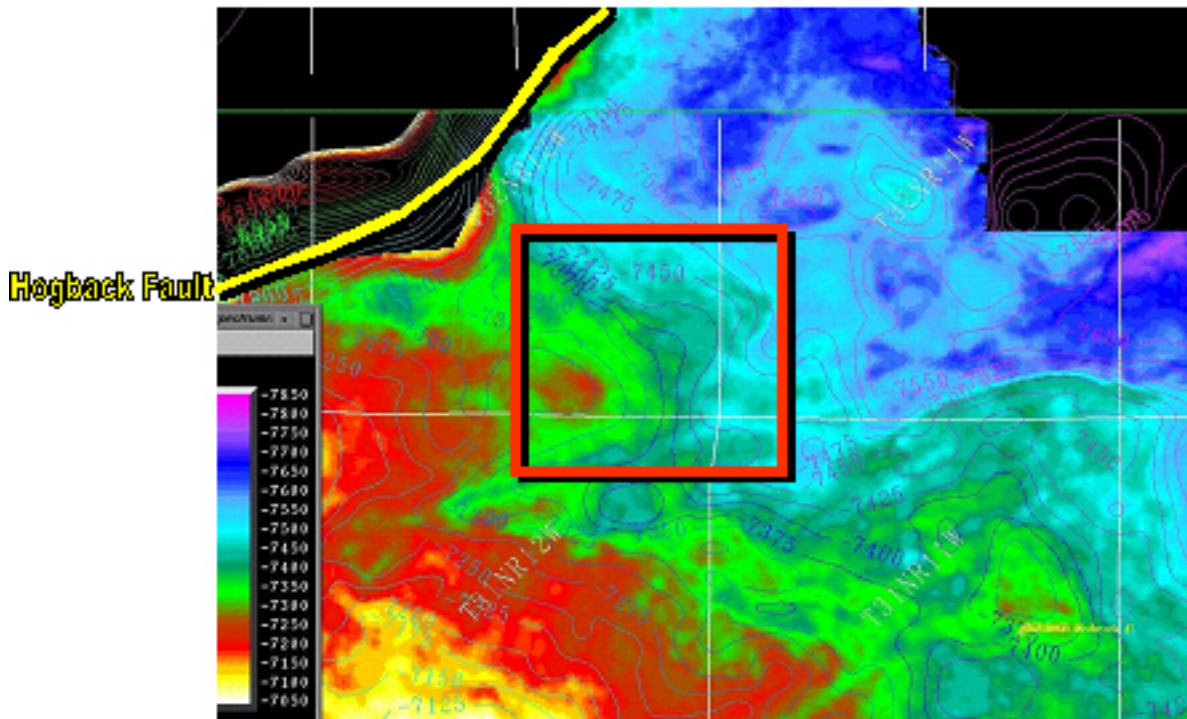


Figure 1-9. An expanded view of the 20 square mile study area in Figure 1-8.

A 2D-3D seismic interpretation performed by Conoco just prior to the beginning of this project and integrated with known geologic data was used to map the lower Paleozoic and Precambrian basement fault structure for the entire San Juan Basin and is displayed in Figure 1-10.

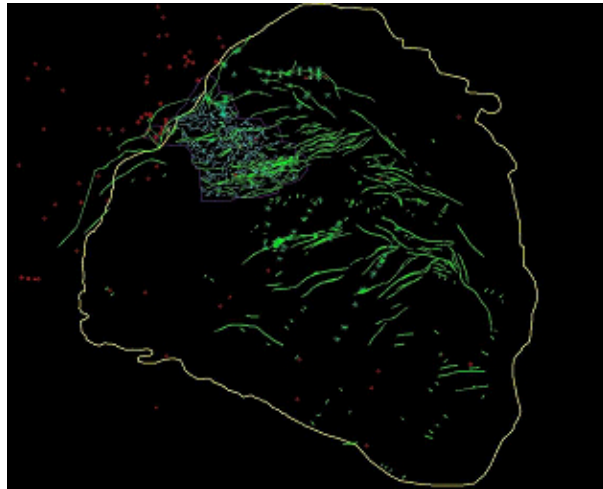


Figure 1-10. The fault structure derived from a compilation of 2-D and 3-D seismic data.

Shown in this figure are the faults defined only from the 2-D data (green) plus faults added as a result of the 3-D data (blue fault traces). Figure 11 shows an expanded view of the area, mainly in the 3-D area. This is a good example of how the density, abundance and detail about faults can be discerned only where there is 3-D coverage to define it, clearly an improvement in fault detection using 3-D over 2-D.



Figure 1-11. An expanded view of the seismic interpretation of the faults in the San Juan Basin. The red box shows the area selected for the 20 square mile study area in which the 3-D surface seismic was reprocessed.

Figure 1-12 shows a further expansion focusing on the 20 square mile study area. An important feature to note from examining the fault images is the complexity of the faulting in this area. The personnel at ConocoPhillips advised us that this was a structurally complex area, probably the most complex in the basin. These fault images in Figures 1-10, demonstrate the probability of a much more complex fracture setting than one would derive from the core data.

Thus we arrive at the purpose of the entire effort in this study. If the area was as simple as the core data indicated (NNE linear fracturing) then one would only have to drill in simple patterns to derive gas from the Mesaverde. However, as seen in Figure 1-13 the production history indicates that production is not at all uniform in the area.

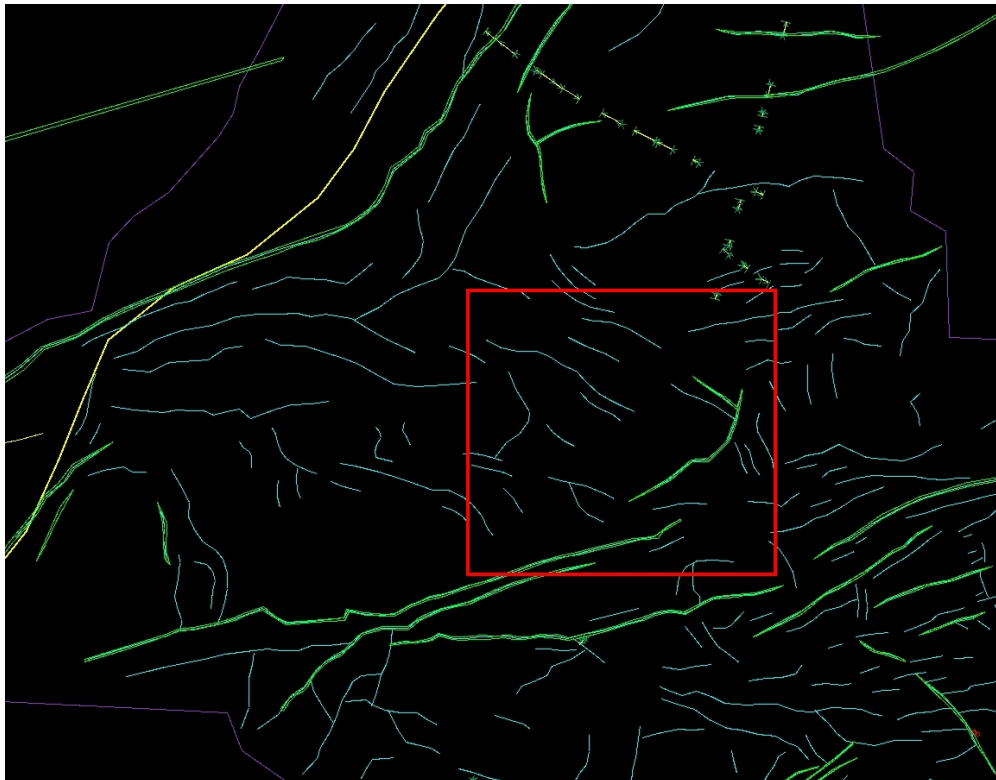


Figure 1-12. An expanded view of the 20 square mile study area in the San Juan basin as it was understood from surface seismic data at the beginning of this study.

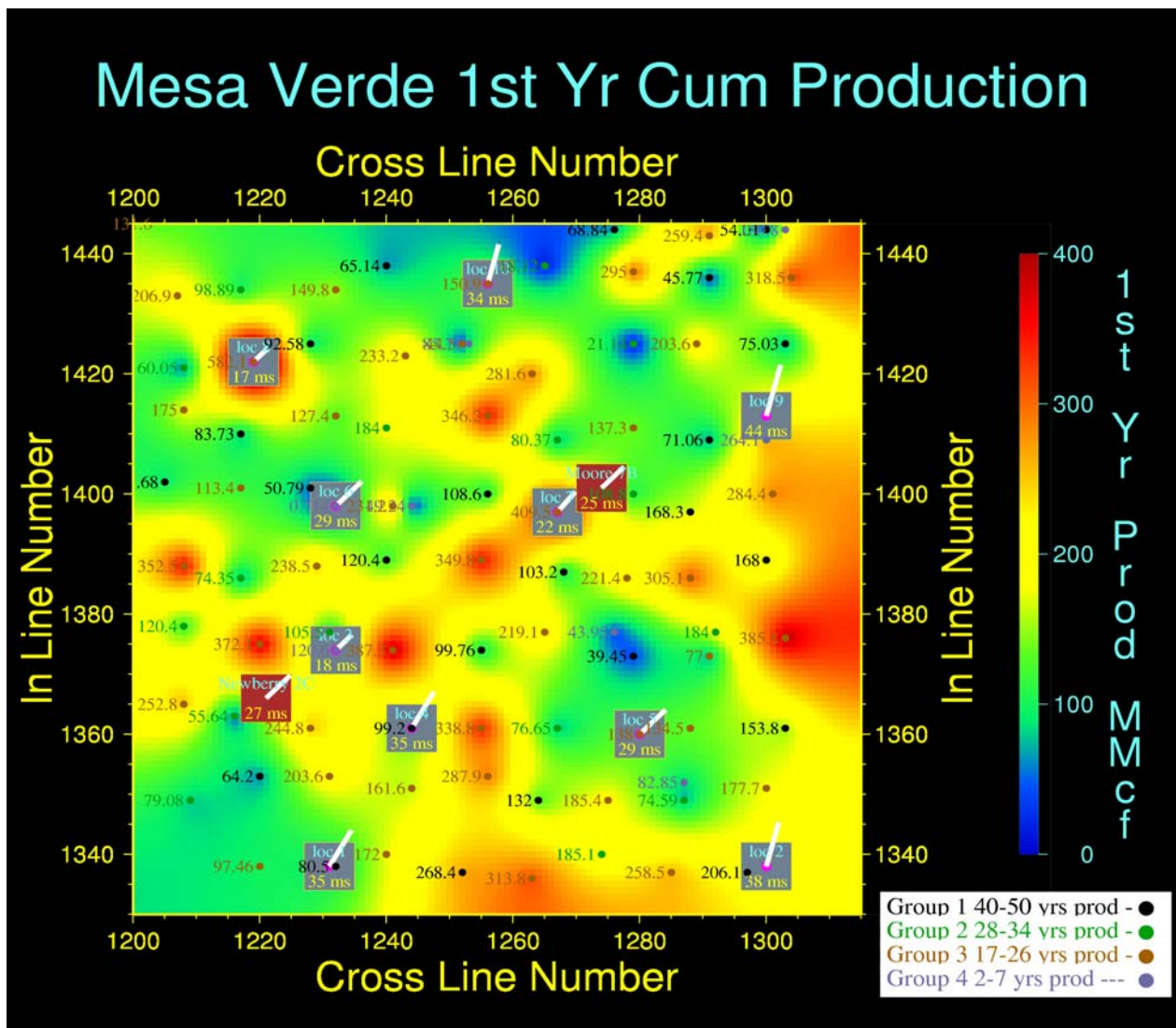


Figure 1-13. A map of the first year gas production out of the Mesaverde, note the inconsistency across the area.

In order to reduce the uncertainty in drilling locations one must be able to locate the productive fractures. As can be seen in Figure 1-13 there is somewhat of a lineament to the contoured production data, (reds are high, blues low) but it is inconsistent over the whole area. The purpose of this study was to examine the use of seismic methods for finding and characterizing the fractures controlling the gas production.

## **2. PROJECT ORGANIZATION AND TASKS**

The purpose of characterizing a reservoir is to create a model that will be a useful for planning the development of the reservoir. In highly heterogeneous and fractured reservoirs, such as the San Juan Basin, the characterization process is both difficult and critical to efficient recovery. In such systems, current practice does not provide sufficiently accurate predictions.

Our past work and results (Majer et al, 1997) pointed to a need for improved resolution and a means to scale results from the lab and small scale experiments to the field scale. Prior to this project the focus was on well-controlled tests at highly characterized test and field sites (Conoco test site in Oklahoma, Michigan Institute of Technology test site in Michigan, and the NIPSCO gas storage field in Indiana) all of which are in fractured rock media. Work was carried out in both shallow and deep wells. The fieldwork in the subject work was in iterative fashion, going between processing, modeling and field validation.

As stated above the field site selected was the Conoco (now ConocoPhillips) property in the San Juan Basin of New Mexico. The criteria we set for the field site is that it must be in an area of ongoing commercial interest, must have a wealth of geologic and other geophysical information, have ongoing access throughout the project and of course be in a fractured or suspected fractured controlled environment. Ideally, we also wanted be involved with the producer to such an extent that if our approaches and methodology are successful that they be integrated into their operational plans in the future.

### **2.1 SPECIFIC TASKS**

The seismic work plan was divided into three broad tasks:

1. Modeling
2. Field Measurements
3. Processing and Interpretation

As stated above the tasks were not in sequence but intermixed and somewhat iterative. As in the case of most research each task influenced the other and was modified as the project progressed.

#### **2.1.1 Task 1. Modeling**

Present methodologies for modeling and extracting fracture properties from seismic data utilize effective media approximations in which fracture systems are represented by their zero-frequency anisotropic elastic moduli. Equivalent anisotropic properties may be useful for predicting fractured-related AVO and shear wave splitting when fractures are aligned, many wavelengths in planar extent, and closely-spaced relative to the seismic wavelength. However, the primary limitation of the equivalent fracture anisotropy approach is that it does not include wave phenomena such as diffractions off fracture tips, generation of fracture interface waves, fracture head waves, and fracture channel waves. These wave phenomena are potentially more sensitive to fracture properties and geometry. In addition, methods of analyses that utilize these

waves may offer higher resolution methods for extracting fracture properties from surface, VSP, and crosswell seismic measurements.

In general we drew upon our past and ongoing theoretical efforts in scattering theory as a basis for the modeling. The purpose of the modeling will be to not only understand the data collected but to aid in the design of the field experiments. The modeling and analysis effort consisted of a series of parametric studies of the effects of finite length fractures embedded in sand-shale lithologies. The fracture spacing, dimensions, and stiffness was then varied to include a full range of possible values that may exist in situ.

The initial plan was to use surface seismic, vertical seismic, single well and crosswell acquisition geometries and frequencies. Crosswell was not used because well access did not allow it. The data was examined for possible fracture generated waves such as fracture interface, fracture head, and fracture channel waves. The partitioning of an incident body wave into the various fracture-related waves and the subsequent radiation off the fracture back into body waves was examined for both P- and S-wave sources. These simulations were performed using existing finite difference, boundary element, and global matrix (two-dimensional, elastic) codes developed at LBNL. The second effort utilized the synthetic data to develop new methods for extracting fracture properties such as fracture orientation, spacing, and stiffness from the fracture-generated waves.

The overall objective of this modeling was to:

1. Extend to elastic solution for variation of fracture properties
  - (a) Stiffness (include filling of fracture air, fluid, etc.)
  - (b) Dimensions vs. wavelength
  - (c) Multiple fracture interaction
2. The explanation of amplitude and frequency variation: i.e. frequency dependent (AVO-AVA) as a function of azimuth for
  - (a) Single fracture (P&S)
  - (b) Multiple fractures (P&S)

### **2.1.2 Task 2. Field Testing**

Controlled field experiments was an integral part of the program in an iterative fashion, much time is gained by performing well-controlled field experiments to validate and guide theory and interpretation efforts, progressing from simple cases to increasing complexity. The overall goal of the fieldwork was to provide data and testing of methods that can be used to determine if one can “pick out” the significant (permeable) fracture(s) from non-permeable and from natural heterogeneity. The fieldwork was carried out in full-scale fieldwork at scales from the well logging to the surface seismic, (1 m to 1 km scale).

Several data sets already existed within the San Juan basin. The objective of the field tests was to augment these data as well as collect new data sets at both the borehole scale and surface seismic scale. Field-testing involved performing multi-component/multi-azimuth VSP and single well seismic in an area where surface 3-D seismic had been performed. This allowed a range of resolution of data in the same site where well data exist. This also provided a fundamental data set upon which to base the work.

The field components had the following elements:

1. Surface studies
  - (a) 3-D P-wave Reflection seismic. AVO, AVA, vs. frequency content with P wave,
  - (b) P-wave anisotropy
2. 3-D VSP (9-C)
  - (a) Multicomponent sources to 3-components receivers in fractured media for same contribution as 1(a and b) in addition to S-wave effects
3. Single well studies using both P&S wave for imaging fracture to derive fracture properties
  - (a) CDP imaging
  - (b) Guided wave
4. Well Logging
  - (a) Acoustic (monopole compressional and shear wave)
  - (b) Four arm caliper
  - (c) Gamma- Ray
  - (d) Resistivity
  - (e) Neutron Density
  - (f) FMI

### **2.1.3 Task 3. Processing and Interpretation**

The objective of the processing and interpretation was to derive images that are indicative of the fracture characteristics. Each method (surface seismic, VSP, single well, well logs) results in a different image at different scales. Our initial hypothesis that higher resolution is necessary to define the important (permeable) fractures was tested by the different images produced. A second hypothesis tested was that there is information in surface seismic that is indicative of the “important” fractures, but those attributes are not usually identified (they were generally thought

to be “noise” and processed away). Processing was performed on all scales of data types, surface, VSP, logging and single well. The sequence was as follows:

The existing 3-d data from the target area was reprocessed at Conoco with current state-of-the-art processing methodologies of Conoco. Lynn Inc. also had a specific processing requirements to enhance the azimuthal P-wave analysis that Conoco performed.

The VSP and single well data was processed for fracture anisotropy and fracture reflectivity using codes at LBNL, Conoco and Schlumberger. Stanford and Virginia Tech performed analysis on the VSP data. Modeling was done at Stanford and LBNL for the single well data. LBNL, ConocoPhillips, and Hi-Q performed discrete fracture modeling. Sandia performed the core analysis. Geomechanical modeling was also performed by Hi-Q and LBNL.

In terms of interpretation, modeling played a key role in the interpretation to separate matrix effects, lithologic effects (layering) and heterogeneity (i.e. lenses, channel sands, etc.) from fracture effects. It was also necessary to design data acquisition parameters, thus modeling played a key role throughout the project

Typically, individual fractures are too small to be detected with a seismic experiment. Instead of trying to detect the fractures individually, one can also pursue a stochastic description of the fractures. A first stochastic parameter of interest is the fracture density. The next parameter of interest is the average spacing between clusters of fractures. The fractured material is described as a random media with a particular spatial correlation length which may be below the probing seismic wavelength.

Based on the Born approximation, a method was developed by Virginia Tech to estimate the spatial autocorrelation from seismic experiments. Although the method can estimate the true correlation function, a more robust approach is to use an inversion scheme to fit, e.g., a Gaussian auto-correlation function to the seismic data. These model functions contain parameters such as fracture density, orientation, and, for perpendicular directions, characteristic distances between sets of fractures. So far, the scheme has been developed for scalar input-data only. However, an extension to multi-component data is straight forward. Furthermore, the method is independent of the geometry of the seismic experiment providing its input-data.

Multicomponent data is very expensive to collect. However, it is rarely used for more than estimating shear-wave anisotropy. Instead, one can use this data to better characterize the reservoir, i.e. the fractures. For example, the traditional P-wave AVO attributes can be extended to the converted waves. New attributes, e.g. ratios between frequency content of different phases, can be built. All these attributes need to be understood in terms of tight gas sands to be of interpretational value.

In the upcoming sections the task results will be reported in the sequence in which they were performed. If we were to repeat our effort we would not carryout the same work in the same exact sequence (see Conclusions and Recommendations). However, reporting it in the fashion in which we proceeded will hopefully help the reader see the logic of our approach and learn from our efforts, both the positive and negative results. It should also be noted that while we learned a

great deal from this work this study is just “one data point”. More studies will follow by others and we hope that they are built on our experience and not duplicate them.

The actual work flow was as follows. We first selected a site in the San Juan Basin based on current geologic, 3-D surface seismic data and well access data that met our criteria above. A large 3-D surface P-wave study was carried out in 1998 as part of a basin wide exploration program in the San Juan basin by several different companies in the San Juan Basin. A 20 square mile study area was selected within this 3D survey to focus our studies. The 20 square mile study area was based upon the future drilling sites of Conoco in order to carryout well bore studies (VSP, single well and well logging), validation, and for production data for reservoir engineering studies. Once the 20 square mile study area was selected the first step was to select and reprocess the 3-D P-wave surface seismic data so that it was suitable for studies such as identifying discrete scatterers and P-wave anisotropy studies. Analysis of the surface seismic was carried out using P-wave anisotropy analysis in time and some limited amplitude studies. Finite element 2-D and 3-D modeling of the geologic model derived from the surface seismic and available well logs was carried out to design the VSP work within the 20 square mile study area. The geologic model was derived by using well logs and a statistical approach to defining the heterogeneity of the lithology. A critical assumption in this work is that seismic methods can differentiate between matrix heterogeneity and fracture properties. Thus it was important to have a geologic model that included the lithologic properties as well as the fracture properties. Models with and without fractures using the discrete-continuity approach were used in the modeling. Modeling was used through out the project to refine our understanding of fractures as well as in aiding our interpretation of the data. The next step was to collect additional field data using VSP (3-D 9-C), multicomponent single well and well logging data. The data collection was one of the main efforts in this project and was used as one of the primary products of this work. At the time it was one of the largest 3-D 9-C VSP data sets ever collected. Combined with the single well and well logging data it is a unique seismic data set that scales from the sub-meter to the kilometer scale. After the data was collected the data were processed in a variety of different ways to look for fracture effects.

### 3. DATA ACQUISITION

#### 3.1 SURFACE SEISMIC

##### 3.1.1 Reprocessing of the 3-D P-wave Surface Seismic in the 20 Square Mile Study Area

The scope of work for this task by Conoco was to process data from the San Juan Basin 3-D survey necessary to produce approximately 20 square miles of fully imaged data, using the advanced seismic processing techniques selected by LBNL. Figure 3-1 shows that area of interest. It was selected to cover a set of existing wells and subsurface zones which were expected to be fractured. Also shown in this figure is the geometry of the survey. As can be seen the shot geometry (green lines in Figure 3-1) is not regular because the vibrators were not allowed off road. The receivers, however, were in a regular pattern (blue lines). This points out one of the limitations of using surface seismic in some areas of the San Juan Basin.

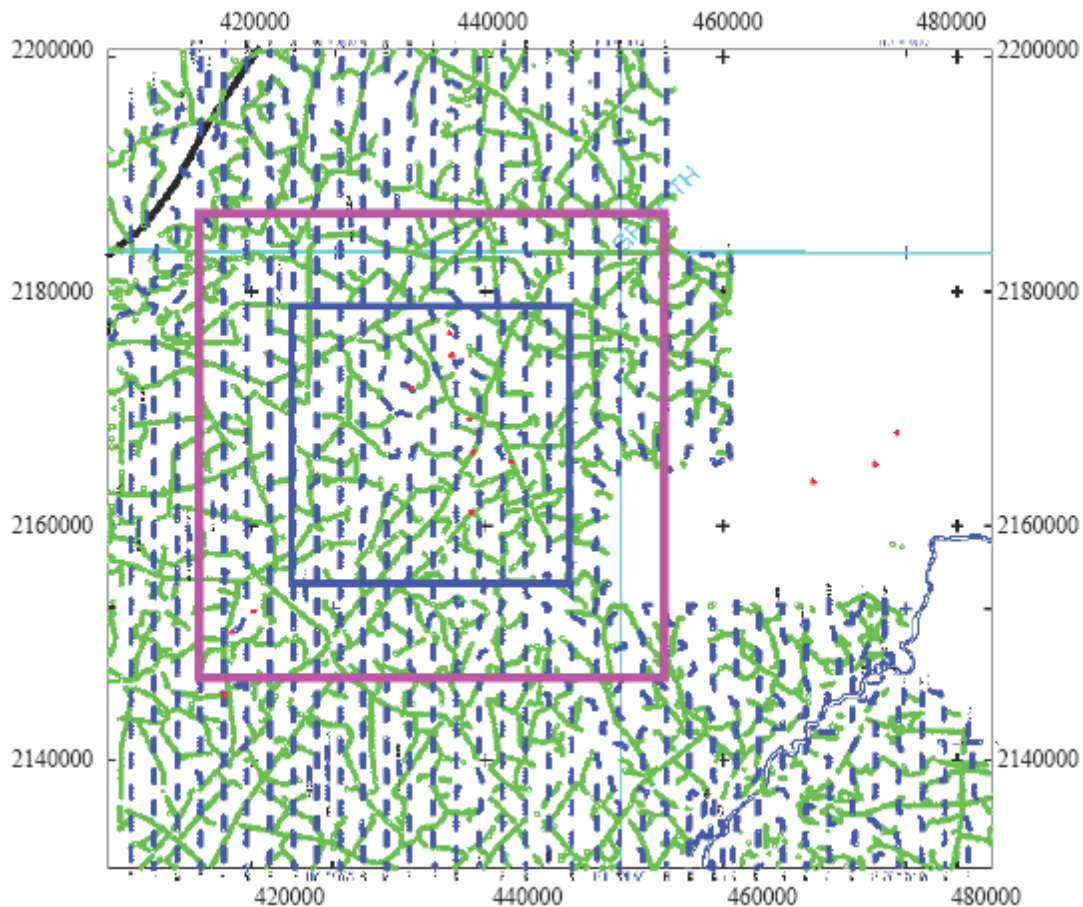


Figure 3-1. The dark blue rectangle shows the outline of the output prestack time migration. The area covered by the input data is indicated by the pink rectangle. Source positions are shown in green. Receiver positions are shown in blue.

The objective of this task was to provide the other project participants with data that can be interpreted for fracture characteristics. The final version of the processing sequence is listed in its entirety at the end of this section. The final version includes many more velocity analysis steps due to the low signal to noise, multiples, and other issues.

### 3.1.2 Geometry, Trace Edit, First Break Picking, Refraction Statics

Due to the random nature of the source positions and the brick receiver pattern this part of the preprocessing took much longer than expected. The data's poor signal to noise ratio made it difficult to find any conclusive errors in the original geometry except for 6 cable boxes (8 receivers each) with reversed plugs. Generally, predictable moveout characteristics of the refraction and reflections events in shot gathers can be used to quickly identify trace with incorrect geometry. This includes traces where the channels in the field receiver box (RSR) are reversed. We could not rely on this traditional approach and had to hand edit all the traces used in the reprocessing. Hand editing revealed that about 1% of the traces were recorded with receiver channel number reversed, resulting in correctable geometry errors. The hand editing also deleted about 1% of the traces that had obviously high noise conditions. The total volume examined was about 5 million traces.

Review of the first breaks identified three refractors (Figure 3-2). Characteristic offset ranges and velocities as listed below identified these refractors.

<u>Velocity</u>	<u>Offsets</u>
10,000 ft/s	0-6,000 ft
12,000 ft/s	6,000-12,000 ft
14,500 ft/s	12,000(+) ft

The original processing only used picks from the first refractor. The first and second refractor picks had significantly different arrival structures, while the second and third refractors had the same structure. This indicates the second refractor contains important statics delays that would not be accounted for by using picks from the first refractor. A refraction solution using picks from the second refractor would lump the effects of the first and second refractors.

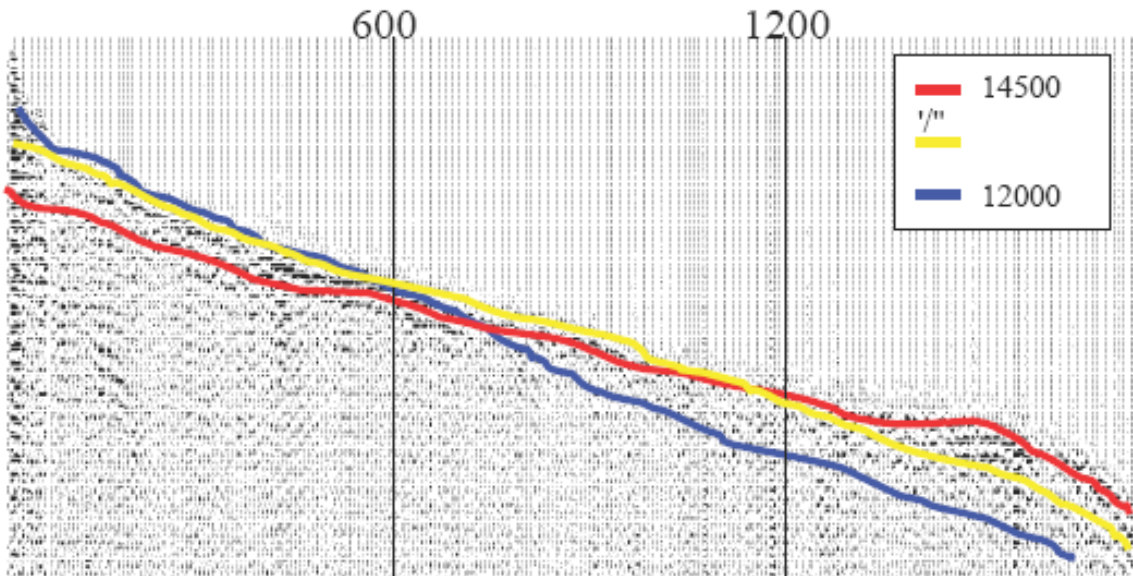


Figure 3-2. Example of a shot gather sorted with increasing offset to the right. The colored lines highlight the three refractions.

Therefore only the second refractor, between 3,000 and 6,000 ft offsets, was picked.

Picking the first breaks turned out to be the most difficult part of the reprocessing. Due to the random source locations and brick receiver pattern, shot and receiver gathers displayed little regularity (Figure 3-3) that would normally speed picking. In addition, the S/N on the first breaks was poor. An autopicker could only pick the first breaks on a very localized scale. Slow hand picking was the only option.

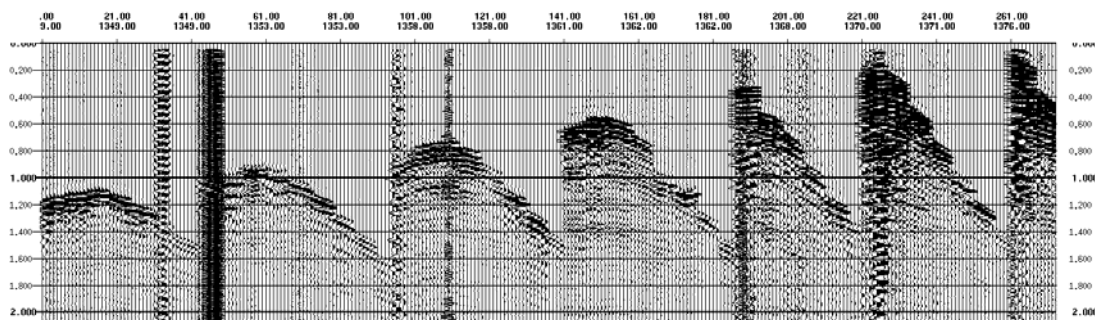


Figure 3-3. This is part of one shot gather. Each trace was recorded at a different receiver location. Notice the rapid variation in moveout, discontinuous moveout trends, and significant changes in waveform character.

### 3.1.3 Gain

Geometrical divergence was partially corrected by using a time and offset dependent gain of the form

$$\text{Gain}(T, X) = (TV^2/V_1)\text{SQRT}(1 + A).$$

With,

$$A = (V^2 - V_1^2)X^2/(T_0^2V^4).$$

Where,

X = offset of the trace,

T = Two-way traveltime at offset X,

T<sub>0</sub> = zero-offset Two-way traveltime,  
assuming

T and T<sub>0</sub> are related by the NMO equation,

$$T^2 = T_0^2 + (X/V)^2$$

V = stacking velocity, extracted at time  
T<sub>0</sub>,

V<sub>1</sub> = surface velocity, i.e., the velocity  
at T<sub>0</sub>=0.

The velocity function used to compute the gain function  
was:

T <sub>0</sub> (s)	Velocity (ft/s)
0.0	9,580
0.5	10,485
1.0	11,287
1.5	12,721
2.0	13,883
2.5	14,309
3.0	14,529
3.5	14,702
4.0	14,848

### 3.1.4 Noise Attenuation

Significant airwave, ground roll, and cultural noise are evident in the raw data (Figure 3-4). Some noisy traces manifest themselves as non-seismic ringing with monotonically increasing amplitudes. Noise de-spike in the wavelet domain, automatic trace editing, hand editing, and noise de-spike in the space-time domain were used to attenuate the various types of noise.

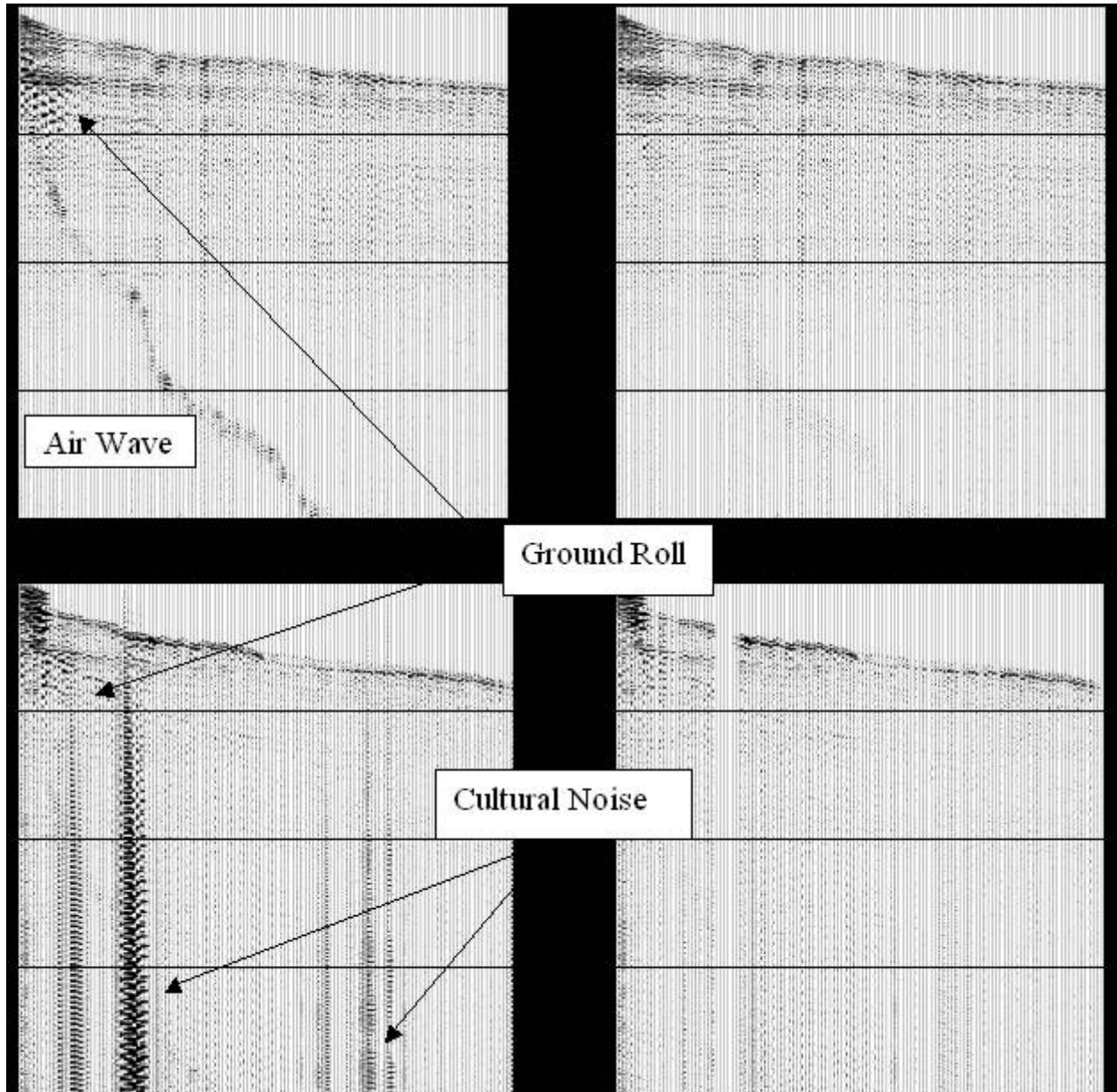


Figure 3-4. Example of two shot gathers after geometrical divergence correction and muting, but before statics were applied. Cultural noise, airwave and ground roll are noted. Left side is has no noise attenuation. Right side shows the same gathers after noise attenuation.

### 3.1.5 Deconvolution

There appears to be a shallow reflector that in combination with the free surface sets up a significant amount of ring (Figure 3-5). The best technique to handle this problem would be predictive deconvolution in the Tau-p domain. However due to the brick receiver pattern in acquisition, transforming into the Tau-p domain is not possible. Therefore a predictive deconvolution was applied in X-T space.

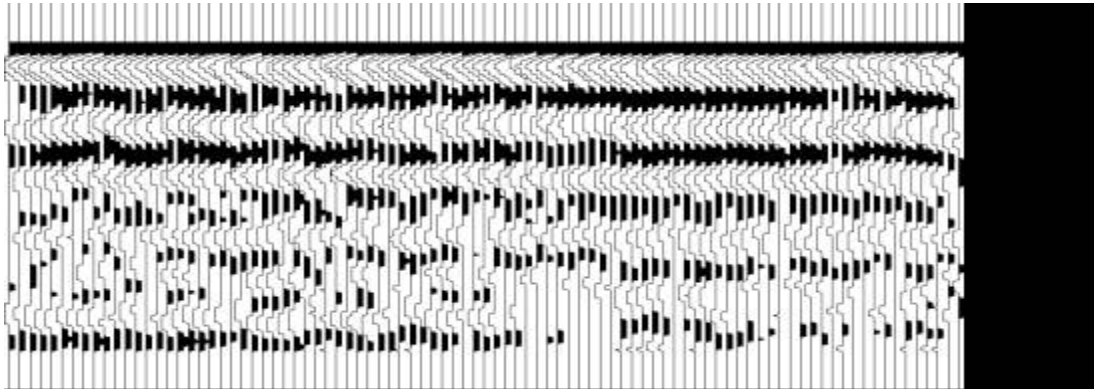


Figure 3-5. Example of auto correlations

### 3.1.6 Multiples

The discrete reflector packages in this area act as multiple generators (Figure 3-6). Tau-p demultiple was used to attenuate these multiples.

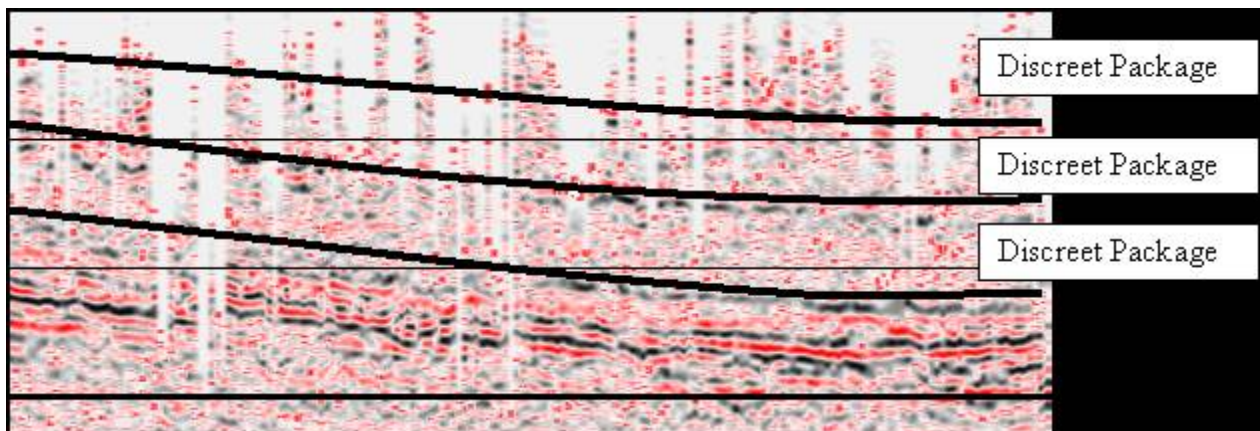


Figure 3-6. Example of multiple reflections in a stacked section.

### 3.1.7 Surface Consistent Amplitude Balance

Surface consistent amplitude corrections were computed for each offset, source location and receiver location. All three factors were computed simultaneously using all traces with data between 1.0 and 3.0 seconds. Figures 3-7 and 3-8 show the amplitude corrections applied to the data prior to prestack Kirchhoff time migration. The offset scale factors with their general increase with offset, shows that the geometrical divergence correction did not account for all of the amplitude decay. Neither the source nor receiver factors can be obviously correlated to topography. We do not know if those two factors have any correlation with surface conditions during field acquisition.

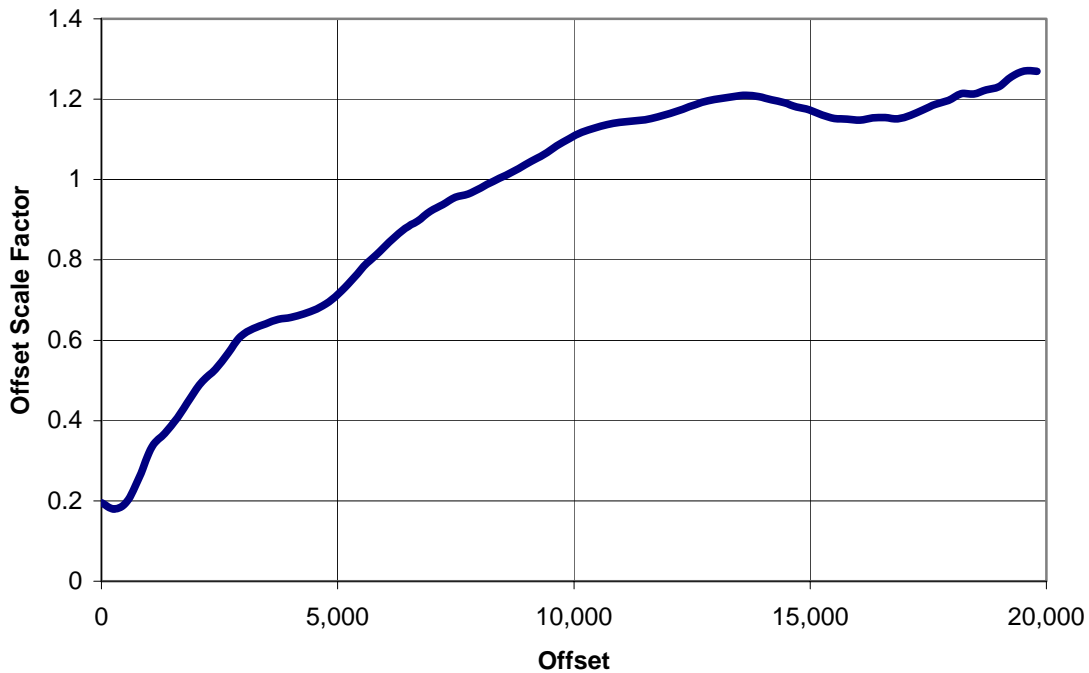


Figure 3-7. Scale factor as a function of offset that was multiplicatively applied to the seismic data prior to migration.

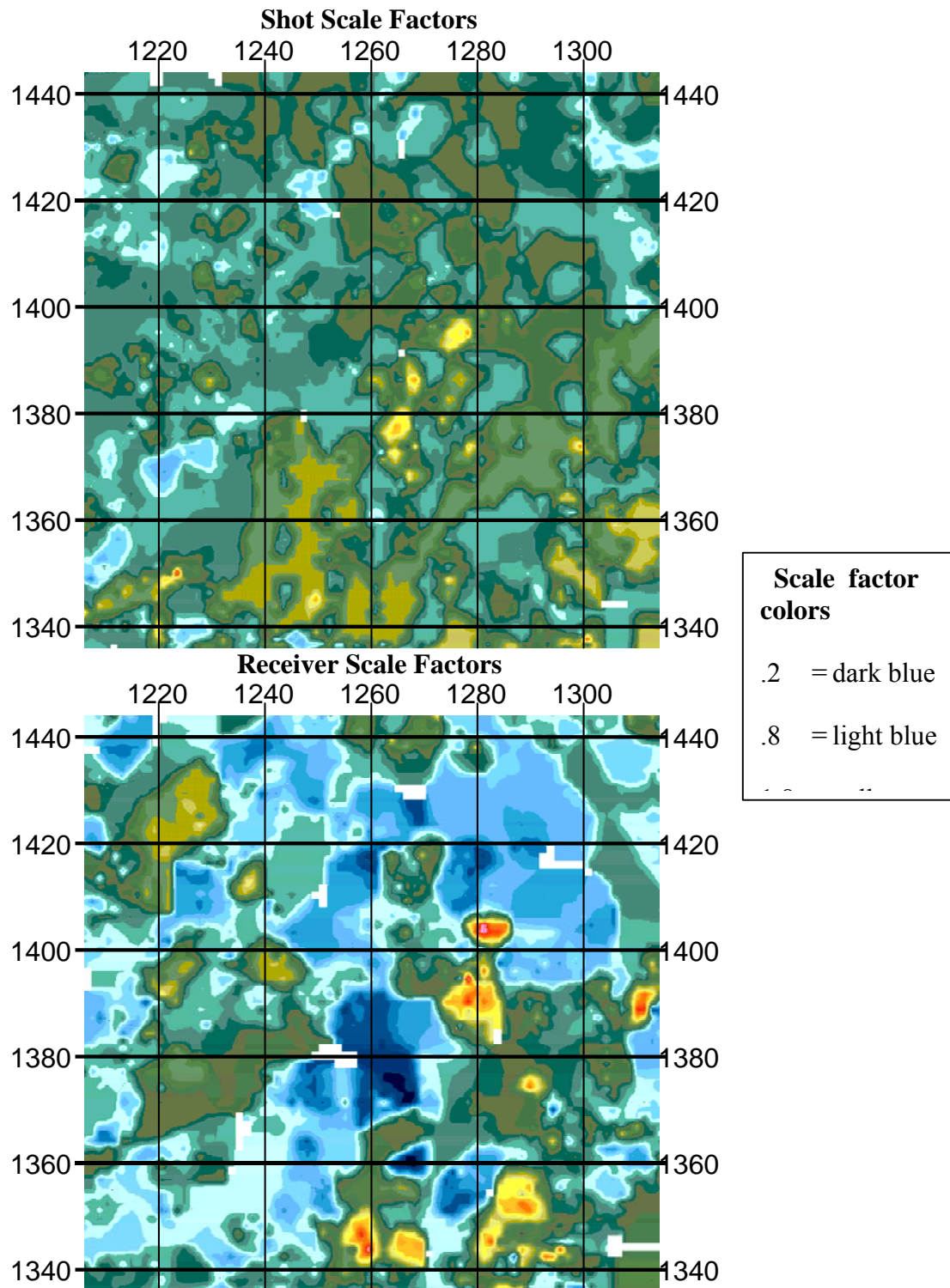


Figure 3-8. Scale factors as a function of source and receiver position that was multiplicatively applied to the seismic data prior to migration. The top map shows the factors for the source positions. The bottom map shows the factors for the receiver positions.

### 3.1.8 Velocity Analysis

Velocity analysis was complicated by the multiples and poor S/N. Constant velocity stacks were run along with semblance panels each time velocities were picked. The velocities for demultiple were picked by running a series of velocity analysis stripping off the slow velocities. For example (Figure 3-9) the multiples at velocity V1 and slower would be removed and a new velocity analysis run. A slightly higher multiple velocity (V2) would be picked and the process is repeated until the fastest “safe” multiple velocity is identified. Without using this method a primary-multiple combination can be picked and the demultiple could remove the primary event.

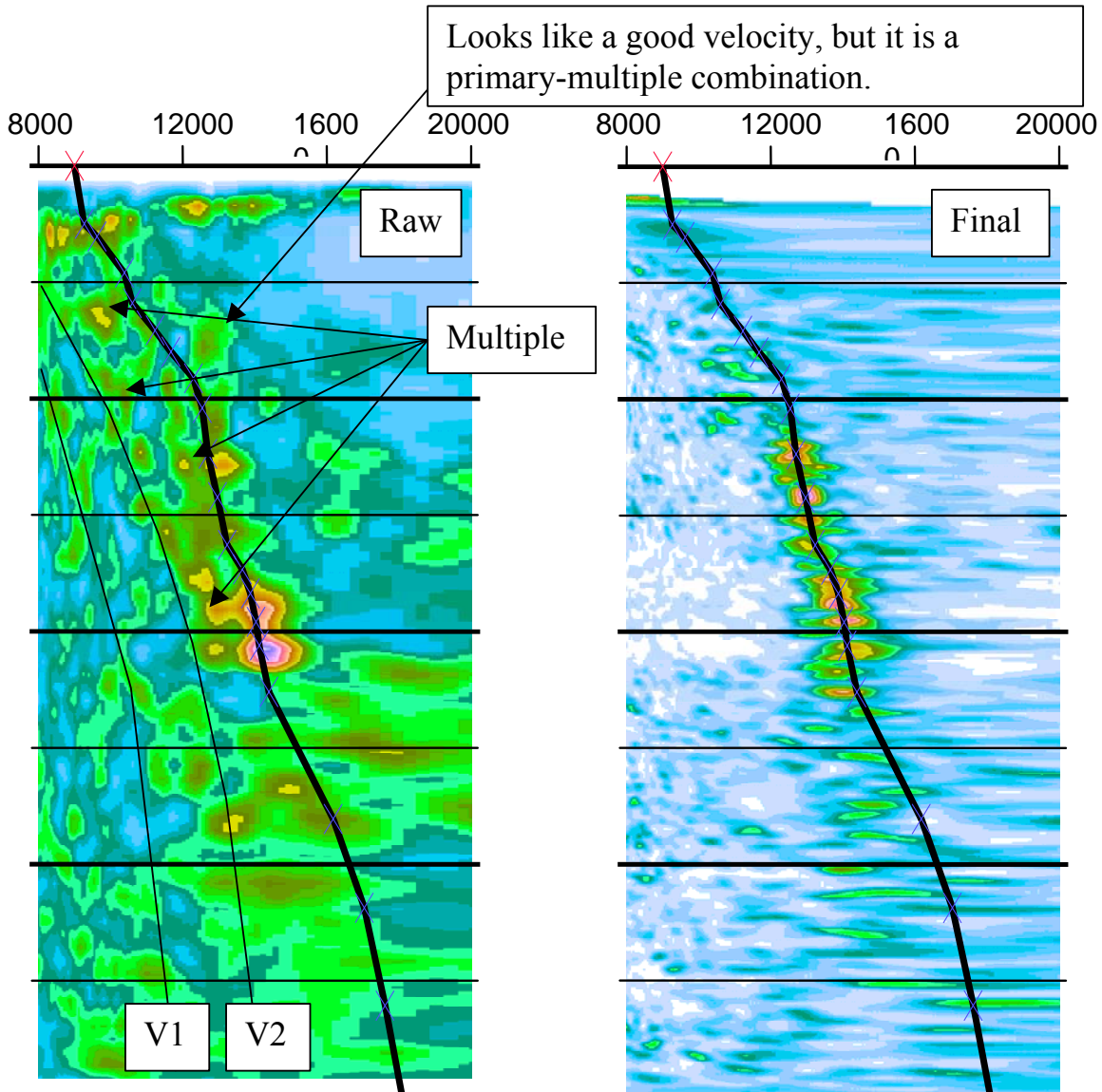


Figure 3-9. Velocity analysis before (left) and after (right) Radon demultiple

### 3.1.9 Fold of Stack Plots

Two types of maps were created based on input from various participants of the project. The first set of maps displays the fold-of-stack for specified azimuth ranges and specified offset ranges. Figure 3-9, shows the map for the N45W±45°, 0 to 3,000 ft combination. The table below lists the four combinations delivered.

<i>Azimuth Range</i>	<i>Offset Range</i>
N45E±45°	0-3,000 ft
N45E±45°	3,000-6,000 ft
N45W±45°	0-3,000 ft
N45W±45°	3,000-6,000 ft

The second set of maps displays a matrix population count for super bins of size 5 by 5, 7 by 7, and 10 by 10 CMP's. The matrix has one bin for each of eight azimuth ranges and six offset ranges. The first azimuth range is N(0-45)E and subsequent ranges increment at 45° between 0 and 360°. The first offset range is 0-1,000 ft and subsequent ranges increment at 1,000 ft up to a maximum offset of 6,000 ft. There are 48 bins in the matrix. Only the first trace in a bin is counted, therefore, the maximum fold-of-stack in at any super bin location must be 48. This represents a fully populated matrix. The maps are color coded so that any super bin location with 40 or more matrix bins occupied can be easily identified. Figure 3-11, shows the map for 10 by 10 CMP super bins. The dark red color indicates a fully populated matrix, as shown in Figure 3-11 for the red-square labeled with the number 48. An off-yellow color indicates a population of 40, as shown in Figure 3-10 for the square in the middle of the map.

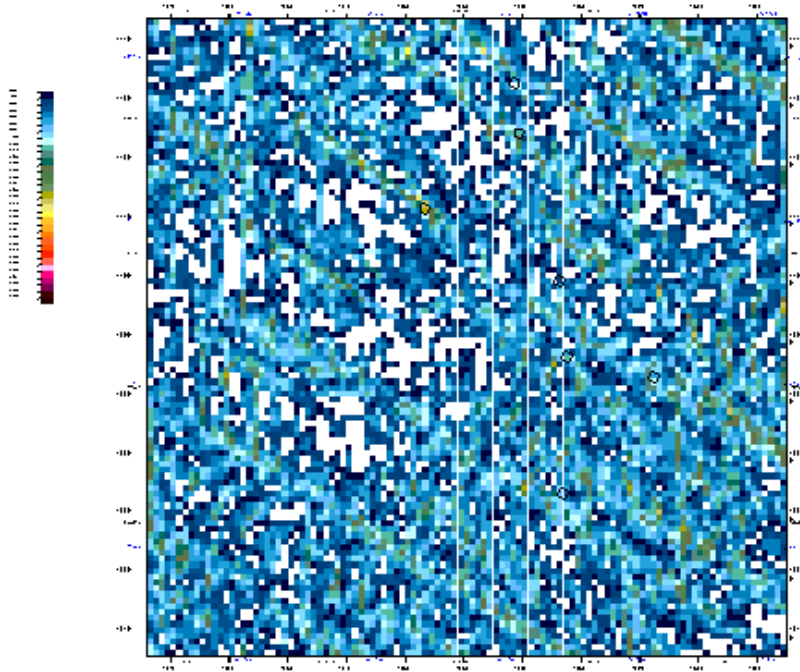


Figure 3-10. Shown is a map of the fold-of-stack for azimuth range N45W±45° and for offset range 0 to 3,000 ft. The color indicates the total number of traces at each CMP location. The small open circles indicate well locations.

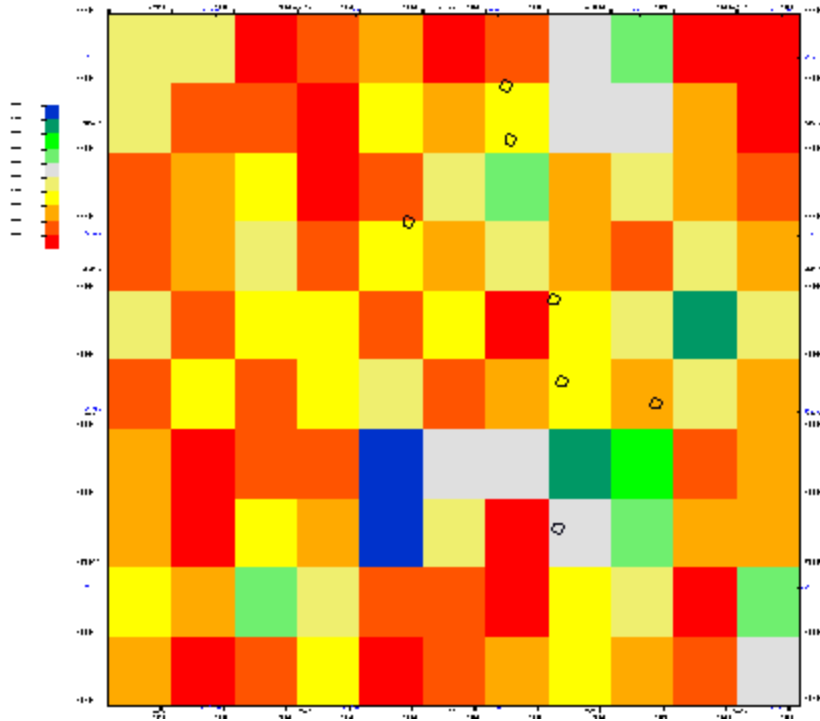


Figure 3-11. Shown is a map of matrix population for 10 by 10 CMP super bins. The color indicates the total number of populated bins in the matrix. The matrix has 48 bins representing eight azimuth and six offset ranges. The small open circles indicate well locations.

### 3.1.10 QC Stack and KASTM

QC stacks (Figure 3-12) show considerable improvement in the reprocessed data. Although the reprocessed data in Figure 3-12 represent a product without the full processing sequence, they are of higher quality than the original processing shown in the same figure. The reprocessed data shows structure consistent with the known geologic dip, while the original processing is effectively dip free (compare time slices). The shallow structure even at 1.0 s highlighted within the red rectangle is much more continuous in the reprocessed data.

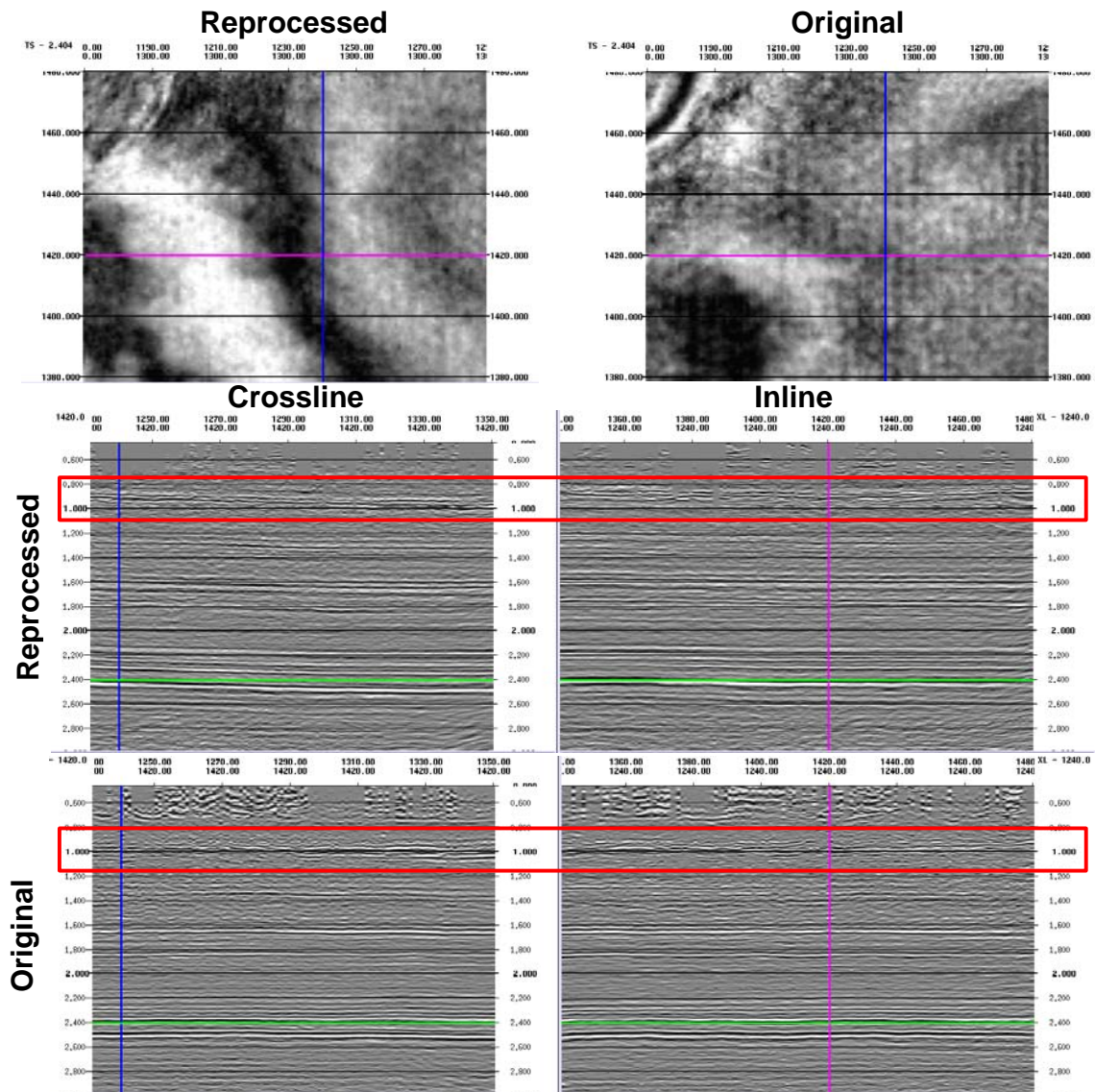


Figure 3-12. Example time slices (top sections), cross lines (left side sections) and in lines (right side sections).

---

### **3.1.11 Pre-Stack Kirchhoff Migration**

Prestack 3D Kirchhoff time migration was applied to the data in common offset mode. The data input to the migration was sorted into 15 common offset volumes. Each volume was imaged independently using a smoothed version of the stacking velocities. After migration, the imaging velocity was removed from the CMP gathers and the velocity was repicked. Finally, the data was stacked using the repicked velocities and post processed. Figure 3-13a and b shows a selected crossline extracted from the new volume and the previous volume. Figure 3-14a and b shows a selected inline extracted from the new volume and the previous volume. Both sections from the new volume again demonstrate considerable improvement in data quality above 1.2 s, correct geologic dip, better overall signal to noise, and more consistent amplitudes.

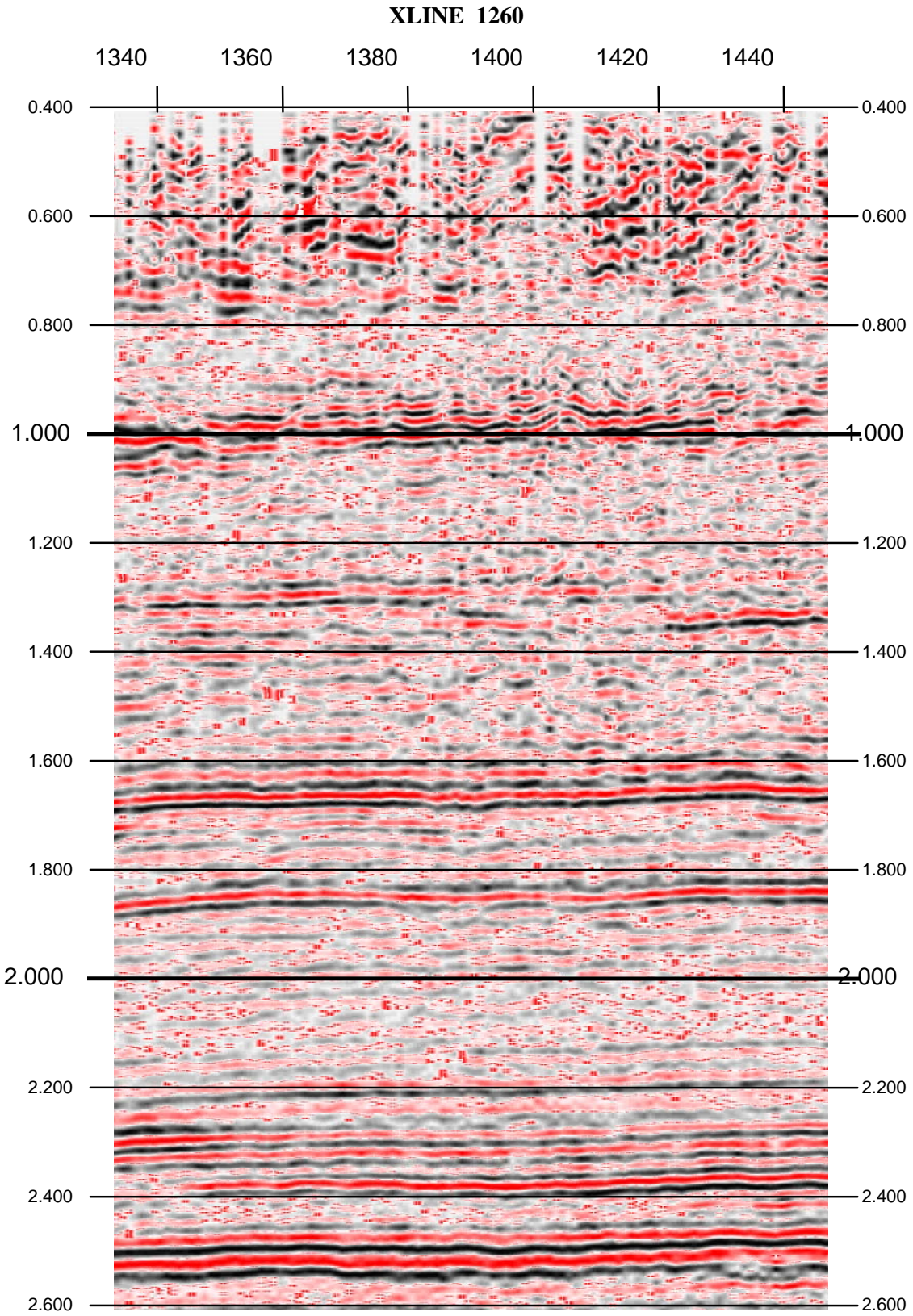


Figure 3-13a. Crossline section extracted from the original processed volume.

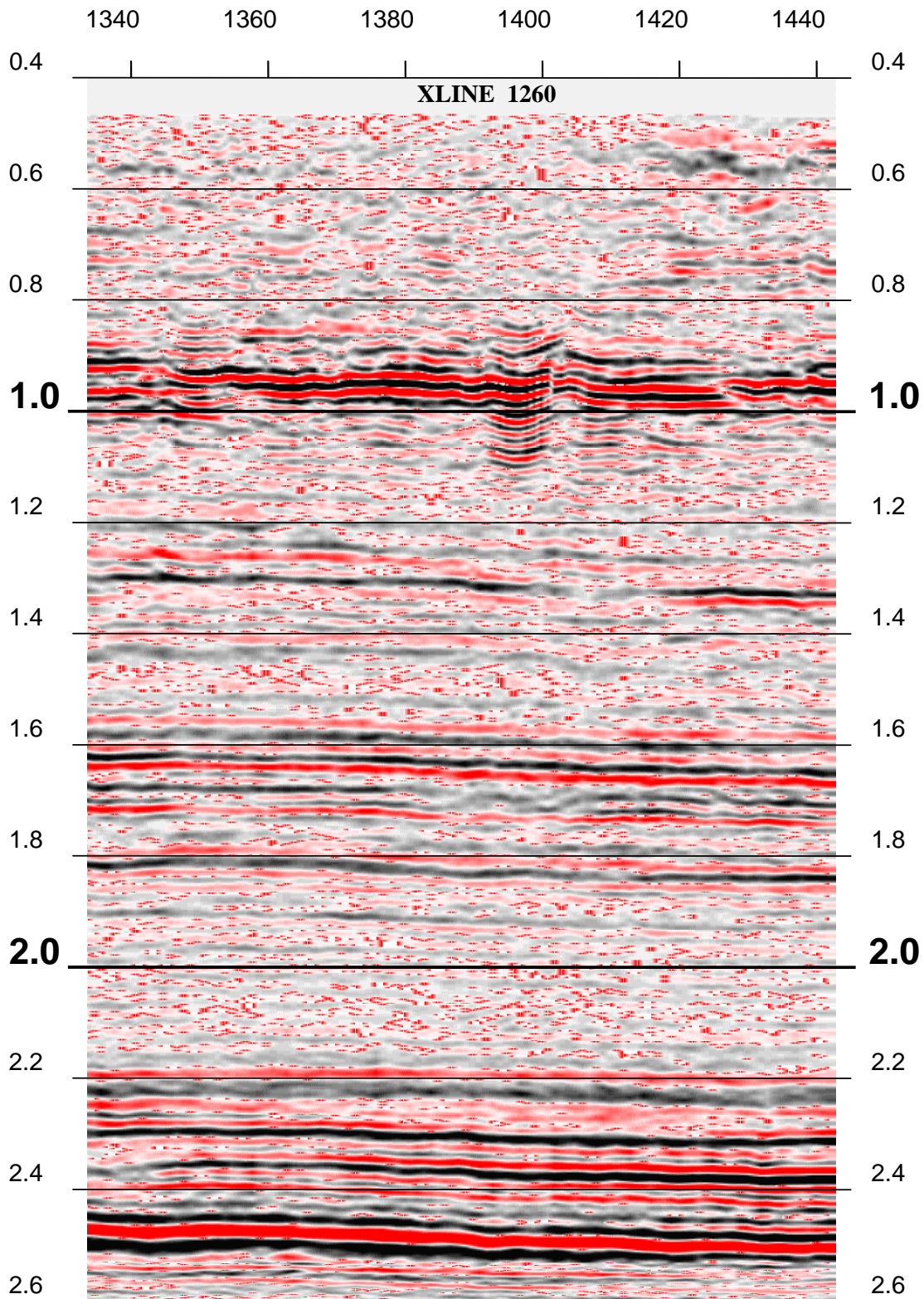


Figure 3-13b. Crossline section extracted from the new processed volume.

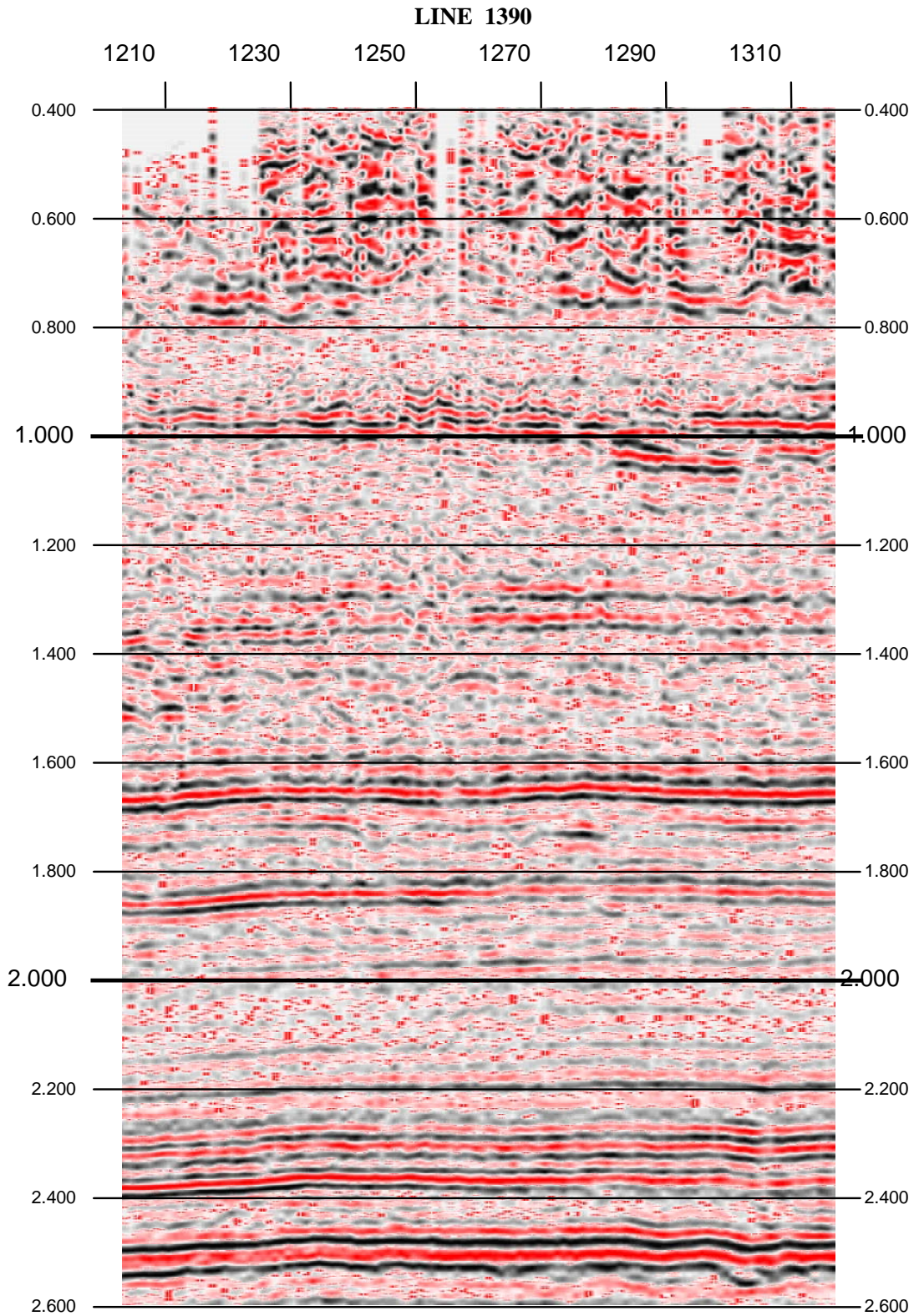


Figure 3-14a. Inline section extracted from the original processed volume.

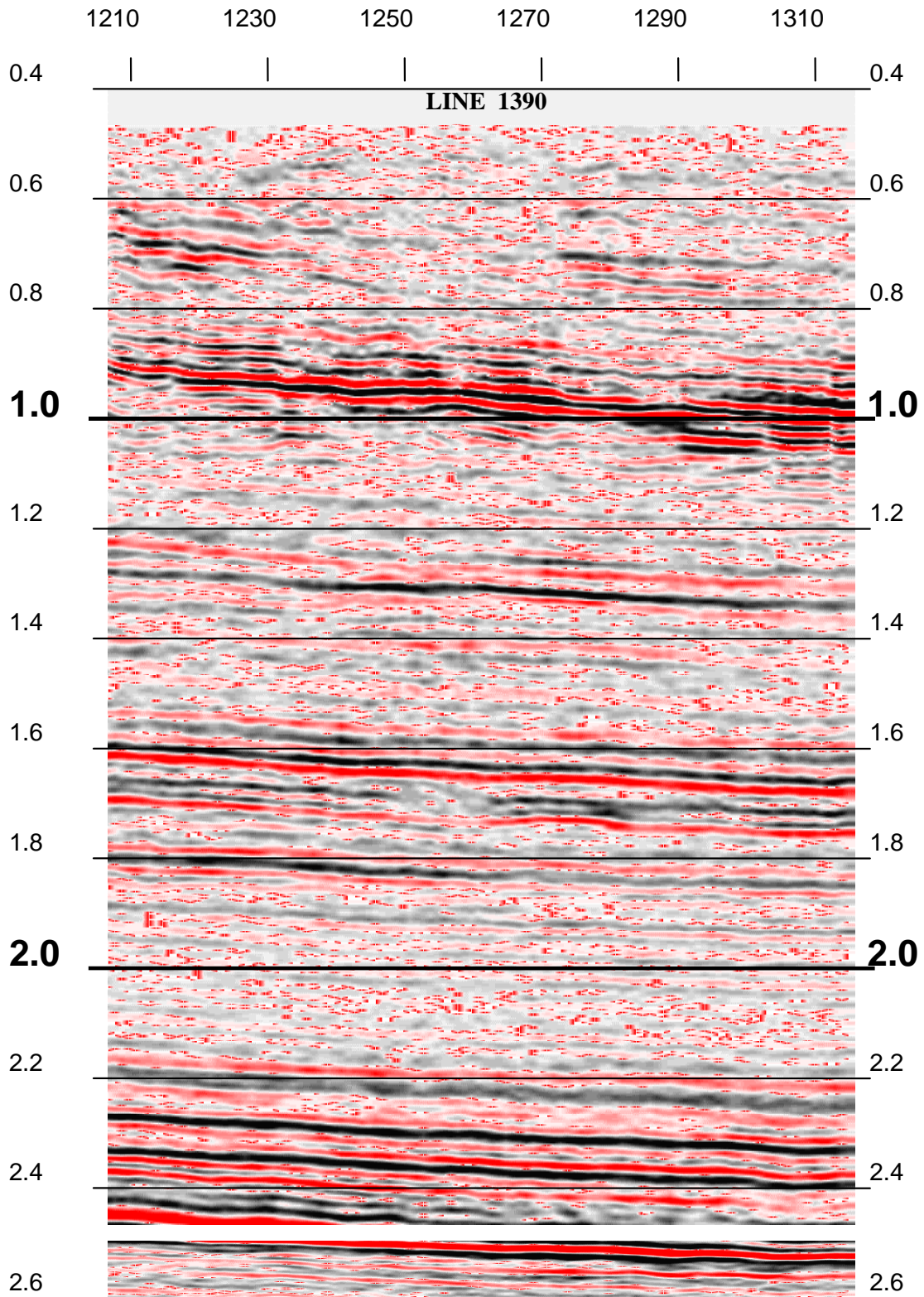


Figure 3-14b. Inline section extracted from the new processed volume.

---

### 3.1.12 Data Acquisition Parameters

Recording Company	Dawson
Crew	#23
Date Recorded	May 1998
Recording Unit	I/O SYSTEM_TWO_RSR
Format	IEEE SEG_D 4_BYTE
Field Filter	Out- 135 <a href="#">Hz@298dB/Oct</a>
Sample Rate	2 ms
Record Length	4 seconds
<b>Source Parameters</b>	
Vibrator Type	Mertz 26 buggy
Vibrator Electronics	Pelton Advance II
Peak Force / Unit	62500 lb.
Sweep Frequency	6 - 80 Hz
Non-linearity	3 dB/Oct
Sweep tapers	300 ms on both ends
Number of Vibrator / Array	3
SRC Array Description	Spread 80' - Drag 30'
Number of Sweeps	8
Source Point Interval	220 Ft
Source Line Interval	Random
Source Orientation	Random
Gun Depth	6 m
Phase Lock Reference	Ground Force
Force Control	Yes
Encoder Sweep Phase	90
<b>Receiver Parameters</b>	
Geophone Type	GSC-20 DX
Geophone Frequency	10 Hz
Geophones / Group	12
Receiver Array Description	35 Ft. Radius Circle
Receiver Group Interval	220 Ft
Receiver Line Interval	1980 Ft. Brick
Receiver Orientation	S -->N
Number of Lines per Patch	12
Number of Groups per Line	64

---

### 3.1.13 San Juan Processing Sequence

Steps 1 through 23 constitute the preprocessing sequence applied to prepare the data for prestack imaging. Two parallel processing sequences were applied to the preprocessed data. Steps 24a through 31a produced a two-pass FK migrated volume. Steps 24b through 41b produced a Kirchhoff prestack migrated volume. Items highlighted in bold text are either velocity analyses or data output to tape.

1. Set trace header values and delete bad traces
2. Check geometry
3. Apply corrected geometry

#### Output Raw Shot Gathers

4. Refraction Statics

#### Velocity Analysis

5. Geometric Divergence Correction
6. Shift Data to Floating Datum
7. Calculate Azimuths and put in trace header
8. Filter 2 - 55 HZ
9. Noise Filter in Wavelet Domain (2 Passes)
10. Mute Data above direct arrival
11. Sort to CMP's
12. Trace Reject based on increasing amplitude with time
13. Trace Reject based on maximum amplitude
14. Surface Consistent Amplitude Adjustment
15. Noise De-Spike

#### Velocity Analysis

16. 1st pass reflection statics

#### Velocity Analysis

17. 2nd pass reflection statics

#### Velocity Analysis

18. Apply NMO

#### Output CMP Gathers with NMO Applied

19. Sort to super gathers (Composite 5 CMP's)
20. De-Multiple in Tau-P Domain
21. Remove NMO
22. Sort to CMP's
23. Apply Average Decon Operator (28ms gap 170ms operator length)

#### Velocity Analysis

#### Output CMP Data with Decon and Demultiple (Without NMO)

- 24a. Apply NMO
- 25a. Stack
- 26a. Shift to Flat Datum at Average Elevation
- 27a. Inline FK migration
- 28a. Sort to crosslines
- 29a. Crossline FK Migration
- 30a. Sort back to lines
- 31a. Shift Data to Final 8000 Foot Datum

#### Output Post-Stack Migrated Data

- 24b. Median Gain applied using 1-sec windows
- 25b. Apply NMO
- 26b. CMP Residual Static Correction
- 27b. Remove NMO
- 28b. Shift to Flat Datum at Average Elevation
- 29b. Re-Sample data to 4ms
- 30b. Sort data to common offset bins
- 31b. Kirchoff Pre-Stack Time Migration
- 32b. Remove NMO
- 33b. Sort to CMP's

#### Velocity Analysis

#### Output Pre-Stack Migrated CMP's

- 34b. Apply NMO
- 35b. CMP Residual Static Correction
- 36b. Median Gain applied using 1-sec windows
- 37b. Stack
- 38b. Time Variant Spectral Whitening
- 39b. Random Noise Attenuation
- 40b. Shift Data to Final 8000 Foot Datum
- 41b. Median Gain applied using 1-sec windows

#### Output Pre-Stack Migrated Stacked Data

### 3.2 VERTICAL SEISMIC PROFILING DATA ACQUISITION

One of the main efforts in this work was the acquisition of a multi-component, multi-offset VSP in the 20 square mile study area. The purpose of this work was to collect a comprehensive data set that could be used to examine the utility of having three component data, higher frequency data than the surface seismic, and have quasi-3-D coverage, i.e., the coverage was not expected to be the same as the 3-D surface seismic but it was meant to have higher frequency content. As stated above one of the main hypotheses of the entire project was to examine the utility of such data for detecting fractures controlling production in the San Juan Basin. Figure 3-15 shows the 20 square mile study area and the location of the well in which the VSP was carried out in August of 2002, the Newberry LS-2 well in the southwest corner of the study area. Prior to the initiation of the VSP the 3-D P-wave surface seismic had been analyzed by Lynn Inc. for indications of anisotropy. Figure 3-15 shows the VSP location plotted on one of the many analysis (travel time difference as a function of azimuth between two different horizons in the Mesaverde) that was carried out on the 20 square mile reprocessed surface seismic. One of the conclusions of the anisotropy analysis on the surface seismic indicated that the Newberry well (a new well that was drilled for the VSP, single well and well logging after the P-wave analysis had been carried out) should be a good producer. It was originally planned to have two full VSP surveys run in this area, one in the Newberry well and one in the Moore well in the northeast part of the 20 square mile study area. However drilling problems prevented adequate casing size in the Moore well to accommodate the VSP instrumentation used.

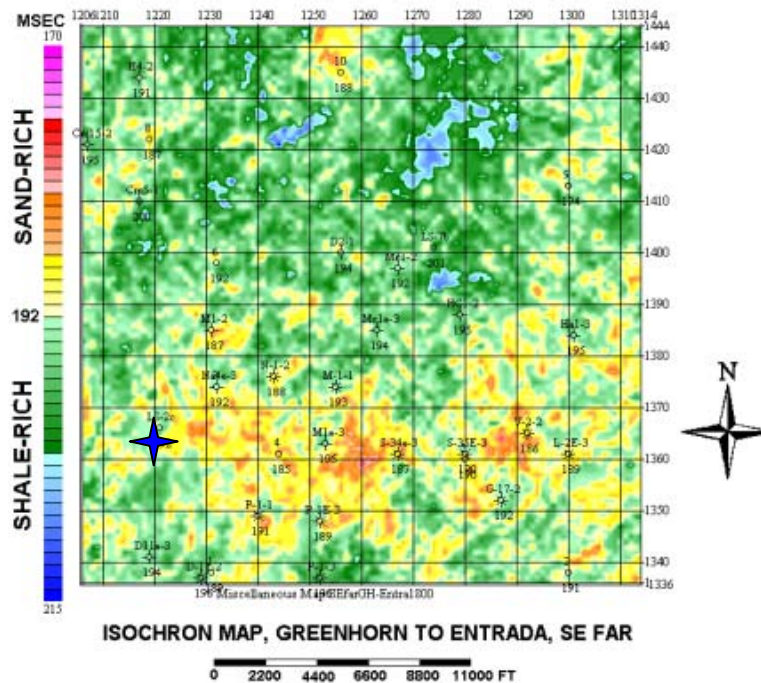


Figure 3-15. The location of the VSP well (blue star) in the 20 square mile study area. It is plotted with respect to an attribute derived from the P-wave anisotropy analysis, the traveltime between two reflectors as a function of azimuth (SE far offset).

A commercial contractor was used to acquire the VSP data, P/GSI. The company provided an 80 level, three-component per level clamping geophone string. The clamping force over hydrostatic was 100 psi. at each level. All 80 levels were recorded on a 240 channel recording string with a 24 bit recording system at 1000 samples per second. Two different sources were used during the survey, an Input/Output “Sidewinder” three component vibrator and an IVI three component vibrator. Both were specified to have 70,000 lbs of vertical force. The procedure was to have both of the vibrators operating; alternating at different shot points until all of the shot points were done. The P-wave sweep was from 10 to 120 hertz, and the S-wave was from 10 to 70 hertz. The spacing on the geophone string was 50 feet, covering 4000 feet all at once. After all of the shot points were finished the geophone string was moved up 25 feet and another round of shots was done (reversing the vibrators) resulting in a 160 level, 25 foot spacing, multi-component, multi-azimuth/multi-offset VSP. The shot point locations are shown in Figure 3-16. The VSP coverage was from 5100 foot depth in the well to 1100 foot depth at all shot points. In addition a zero offset VSP was carried out to the surface. The VSP was designed to cover the Mesaverde formation in the well. The VSP begins above the coal-bearing Fruitland formation, passes through a thick interval of Lewis shale and covers the upper 1200 ft of the Mesaverde Group.

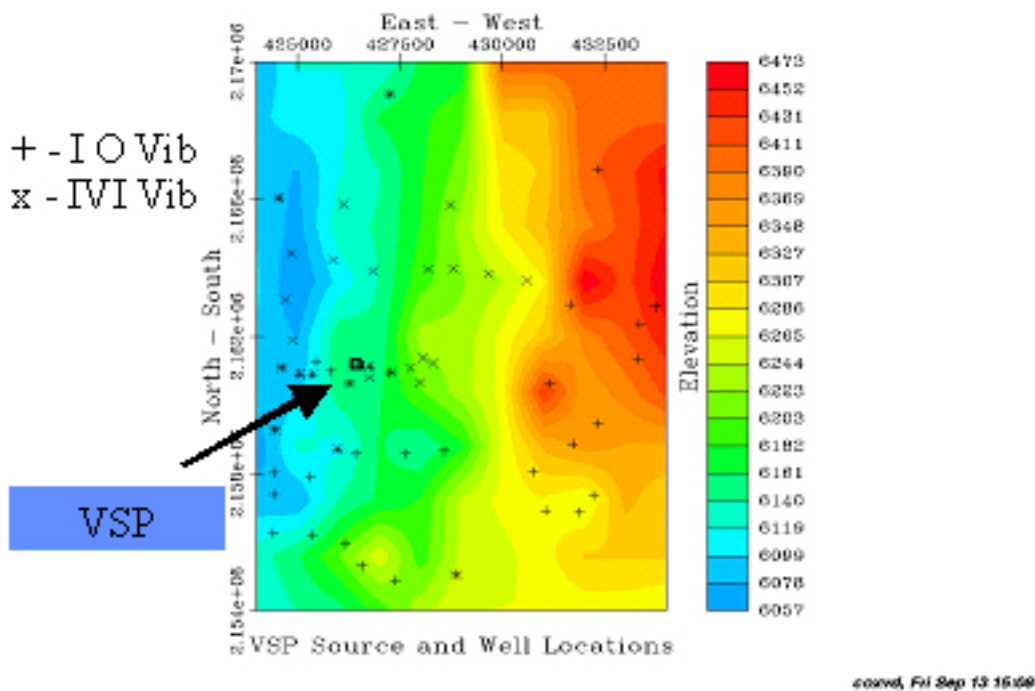


Figure 3-16. Shot locations of the VSP work. The double stars are where we duplicated the two different vibrators used. The color contours are the surface elevations. The lack of symmetry was due to land access issues.

A concern we had was the similarity of the vibrators. Similarity tests were run for each vibrator, but we also performed tests to determine how each of the vibrators performed against each other. Figures 3-17a and 3-17b show the result of the amplitude and phase tests when each vibe was at

the exact same location and the geophone string also clamped at the same location. There is a remarkable similarity between the vibrators as can be seen.

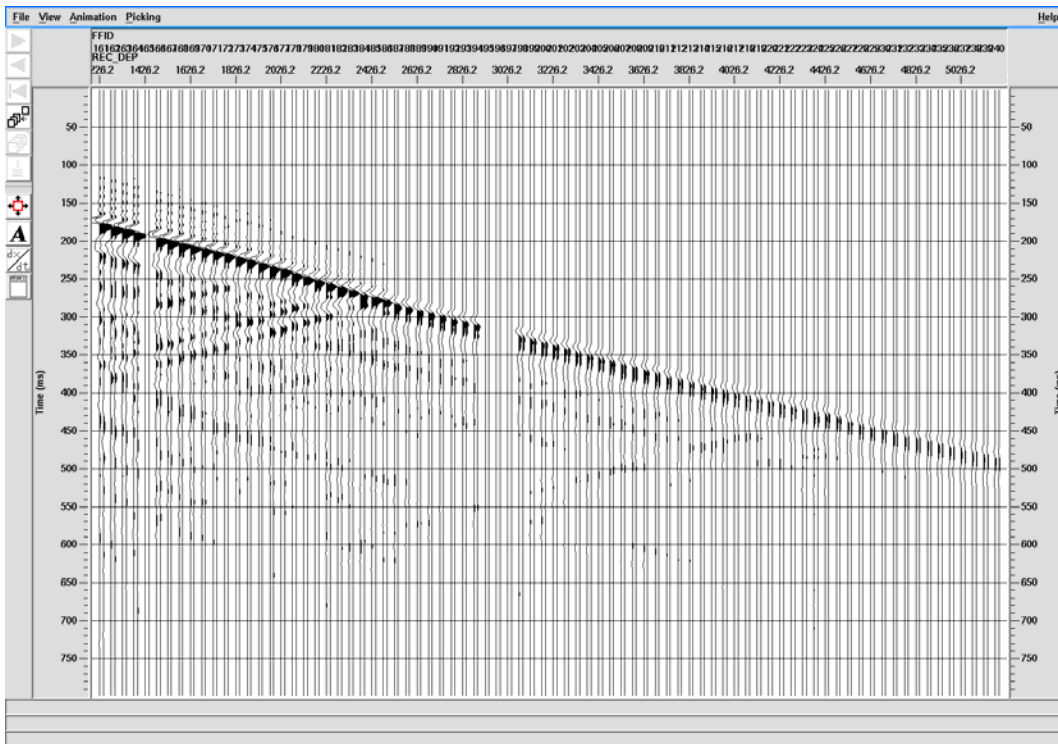


Figure 3-17a. A comparison of the I/O and IVI traces, at each level the traces are plotted next to one another. The data have been bandpassed filtered from 10 to 90 hertz

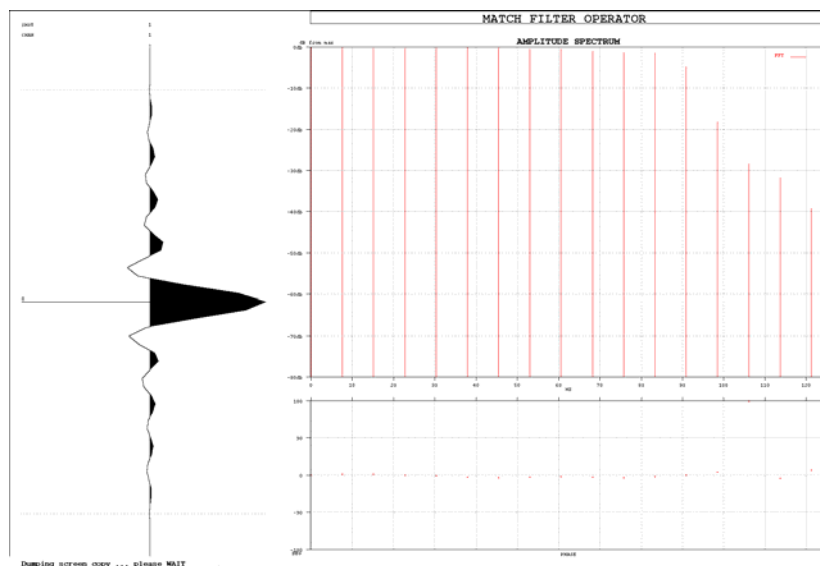


Figure 3-17b. The difference between the I/O and IVI Transfer Function filtered to 10-90 hz., note the lack of a difference between the two different data sets.

After the data were acquired over a four-day recording period the data were processed to prepare for the various different interpretation schemes. Figures 3-18a and 3-18b show examples of the raw data at near and intermediate offsets. The overall data quality was regarded as good, the best data being on the vertical component using the vertical source at the near offsets, and the poorest on the horizontal components with the horizontal sources at the far offsets.

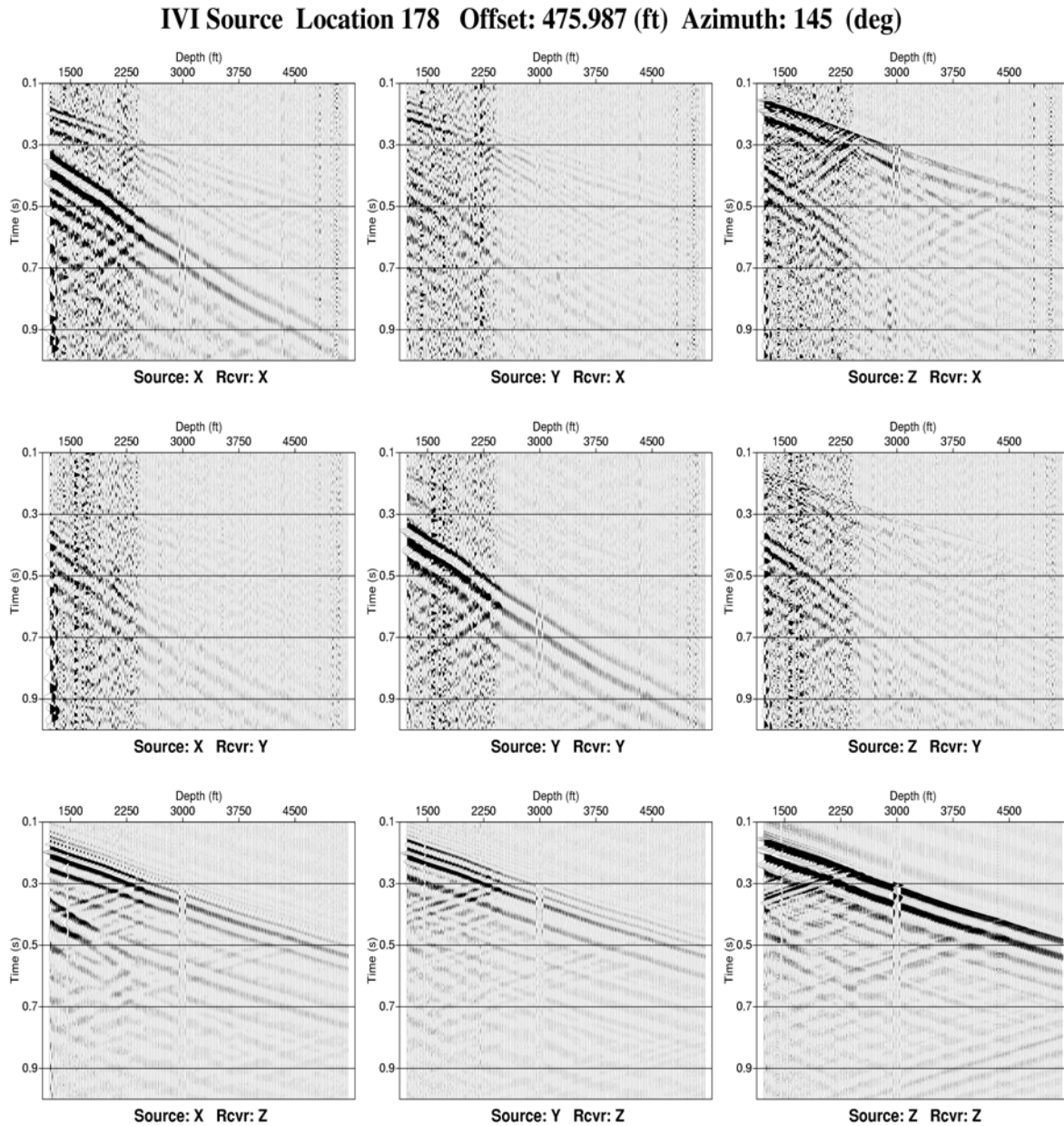


Figure 3-18a. An example of the raw data quality at a near offset (475 feet from the well head) for the 9-C VSP. The depth of interest is approximately from 3500 to 5000 feet.

**IVI Source Location 183 Offset: 816.894 (ft) Azimuth: 217 (deg)**

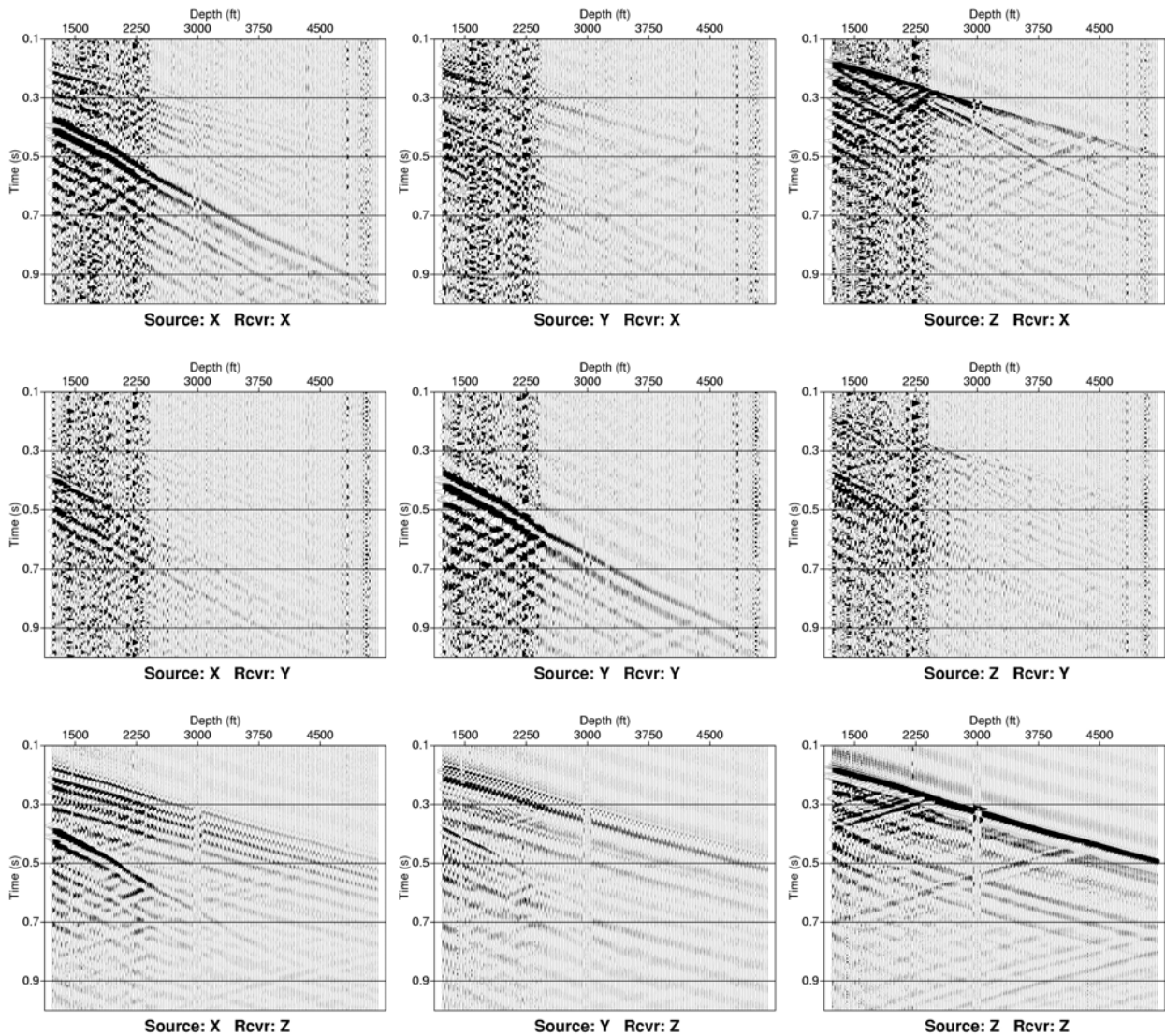


Figure 3-18b An example of the raw data quality at a intermediate offset (817 feet from the well head) for the 9-C VSP. The depth of interest is from 3500 to 5000 feet.

In terms of data processing the raw data were read and the recorded pilot was used to correlate the data. No additional filter was applied to the data. Because of the volume of data, individual bad traces were not eliminated before stack as would usually be done on VSP data. Scans of the prestack data support this step. Repeated shots at a given source location were stacked (vertical stacking). After correlation and stacking a rotation analysis to determine the receiver rotations was performed. A set of shot points were selected which included all the near offsets that

- 1) Had clean P-wave first breaks and

- 
- 2) Were near enough that the P-wave first-break time increased monotonically with depth.

An eigen rotation analysis of the first break correlation matrix was performed for each selected shot location to determine receiver rotation angles. Two windows were used, one included a half cycle of the first break, the other a full cycle. Analysis of the results showed greater than 90% of the energy was in single direction i.e. the first breaks were fairly linear. This result is consistent with most “zero offset VSP” data. The angles determined from both windows were consistent. The half cycle window was selected for further analysis. As a quality control the angle the major eigen direction makes with the vertical was calculated and compared with the angle given by the source receiver geometry. The comparison was very good except one shot had a large error. When the plot was made of all the shot and receiver locations it was apparent that the shot’s location was in error. P/GSI was contacted and they discovered there was an error in transcription in the location for that shot and sent the correct x and y for the source. This reduced the error.

For each shot location analyzed, the angle calculated from the analysis was corrected by the shot’s azimuth. The result for each receiver was plotted for all shots. Eigen value analysis gives a angle that points along the correct line but may have the wrong sense i.e. a 180 degree correction may have to be applied. The calculated angles were hand corrected for this effect. Once all the corrections were applied a fairly consistent angle was obtained for each receiver (except for the receivers that were bad). The median and several different weighted mean values were calculated for the receiver angles. All gave similar answers and the median value was used for the azimuth of each receiver. This angle was used to rotate the data for all shots (both those used in the analysis and those not used in the analysis) into receiver inline-crossline directions, i.e., for each shot the receivers was rotated so that one component pointed at that shot.

After the receiver rotations angles calculated from the subset of the data were applied to all the data another eigen-rotation analysis was made for all the rotated data. The new calculated angles were fairly randomly centered about 0 with a range of plus or minus five degrees, indicating an error of 5 degrees in the determination of the receiver angles.

The azimuth of the direction the vibrators were pointed was given by a compass mounted on each vibrator and was recorded at each shot location. In addition the location of each shot and the well head was know and that allowed the source azimuth to be calculated. From these two measurements a rotation angle can be determined. This angle was used to rotate the data into inline-crossline source components, i.e. for each shot the source was rotated so that one component of the source was pointed at the receiver.

After the source rotation was applied to the data a source eigen-rotation analysis was made. The results indicated a random error of 5 degrees in the source rotation angle. It also indicated that the vibrators did not produce linear shear waves. Under the surface conditions present at this location the vibrators produced elliptical shear waves. The data were rotated so that the long axis of the elliptical motion was pointed at the receiver.

At this point the data were ready to processed and analyzed for fracture effects. (see processing and interpretation sections)

---

### 3.3 SINGLE WELL SEISMIC DATA ACQUISITION

The single well seismic method is a recently developed technique which is designed to probe the volume of rock around a well at a scale which is intermediate between well logging (scale of 0.1 – 1 m) and VSP or crosswell (scale of 100 – 1000 m) (Majer et al 1997). In a single well survey, seismic sources and sensors are placed in the borehole with separations of 10 – 100 m. This method has required specialized acquisition development (Daley, et. al., 2000a, Daley, et. al. 2000b) which included development of a tube-wave suppressor (Daley, et al, 2003) because the high amplitude tube-waves are generally just noise, normally without useful information content (some use can be made of tube waves generated at fractures in open wells however). The single well method is important because it has the potential to locate a discrete gas-filled fracture zone which is near a well but not intersecting the well (Majer, et al, 1997, Daley et al, 2003, Gritto, et al, 2004). This information could be used to directionally drill into nearby productive fracture zones.

In July of 2002 after the VSP LBNL's single well data acquisition equipment was deployed in the Newberry LS-2C well. Two sets of data were planned; a high frequency (1 – 4 kHz) piezoelectric seismic source with 24 hydrophone sensors (at 10 ft spacing), and a lower frequency (70 – 350 Hz) orbital vibrator seismic source with five 3-component geophone sensors at 10 ft spacing. Each source has its advantages. The piezoelectric source is easy to deploy, requires no clamping and is relatively fast in data acquisition. It is either driven with a swept or pulse. In most cases we use a pulse input, stacking from 8 to 32 pulses in just a few seconds. This source produces a P-wave and a shear wave polarized in the vertical direction (SV). The orbital source is a mechanical source using rotating eccentric weights to produce an “out of balance washing machine” motion to generate radial motion. If it is rotated in both the clockwise and anticlockwise directions the data can be processed to produce a shear wave in the horizontal direction (SH) and a P-wave. Because the objectives were to image fractures we desired multi-component data. Thus the optimal source was the orbital source, recording with multi-component receiver. It was also the strongest source thus capable of imaging deeper into the formation. The volume imaged also depends on the source – receiver spacing (similar to surface seismic CDP imaging), the larger the source receiver spacing the deeper the imaging away from the borehole, thus the need for a stronger source. Typical distances away from the borehole are 10 to 50 meters, and possibly up to 100 meters with resolution on the same order as conventional well logs.

#### 3.3.1 Orbital Vibrator Source Data:

The orbital vibrator is a unique borehole seismic source capable of producing both P and S-wave energy (Daley and Cox, 2001). The Newberry single well acquisition had source points at 5 ft. intervals from 4900 to 4245 ft. with 3-c sensors at offsets of 87, 97, 107 and 117 ft for each shot. Since the orbital vibrator generates two components of source motion (equivalent to horizontally oscillating sources), there are six components recorded for each shot. Similarly, for each sensor we can make a 6-component common-offset gather, which is all the shot depths, recorded for a single sensor. Figure 3-19 shows a 6-c common-offset gather for the 87 ft offset data. The dominant energy is again tube-waves, however there is one anomalous zone observed. The other 3 sensor gathers show similar signals.

# Six component O.V. Gather

## Offset = 87 ft (26.5 m)

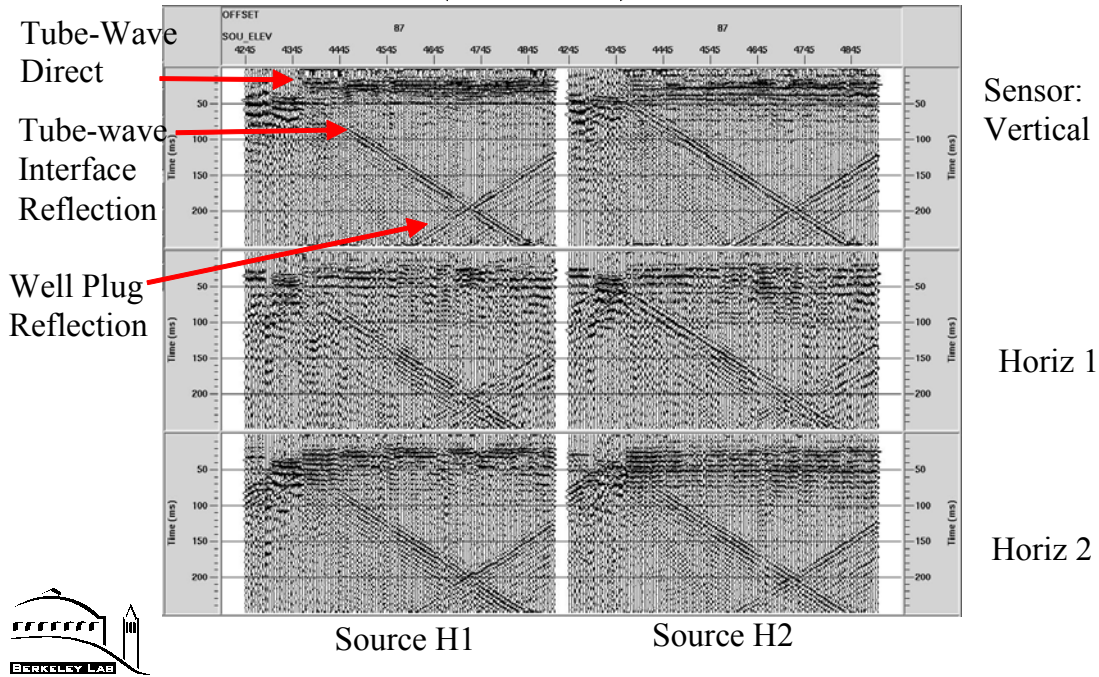


Figure 3-19. Six-component single well common offset gather. The data is all shots for one 3-component sensor at an offset of 87 ft. below the source. Source depth is shown on the top horizontal axis. All components have similar arrivals, which are dominated by tube waves, including direct, reflected and multiple arrivals.

### 3.3.2 Piezoelectric Source Data:

A limited set of data was acquired with the piezoelectric source with only about 90 feet (45 shots) of data acquired in the reservoir interval (shots points from 4850 ft to 4764 ft). Figure 3-20 shows a shot gather (one shot, all sensors). The tube-wave and multiples of the tube wave is the dominant signal. The high level of tube-wave noise, along with the limited depth range, precluded useful analysis of this data set.

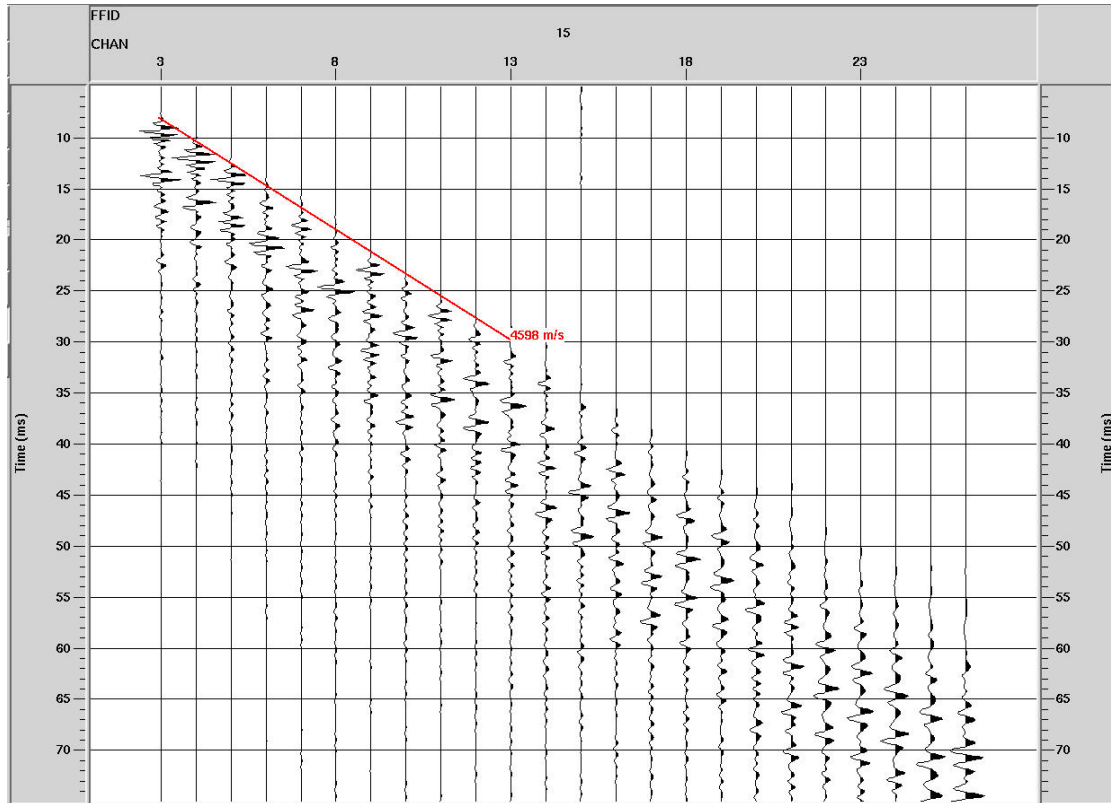


Figure 3-20. Shot gather of piezoelectric source single well data. The source is at 4822 ft. depth with the 24 sensors offset from 32 to 262 ft. below the source. The red line indicates the moveout velocity of the dominant event (4598 ft/s which is the tube-wave).

### 3.4 WELL LOGGING ACQUISITION

A state-of-the-art logging data set was needed to complement the VSP, surface seismic, and single well data sets. The four data sets would form the basis of the overall integrated fracture model. Schlumberger performed the well logging on two different wells within the 20 square mile study area. Both wells are located in San Juan County, New Mexico, in the Blanco Mesaverde / Basin Dakota field. The first well – Moore LS #7B – was logged on January 30, 2002, over the depth range 500 feet – 5200 feet. The second well – Newberry LS #2C – was logged on February 13, 2002, over the depth range 3900 feet – 7050 feet.

In each well the Schlumberger Platform Express™, Dipole Sonic Imager™ and Formation Micro Imager™ were recorded. Collectively the tools made the following collection of measurement logs:

- Acoustic
  - o monopole compressional and shear waveforms
  - o cross-dipole shear waveforms
  - o Stoneley waveforms
- Four-arm caliper
- Gamma-ray

- 
- Resistivity
  - Neutron density
  - Formation Micro-Imager (FMI)

These raw measurement logs were processed and interpreted to provide petrophysical and lithology logs using Schlumberger's ELAN software. These lithology logs acted as input to the geostatistical work performed by Virginia Technology for this study.

The FMI images were interpreted to identify natural and drilling induced fractures and are in turn integrated with 4-arm caliper datasets to provide logs of borehole ovality and breakouts. These interpretations in turn indicate the in-situ stress directions. Finally, this information is integrated with the results of acoustic cross-dipole logs processed for anisotropic parameters to provide a characterization of fractures from the sub-millimeter to meter scale.

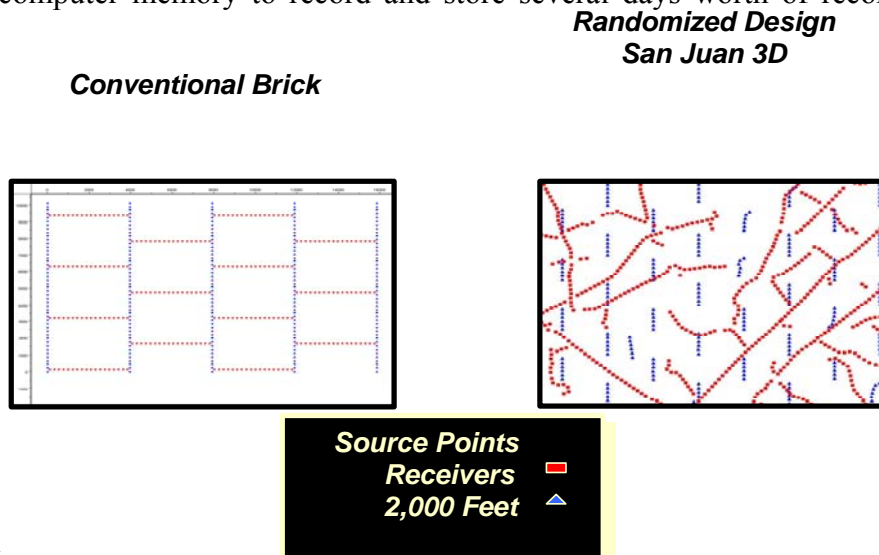
---

## 4. PROCESSING AND INTERPRETATION OF THE DATA

### 4.1 3-D SURFACE SEISMIC FOR FAULT STRUCTURE

As part of the process in deriving an overall integrated fault and fracture model a key element was interpreting the reprocessed 3-D P-wave seismic surface reflection data in the 20 square mile study area. To understand the limitations of the data one must know how the data were acquired in this area. The San Juan Basin presents some challenges for cost effective acquisition of surface seismic data. Shown in Figure 4-1 on the left is a typical source and receiver geometry for acquiring 3D data in the late 1990's. Groups of geophones (displayed in blue) are connected by cables laid in parallel rows. Shots (in red) acquired by vibrators or with dynamite are aligned perpendicular to the receivers in such a way as to give the appearance of a brick wall, hence the derivation of the term "bricked source effort". Many 3D surveys of this general style have been recorded in recent years. Surveys of this type acquired in the San Juan Basin would likely cost in excess of \$30,000 per square mile, which was much more than either Conoco or Burlington (the underwriters of the survey) were willing to pay. Additionally this geometry has the potential to pose serious environmental and archeological problems.

As a result of these concerns Conoco and Burlington (under a cost sharing effort) implemented the semi-random survey style depicted on the right side of Figure 4-1, an example of an unusual, some (processors) might even say perverse, geometry. Vibrator source points are distributed on the roads, with all the randomness that is imposed by a road system. Receivers, on the other hand, are laid as closely as possible in a brick pattern, subject to topography, similar to that shown on the left for the sources. However, unlike the conventional layout on the left the receivers are not connected together by cables, each group of six receiver stations had access to enough onboard computer memory to record and store several days worth of recorded traces



from the shooting.

Figure 4-1. Two different examples of shooting patterns for 3-D seismic. The conventional example on the left is used in areas of good access. The pattern on the right was implemented in the San Juan due to access and cost issues.

Figure 4-2 shows the resulting full offset fold of stack derived from the acquisition geometry used in the San Juan Basin study area. Seismic fold (or how many times a given area in the subsurface is sampled and recorded by the seismic waves) varies in response with the quasi randomized source acquisition. Not quite truly random it is nonetheless still fairly even, more even than achievable by a typical conventional survey. Displayed fold varies from about 80 in blue, to a maximum of around 120 in yellow for the surveys' deeper Pennsylvanian objective. Displays such as these were constantly being generated and updated throughout the planning and execution of the project and any unacceptable fold gaps or concentrations were adjusted by judiciously moving or adding more receivers. Within Figure 4-2, the set of red lines depict the location of the seismic line displays which are to follow.

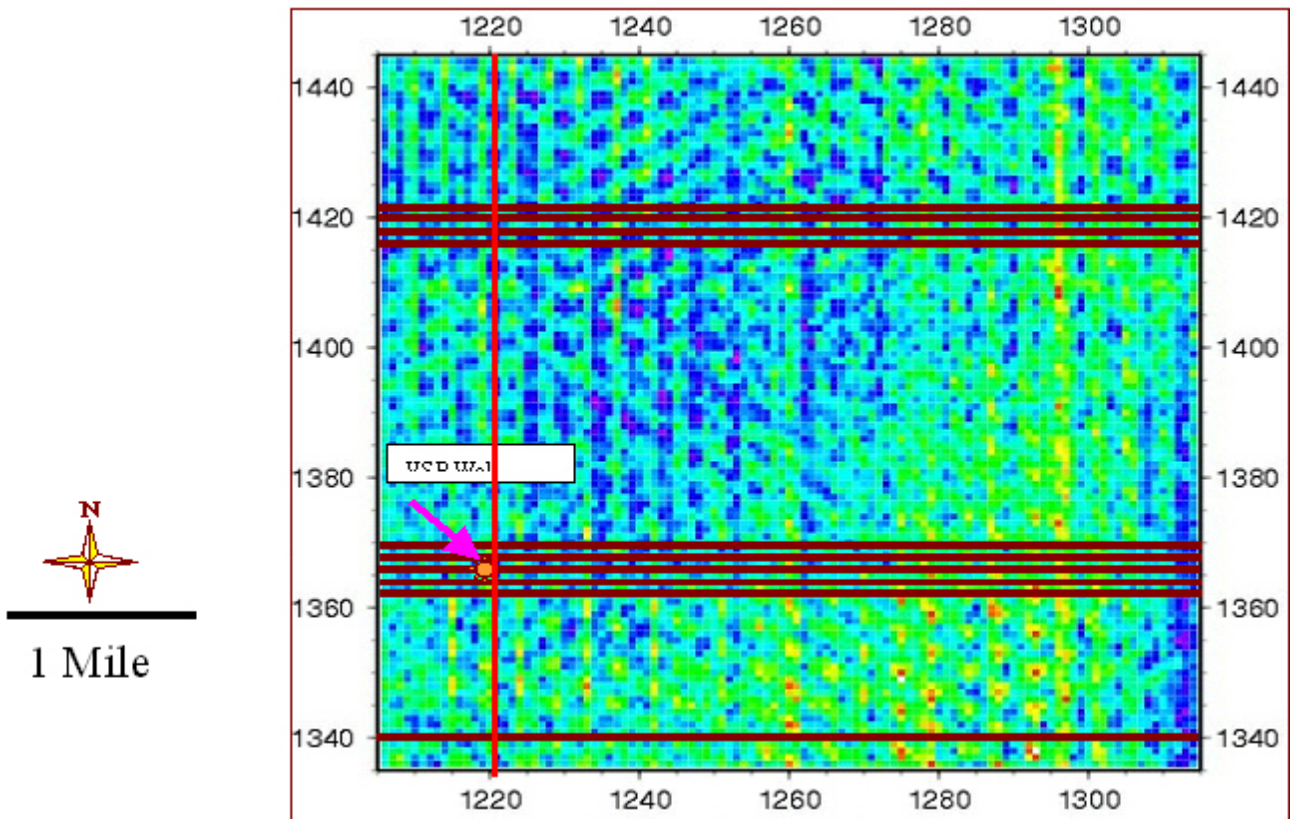


Figure 4-2. The fold of stack display for this area. The blue is 80 and red is 120 fold. The red lines are the locations of the seismic cross sections to follow.

Figures 4-3 and 4-4 are examples of two different styles of fault interpretation investigated for this study. Approach A is a style often applied onshore in the U.S. (Figure 4-3- red-blue seismic, yellow faults) and approach B more often used offshore and in the Gulf of Mexico region (spectrum seismic, multicolor faults in Figure 4-4). The technique adopted by A was to interpret every other seismic vertical in-line and crossline, visually identifying and picking fault displacements that appear on at least two consecutive interpreted lines. Fault cuts from inlines and crosslines would then be displayed in map view and the cuts points connected if and when fault strike and direction of throw were in agreement.

The B approach chose to examine every 10<sup>th</sup> in-line and 10<sup>th</sup> cross-line, followed by NE and NW bisecting diagonals, and finally time slices at every 4 to 8ms. B's interpretation consisted of picking visible offsets in the vertical displays and connecting these break points using amplitude alignments or offsets on time slices. The sampling technique of Method B resulted in a more smoothed and laterally extensive set of faults, while A exhibited a more discrete faulting result. While the gross fault strike trends between the two styles often differed, in map view, individual fault picks when made on the same line were remarkably similar.

It is most likely that the differences between the two separate fault maps can be ascribed to the possibility of spatial aliasing the fault picks and fault throws and the use of multiple criteria for selecting the continuation of faults between interpreted points in the B approach.

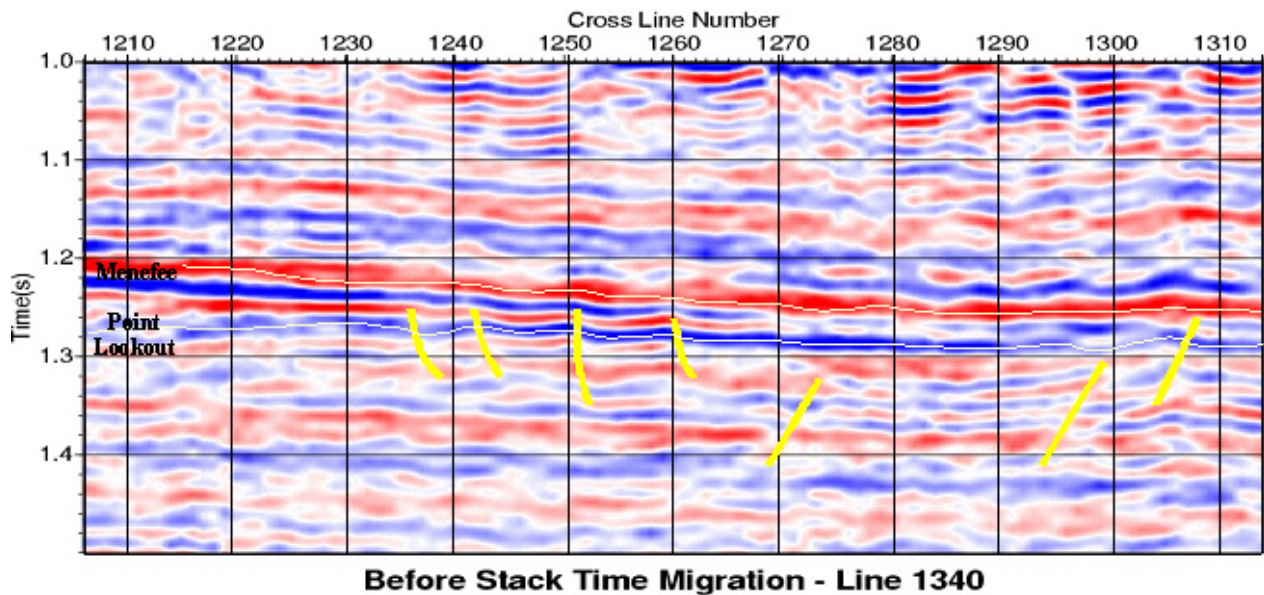


Figure 4-3. Fault picks using method A. This cross section is the southern most line in Figure 4-2.

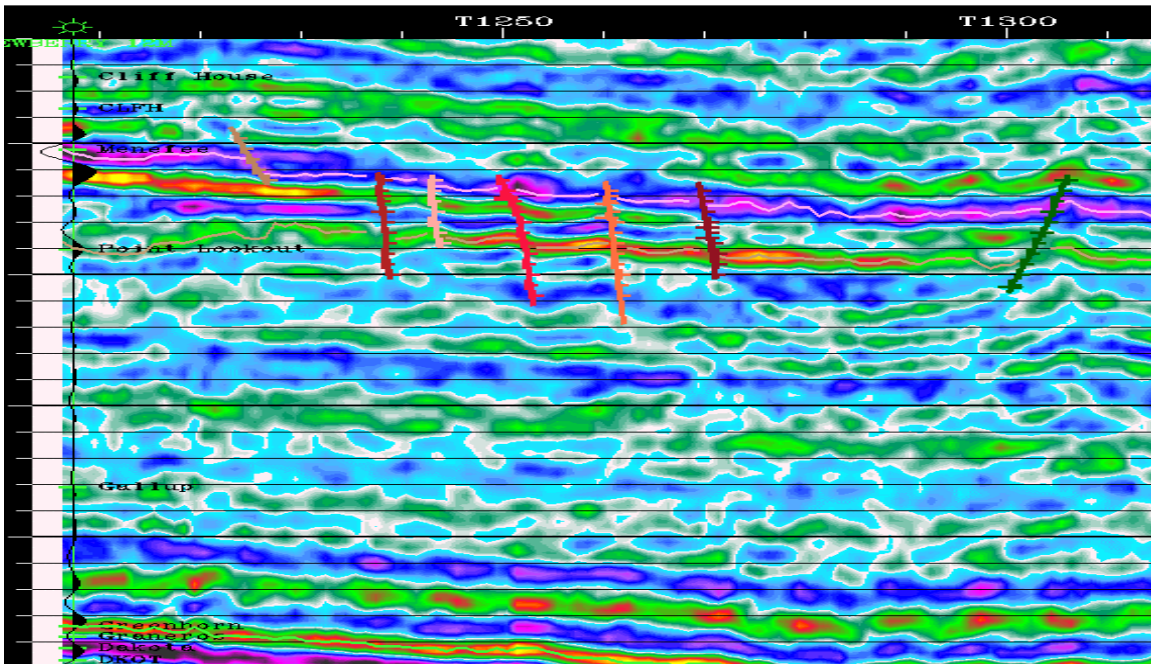


Figure 4-4. Fault picks using method B along same line (1340) as Figure 4-3.

Note on the left side of the rainbow spectrum seismic is posted a synthetic seismogram tie of well formations to the seismic. Formation ties can be read posted to the right of the trace. Figure 38 is a N-S line through the study area.

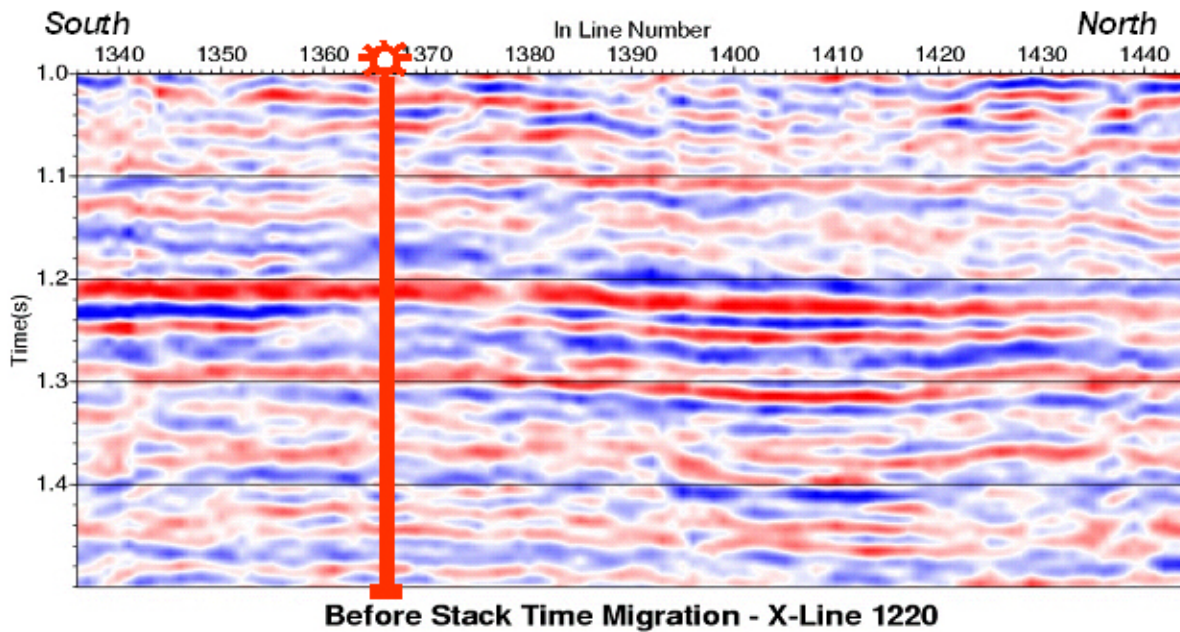


Figure 4-5. North - South line through the VSP well, note lack of picked faults.

The next series of Figures (4-6 to 4-13) show the seismic cross sections (red lines in Figure 4-2) shown plotted on the fold of stack map (Figure 4-2).

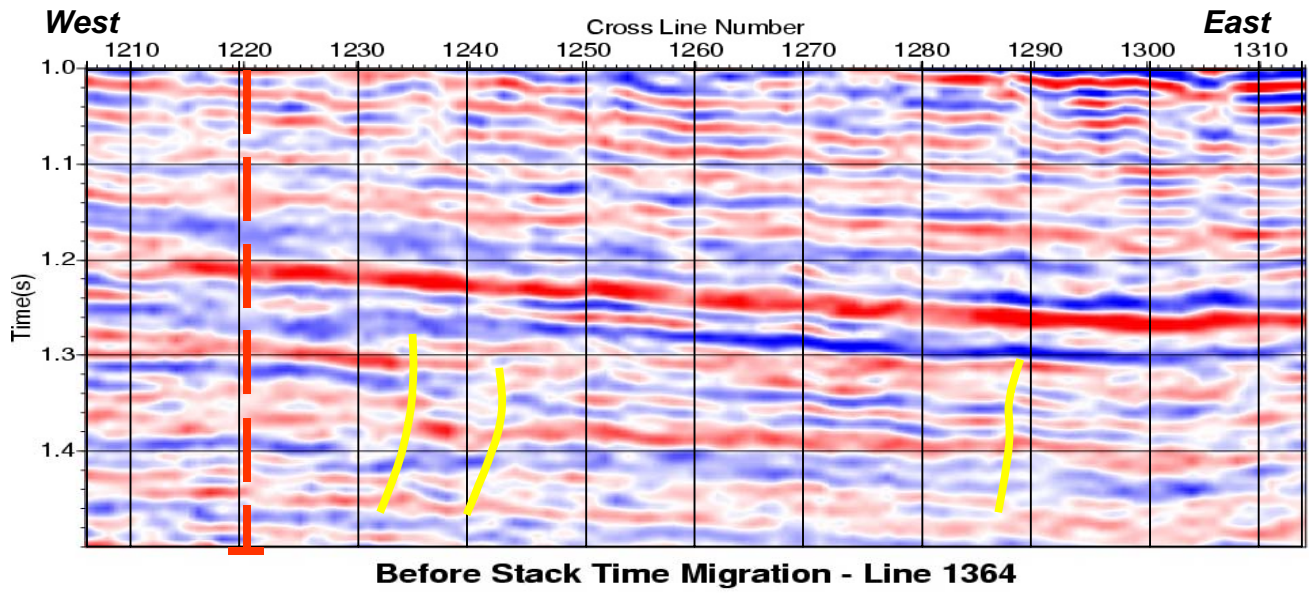


Figure 4-6. East-West line in the vicinity of the VSP well.

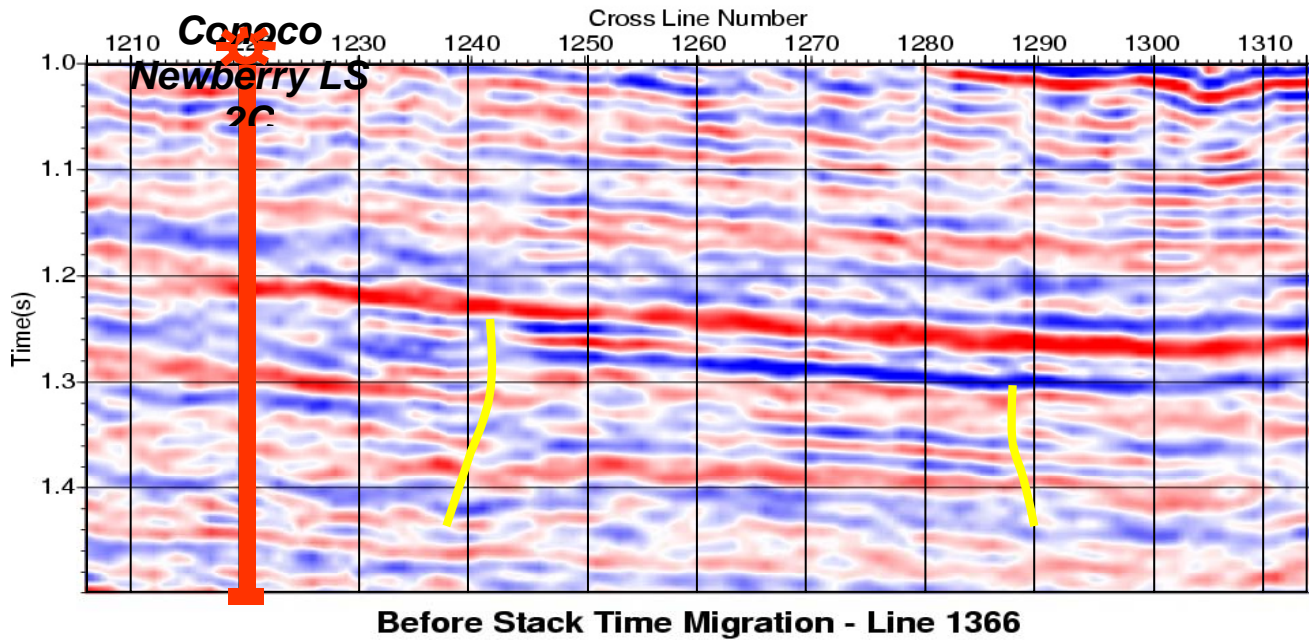


Figure 4-7. East-West seismic line (1366) through the VSP well.

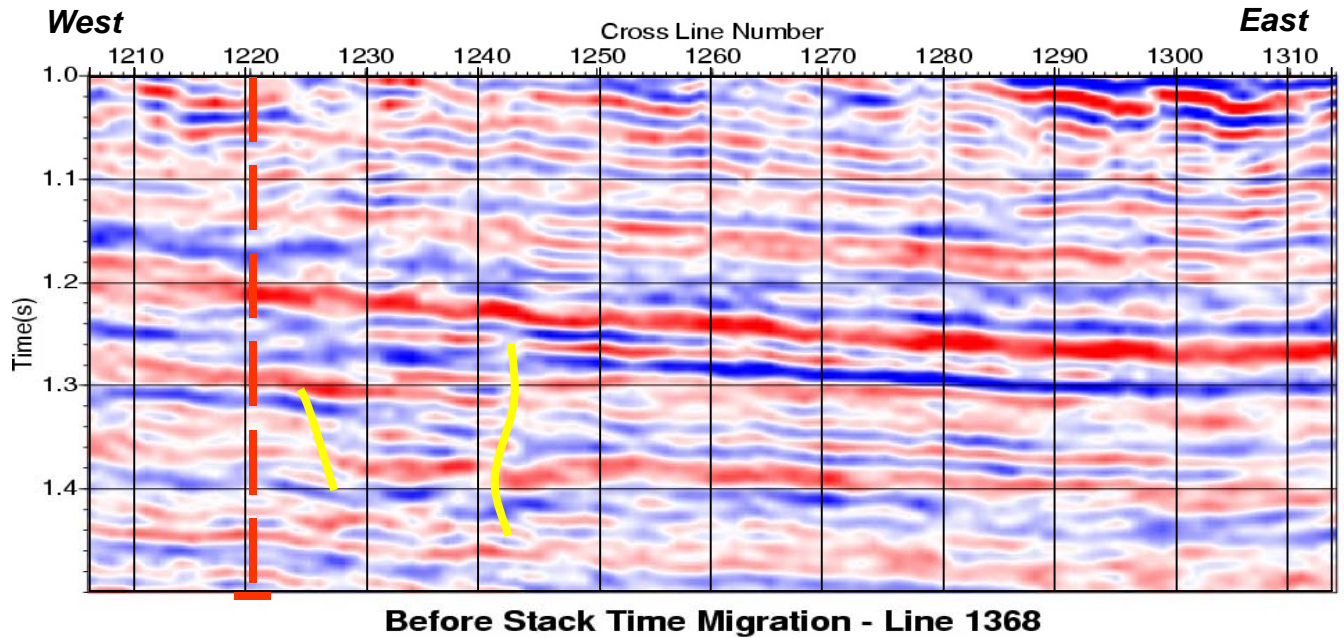


Figure 4-8. East-West cross line (1368), just north of the VSP well.

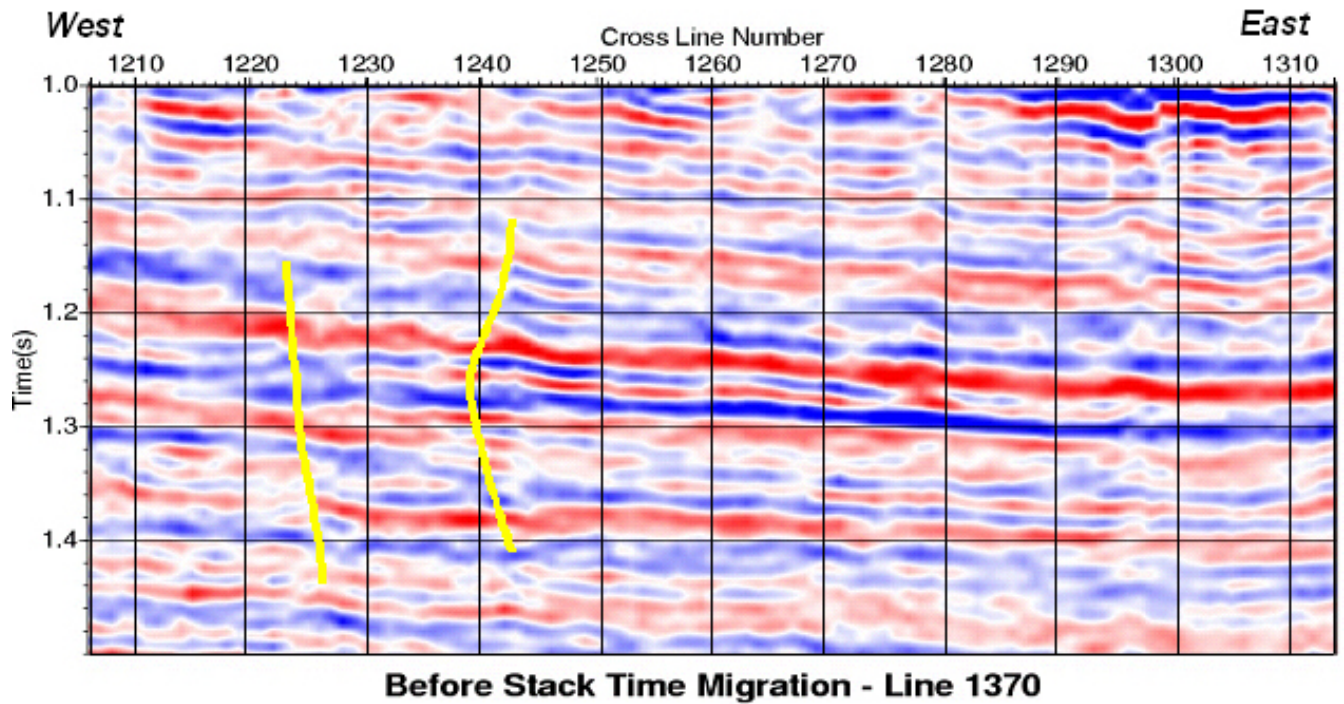


Figure 4-9. A seismic line 440 feet north of the line in Figure 4-8.

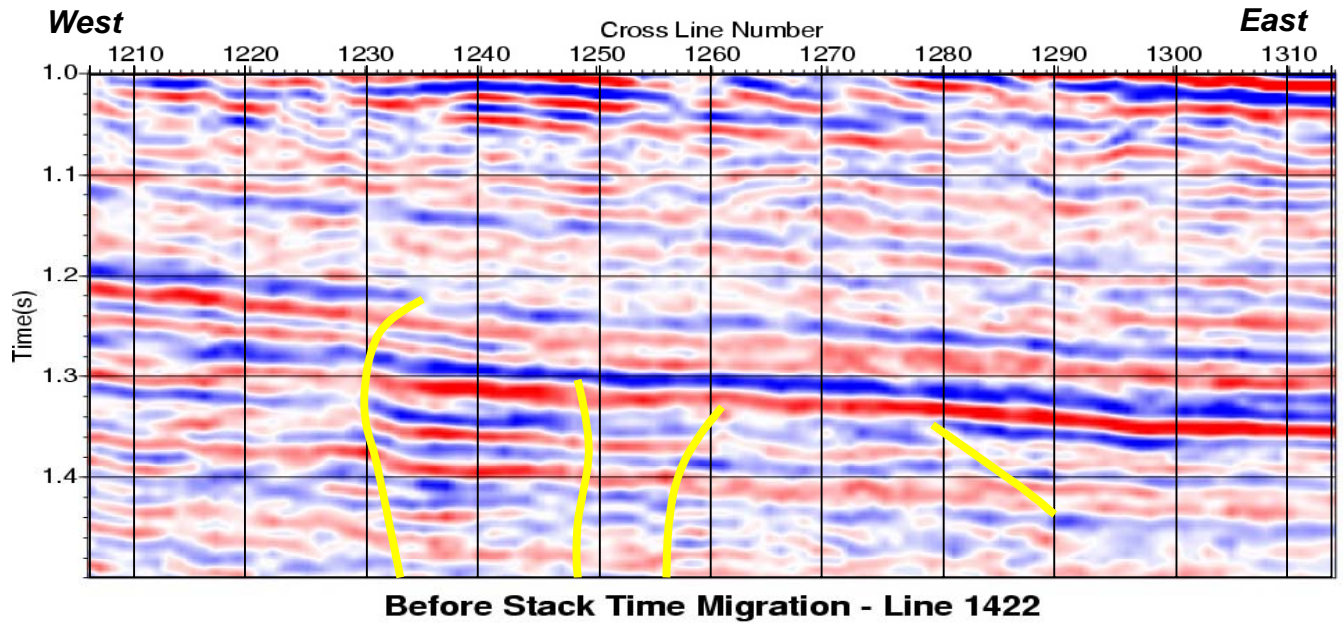


Figure 4-10. Seismic crossline located in the northern most part of the study area.

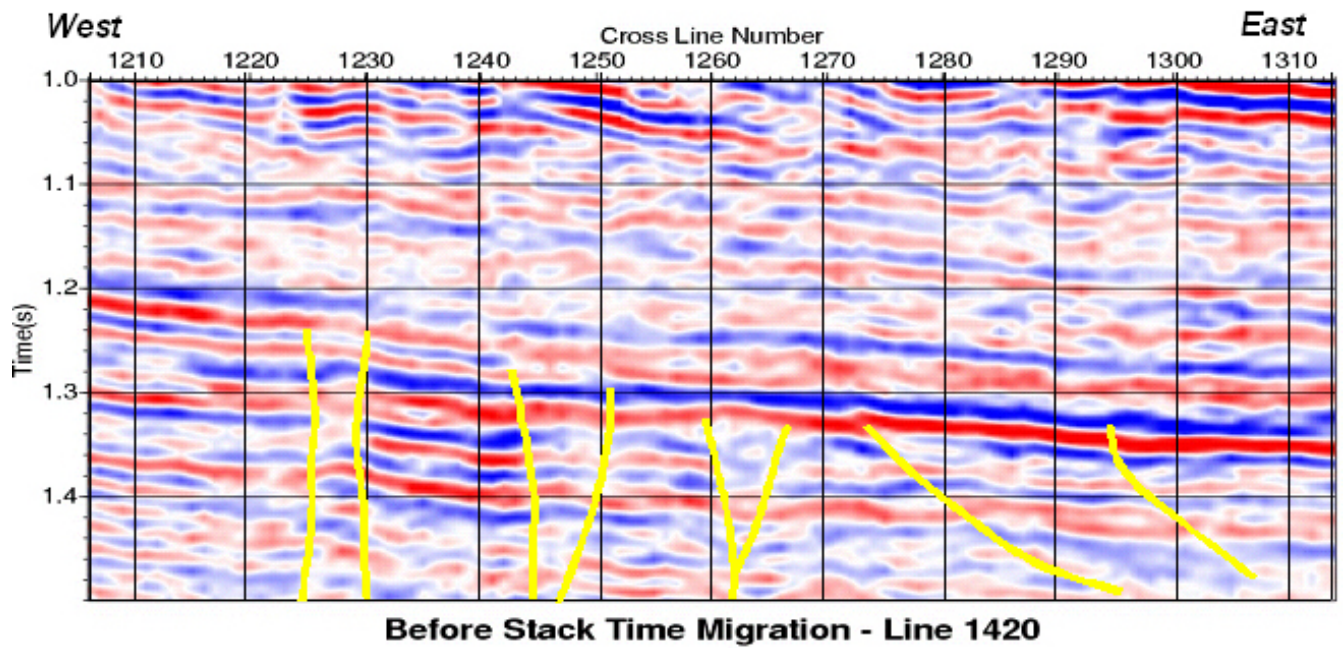


Figure 4-11. Seismic cross line just 440' south of the line in Figure 4-10 towards the VSP well.

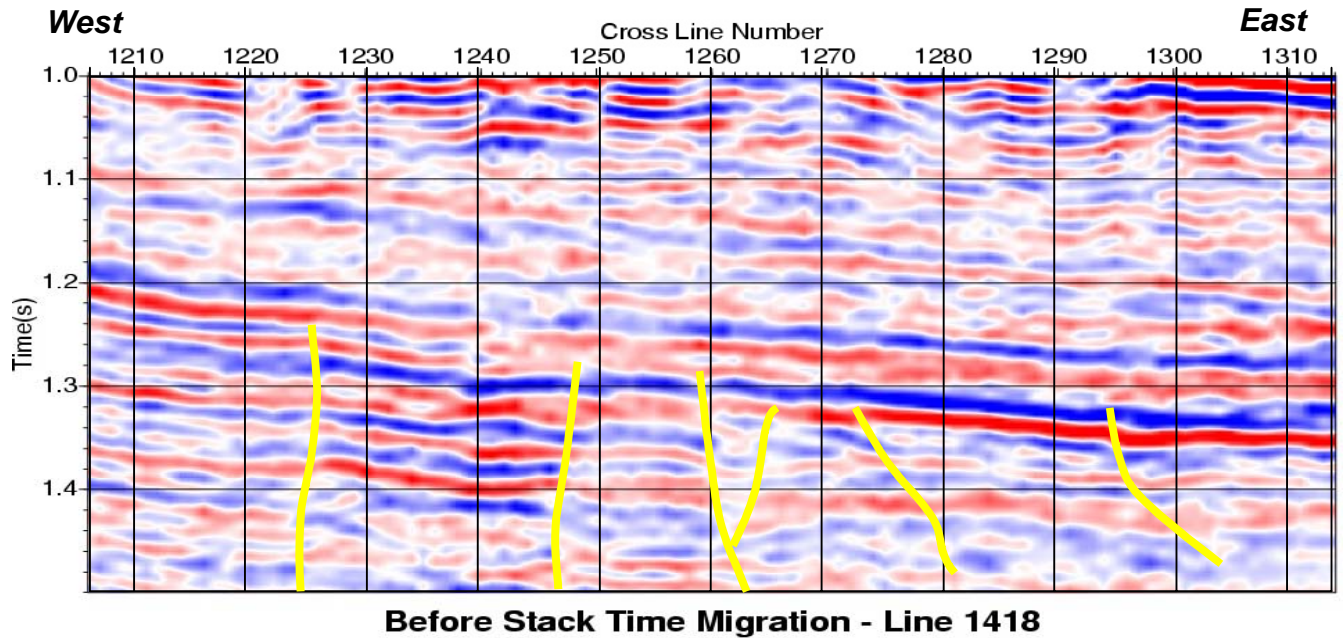


Figure 4-12. Seismic line 440 feet south of the line shown in Figure 4-11.

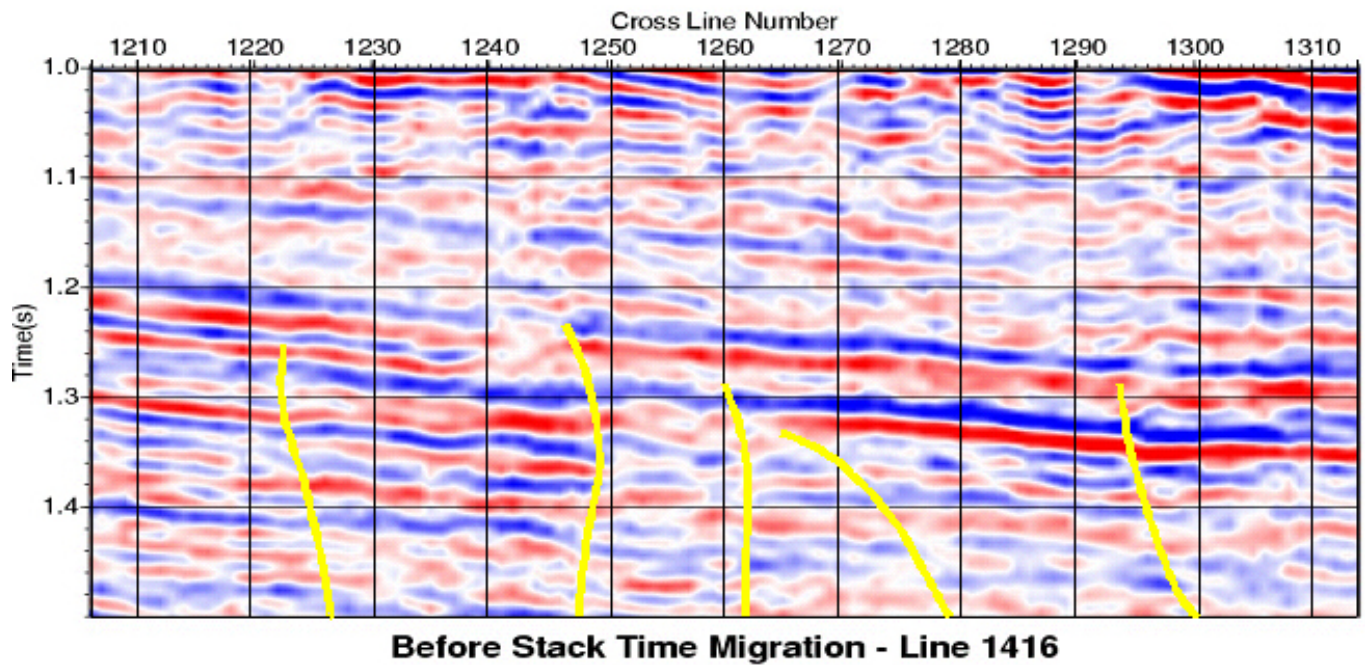


Figure 4-13. A final crossline, another 440 feet south of the line in Figure 4-12 towards the VSP well. Note how the placement, orientation and even number of faults vary significantly from line to line while separated by only 440 feet in horizontal distance.

It clear from an examination of Figures 4-3 through 4-13 that there are numerous faults present in the subsurface oriented at various angles and indicative of a series of different tectonic events that have had a role in shaping the observed present day fault and fracture characteristics of the basin.

Due to the complexity of the area it ultimately became obvious that using only method A or B would be insufficient and therefore it was decided to use a combination of the two plus an integration with seismic and horizon based attributes. Figure 4-19 shows the final picks as derived by using this combination of methods a and b. Prior to that realization, however, both methods A and B were applied independently. Figure 4-14 displays the results using method A. The faults displayed on top of this Menefee sub sea depth structure map were constructed by using visual interpretation of the inline and crossline seismic displays, and by detailed evaluation of velocity maps where the interpreter searches for deviations from the expected local surrounding velocity field and corrects by reinterpreting the seismic data and changing the time interpretation if it is determined that the change supports an alternative faulted model and the local velocity field is restored to background. This velocity interpretation approach only works in areas where the well control is as adequately dense, as in the San Juan basin, to support this technique.

The small tick marks on the fault lines are located to denote the down thrown side of the fault (pink faults are generally down to the west and red faults are generally down to the east).

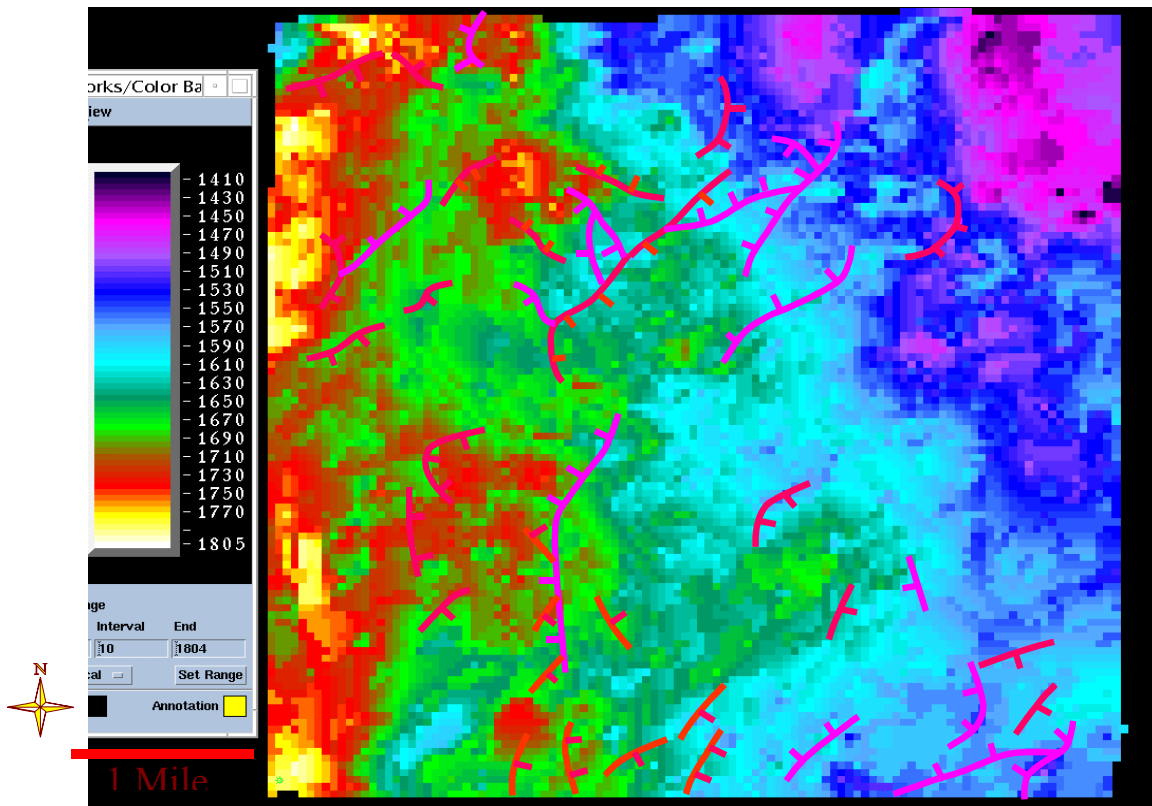


Figure 4-14. Fault picks derived from Method A overlain on the Menefee time horizon for the 20 square mile study area re-processed data. Ticks indicate down dip direction.

Shown below in Figure 4-15 is an intermediate compilation of the results of the method B analysis steps. On this Menefee time structure map has been posted the raw fault pick locations using the B approach which were derived from interpreting in-lines, cross-line traces, 45 degree oblique arbitrary lines and time slices. In this approach after picking fault cuts on the vertical seismic lines, time slices displays were used to extend and connect the sparse fault picks made on every 10<sup>th</sup> in-line and cross-line by examining reflection amplitude alignments and offsets. The map on which these time slice fault segments have been displayed is the Menefee times structure map. Additionally depicted on this figure is an inferred left lateral strike-slip/wrench fault, identification based on apparent fault groupings (red and tan) offset across a zone that appears relatively devoid of faults.

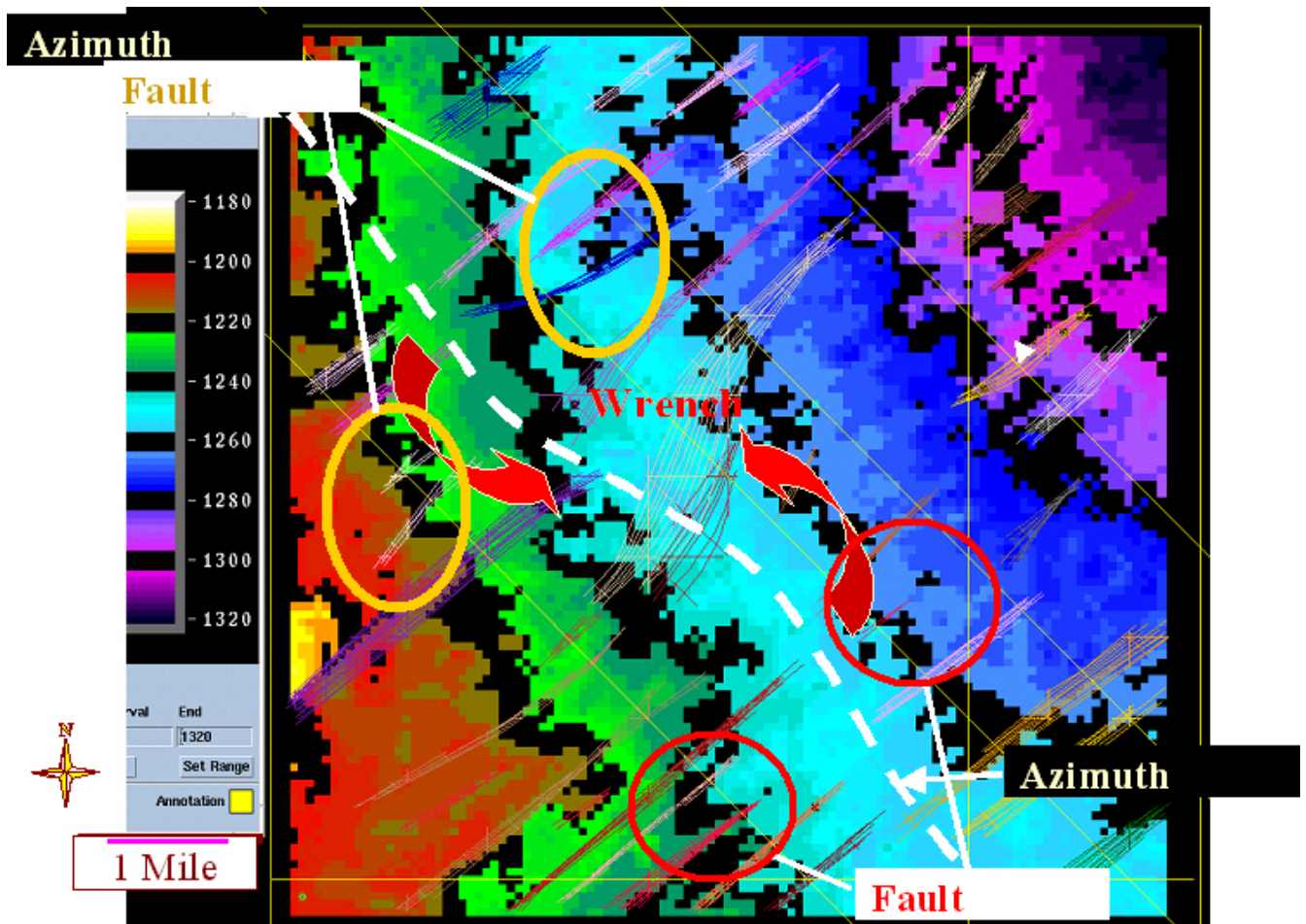


Figure 4-15. Fault interpretation overlaying the Menefee horizon showing the “smoothed/aliased” results of Method B.

As can be seen from a review of Figures 4-14 and 4-15 the resulting fault interpretation is likely quite complex. One could reasonably expect many sub-seismic faults to be present between the 3D seismically imaged faults as possibly suggested by the core analysis results.

The Northwest San Juan basement depth structure map shown on Figures 4-16 and 4-17 (actually ~600 feet above basement at the Mississippian Leadville) provides a useful backdrop for contrasting the effects and orientation of Precambrian and Pennsylvanian structural features with those imprinted later with the movement on the Hogback Monocline. Outlined in green is a regional seismic line that is shown farther below in Figure 4-18. Within the pink box in Figure 4-16 is the “basement” fault interpretation. Following, in Figure 4-16 is the combined A&B Mesaverde fault interpretation (Figure 4-17) and the putative left lateral wrench zone. Notice the reasonable conformance between deep and shallow fault orientations in the southern and eastern quarters of the study area and extreme departure from conformance in the northern half of the area, due most likely to influence from the Hogback structural terrain. Figure 4-18 shows the Northwest-Southeast oriented regional slice of the 3-D seismic from the reprocessed portion of the NW San Juan 3D survey. It vividly illustrates the location and influence of the Hogback Monocline at the northwest corner of the study area. Note the presence of a possible down to the northwest strike-slip/wrench fault in the Mesa Verde section.

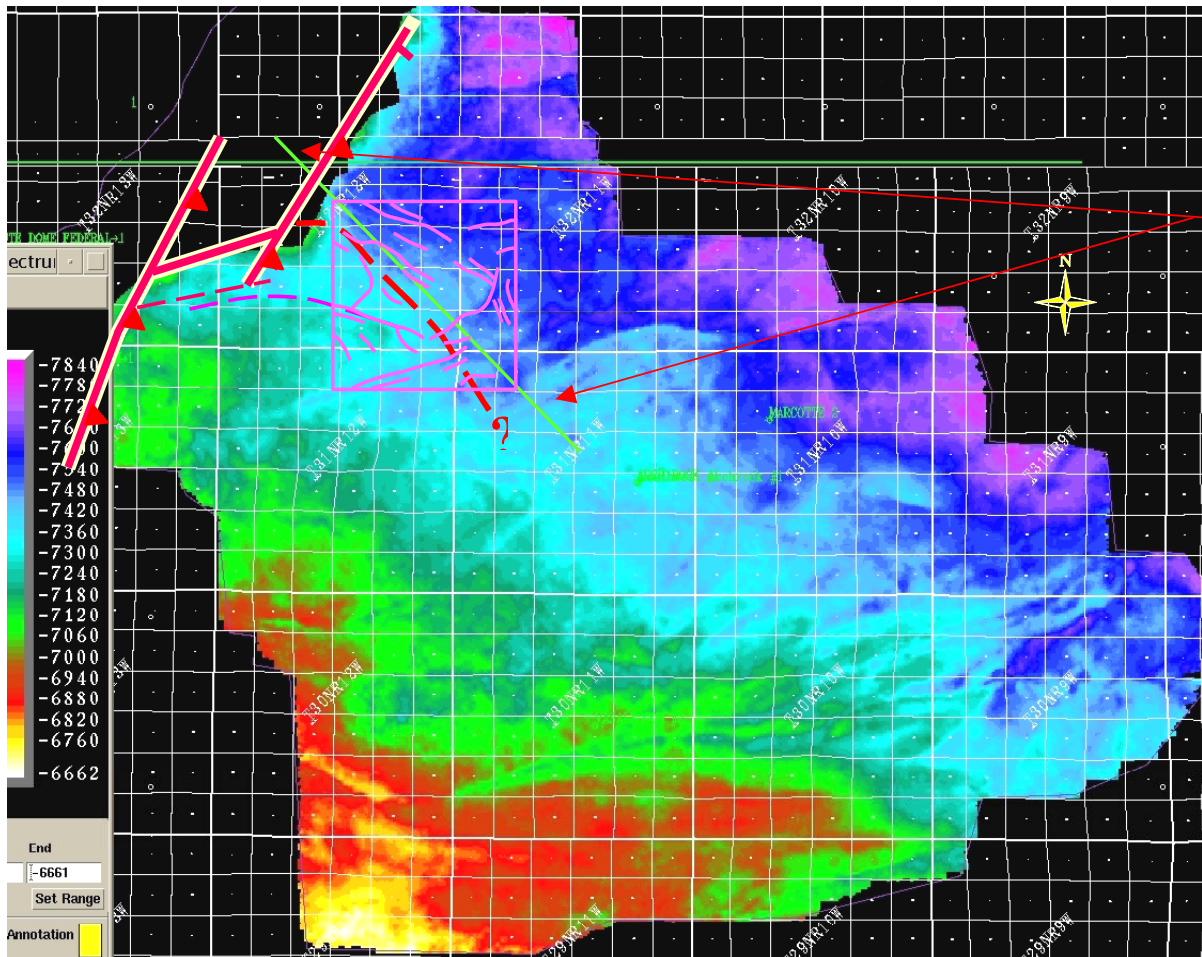


Figure 4-17  
Seismic Line

Figure 4-16. Mississippian sub sea depth map with basement fault interpretation (pink faults).

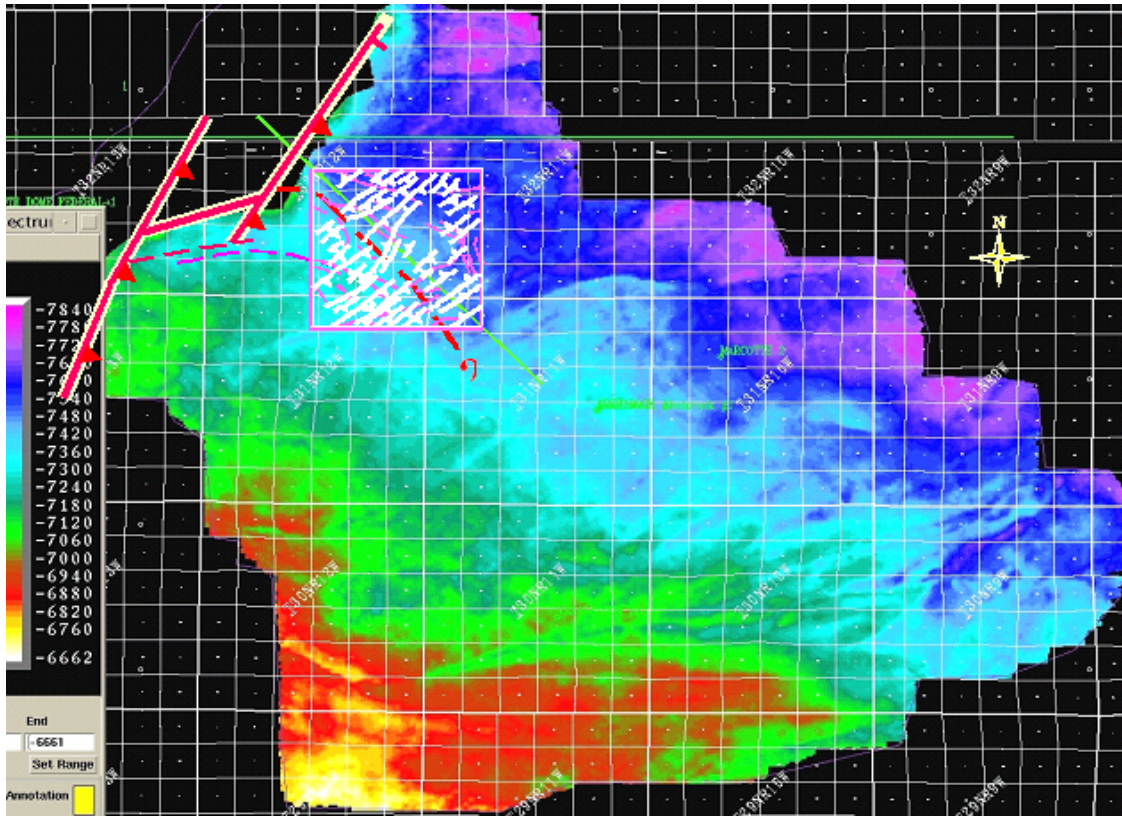


Figure 4-17. The Mesaverde combination fault interpretation (white faults), superimposed on the previous fault (pink) and Mississippian structure map.

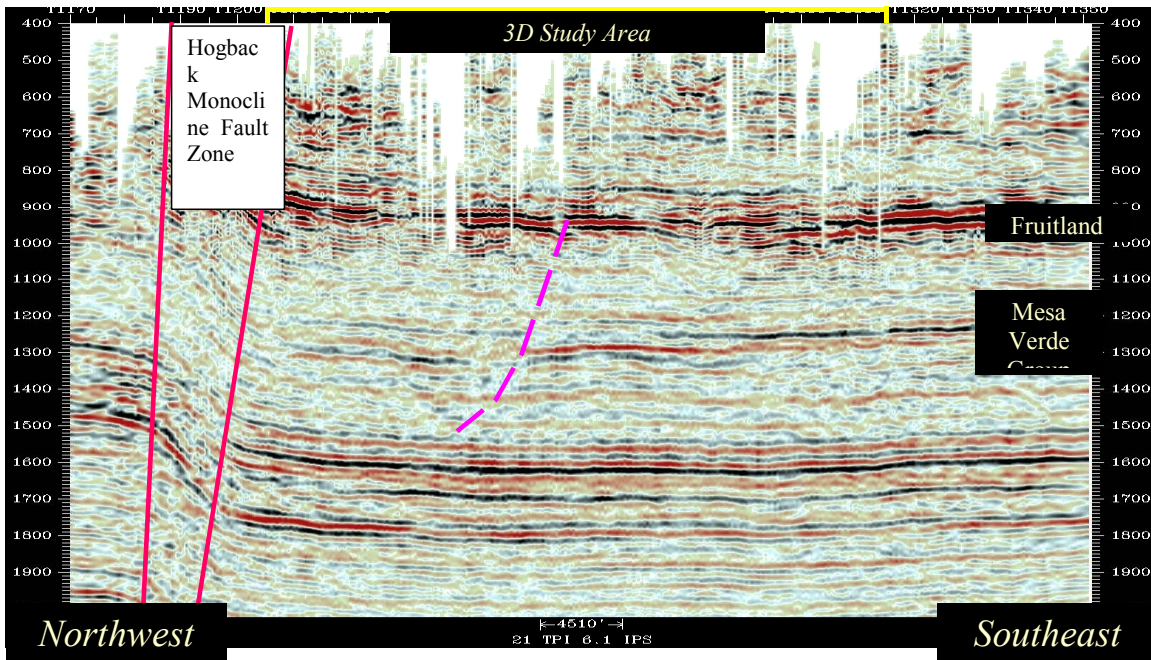


Figure 4-18. A cross section across the NW part of the San Juan basin as shown on the green line in Figure 4-16.

Due to the complexity of the area it ultimately became obvious that by using method A or B alone would be insufficient and therefore it was decided to use a combination of the two plus an integration with seismic and horizon based attributes.

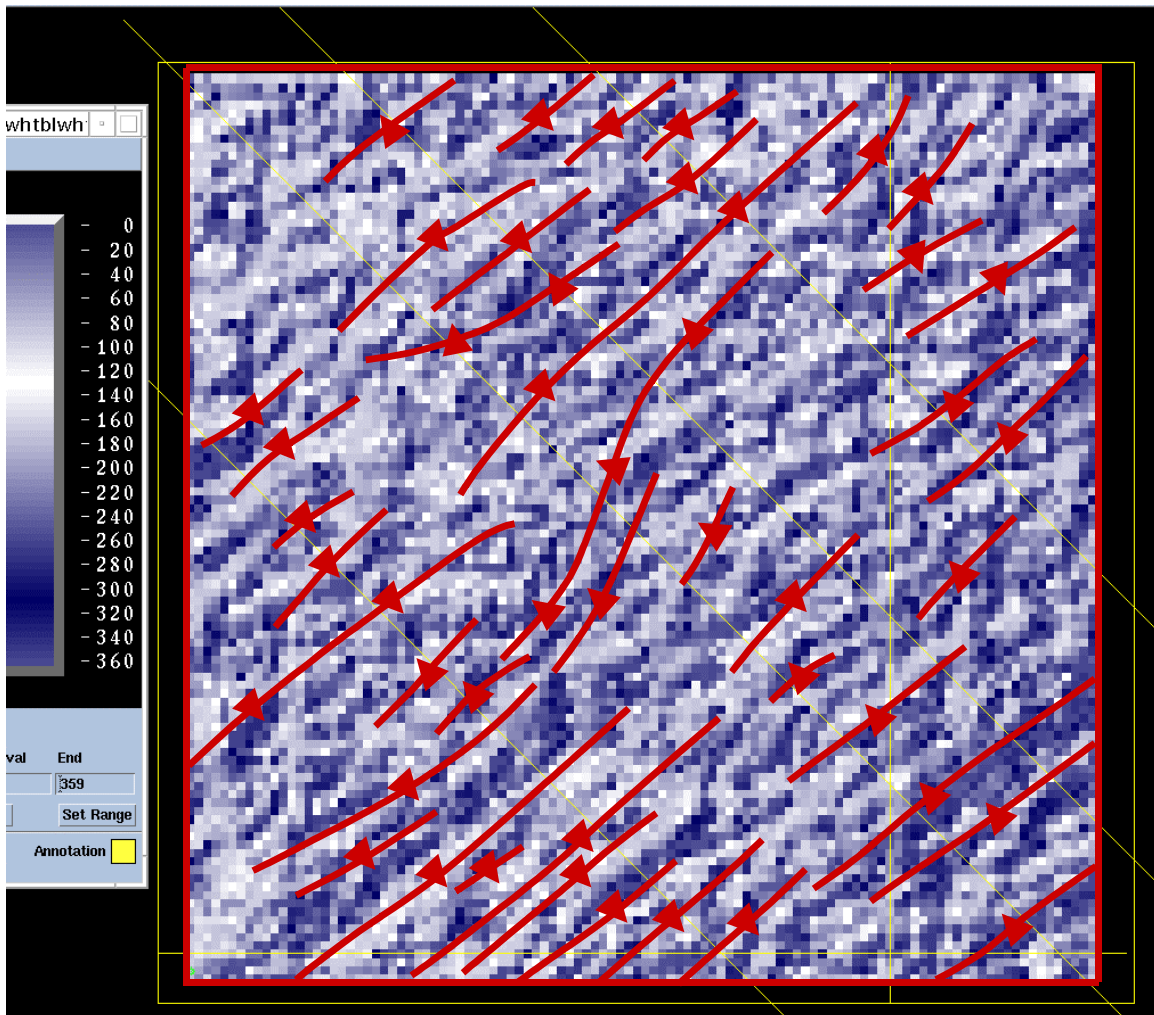


Figure 4-19. Azimuth attribute display created from the Menefee time structure map with overlay of the summary combined A&B methods fault interpretation (triangles point to the downthrown hangingwall side of the normal faults).

Figure 4-19 shows the final fault picks as derived by using this combination of methods A and B overlain on the Menefee time horizon attribute map. This attribute is termed the azimuth. It shows changes in true dip direction from 0 to 360 degrees. Azimuth maps can be used to detect subtle changes in dip direction that might represent faults. They are also useful for confirming structural closures and for locating the crest of an anticline or the trough of a syncline. This azimuth map shows the direction of maximum dip, at each point (bin/pixel) by calculating the difference in structural position between that point and the two adjacent samples in orthogonal directions. A plane is then fit through the three points that has a corresponding direction of dip in degrees. The calculation for computing azimuth is:  $\text{Azimuth} = \arctan \left[ \frac{dt/dy}{dt/dx} \right]$  where:

---

$dt/dx$  is the dip in the  $x$  direction (inline), and  $dt/dy$  is the dip in the  $y$  direction (crossline or trace). An azimuth value of 0 is aligned with true north, while 90 coincides with East, 180 with South, and 270 with West. The display is best analyzed with a black/white color bar (black 0 and white 180 degrees) (previous slide) or a black/white/red/blue color bar (black 0, red 90, white 180, and blue 270 degrees). When this is done it can be used to selectively illuminate structural features of differing orientations or azimuth, as in the interpretive left lateral wrench zone. Lacking picked faults from the seismic, azimuth is a good first approximation for their location and extent.

Interestingly, of all the various map, seismic and horizon derived seismic attributes analyzed, only Azimuth appeared singularly able to yield consistent fault/fracture information. Indeed, each of the faults, picked from a combination of lines, traces, arbitrary lines and time slices, generally correspond to an Azimuth lineation. Each Azimuth lineation does not, however, have a corresponding identified fault. Since the faults range in throw from ~20 ms (~120 feet) down to ~6 ms (~35 feet) or about one sample - 4 ms it may be that the azimuth attribute is possible that many of the lineations seen on the Azimuth display that do not correspond to currently identified faults/fractures may in fact tie to features that lie on the border of seismic resolvability.

In summary, while an analysis of the surface P-wave seismic data has not been able in this study to define reservoir scale fractures it has been of sufficient quality to image and orient regional to local scale faults. As such it can likely yield valuable information about the sub-seismic fracturing. In future work it would be recommended that higher fold, high frequency data be acquired prior to performing the interpretation outlined earlier. Specifically, interpretation should include the following practices, 1) an analysis of every line or every other line (and cross-line) – method A. If small scale reservoir fracturing (in the 10's to 100's of meters) is expected or present in the subsurface, then one should interpret seismic lines on the same physical scale. While every 10<sup>th</sup> line is sufficient in the Gulf of Mexico where line spacing is 12 meters, that same interpretation spacing is woefully insufficient in the San Juan Basin study area where the line spacing is almost 75 meters. 2) Time slices over the target horizons should be interpreted for faults (method B) but arbitrary line analysis should be undertaken with caution due to the possibility of bin jumping in displays. 3) Seismic volume and horizons based attributes should be analyzed for use with particular concentration on horizon azimuth.

## **4.2 ANALYSIS OF P-WAVE ANISOTROPY FROM SURFACE SEISMIC**

### **4.2.1 Background**

At the beginning of this project one of the primary tools for fracture detection was using surface seismic data to examine either time or amplitude variation as a function of azimuth to infer the presence of fracturing in the subsurface. This project spent a considerable amount of time performing this type of analysis on the P-wave 3-D surface seismic. We recognized the fact that anisotropy can be caused by a number of different effects, however since P-wave analysis was being used commercially we wanted a state-of-the-art comparison to other techniques. The analysis was performed by Lynn Inc.

Fracture detection from surface reflection surveys was initially done using four-component shear wave methods, which employ two oriented shear sources, and oriented three-component

---

receivers. S-wave 3-D surveys are much more costly (acquisition and processing) than 3D P-wave surveys. Thus the development of P-wave technology for mapping fractures has been high on the list of priorities; the better S/N of P-P reflections, the comparative ease in processing, and the reasonably quick turnaround in processing all serve to increase the probability of successfully mapping the fractured zones. Recent publications of field data results, mostly from the Dept. of Energy funded projects, are available (Grimm et al., 1999; Lynn et al., 1999a; Lynn et al. 1999b).

Aligned vertical fractures and/or unequal horizontal stresses can create the physical property of azimuthal anisotropy within a rock formation. The effect is caused by the variation in the stiffness of the fractures as a function of azimuth. Actually, the P-P seismic response after reflection and transmission in an azimuthally anisotropic medium depends upon the total compliance of the entire system, as probed by the ray that left the source and came to the geophone. The total system includes the solid rock {lithology/mineralogy} plus pore {non-rock, which is the matrix porosity plus the fracture porosity, which would include the effective crack parameters (height, density and aperture)} plus in-situ stress field (a combination of the vertical overburden stress and the horizontal stress in the direction of the ray) plus fluid fill {liquid or gas}, and possibly (an ultimate goal) the effects of the interaction of the movable fluids with the wavefront, that is, the effective permeability of the fractures-matrix interaction on the scale of the wavelength. This last item is suggested as affecting the azimuthal variation in attenuation. Azimuthal anisotropy means that the properties of the rock, as measured by a propagating wave varies with the source-receiver (s-r) direction azimuthally. The seismic wave propagation characteristics depend upon the azimuth of the s-r raypath and the s-r offset (angle of propagation off-vertical); i.e. velocity, reflection amplitude, frequency content and attenuation. In a medium with vertically aligned fractures, and/or unequal horizontal stresses, these transmission and reflection properties differ for propagation parallel to the fractures and perpendicular to fractures. Vertical aligned gas-filled fractures introduce additional ordered compliant elements to the rock because gas is highly compressive. Propagation normal to such fractures would sense the greater compliance (less rock stiffness), and slower velocities, and greater attenuation. Water-filled fractures may also introduce some additional compliance if the fractures offer permeable conduits to flow over a distance greater than the wavefront. If the water-bearing fractures or cracks are isolated (no permeable connectivity), then no additional compliance would be expected, since water is not compressible. There are even some arguments (Grimm et al., 1997) that isolated vertical aligned water-filled fractures could serve as additional stiffening members to increase the effective compliance sensed by waves traveling perpendicular to the cracks.

If one were working with P-S (mode-converted) data, then fracture information could also be retrieved from the S-wave birefringence observable between P-S1 and P-S2, and/or reflection amplitude differences, and/or frequency differences. However, the work published by Wild and Crampin (1991) suggest that the magnitude of the layer anisotropy is an important variable which affects our ability to measure S-wave birefringence effects associated with vertical aligned fractures. According to their model calculations, the greater the magnitude of the layer anisotropy, compared to the magnitude of the crack anisotropy, the less our ability to detect S-wave travel time anomalies due to the cracks.

---

However, there is another consideration with regard to thin layers: tuning in the presence of azimuthal anisotropy may introduce azimuth-dependent amplitudes in thin-bed reflections. An azimuthal tuning effect would be a sensitive indicator of the presence of vertical aligned fractures and/or unequal horizontal stresses. The lower the frequency, the longer the wavelength. The longer the wavelength, the greater the potential cracks per wavelength. The cracks/wavelength number is considered to be the most important parameter (using effective media theory) which determines the magnitude of the azimuthal anisotropy. Therefore, the lower the frequency, the greater the potential for the detection of azimuthal anisotropy (using effective media theory). Moreover, it is common to find a frequency variation from near offset to far offset: commonly, the near offsets are higher frequency, and the farther offsets are lower frequency (the difference is due to the length of the travel paths and the number of cycles involved). For the thinnest beds (50 ft and less), the frequencies are too high for us to routinely expect to see. For the thicker beds, the frequencies are recordable, and the traveltimes differences in period (frequency) are measurable. The 10% azimuthal variation in interval velocity, taken to mimic the change in P-wave velocity when a fractured reservoir is present, can potentially be linked to a 10% azimuthal change in highest-amplitude frequency. Herein is suggested a mechanism to change the dominant frequency observed by azimuth, related to a change in velocity due to high fracture density, but not related overtly to a change in effective horizontal permeability.

3D P-wave reflection surveys can be designed to capture the azimuthal differences in the reflected wavefields. The method is 3D P-wave multi-azimuth, and is essentially a full-azimuth, full offset (offsets greater than/or equal to target depth) survey. The first generation-azimuthal techniques separated the data into 2 or 4 limited-azimuth volumes (Tsvankin et al. recommended 3 volumes, but their Colorado School of Mines Center for Wave Propagation software is not commercially available). The coming 2<sup>nd</sup> generation techniques use software that scans each COP over all offsets and all azimuths to determine the ellipticity in either travel time or amplitude, and outputs various information concerning the ellipticity found. The first generation techniques are widely available throughout industry, because they are simply the current tools working on limited-azimuth input. The second generation tools are currently restricted to Western Geophysical (“fractograms” for either traveltimes or amplitudes) and Veritas DGC (azimuthal variations in AVO, for 3D data). Decisions as to how you shall process the data affect how you acquire the data.

If a first generation approach is chosen, we can then process by separating the data into two or more limited-azimuth data volumes, each of which represents a particular s-r propagation azimuth. In practice, a two-azimuth data set will be characterized by some azimuth  $\pm n$  degrees, e.g. north-south (NS)  $\pm 45^\circ$  and east-west (EW)  $\pm 45^\circ$ . The benefits of this approach are lesser costs in acquisition (less data acquired); the disadvantage is that fractures at 45 degrees to the processing axes, for this example N45E and N45W, will have equal effect on both azimuths. Thus, differencing the azimuths will yield no azimuthal variation, so we cannot distinguish between the azimuthally isotropic matrix response and the fracture response when the fractures are at 45 degrees to the processing axes.

In practice, it is also possible to separate a full azimuth data set into four separate azimuthal volumes, for example: NS $\pm 22.5$ , N45E $\pm 22.5$ , EW $\pm 22.5$ , and N45W $\pm 22.5$ . In our case we separated the four azimuths into the NW, SE, SW and NE quadrants. This would offer greater

---

resolution of fracture azimuth and density from the difference in p-wave properties with azimuth due to aligned vertical fractures that are oriented at some arbitrary azimuth. However, separation into four azimuth volumes comes with the price of either more data acquired (more cost of acquisition) or reduced signal to noise in each limited-azimuth volume, or a larger bin size. The benefit to this approach is the sensitivity to **any** fracture azimuth, plus the benefit of testing the hypothesis that a 90-degree variation exists between the minimum and maximum azimuthal variation (traveltimes and amplitudes). The 90-degree variation between minimum and maximum value recorded fits the model of vertical aligned fractures which add ordered compliance; a 45-degree variation between minimum and maximum would be interpreted as either two or more fracture sets with flat layers, or some dip to the cracks combined with a dip of the strata, or some other complication.

The consideration of how the azimuthal AVO analysis is to be performed helps direct the acquisition and processing parameters. Since it is highly recommended that the azimuthal variation in the AVO response of the top and base of the target(s) be mapped, as well as in the overlying mapable reflectors, some consideration of how those quantities shall be calculated is necessary. There are two techniques currently available:

- 1) Stack-migrate the near half of the live fold; stack-migrate the far-half of the live fold; Far Minus Near is the approximation to the AVO gradient.
- 2) Veritas DGC offers a processing program that will evaluate the ellipticity of the AVO amplitudes, looking at all the offsets and all the azimuths.

If option a) above is chosen, then sufficient fold must be present at and above target depths for each limited offset-limited azimuth so that the acquisition footprint is minimal (or nonexistent).

There is currently considerable interest in “exactly” how far do the offsets need to be in order to discern azimuthal variations in travel times and/or amplitudes. The Bluebell-Altamont, Utah, Dept. of Energy dataset revealed that the azimuthal P-P AVO needed offsets starting at 8650 ft for a series of targets from 6650 to 8800 ft depths. However, the travel times (moveout velocities) showed no reliably measured azimuthal travel time differences even at those far offsets. A more recent field data set, from the Gulf Coast onshore, recorded azimuthal variations on the mid-offsets’ (6000-8000 ft) amplitudes for a target at 14,000 ft. However, the far offsets (14000 ft) were needed to obtain the azimuthal velocity (travel time) information desired.

#### **4.2.2 Analysis of the P-wave data**

In order to derive the desired information both the coherent reflection portion of wave field and the incoherently scattered reflection portion of the wave field shall be analyzed. The coherent reflection portion of the wave field is viewed as that part of the recorded data that shows strong similarity in amplitude, frequency, phase, and travel time from trace to trace, as well as hyperbolic moveout at primary velocity, in shot-receiver domain, or offset domain; similarity in azimuth, and/or cdp space is expected. The incoherently scattered portion of the wave field is viewed as that part of the recorded data which shows little or no similarity in amplitude, phase, frequency, or travel time from trace to trace. These incoherently scattered reflections are thought to be generated from localized “small-scale” heterogeneities in the subsurface. A localized

---

heterogeneity could be a fault, a fracture, a set of fractures, a set of evenly -spaced fractures, a set of unevenly-spaced fractures, a sand body somewhat similarly sized relative to the Fresnel zone (maybe approximately  $\frac{1}{2}$  to 2 times the Fresnel zone) encased in shale, any localized lithologic heterogeneity, etc. The incoherently scattered wave field may be manifest as a “coda” effect, or “trailing leg” effect. Thus, any alteration of the amplitude, phase, or frequency of the coda is inappropriate at least in these beginning stages.

The incoherently and coherent reflected wave fields shall be viewed without: filtering, deconvolution, spectral whitening, dereverberation operators, CDP stacking, binning and summing of any kind being applied. Thus it was important to interact closely with the ConocoPhillips personnel on the reprocessing of the data and extract the data in the processing stream at the correct point. The properties of the 1-fold wave field are the signals desired, at least for the incoherent reflections, and probably for the coherent reflections as well. For the purpose of comparing what “effective media theory” says about coherent reflections in anisotropic media, careful dereverberation, and ground roll removal, should be attempted. If successful, these steps might become part of the 1-fold flow designed for the incoherent scattered energy, after discussion. Careful dereverberation means removing those trailing legs or coda attributed to the near surface layers, commonly described as the unconsolidated section that can have rapid lateral variation in properties. The reverberation attributable to those layers overlying the target, typically called the “overburden”, might also be looked at, since the “overburden” properties need to be distinguished from the target properties.

Complicating circumstances can be envisioned when vertical geologic discontinuities reach from Mesaverde to surface. In this circumstance(s), scattering from the near surface discontinuity is one of the signs that a discontinuity (fracture) is present in the Mesaverde. In fact, due to attenuation, the incoherent reflections from the vertical discontinuity in the subsurface ought to be more easily detected and recorded with a broader-bandwidth, compared to those generated by a vertical discontinuity in the Mesa Verde. Therefore, removal of some of the scattering attributable to the near surface or overburden may be inappropriate.

In order to view the azimuthal variation of the P-P seismic reflected coherent wave field azimuth gathers were formed, from supergathers (9x9 selected for our data set) to be sorted 0-180 and 0-360 degrees, with azimuth binning and offset binning, which were decided based upon fold-offset-azimuth plots generated. Stacking with the azimuth bins and offset bins increased the signal to noise ratio (S/N) of the coherent reflections, and decreased the S/N of the incoherent reflections. For the incoherent reflections azimuth gathers were formed from supergathers sorted 0-360 with no stacking. 1-fold data was ordered such that no more than 5-15% of the allotted (regularized) bins are empty. The supergathers (azimuth gathers) thus looked like tiny 3D surveys to 3D interpretation software packages.

Typical outcomes is that some of the azimuth gathers will show little or no azimuthal variation in the seismic signature (travel time, amplitude, frequency, S/N, attenuation, dispersion, etc.), while others of the azimuth gathers will show measurable to significant azimuthal variation. Another possible outcome is that all of the azimuth gathers will show a measurable amount of azimuthal variation, but that some will show a large magnitude, while others show a small magnitude. It is possible but improbable, that all the azimuth gathers will show no azimuthal variation in seismic signature. However, it does appear that for the 20 square mile area to be a

---

viable choice for this project, the magnitude and/or orientation of the azimuthal variation of the seismic signature needs to vary spatially for the target zone, or the zone under the target.

Upon inspection of the azimuthal display of the data, an important question to address the question, is it possible to tell the difference between the scattering energy from a lithologic variation and the scattered energy from a high-fracture density zone?

Another question is, is it helpful to remove the coherent reflected wave field from the 1-fold data so that the ‘preponderance’ of apparent energy is incoherent reflections?

### **4.2.3 Results**

As stated above the data used for the P-wave analysis were a subset of the reprocessing effort that Conoco carried out. After the proper processing was finished many different correlations were performed to examine different attributes to determine if for this area there was a reliable attribute that was a predictor of production. One of these was isopach maps (the variation in travel time between two different horizons as a function of azimuth either for individual traces from the “inline” data and the “crossline” data sorted into 90 degree segments, or CDP gathers).

Figure 4-20 shows the isopach map for the Greenhorn- Entrada within the Dakota formation. Although the Dakota was not the primary target of this study it did have good quality reflection data in this area and there was well control on the production. Figure 4-21 is the SE far Greenhorn-Entrada isochron correlated against the production in this interval, the better wells showed minimum travel times, the poorer wells showed maximum travel times. An hypothesis for this observation was that the SE ray paths traveled approximately parallel to trend of sand bodies and traveled within the sand-rich units at their faster velocities and the NE ray paths (traveled approximately perpendicular to trend of sand bodies) and spent less time in the faster velocity of the sands, and more time in the slower velocity of the shale-rich units. Or another way to explain it is that the SE strike direction of the sand bodies allows the SE ray paths to travel within the sand and to sense the sand’s higher velocity (compared to the shale lower velocities). The sonic logs in the Dakota section confirm the higher velocity of the sand and the lower velocities of the shales. The NE (dip) ray paths cross the sand bodies at a high angle and spend only a negligently small time in the actual sand body, and so do not pick up on the lithologic difference between shale and sand. The thin isochron associated with the best production and the isochron thick associated with poor wells could be interpreted as an isopach phenomenon, i.e., the thin isochron is a thinner section, deposited over old highs, and represents shoaling (sandier section); the isochron “thicks” represents a thicker section, deposited in old lows, and are shalier. Thus, one sees that in this interpretation, the velocity in the interval plays a secondary role to the thickness of the interval. However, if one wished to argue that the interpretation should be an isopach interpretation, one has to explain why the NE ray paths did not show the correlation with production. We therefore conclude that at least some element of the lithologic alignment of the sand bodies (SE/NW direction as observed on seismic) is correct for the interpretation. There may be a secondary element in the isopach argument, but it is not necessary for the interpretation.

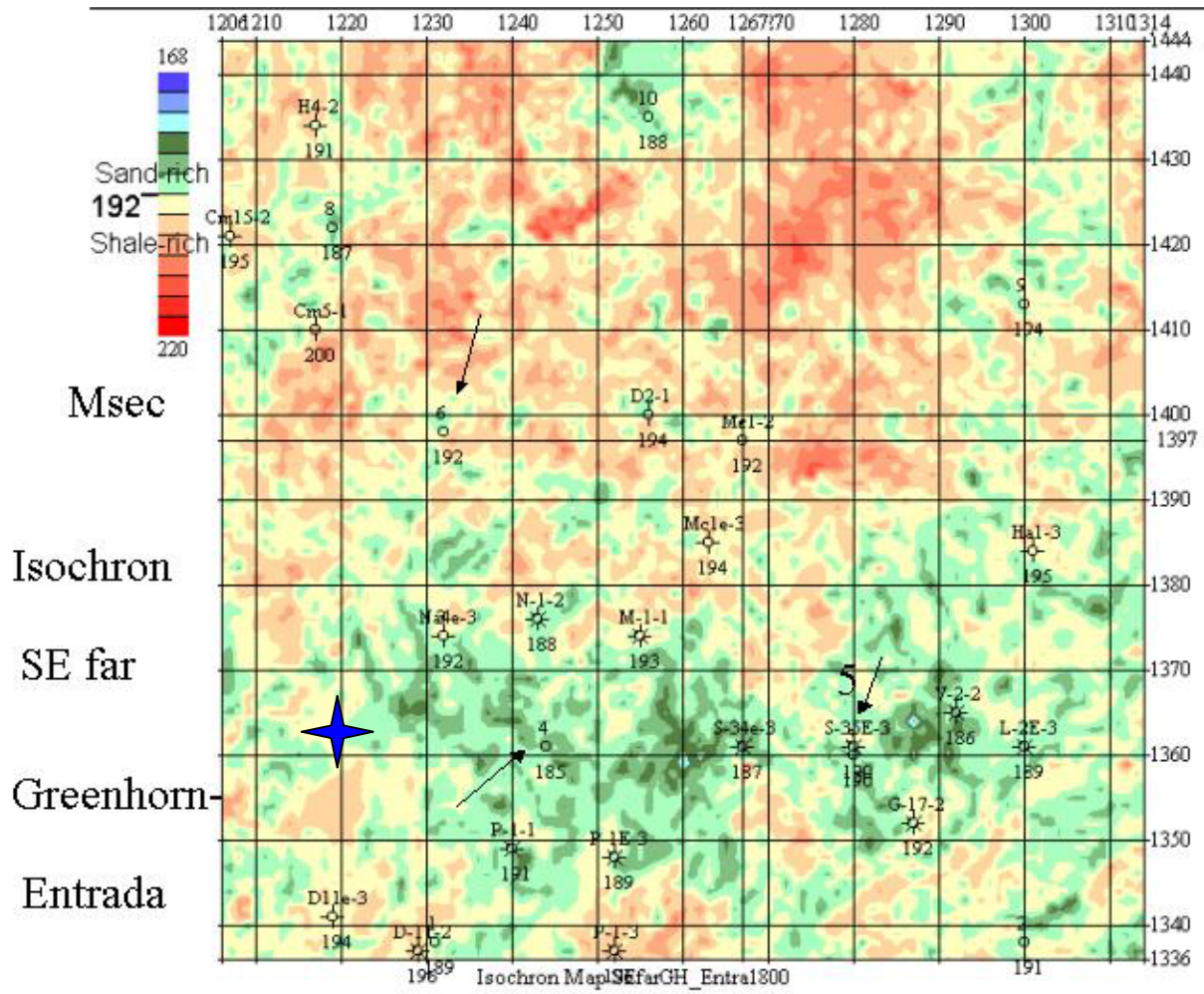


Figure 4-20. The SE Greenhorn-Entrada isochron. The reds turn out to also correlate to the shale rich material and the greens to the sand rich formations. Blue star is the location of the VSP Well.

## SE far Greenhorn-Entrada Isochron

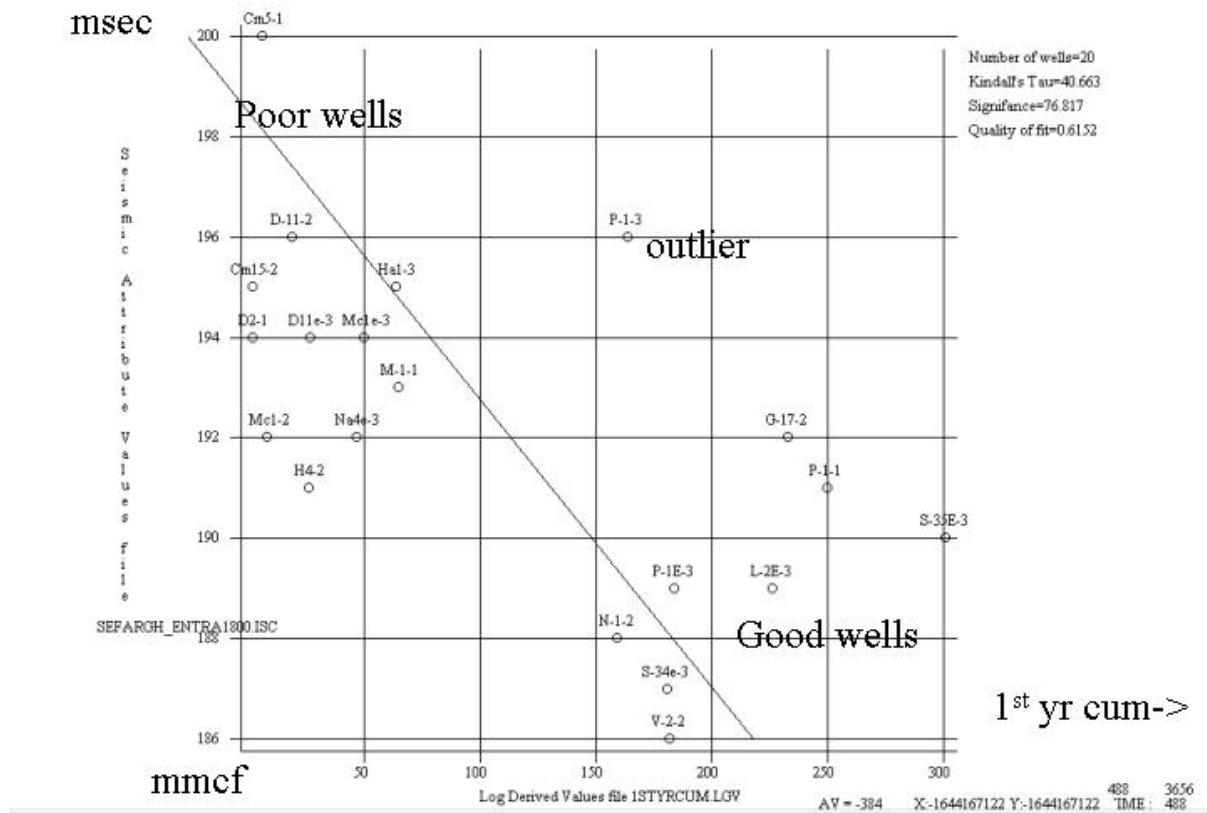


Figure 4-21. The SE far Greenhorn-Entrada isochron correlated with first year production of the wells.

As mentioned above two areas were concentrated on to perform these studies, the Newberry LS 2C well (VSP well) and the Moore LS 7B well. For the Dakota the main observations were that around the LS 2C well in the SE-NE Greenhorn-Entrada travel time the average difference was almost zero. The Greenhorn-Entrada isochrons suggest a sandier section, especially southwest of the LS 2C well. The ratio of the interval velocities (SE/NE) is isotropic, suggesting either no fractures, equal fracture density, or sub-seismic fractures. In addition, the Greenhorn-Entrada AVO is strongly negative with both azimuths suggesting a low fracture effect, in essence the seismic looks “isotropic” in this region.

In the Moore well (LS 7B) the situation was slightly different in that there was 7 millisecond azimuthal variation in the interval travel time (Greenhorn-Entrada interval) with the NE-SW time being faster than the NW-SE times. The isochrones also suggested a shalier content with a small possible sandier section west of the well. There was also a flat Greenhorn flat AVO in the NE direction, and negative in the SE direction indicating an azimuthal variation in P and S velocities. All adding up to indicate a more anisotropic situation than in the LS 2C well. These points are demonstrated in Figure 4-22.

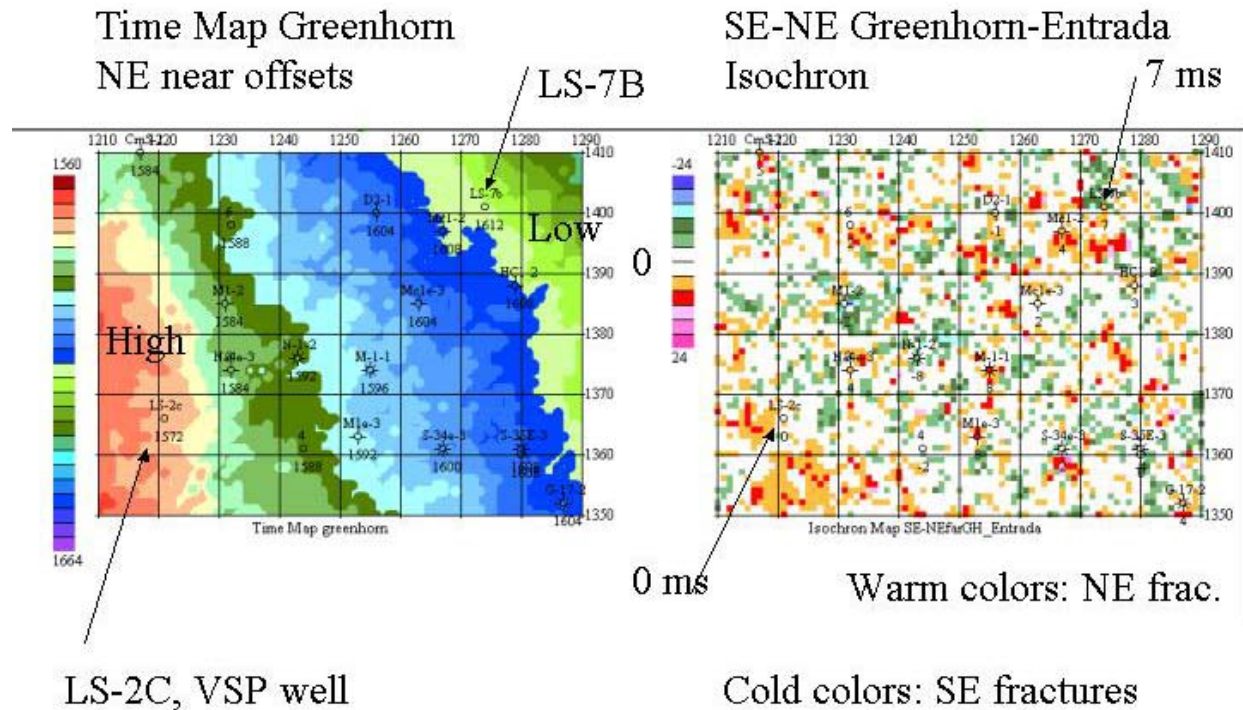


Figure 4-22. An analysis of the P-wave anisotropy in the Greenhorn-Entrada (Dakota section) in the 20 square mile study area.

In the Mesaverde section, however, the story is somewhat different. As stated above in the Dakota section, LS-7B was found to be “anisotropic” and the LS-2C location “isotropic”. The methodology used for interpreting the data in the Mesaverde was to perform the analysis on the reservoir rock (lithology): sand, not shale. This meant using the Menefee to the Greenhorn interval. The procedure was to examine the interval velocity and determine if the interval velocity can discriminate between the sand and shale. The next step was to use the AVO information in this interval. The logic being that a measure of the porosity can be the AVO or amplitude data, i.e., are there azimuthal differences in effective porosity. The final step was to examine the frequency content to infer if gas is present. This assumes that gas presence will attenuate the signals more than water filled rock, thus lowering the average frequency content. Figure 4-23 and 4-24 show the results of this analysis around the Moore LS 7B well and the Newberry LS2C well, respectively. In the areas of higher gas content one would expect more seismic attenuation, i.e. a lower average frequency content. In Figure 4-23 the crack parallel direction is the lower frequency direction, inferring substantial commercial gas is present. It was found that in the LS 7B case the NE average frequency content was 29 hertz and the SE average frequency was 20 hertz, thus giving a difference of 9 hertz in the two different azimuths. In the LS 2C case the NE average frequency was 27 hertz and the SE average frequency was 26 hertz, giving a difference of 2 hertz. Assuming that the difference in the average frequency content between the two azimuths is an indication of fracture content, and the average frequency content is a measure of the fracture content, then one would predict that the LS 7B well would be a better producer than the LS 2C well. An empirical result from examining a variety of different attributes for Mesaverde concluded that the three most successful attributes in predicting successful gas production are having SE frequency less than 26 hertz, NE less than 26 hertz and

the SE minus the NE greater than 2 hertz. It is important to note that the NE direction have less attenuation (higher frequency content) to be consistent with attenuation theory of parallel fractures, i.e. less attenuation parallel to the fractures. Last but not least it was noted that if all azimuths are summed for imaging not one of the many different attributes examined show a correlation to historical production.

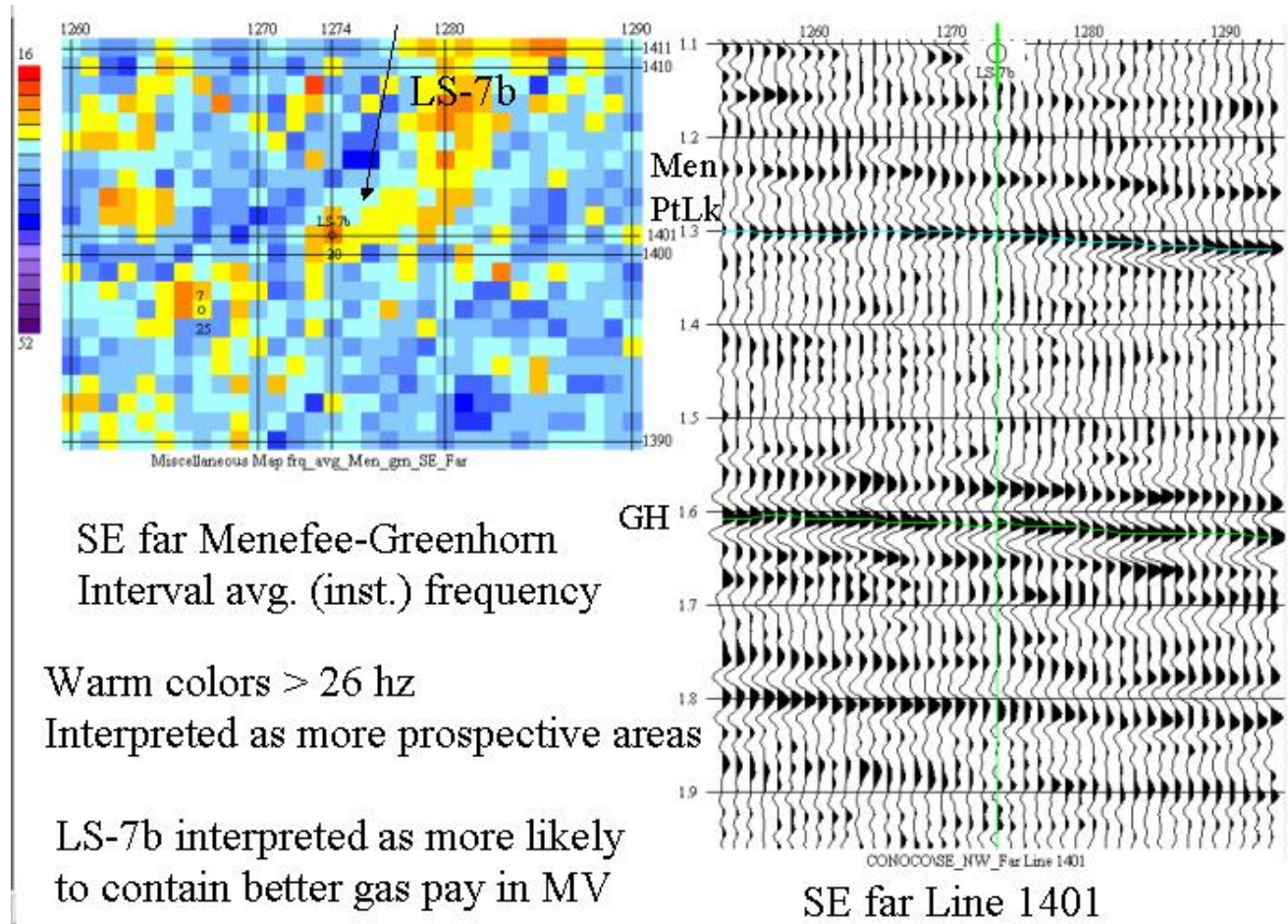


Figure 4-23. The results of analyzing the interval velocity data in the Mesaverde for frequency content.

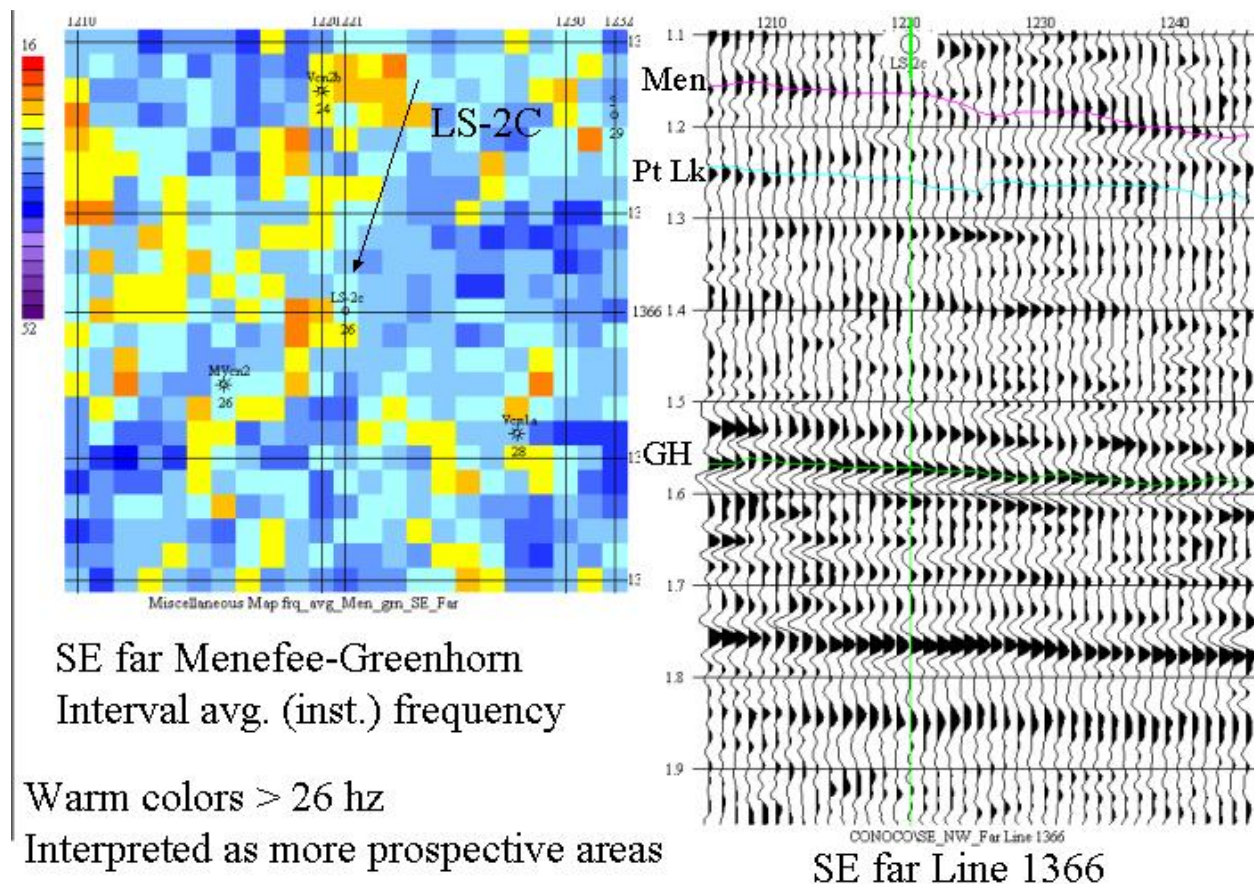


Figure 4-24. The result of analyzing the data around LS2C for average frequency content. Compare to Figure 4-21.

#### 4.2.4 Conclusions of P-wave Anisotropy Analysis of the 3-D Surface Seismic Data

After a considerable analysis of the data there was some evidence that the data did have indications of anisotropy in time and amplitude. We of course have no absolute ground truth that this was due to fractures other than inference from core and well log data (see results in well logging section). On the other hand as we have seen from the interpretation of the surface seismic and cores the study area was in a very complicated stress zone and fault zone. As discussed earlier a random set of fractures can give an appearance of no anisotropy, which would of course would be the wrong conclusion for this area. If one compares the results of the surface P-wave anisotropy studies (for example Figures 4-22, 4-23 and 4-24) to the contours of the production history there is little correlation. A possible explanation is that the production history map covers both the Dakota and Mesaverde zones thus that is an integrated result where as Figures 4-22 to 4-24 are specific to different horizons and one would a direct correlation. Another explanation is that the seismic is a snap shot in time of the reservoir. The production diagram is an integration of the first year production over 50 years. If production is changing the stress distribution in the reservoir the direction of open fractures may also be changing. Thus the integrated production map would not expected to correlate with the seismic data. Last but not least an alternative conclusion is that the surface seismic is not detecting the fractures controlling

---

the production. Although a negative conclusion it is important to note so that other data sets with higher resolution can be pursued.

### 4.3 VSP DATA ANALYSIS

#### 4.3.1 Shear Wave Analysis

The characterization of anisotropy in the subsurface can provide valuable information about reservoir properties, such as the presence of fractures and their orientation. Furthermore, the detailed description of an anisotropic velocity model in the overburden and the reservoir is often required to obtain high-resolution seismic images. Azimuthal anisotropy is commonly analyzed from shear-wave splitting in near-offset VSPs, where the orientation of aligned fractures is inferred from the polarization of the fast shear wave, and the time delay between the split shear waves is interpreted as a measure of the fracture density (e.g. Queen and Rizer, 1990; Crampin and Lovell, 1991; Lynn *et al.*, 1999; Winterstein, De and Meadows, 2001). Both shear-wave splitting and P-wave travel times have also been analyzed from walk-around VSP data for parameters of azimuthal anisotropy (Winterstein and Meadows, 1991). In addition, Winterstein and De (2001) have used shear-wave splitting in a walk-around VSP to constrain Vertical Transverse Isotropy (VTI). These analyses, however, are based on the assumption that the rock is transversely isotropic with either a vertical or a horizontal axis of symmetry. The combination of thin-layer anisotropy and a set of vertical parallel fractures yields orthorhombic symmetry. Wild and Crampin (1991) discuss 3D shear-wave splitting patterns for a wide range of orthorhombic models and find that the shear wave behavior is very sensitive to the relative proportions of thin-layer and fracture induced anisotropy. It becomes apparent from their work that measurements at multiple azimuths and offsets would be necessary to characterize the anisotropy and differentiate between VTI and Horizontal Transverse Isotropy (HTI) (visualize a deck of cards being either vertical or horizontal) and orthorhombic symmetry (card deck at an angle). This is further confirmed in a modeling study by MacBeth (1991). While shear-wave splitting in a near-offset VSP is not sensitive to VTI anisotropy, an offset VSP at a single azimuth cannot necessarily constrain effects of azimuthal anisotropy. Bush and Crampin (1991) analyzed shear-wave behavior in a VSP dataset from the Paris Basin, where several shotpoints were located at different offsets and azimuths. The authors modeled their observation by qualitatively matching S-wave hodograms, which resulted in a final model consisting of HTI and orthorhombic layers.

The 4C shear-wave data for one of the near-offset source locations are displayed in 4-25. The fact that there is considerable energy in the cross-diagonal components (XY and YX) in Figure 4-25a indicates that there is an effect of shear-wave splitting. The data were processed by performing an Alford rotation, which minimized the energy in the cross-diagonal components and thereby rotated the data into the natural coordinate frame of the anisotropic system (Alford, 1986), Li and Crampin, 1993). The result of this rotation is shown in Figure 4-25b. The rotation analysis yields the polarization angles of the fast and slow shear waves (also called S1 and S2). The time delay between the two shear waves is estimated subsequently by cross-correlating the rotated traces. At far offsets it is important to incorporate the vertical geophone component into the analysis, because it contains a large portion of the shear-wave energy.

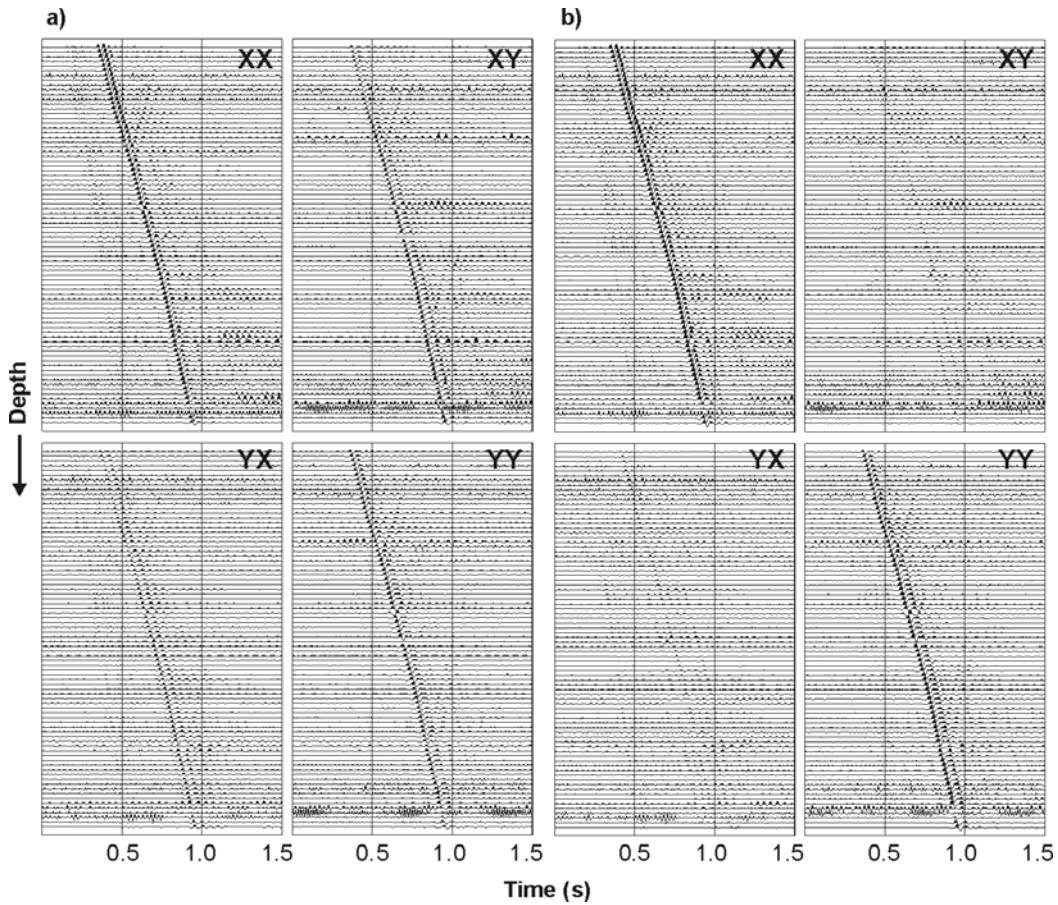


Figure 4-25. Four-component shear-wave data from a near-offset source location, a) before Alford rotation, b) after Alford rotation. The components are labeled according to source and receiver orientation (first and second letter, respectively). After Alford rotation the energy in the cross-diagonal components is minimized, and the data are separated into fast and slow shear wave arrivals, respectively.

The results of the shear-wave splitting analysis for the reservoir interval below 4000 ft are summarized in Figure 4-26. For each shot point a line is drawn parallel to the measured polarization of the fast shear wave, whereas the length of the line is proportional to the increase in time delay over the reservoir interval. The plot represents an equal area projection of a hemisphere of propagation directions, assuming straight rays down to the reservoir depth. For shot points not shown in the figure the data quality is not sufficient to give reliable shear-wave splitting estimates.

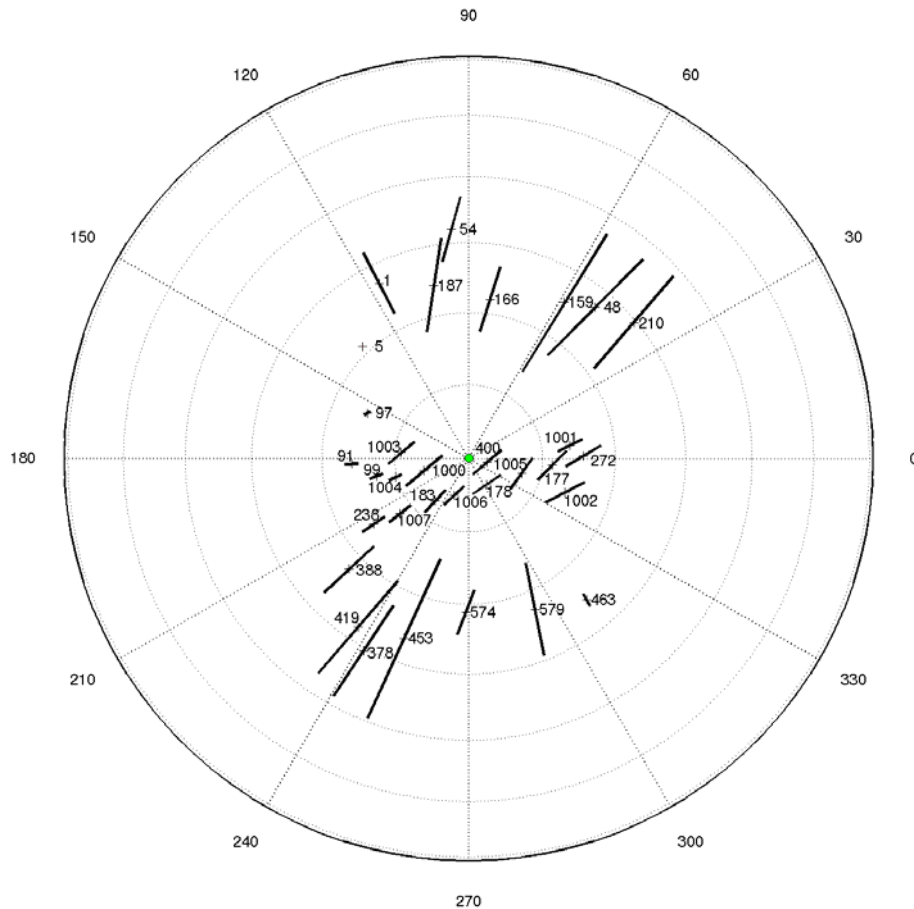


Figure 4-26. Equal area projection of measured S1-polarization and time delay in the reservoir (below 4000 ft). The orientation of the lines is the azimuth of the S1-polarization, whereas the length of the lines is proportional to the time delay between the split shear waves. For instance, the time delay for source 238 is 2 ms, while for source 48 it is 10 ms. Near-offset data (incidence angles  $< 30^\circ$ ) show a consistent polarization of the leading shear wave with an average of N55°E and small time delays. For far offsets the S1-polarization is nearly radial, and time delays are large. At far-offset locations 5 and 463 NW and SE of the well the S1-polarization is still radial, but the time delay does hardly increase in the reservoir.

Overall, the shear-wave splitting data displayed in Figure 4-26 shows a symmetric pattern. The polarization of the fast shear wave measured for near-offset sources follows a preferred orientation of N55°E on average. The magnitude of shear-wave anisotropy, however, is rather small with time delays of 2-3 ms over an interval of 1200 ft. For far-offset source locations (or higher incidence angles) the polarization of the fast shear wave lies within  $20^\circ$  of the source-well azimuth. The time delays measured over the reservoir interval are much larger than for near offsets and reach up to 13 ms. The near-offset pattern resembles that of a medium with hexagonal anisotropy caused by vertical fractures (HTI) aligned around N55°E. The far-offset pattern, however, would be expected in a transverse isotropic medium with a vertical symmetry axis (VTI). This already indicates that at least a combination of the two symmetry systems will be necessary to explain the observed shear-wave behavior.

---

The symmetry that is apparent in the shear-wave splitting signature at the reservoir can also be observed at shallower depths. Figure 4-28 shows sketches, which summarize the measured S1-polarization and time delays as a function of depth for near offsets, far offsets, and two far-offset sources located NW and SE of the well. (For corresponding real data examples see Figures 4-28 – 4-30) For near-offset sources the polarization azimuth of the fast shear wave is constant with depth at 50°-60° NE. The time delay shows a significant increase in the Fruitland formation down to the top of the Lewis shale at 2500 ft. Values vary between 5 and 15 ms, depending on the location of the source. In the Lewis shale, between 2500 ft and 4000 ft, the time delay remains constant. As mentioned in the previous section, it then increases by 2-3 ms in the reservoir. The far-offset data show a different shear-wave splitting pattern as a function of depth. Here, the time delays have high values of up to 30 ms at the shallowest receivers, then decrease down to zero around an offset-to-depth ratio of one, followed by a large increase of up to 26 ms over the remaining depth interval. For some source locations a slight decrease in slope of the time delay curve can be observed at the reservoir depth. The polarization of the fast shear wave in the far-offset data is perpendicular to the source-well azimuth at shallow depths. Exactly where the time delay reaches zero, the S1-polarization flips to 0-20° from the source-well direction.

The shear-wave behavior for the two far-offset sources NW and SE of the well is the same as observed in the other far-offset VSPs except at the reservoir level. We also find large time delays at shallow depths decreasing to zero at an approximate offset-to-depth ratio of one, which coincides with a flip in S1-polarization from 90° to 0°. At the reservoir, however, the time delay shows hardly any increase, in contrast to far-offset data from other azimuths.

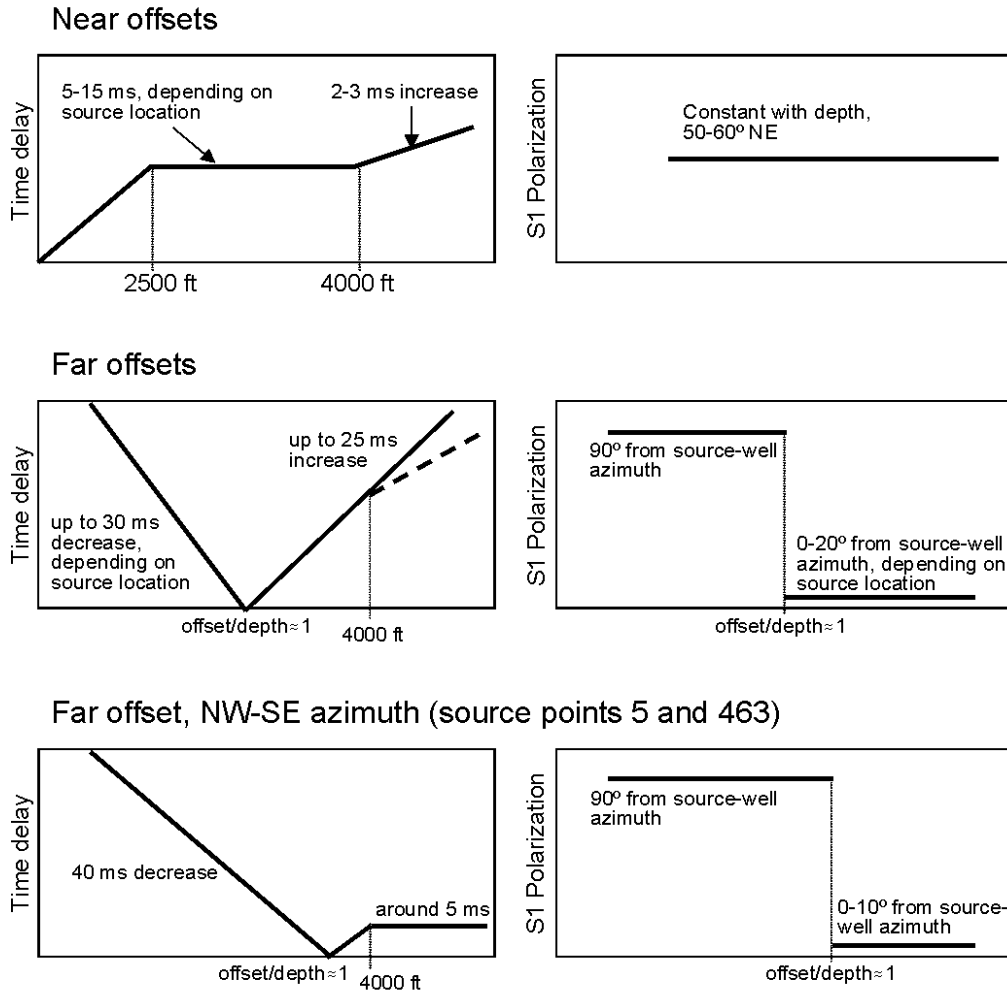


Figure 4-27. Sketches that summarize the measured shear-wave splitting patterns as a function of depth for groups of source locations, in which the shear-wave behavior is similar. Near-offset data show an HTI effect above 2500 ft and below 4000 ft, while far-offset data indicate VTI anisotropy with clear evidence of a shear-wave singularity at  $\text{offset/depth} \approx 1$ .

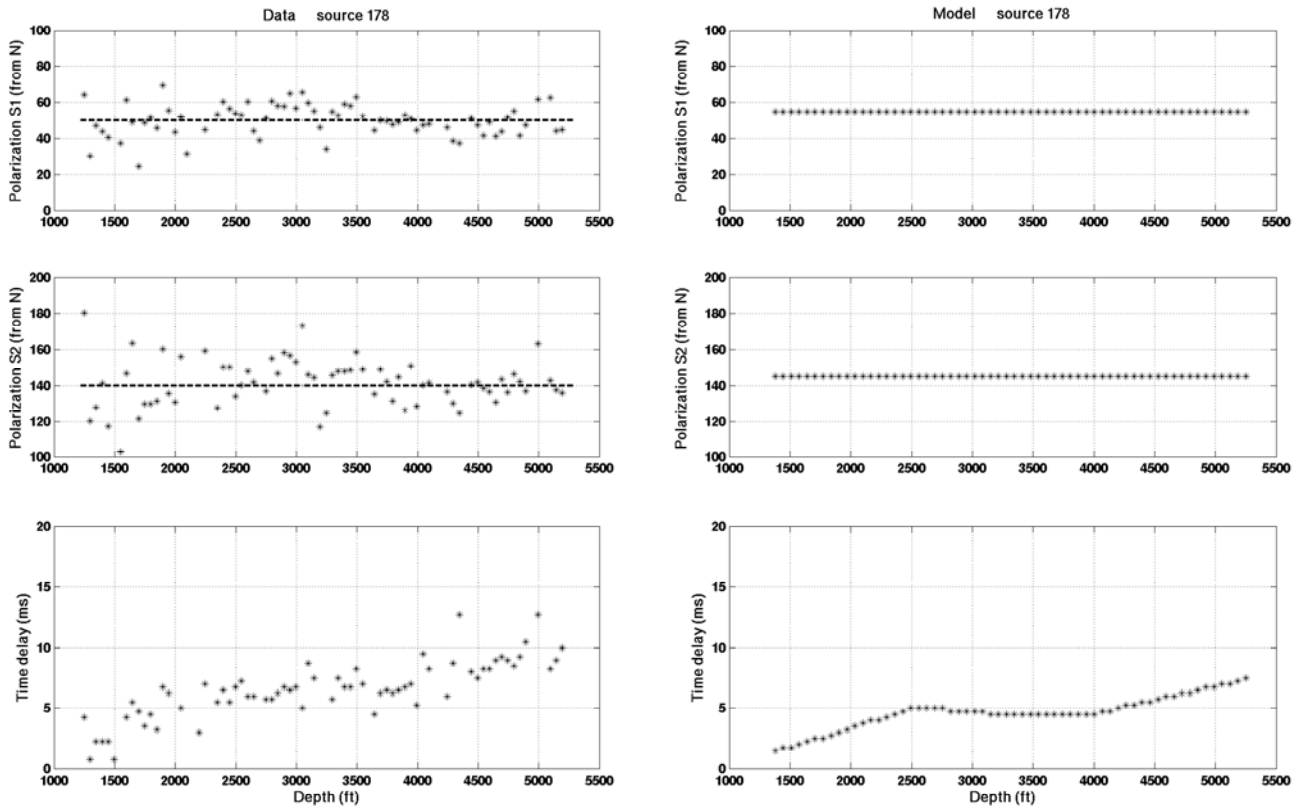


Figure 4-28. Shear-wave splitting data from near-offset source 178 in comparison with the synthetic modeling results. Dashed lines indicate mean values of the measured polarization data. The main features of constant S1-polarization with depth around N55°E, constant time delay in the Lewis shale (2500 ft - 4000 ft), and increase in time delay above and below are well matched. In the real data, there is great variability in time delay with source location at the shallow receivers, which cannot be explained by a single model.

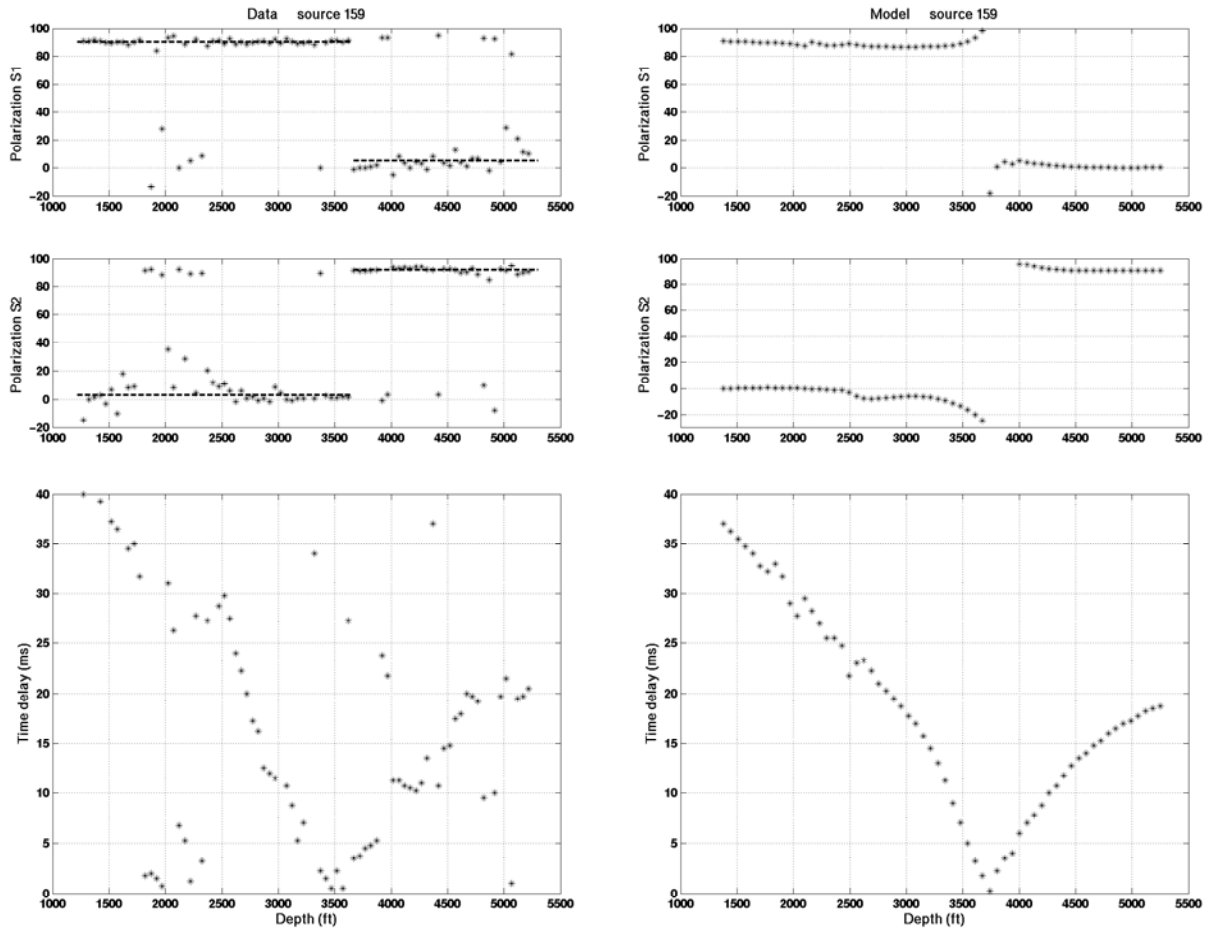


Figure 4-29. Far-offset data and modeling example from source location 159. Both real and synthetic data clearly show the effect of a shear-wave singularity, where the S1-polarization flips by 90° from normal to parallel to the source-well azimuth, and the time delay reaches zero. The magnitude of decrease in time delay above and increase below the singularity are well matched by the model.

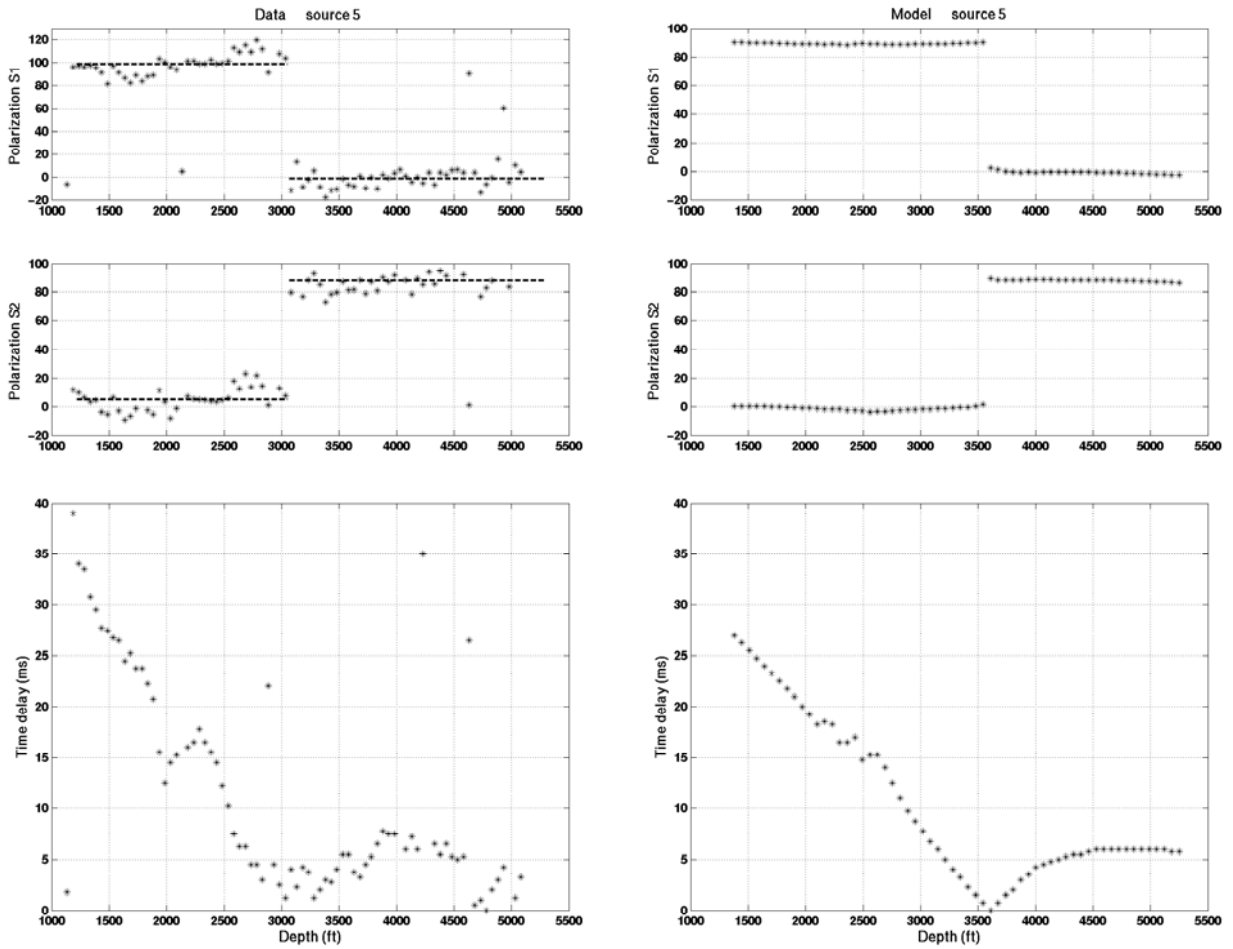


Figure 4-30. Results of shear-wave splitting analysis from real and synthetic data for far-offset source 5 NW of the well. The shear-wave singularity is still clearly observable in data and model. However, below the singularity the time delay reaches a constant level, which is reproduced by the synthetic model.

### 4.3.2 Interpretation of the shear wave splitting results

Media containing vertical cracks or fractures with a preferred alignment are azimuthally anisotropic. Azimuthal anisotropy can be detected and characterized by measuring shear-wave splitting for near-vertical raypaths. In this case the polarization of the fast shear wave is parallel to the fracture strike, while the time delay increases with depth. The magnitude of the increase in time delay can be interpreted as a measure of fracture density (Queen and Rizer, 1990; Crampin and Lovell, 1991). The data from near-offset source locations reveal such a shear-wave behavior, indicating azimuthal anisotropy for the interval between the shallowest receiver and the top of the Lewis shale at 2500 ft, as well as the reservoir sandstones below 4000 ft. In the Lewis shale between 2500 ft and 4000 ft there appears to be no shear-wave splitting for near offsets, so that the time delay remains constant. We can therefore interpret this interval as azimuthally isotropic.

---

Media that consist of many thin layers or contain horizontally aligned mineral grains exhibit VTI anisotropy (transverse isotropy with a vertical symmetry axis). In these media the fast shear wave is polarized normal to the source-receiver azimuth for far offsets (large incidence angles) and parallel to the source-receiver azimuth for near offsets (small incidence angles). In between there is a certain propagation direction where the velocity surfaces of the two shear waves intersect, forming a line singularity (Crampin and Yedlin, 1981). At the singularity the time delay between the shear waves becomes zero, and the polarization of the fast shear wave flips by 90°. There is no shear-wave splitting at vertical incidence, and time delays reach a maximum for horizontal propagation. The shear-wave splitting pattern in VTI media is radially symmetric about the vertical axis.

This shear-wave behavior is clearly apparent in the far-offset VSPs for the interval of the Lewis shale between 2500 ft and 4000 ft. A line singularity is observed around an offset-to-depth ratio of one, where at all azimuths the time delay between the split shear waves reaches zero, and the polarization of the fast shear wave flips by 90° from transverse at larger incidence angles (shallower receivers) to radial at smaller incidence angles (deeper receivers). However, also in the reservoir and in the formations above the Lewis shale the data from far-offset source locations indicate the presence of thin-layer anisotropy. The S1-polarization shows a consistent behavior over the entire depth range. The time delay has very high values (30-40 ms) at the shallowest receivers, which means that there must be an effect of VTI anisotropy in the overburden above the first receiver. Then it decreases more or less continuously until the shear-wave singularity is reached (see 57 and 58). This suggests that there is also an effect of thin-layer anisotropy in the interval between the shallowest receiver and the top of the Lewis shale. Except for the two sources NW and SE of the well, the time delay continues to increase significantly in the Mesaverde Group for all far-offset source locations, and the polarization of the fast shear wave is close to radial. This indicates that in the reservoir the shear-wave behavior is affected by thin-layer anisotropy as well.

### **4.3.3 Synthetic Modeling**

In order to support the findings and interpretations discussed in the previous section we perform full-wave synthetic modeling. The aim is not to match exact travel times, but to understand the characteristics of the anisotropy that can reproduce the shear-wave splitting patterns observed in the data. As discussed in the previous section, the data suggest the presence of VTI anisotropy for all receiver depths. In addition, the near-offset data show azimuthally anisotropy for two intervals: between the shallowest receiver and the top of the Lewis shale, as well as in the Mesaverde Group below 4000 ft. The combination of the two effects in these intervals yields orthorhombic symmetry as the simplest model to explain the observations. Furthermore, the magnitudes of the measured time delays suggest that the VTI effect is stronger than the azimuthal anisotropy.

We build a simple model with the parameters given in Table 1e. Average velocities are chosen from the surface seismic velocity models. The orthorhombic layers contain vertical fractures striking N55°E, which is the average S1-polarization measured in the near-offset VSPs. The fracture-induced anisotropy is rather small compared to the VTI anisotropy with fracture densities being only 1.5% in the reservoir and 2% in the overburden layer.

---

Figures 4-28 to 4-30 show the shear-wave splitting data obtained from the synthetic VSPs compared to the real data results for a near-offset source location, a far-offset source location, and far-offset source location number 5 NW of the well. The general patterns of S1-polarization and time delay as a function of depth are well matched by the synthetic data. The modeling reproduces the shear-wave line singularity observed in the Lewis shale for far-offset VSPs, preceded by a continuous steep decrease in time delay from very high values at the shallowest receivers. Furthermore, the difference in time delay signature at the reservoir level for far offsets NW or SE of the well compared to all other azimuths is reproduced in the synthetic data.

For near offsets, the modeled shear-wave behavior shows the same general features as observed in the real data. However, it is difficult to explain the great variability in measured time delay with source location above the Lewis shale by a single model. This may suggest that there is lateral heterogeneity in the magnitude of azimuthal anisotropy or fracture density of the shallow intervals.

The model represents the simplest case required to explain the main patterns of the observed shear-wave behavior. Layers are only defined in terms of major intervals, where the shear-wave splitting signature shows certain common characteristics. The VTI anisotropy in the Lewis shale is well constrained by the shear-wave singularity. Since it is a line singularity that is radially symmetric about the vertical axis, the symmetry cannot be orthorhombic where there would be point singularities at specific propagation directions (Wild and Crampin, 1991). In the reservoir the VTI effect is required to explain the change in S1-polarization from N55°E at near offsets to approximately radial at far offsets. In addition, the shear-wave splitting pattern measured in near-offset data could not be explained without the fracture-induced anisotropy in the reservoir and above the Lewis shale.

It might be less intuitive, why the data also give evidence of VTI anisotropy above the Lewis shale. Figure 4-31 shows the far-offset modeling results without VTI anisotropy in the first and the second layer, respectively. It is obvious that the VTI effect in the overburden, especially above 1200 ft, is required to explain the high values in time delay at the shallowest receivers followed by the steep continuous decrease down to zero. A refinement of the model in terms of more layers between 1200 ft and the top of the Lewis, which do not all contain VTI anisotropy, may be possible. To constrain a more detailed model, however, it would be necessary to also invert travel times.

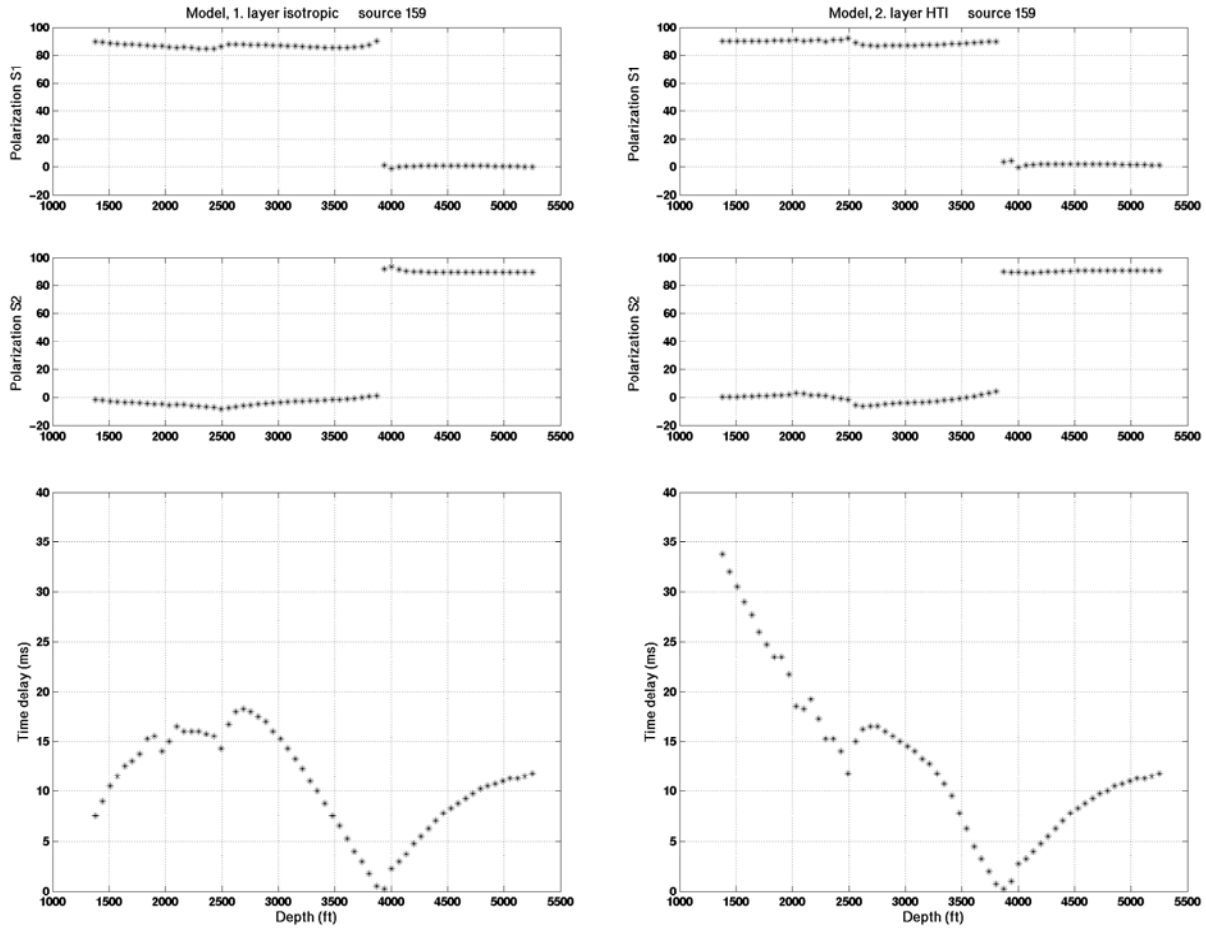


Figure 4-31. Shear-wave splitting data from synthetic VSPs for source 159, where the layer above the shallowest receiver is isotropic (left), or the second layer has only HTI and no VTI anisotropy (right). The graphs demonstrate that the steep continuous decrease in time delay measured in the real data cannot be explained without VTI anisotropy in the overburden, especially above 1200 ft.

While the shear-wave splitting data provide sufficient constraints against models of higher symmetry, this may not be the case with respect to more complicated models. We therefore repeat the synthetic study for a second model, where the symmetry in the reservoir is decreased by inserting a second fracture set. The angle between the strike of the first and second set is  $60^\circ$ , which would be consistent with the fault pattern mapped from 3D reflection seismic data in the study area. The fracture density of the first set is increased to 0.2, while the second set has a fracture density of 0.1. For near-vertical propagation the polarization of the leading shear wave in this medium will be the density-weighted average of the two fracture orientations (Liu *et al.*, 1993). To obtain an average of N55°E the strike of the first set is chosen to be N35°E, while the second set strikes S85°E.

The shear-wave splitting analysis for this second model yields results that are very similar to the previous ones. The differences in S1-polarization and time delay lie within the scatter that is present in the real data. Polarization errors, for instance, are up to  $\pm 10^\circ$ . Figure 4-32 compares equal area projections of S1 polarizations and time delay contours for the reservoir layer of the

two models. The results of the real data from Figure 4-26 are overlain on the plots. It is obvious from Figure 4-32 that there is only a small range of propagation directions (close to horizontal at certain azimuths), where the polarization of the fast shear wave is significantly different between the two models. This is consistent with the findings of Liu *et al.* (1993) who investigated shear-wave behavior in media containing two fracture sets with a synthetic modeling study. The authors concluded that being able to distinguish between the effects of a single set and two sets of fractures from field data within the shear-wave window would be unlikely. Here, there is an additional complication due to the fact that the VTI anisotropy is dominant over the fracture-induced effect. Nevertheless, Figure 4-32 suggests that the interpretation of the data in terms of orthorhombic or lower symmetry could potentially be better constrained, if accurate time delay data from far offsets ENE and WSW of the well were available.

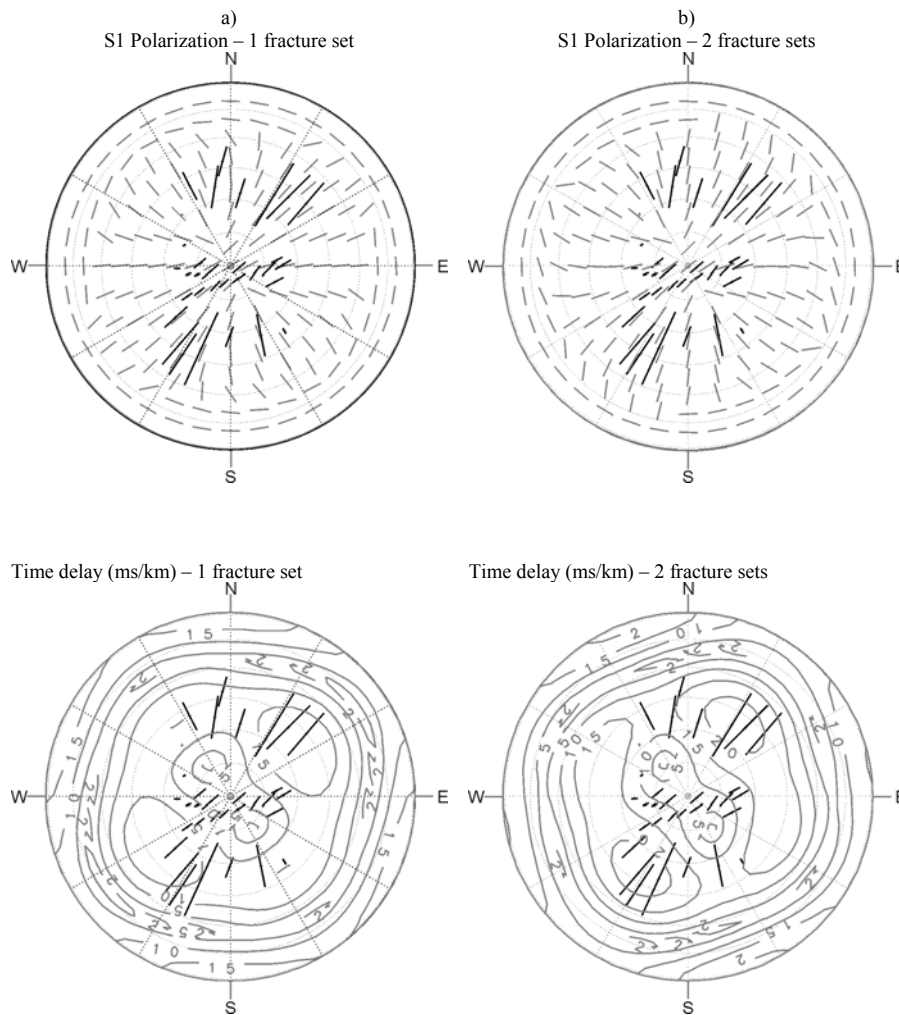


Figure 4-32. Equal area projections of S1-polarization and time delay for models of the reservoir layer. a) one fracture set striking N55°E, fracture density 0.15; b) two fracture sets striking N35°E and S85°E, fracture densities 0.2 and 0.1. The data, which are overlain on the graphs, do not provide sufficient constraints to distinguish between the two models.

Overall, the findings of the shear-wave splitting analysis are consistent with available borehole data from the reservoir zone. FMI logs have revealed fine layering in the Mesaverde Group and

---

only few open fractures striking NE. Furthermore, moveout velocity from the 3D seismic data had previously been examined for azimuthal anisotropy in the reservoir, and the orientation of the NMO ellipse was also found to be NE (Majer *et al.*, 2002). The strong VTI anisotropy as detected in the Lewis shale from the VSP data is a common phenomenon of shale formations (e.g. White *et al.*, 1983; Thomsen, 1986; Wang, 2002). Analyzing the 3D shear-wave behavior from the VSP data provides additional constraints on anisotropy in the overburden, where no detailed information from borehole or reflection seismic data is available.

#### **4.3.4 Conclusions of shear wave analysis**

The analysis of shear-wave splitting from 3D VSP data in the San Juan Basin has given insight into the anisotropy structure with depth around the borehole. We can explain the observed shear-wave characteristics by a model composed of VTI and orthorhombic layers. The model is consistent with other information from borehole and surface seismic data, where available.

In the reservoir, the shear-wave splitting data do not provide sufficient constraints against a model of lower symmetry than orthorhombic, so that the existence of more than one fracture set cannot be excluded. VTI anisotropy in the Lewis shale, however, is well defined by a shear-wave line singularity. Even for shots with low signal-to-noise ratio this singularity can be clearly observed.

Effects of anisotropy are commonly studied in VSP data to gain insight into lithological properties of reservoirs, such as fracturing. In addition, the characterization of anisotropy from shear-wave splitting as demonstrated in this study could provide useful information for the processing of surface seismic data, where incorporating an appropriate anisotropic model in the overburden and the reservoir may improve the final image considerably. Furthermore, P-wave travel times from 3D VSP data are often inverted to obtain a detailed velocity field around the borehole. Jilek *et al.* (2003) have demonstrated, that travel times and polarization vectors can be inverted for local anisotropy, if a large number of data points densely spaced in azimuth and offset is available. In a case such as the San Juan VSP, where the data points are relatively sparse, the results of the shear-wave splitting analysis could provide necessary constraints for a more detailed inversion of travel times.

It has been shown in several studies that shear-wave splitting is a useful tool to characterize fracture-induced anisotropy in near-offset VSPs (e.g. Queen *et al.*, 1990; Winterstein *et al.*, 2001). Here we have demonstrated that also VTI and orthorhombic symmetry can be well defined from field data by analyzing shear-wave splitting patterns, if data from several offsets and azimuths are available. Especially the detection of shear-wave singularities provides clear constraints to distinguish between different symmetry systems.

#### **4.3.5 Tomographic Analysis**

##### **4.3.5.1 Traveltime tomography of 3-D VSP data**

A total of 53 nine-component shot gathers were recorded, the distribution of the sources on the surface, shown in Figure 4-33, is highly irregular. The goal was to produce a 3-D velocity model of the reservoir, including anisotropy. We started from a 1-D inversion first, however, the 1-D results showed enough velocity variations to justify the need for a full 3-D inversion.

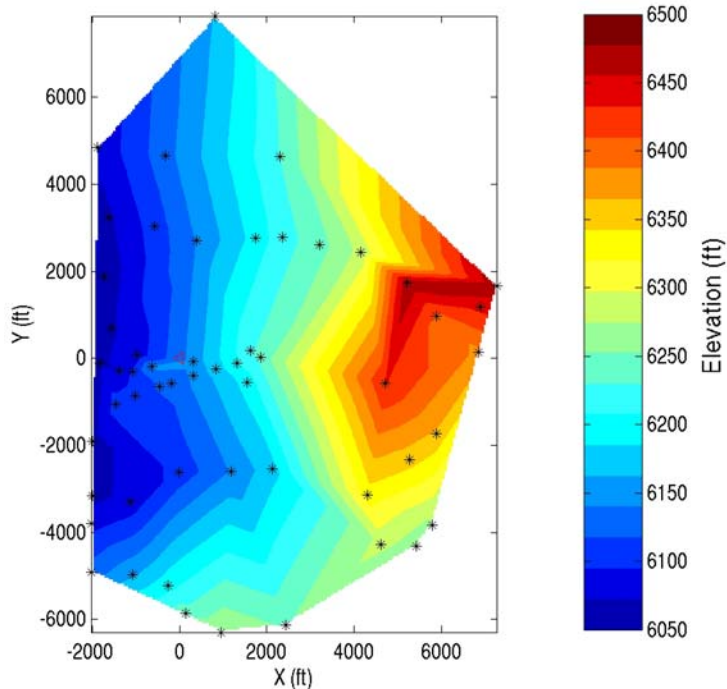


Figure 4-33. 3-D VSP source locations plotted with the elevation map.

#### 4.3.5.2 Travel time picking

The P-wave first arrival travel time picks were extracted from the data using the DSI package's picking tool. Figures 4-34(a) and 4-34(b) show a shot gather with source located at 4,144 ft from the well and the corresponding travel time picks. Indicated on Figure 4-34(b) are turning waves, which are characterized by the change in slope of the first arrivals and change in the vertical component polarity. These turning waves were observed when the source is located 3000 ft and 5000 ft from the well and required new methodologies for the inversion strategy, since current modeling programs do not predict them.

Figure 4-35 presents all the travel time picks organized according to the distance between the sources and the receiver well for purpose of quality control. The top of the figure shows the number of sources located a given distance. Note that the picks for the source located at 8000 ft don't follow the pattern followed by the other picks (travel time increasing with the distance from the well) and this is an indication that the geometry information (source coordinates) for this source position are probably incorrect and the data for this particular shot were discarded in all the subsequent processing.

#### 4.3.5.3 Inversion

**In the first step, individual shots were inverted to generate 1-D velocity models. The comparison of the velocity models obtained at different offsets and azimuths allowed us to obtain information on the lateral velocity variation in the area and anisotropy.**

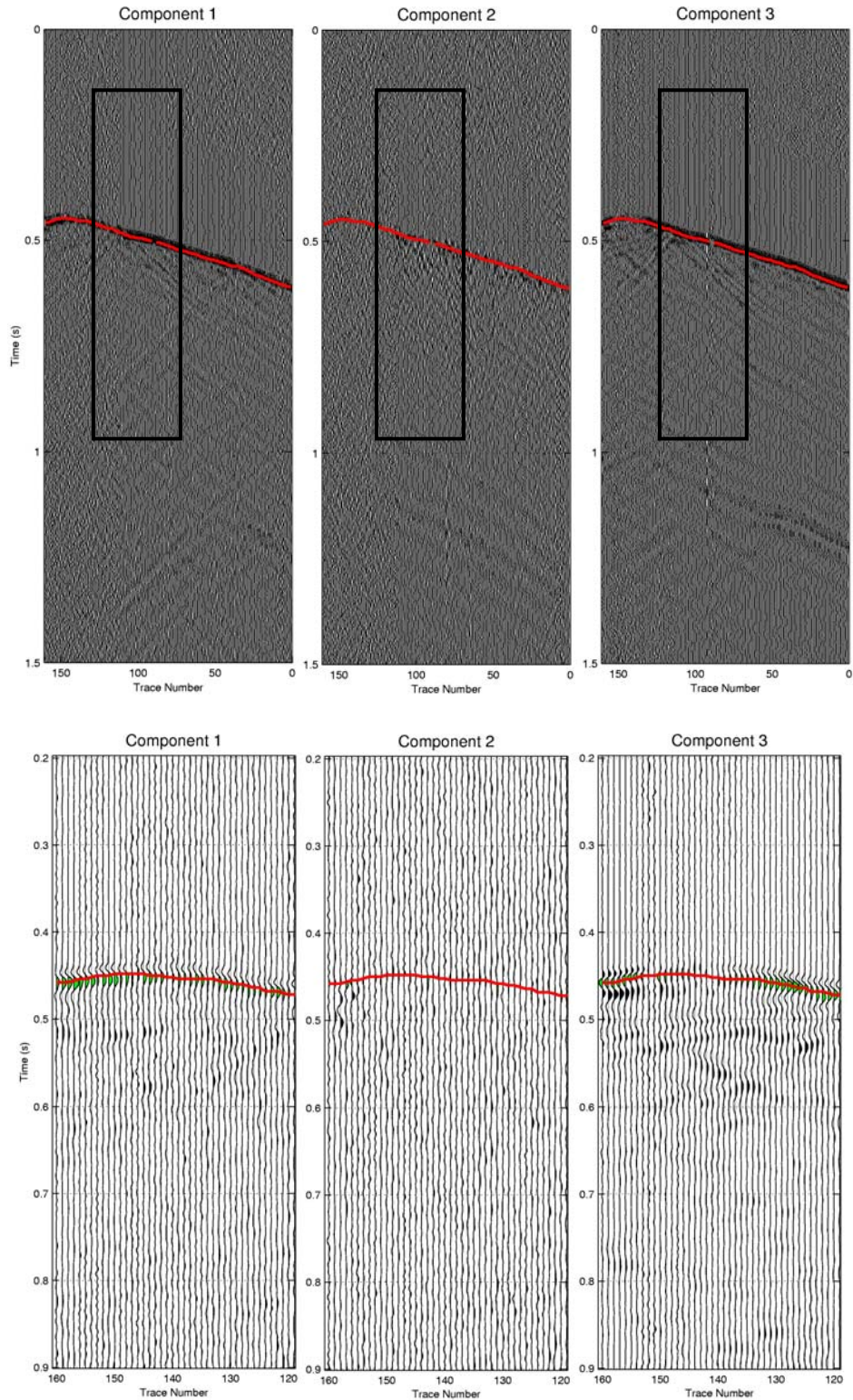


Figure 4-34. (a) Shot gather recorded with vertical vibrator positioned at 4,144 ft from the well (source IVI 187) with P-wave travel time picks; (b) detailed view of the sections indicated on (a). Note the change in the direction of the slope of the first arrival and inversion of polarity in component 3 (vertical).

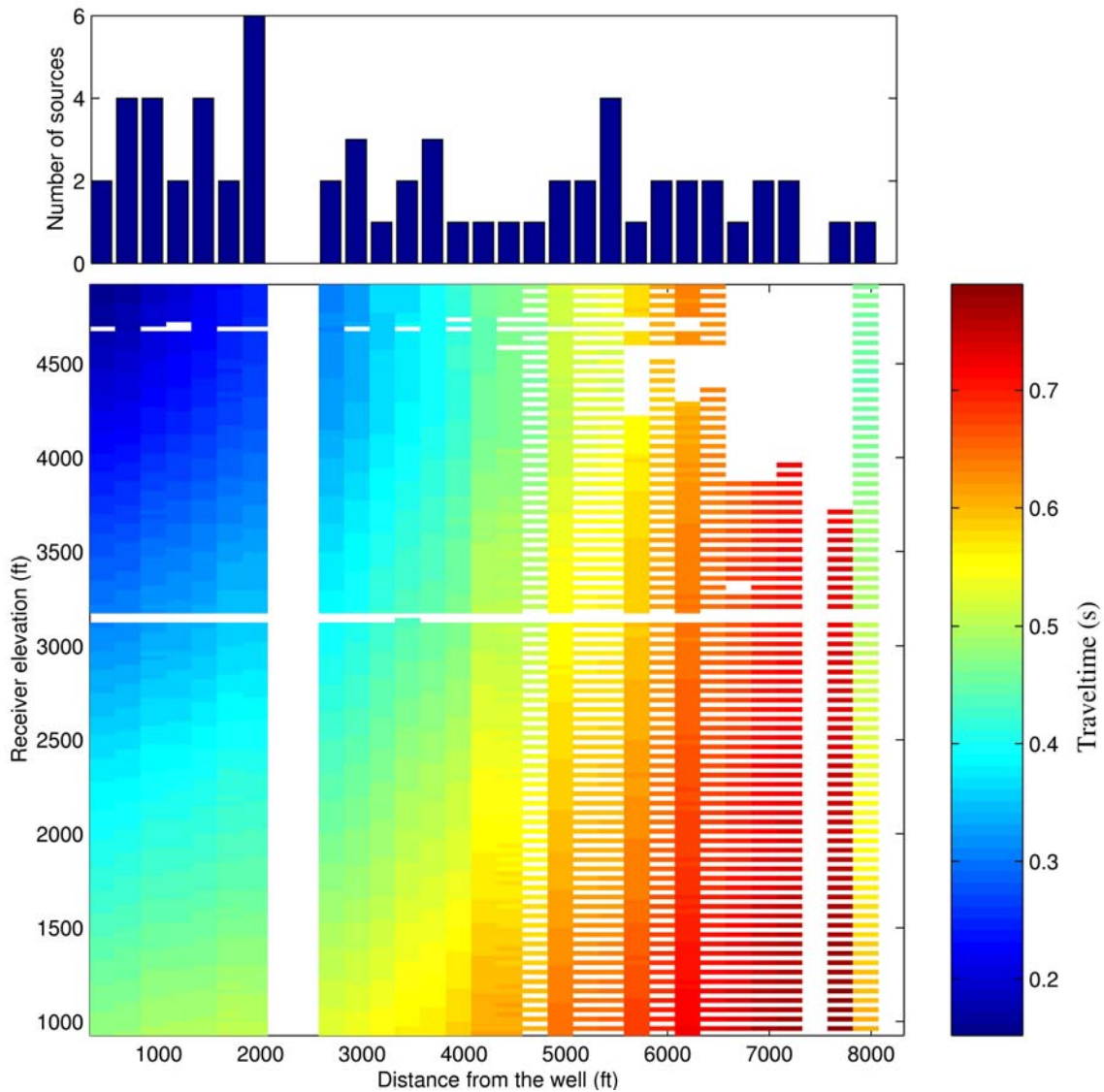


Figure 4-35. P-wave travel time picks organized sorted according to the distance from the source to the well. Note that the travel times obtained from the source located at 8000 ft from the well don't follow the same pattern of the previous data, indicating possible error on the source location coordinates.

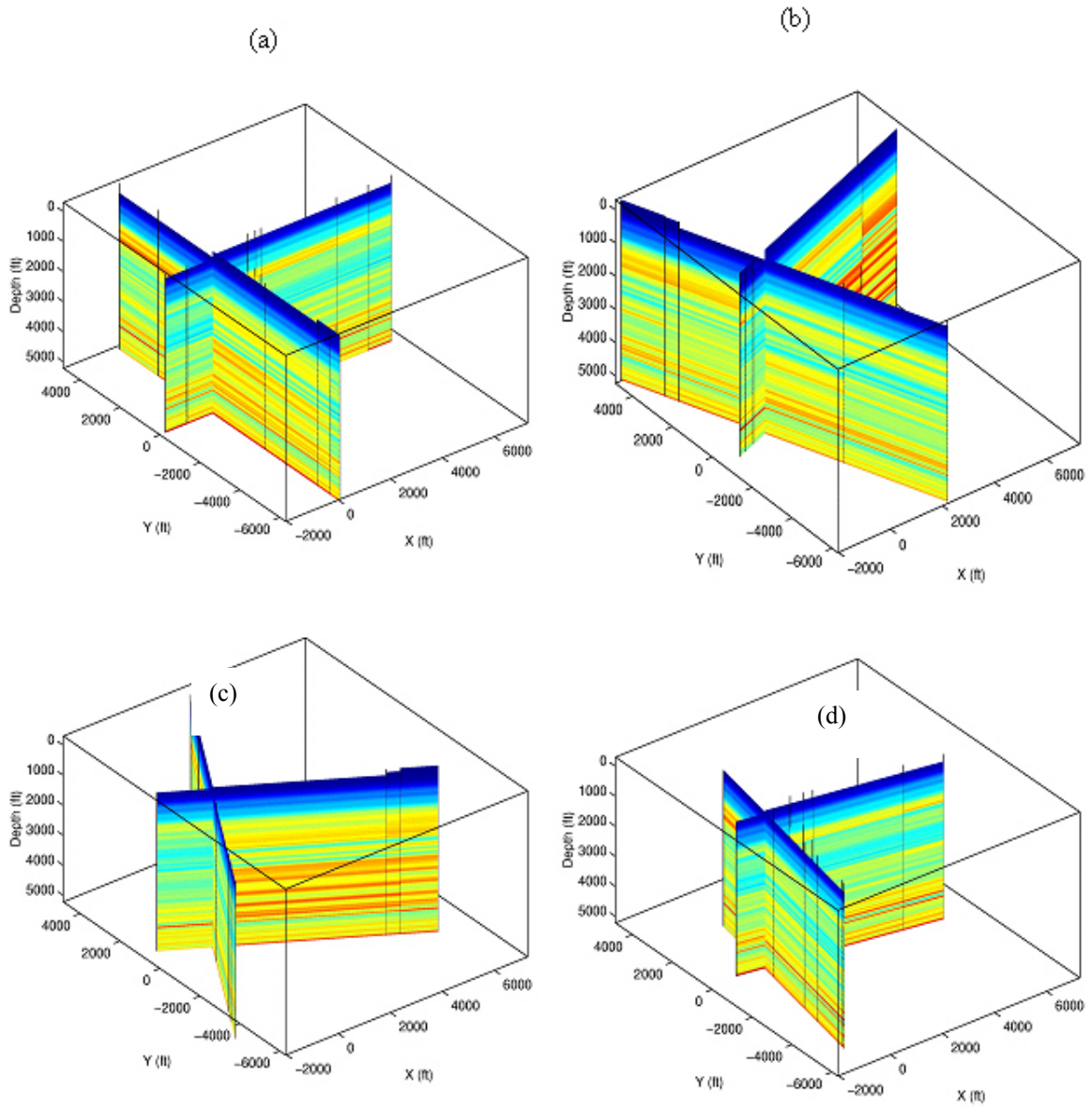


Figure 4-36. 1-D P-wave velocity tomograms displayed in three dimensions. (a) planes located at 0 and 90 degrees; (b) 20 and 110 degrees; (c) 60 and 150 degrees; (d) 80 and 170 degrees from the X direction.

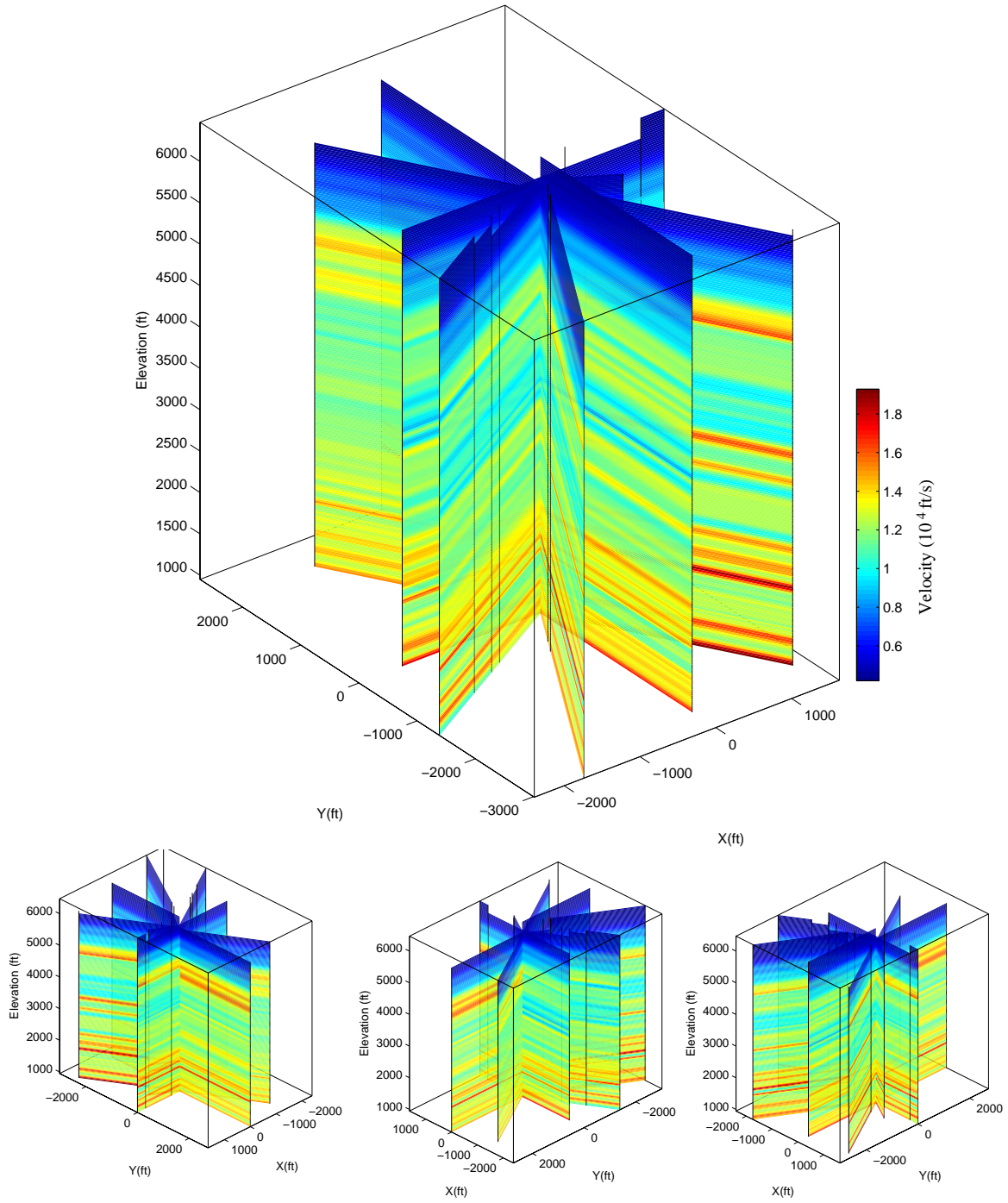


Figure 4-37. Results from 1-D tomography applied to twenty shots from the San Juan 3-D VSP dataset. Estimated layer velocities for long offset and near offset shots are different Pattern of heterogeneity indicates need for consistent 3-D inversion.

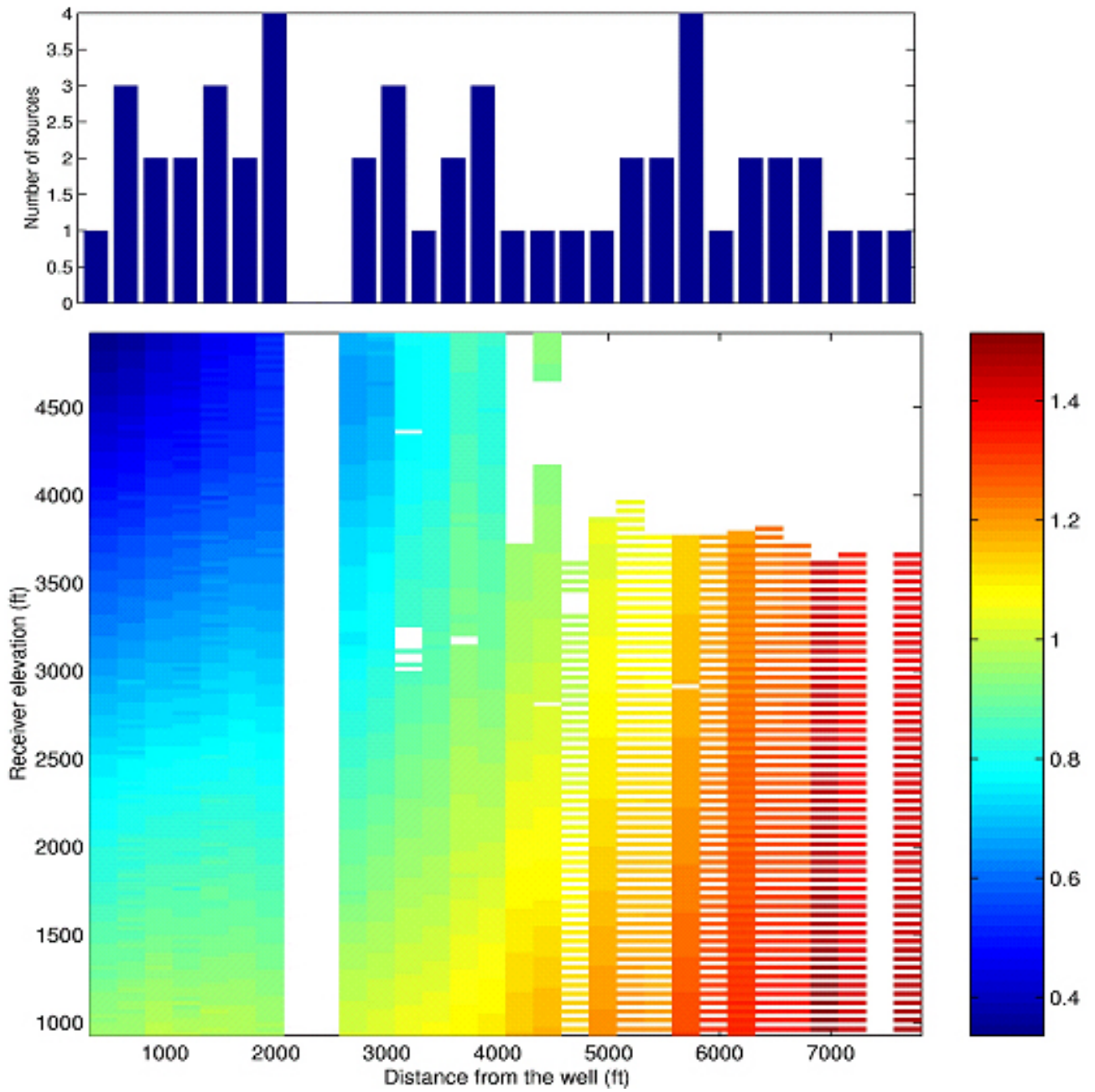


Figure 4-38. S-wave travel time picks organized sorted according to the distance from the source to the well.

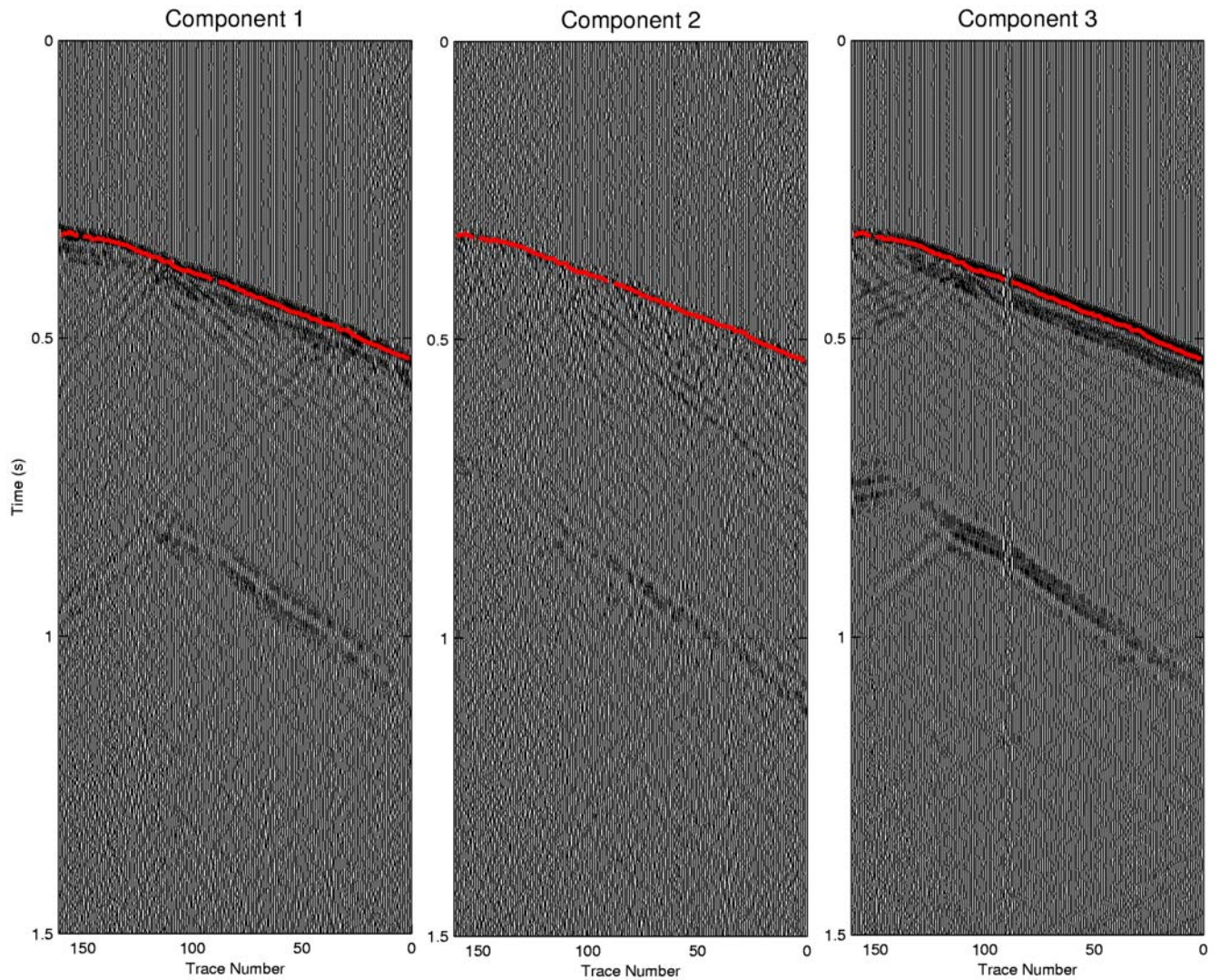


Figure 4-39. P-wave travel time picks. Source IO 238 – Vertical vibrator with P-wave first arrival picks (source-receiver offset = 2732.5 ft).

Figures 4-36 and 4-37 are pseudo-three D plots of the velocity variation from the different VSP shots. As can be seen the data indicate a non-homogeneous velocity model in both P and S-wave behavior. Figures 4-39 and 4-40 are an examples of P- and S-wave picking respectively.

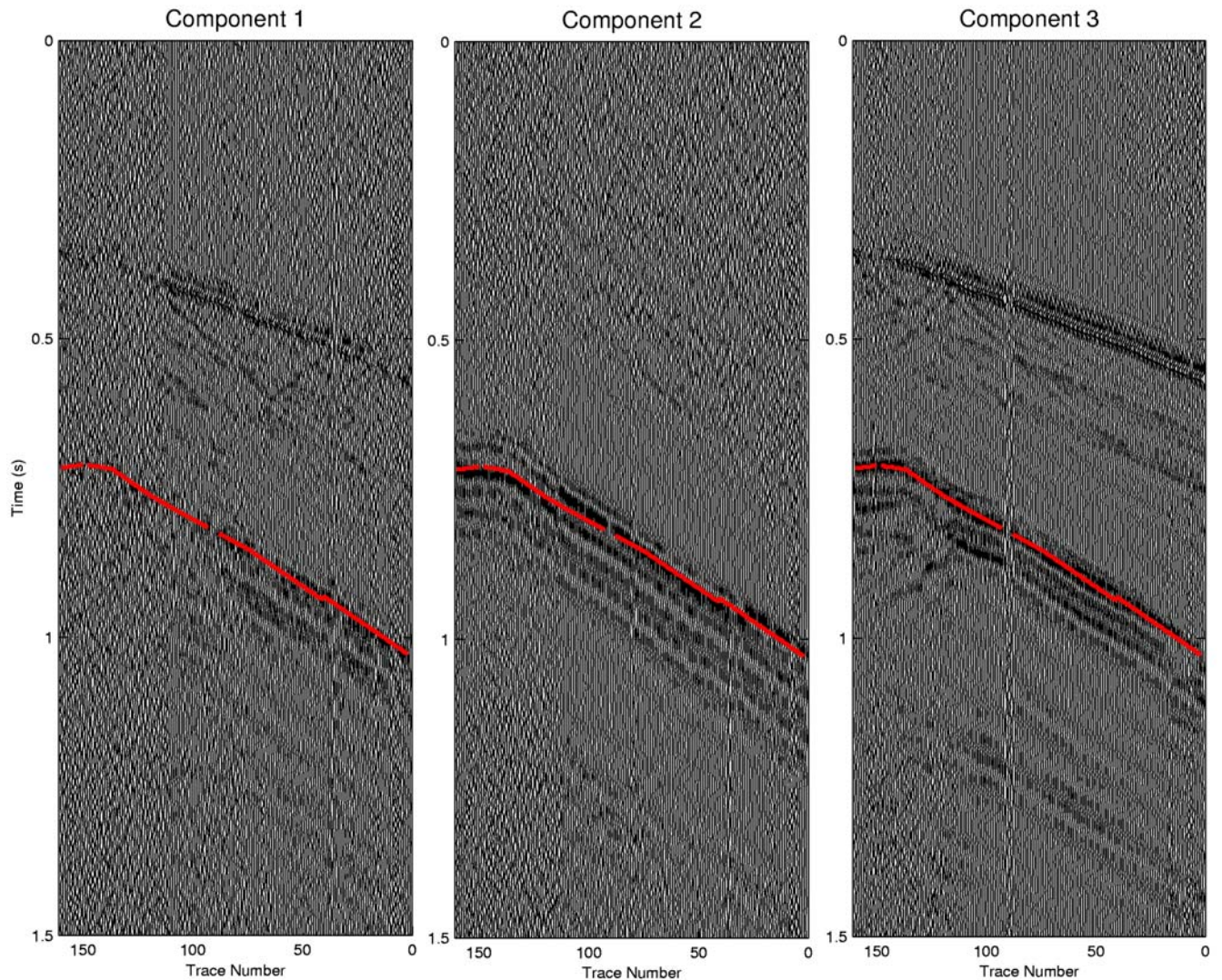


Figure 4-40. Source IO 238 - horizontal vibrator (radial) and shear-wave first arrival picks.

#### 4.3.4 CDP Processing

The objective of the CDP VSP imaging was to derive images in the volume around the Newberry LS 2C well to determine if VSP could pick up fracturing/faulting that was not detectable in the surface seismic. The process to derive the reflection images in the VSP data are similar to surface seismic but the geometry is handled differently, as is the elimination of the down going energy and in the enhancement of up going (reflection) energy in the VSP data. As in surface seismic it is also necessary to have a good velocity model to accurately place the reflectors in the proper space coordinates.

Figure 4-41 shows some corridor stacks of the near surface data at shot points nearest to the well (up to only a few hundred feet from the well, essentially zero offset when compared to the 5000 foot depth). Figure 4-41 shows the corridor stacks from the two nearest offset VSPs. Field File Identification (FFID) 7 and 41 were shot with the shallowest receiver depth at 16.5 feet. The

---

offsets for FFID 7 and 41 are 199 ft and 42 ft respectively. It is interesting to note that these two shots were taken just before the receiver string “lock” failed on the first attempt to collect the VSP data. (the string was repaired and the data were successfully collected ). The data quality for FFID 41 is much poorer than for FFID 7 because the string was losing pressure and failed immediately after the shot. Both VSPs are from the IO vibrator. It was discovered that the receiver string had failed when the IVI attempted to acquire data.

FFIDs 215, 1684, 1708, 1733, and 2544 are from shot point 400. This point was chosen as a test point for the comparison of the I/O and IVI vibrators and has the most VSPs of all the shot points. The offset is 285 feet from the well. FFIDs 215, 1733 and 2544 were shot with the I/O vibrator. As mentioned earlier the receiver was repositioned by 25 ft during the acquisition. Shot 215 was taken in the first position and shots 1733 and 2544 were taken in the second position. The vibrator was moved to other shot points between 1733 and 2544 and then reoccupied shot point 400.

FFIDs 1684 and 1708 were shot with the IVI vibrator. FFID 1684 was shot by the IVI vibrator as the last shot in the first receiver position while FFID 1708 was the first shot after the reposition. The vibrator did not move between these two shots.

All of the VSPs at shot 400 compare very well. A 73 ms time shift and a 20 degree phase rotation was required to match both shallow shots to the shots at shot point 400.

Figures 4-42 and 4-43 show FFID 215 inserted into the inline and crossline surface seismic data, respectively, near the well bore (not exactly because the surface seismic lines only went a few hundred feet from the well and not directly over it). As can be seen the match is very good. A 320 ms shift was necessary to match the VSP and surface seismic data. This shift is about the same as the datum shift present in the surface seismic. The down-going VSP wavelet was used to deconvolve the up going VSP, thus the corridor stacks are zero phase. The seismic data was found to have a phase of 40 degrees relative to the VSP. According to usual practice the VSP has been time shifted and the surface seismic has been phase rotated. This gave us confidence that the VSP data were of high enough quality to proceed with the CDP imaging.

Each individual VSP was processed for reflections. The objective was to determine if the VSP techniques could detect faults that were not detected in the surface seismic. Figure 4-44 shows typical processed data from a near, intermediate and far offset VSP.

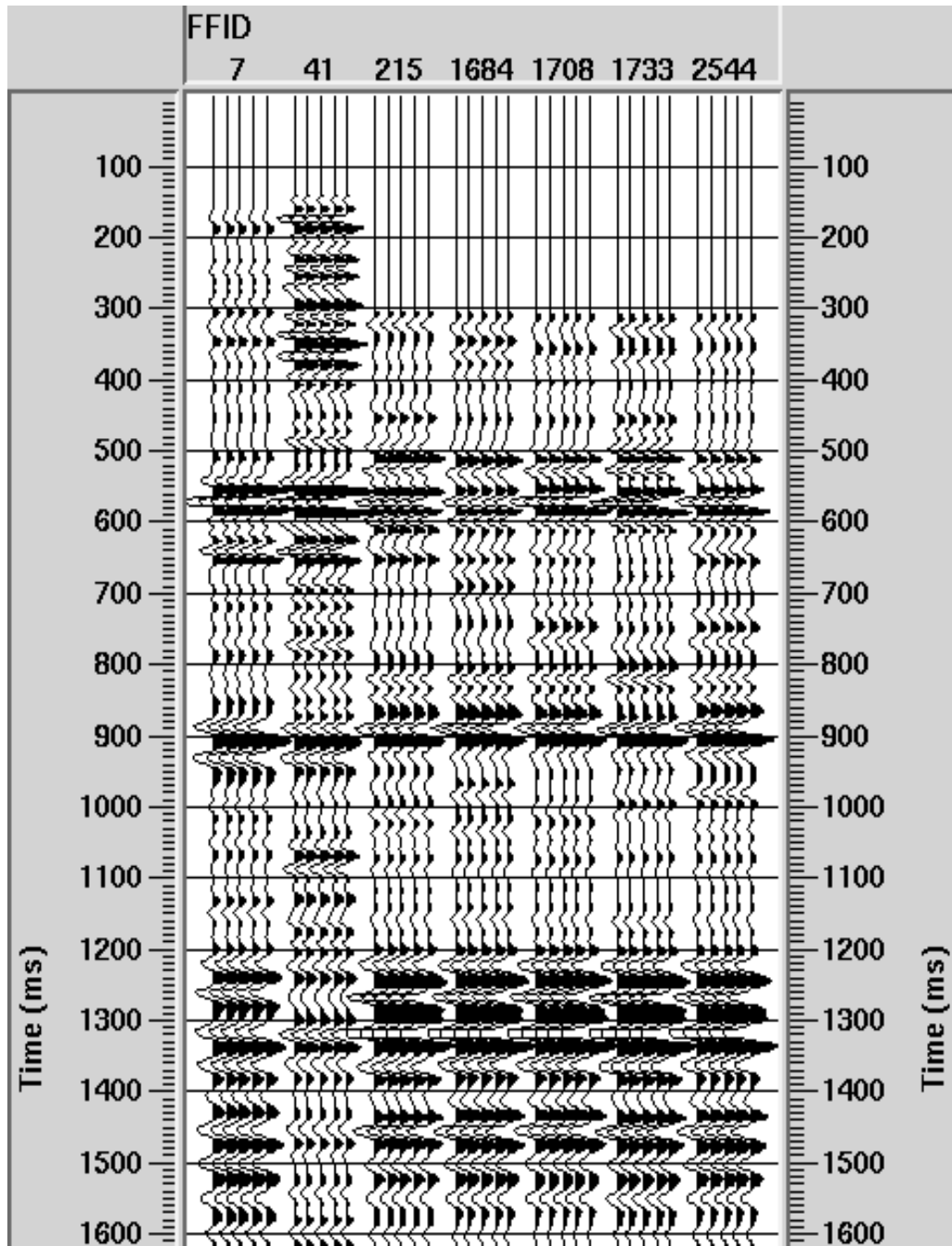


Figure 4-41. Corridor stacks from shot points near the VSP well. Note the difference between FFID 7 and 41, 7 had a “good” lock on the tool and 41 had a bad lock on the VSP tool.

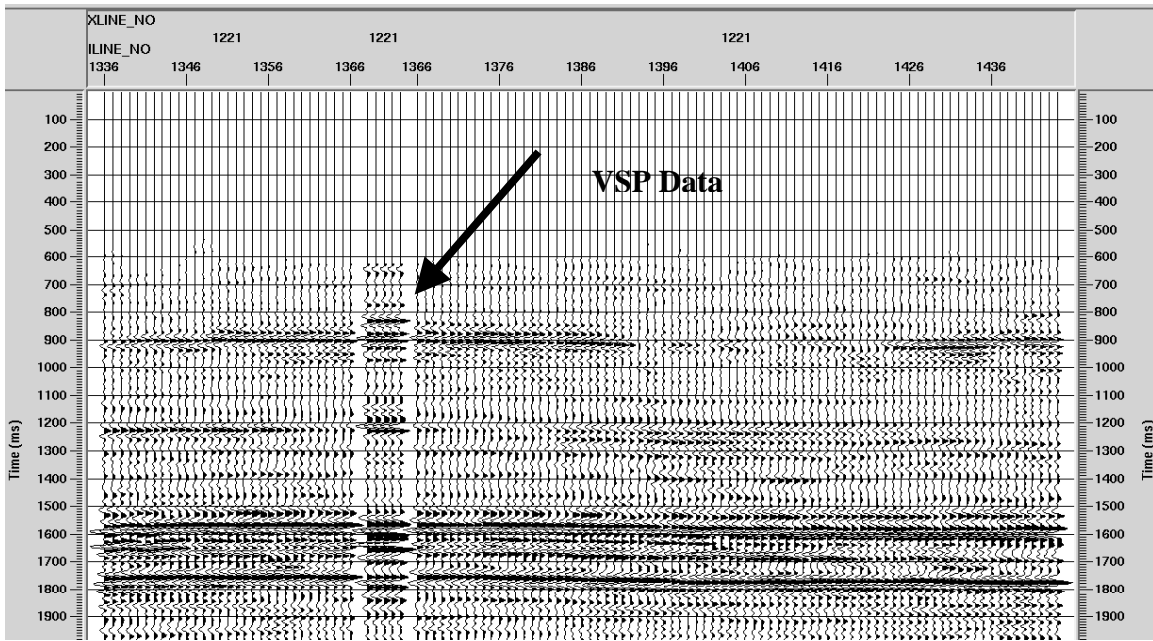


Figure 4-42. A corridor stack from the VSP data inserted into an inline surface seismic line

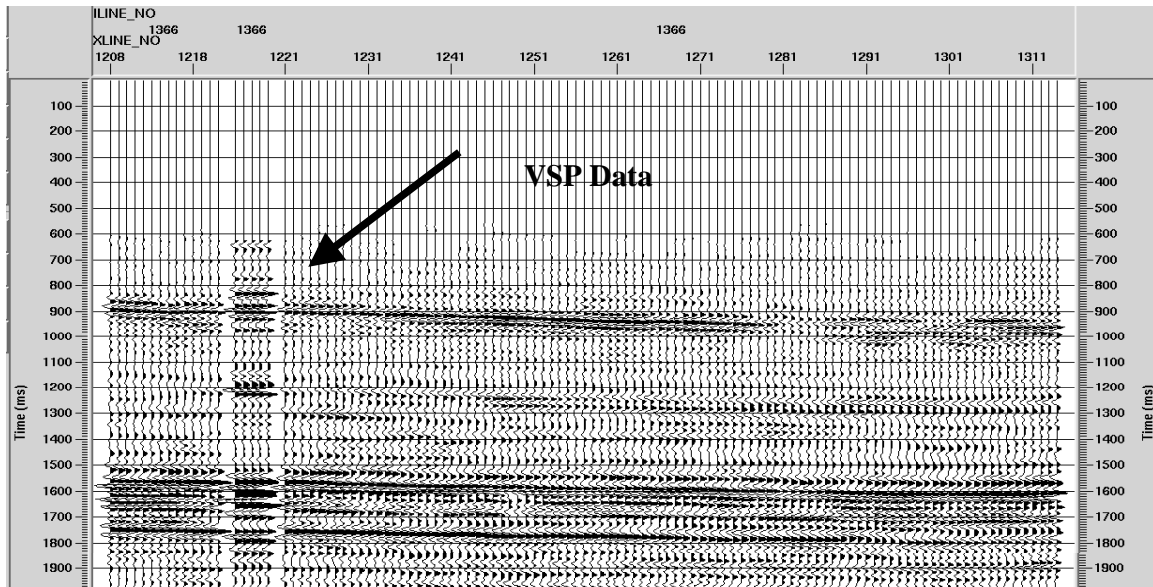


Figure 4-43. A corridor stack from the VSP data inserted into a crossline surface seismic line

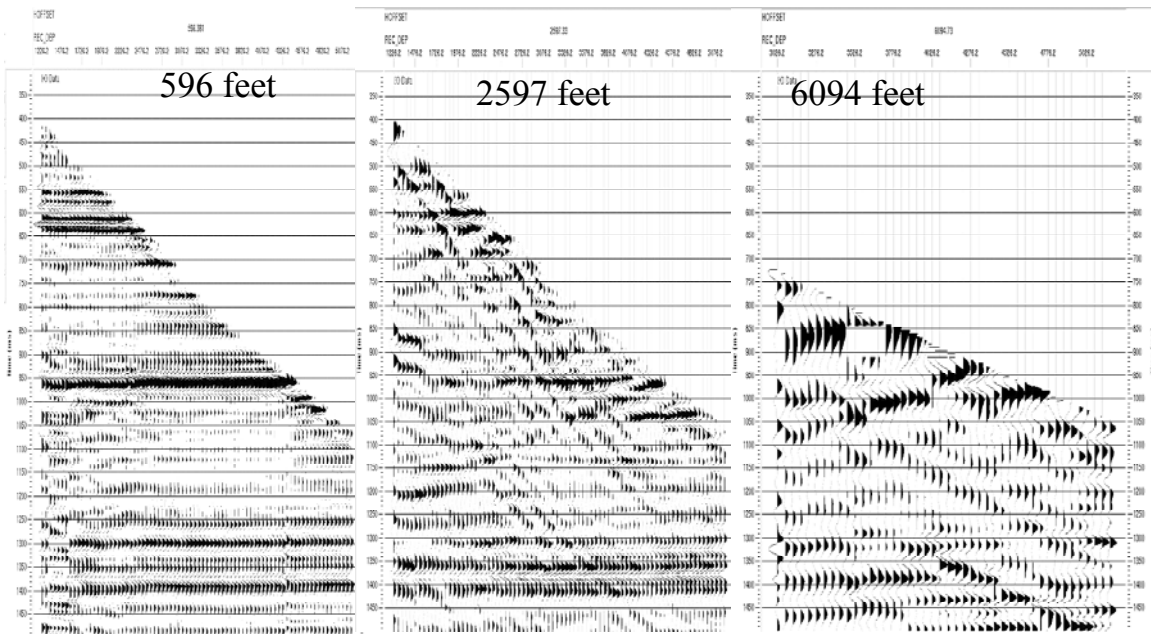


Figure 4-44 Example of VSP CDP data from a short, intermediate and far off set.

As can be seen in Figure 4-44 as the distance from the VSP well increases the data become more complex. This is not solely due to fractures but due to interference from converted waves (P to S) and due to multiples in the data. When one is processing VSP data it is important to remember the geometry of the source and receivers is much different than in surface seismic. If this were surface seismic acquisition the receiver would have nearly the same depth as the source and each reflection event would reflect at the horizontal midpoint between the source and receiver. This is called the common midpoint (CMP) or common depth point (CDP). In a VSP the receiver is not at the same depth as the source. The horizontal positions of the reflections are not at the CMP but vary with the depth of the reflection approaching the CMP point as the depth increases. Thus the recorded VSP time for each reflection is not the surface two-way time for the reflector, nor is it the time that would have been recorded for a surface receiver.

The VSP CDP seeks to transform the VSP time to the surface two-way time and to correctly position the reflection amplitudes at the correct horizontal position for each reflection. To that end image a curve drawn from the receiver to the reflection point at each depth. Figure 4-45 shows an earth model on the right with a vertical axis of DEPTH and a horizontal axis of OFFSET. The right panel is a VSP with a vertical axis of TIME and a horizontal axis of receiver DEPTH. The red stars overlain on the VSP are the calculated reflection times for the model shown on the right. Notice that the calculated times are a good match to the VSP data.

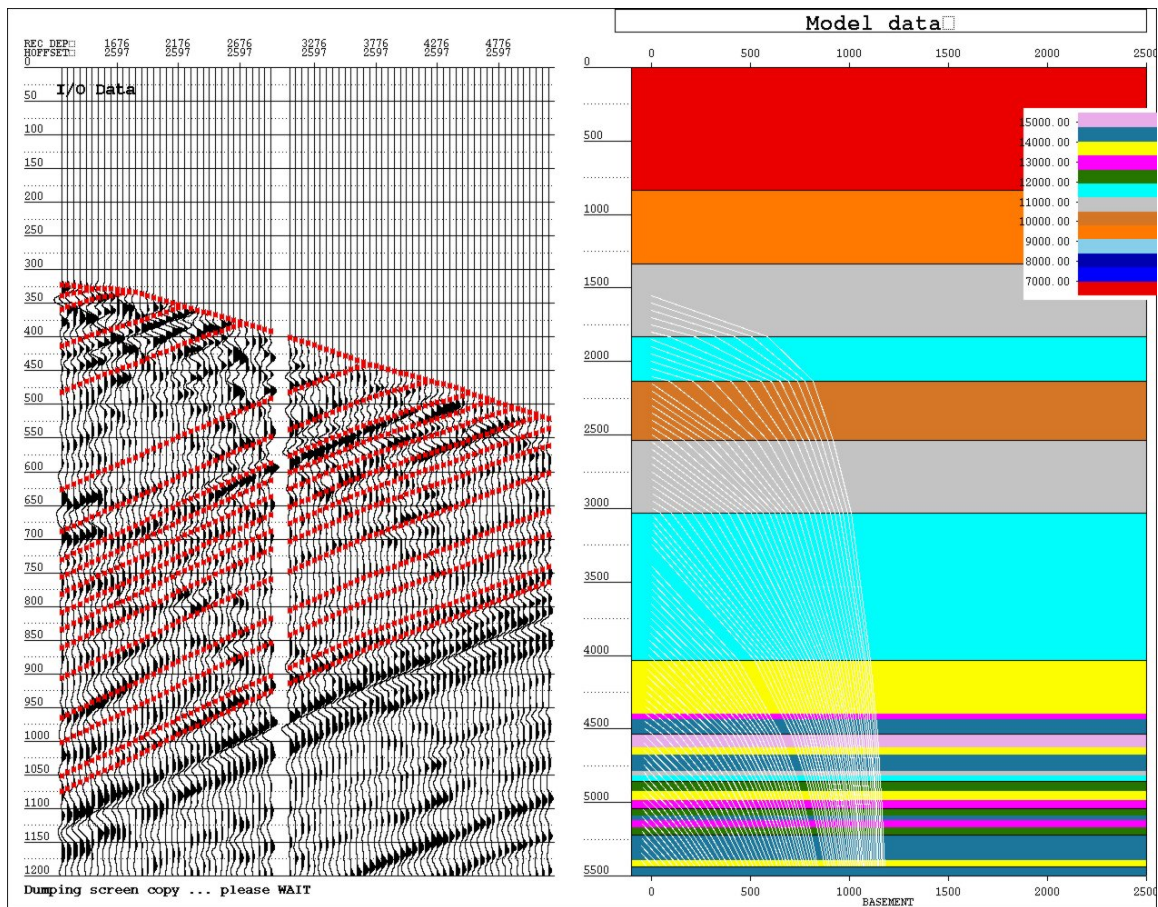


Figure 4-45. The ray tracing model used in the processing of the VSP data.

The white curves on the right panel each start at the receiver and connect the reflection points for each depth. Notice the starting point of each white curve does not lie on a vertical line. That is because the well was slightly deviated. The VSP data for the shallowest level is the left most trace in the left panel. The corresponding white curve is the top curve on the right panel. The VSP data for the deepest level is the right most trace in the left panel. The corresponding white curve is the bottom small segment on the right panel. The ray tracing gives the following information for a given trace.

- 1) The (x, z) location of each reflection.
- 2) The VSP time for that reflection.
- 3) A ray that can be traced from the surface to the (x, z) location to give the two-way time

Because we have for each reflection the VSP time and a two-way time, one can remap the data from VSP time to two-way time. The analog process for surface data is called NMO. This is the first step in the processing. At this point for a flat geometry the reflection should be flat. Additional processing used in surface seismic can also be applied to enhance the reflections. The

---

processing has to continue because the “NMO”ed VSP data is not correctly mapped in space. The white curves on the right side of Figure 4-45 show how the data needs to be mapped in space. The ray tracing gives the x (offset) location and the two-way time for the reflection. From this information the trace amplitudes can be mapped in space. As in surface seismic data the horizontal distance is divided into bins. The data in each bin is horizontally summed (stacked) and a CDP trace is output to derive plots as shown in Figure 4-44.

#### **4.4 SINGLE WELL ANALYSIS**

Initial modeling of the single well data focused on reflection imaging for both horizontal velocity interfaces and potential near-vertical fracture scattering or reflections. Initial modeling used 2D finite difference code. Figure 4-45a shows a layered model with single well geometry acquisition and Figure 4-45b shows the modeled response for a single sensor shot gather. Direct arrivals and reflections from the velocity interfaces can be seen. However, interpretation of the field data indicates that the dominant energy is trapped borehole modes, either tube-waves or anomalous arrivals observed in the reservoir. The anomaly is a high amplitude, low velocity event. Figure 4-46 shows seismograms for the anomalous zone that is at approximately 4350- to 4400 ft. The arrival in this zone is too slow for a tube-wave or a flexural wave (both of which are borehole waves whose velocities are estimated using formation velocities derived from well-logs). The attributes that define this anomalous zone are amplitudes about 50 times larger than the rest of the data, velocities much slower than tube-wave (or body waves) and polarization which is horizontal (rather than dominantly vertical which is seen for tube-waves).

The most notable attribute of this anomalous zone, as defined by the high amplitude of seismic energy, is that it correlates with the highest permeability and highest estimated gas production zone in the reservoir, as measured by well logs. Figure 4-47 shows a plot of the single well RMS (root mean squared) amplitude as a function of depth (plotted at the midpoint between source and sensor) compared to the interpreted well logs showing permeability. The correlation of gas shows and single well amplitude is a unique and unexpected observation. This potentially important observation needs further research to be generally applied. Complete analysis requires a more intensive 3D borehole modeling containing the borehole itself is necessary. A working hypothesis is that intensive fracturing in the anomalous zone is located at some distance away from the well, where well log data is not affected, but where the single well data is affected as a type of low-velocity wave guide which traps energy, giving a high amplitude, low velocity arrival. It is notable that the VSP data also has a high amplitude borehole wave in this zone, while the well log data (including Stonely (tube) wave log) does not indicate any anomaly. While a conceptual model has been developed, a modeling study could not be completed pending code modification to allow for 3D variable grid, anisotropic borehole models.

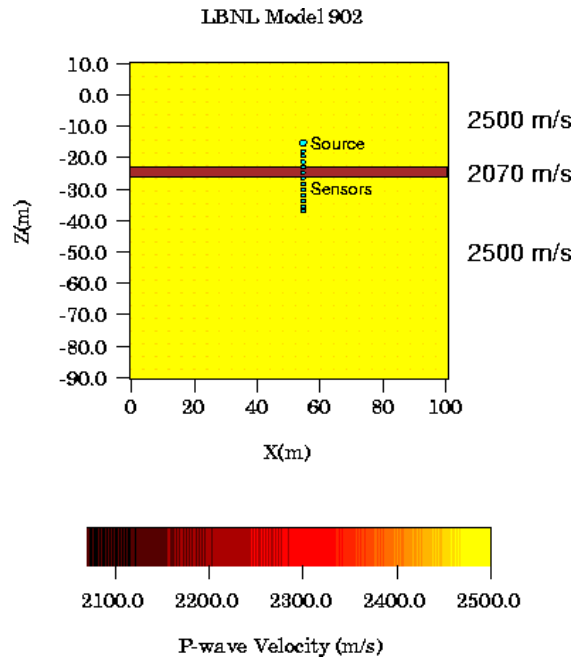


Figure 4-45a. Single well model with single layer, no borehole is include in this initial model.

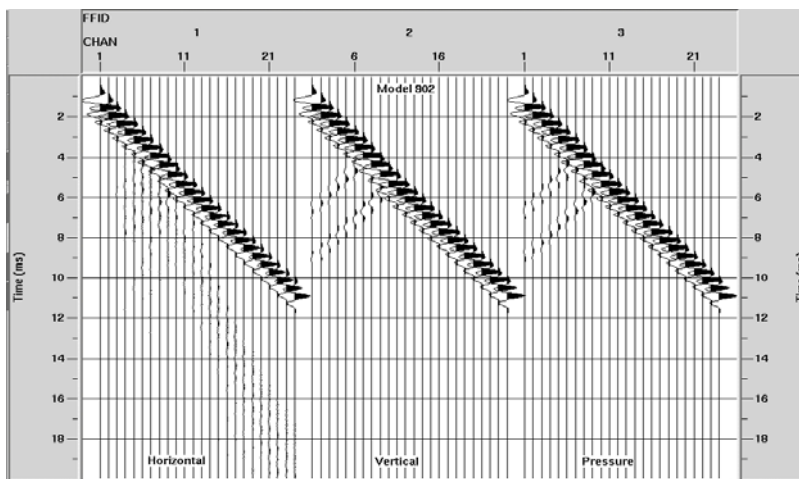


Figure 4-45b. Model seismograms for a shot gather (one shot, 24 sensors) using the model shown in Figure 4-45a for three components of sensors, horizontal, vertical and pressure (left to right). The large arrival from 1 to 11 ms is the direct P-wave while the two events intersecting the direct arrival are reflections from the top and bottom of the layer. The pressure response (right) is modeling the hydrophone response.

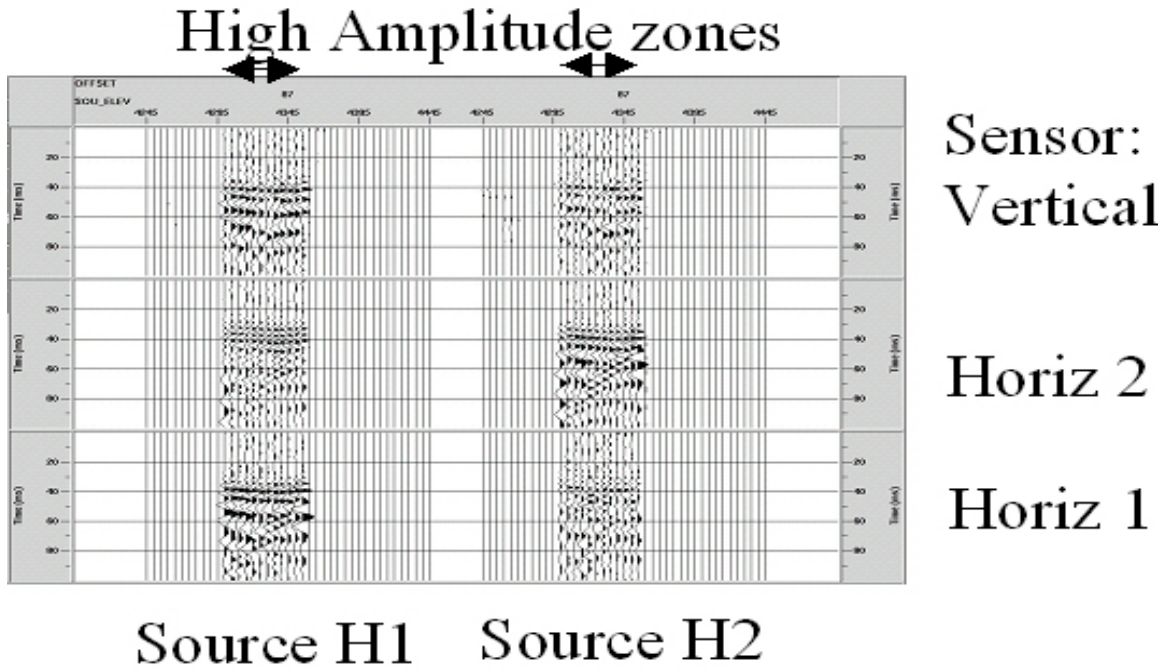


Figure 4-46. True amplitude 6-component single well common offset gather showing data in the anomalous zone (arrows, approximately 4350 to 4400 ft.) and nearby traces. Traces outside the zone, that appear blank, do have data, but are much lower in amplitude than arrivals in the anomalous zone.

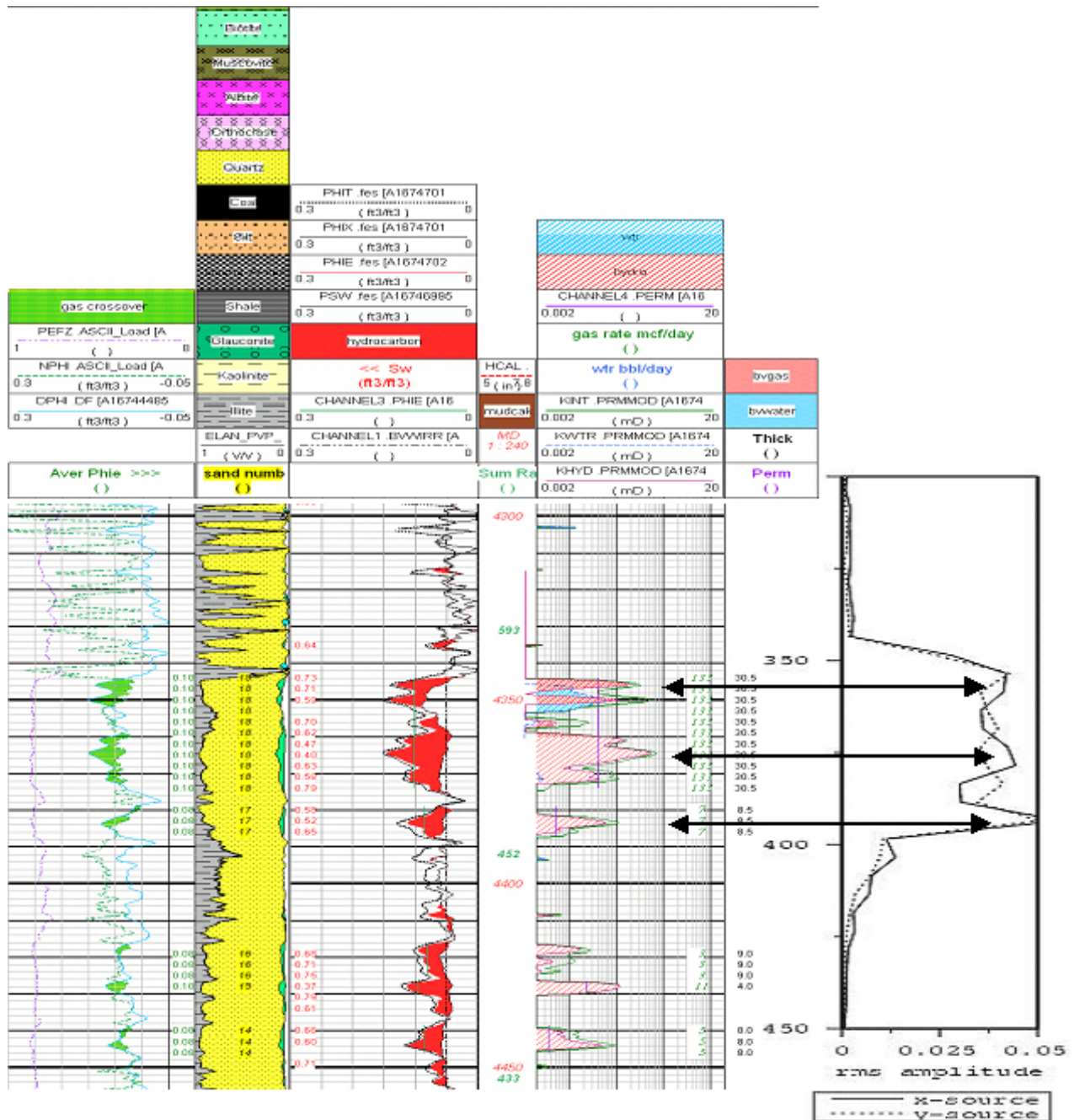


Figure 4-47. Relation between interpreted well logs and single well amplitude. Logs, left to right, are gas porosity (green), stratigraphy, hydrocarbon porosity (red), permeability (gas=green, water=blue, hydrocarbon=red). Single well amplitude (far right) is r.m.s. amplitude for x and y source (solid and dashed line respectively) for 3-component sensor. Arrows indicate correspondence between high gas shows and high single well amplitude.

To further investigate the “high amplitude zone” forward modeling using a variable-grid finite-difference parallel code developed at Stanford University was performed. Figure 4-48 shows one component (source H2, receiver V) of the common offset gather of channel 1 (offset 87 ft). Direct and reflected waves are generally visible. A low velocity zone between depths 4387-4442 ft is observed.

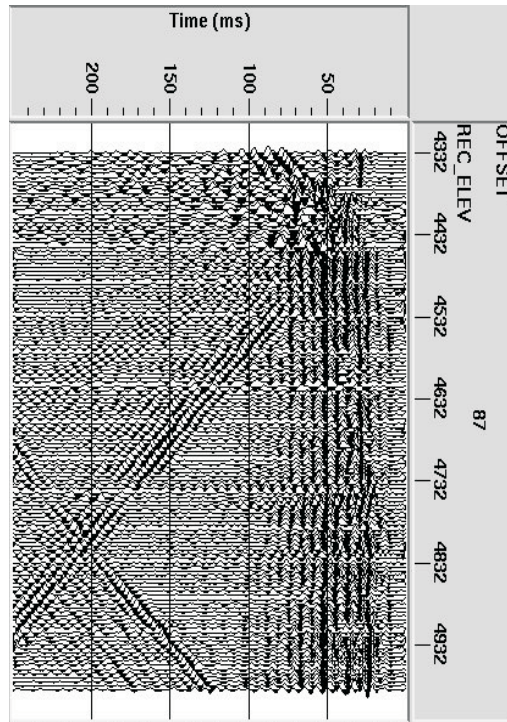


Figure 4-48. One component (source H2, receiver V) of the common-offset gather of channel1 (offset 87 ft) with AGC.

Logs and survey geometry was used to help us to identify the events observed in the field data (Figure 4-49a). Figure 4-49b shows sonic logs (P- and fast S-waves) and the estimated low frequency (< 1000Hz) tube-wave velocity (White, 1983). Using these velocities, we predict the arrival times of the direct P-, S- and tube-waves which indicate that the consistently observable direct arrivals (event 1) in the field data are tube-waves, though weak S-waves are visible on some sensors. Primary tube-wave reflections, events 2u/2d and 4, are from the C/M interface (Cliffhouse sand/Menefee shale interface) and the well plug, respectively. Event 3d is due to multiple reflections between the tool and the C/M interface.

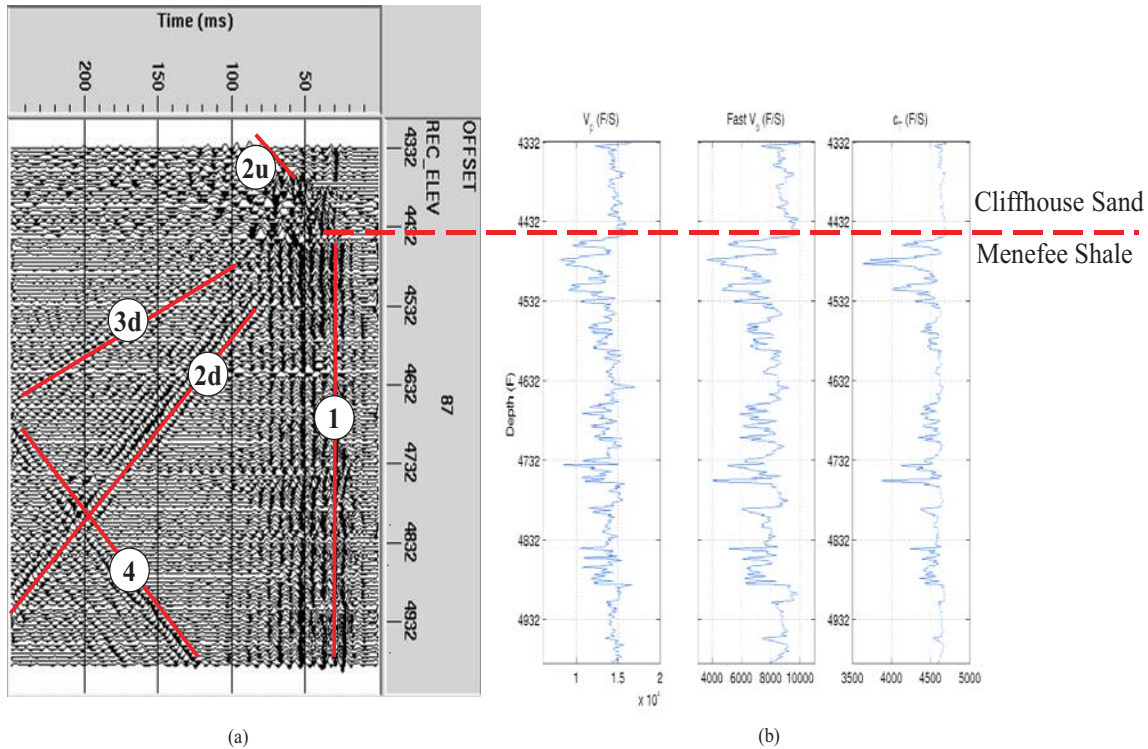


Figure 4-49 (a) Generally visible events in the field data; (b) Sonic logs (P- and fast S-waves) and the estimated low frequency tube-wave velocity from logs. Velocities are used to predict the arrival times to identify the events in the data: 1 - direct tube-wave; 2u/2d - up/down-going interface reflections; 3d - down-going multiple reflections; 4 - reflected tube-wave from the well plug.

Figure 4-50 schematically illustrates the ray paths (Figure 4-50a) and associated arrivals on the seismogram (Figure 4-50b). Except the direct tube-waves (1) and the well plug reflections (4), the C/M interface reflections and multiples are affected by the tool position. When the tool is above the interface, there are up-going primary reflections from the interface (2u) and multiple reflections between the tool and the interface (3u). When the tool is across the interface (the source is above and the receiver is below the interface), neither primary nor multiple reflections will be observed (dash lines in Figure 4-50b). When the tool is below the interface, there are down-going interface reflections (2d) and multiple reflections (3d).

For a common offset gather, slopes of events on the seismogram are their apparent velocities. Using the ray paths for source/receiver at two depths, we get the formulation to calculate the true velocities of the events in Figure 4-50b:

$$c_1 = S - R \text{ offset} / \Delta t$$

$$c_{2u} = c_{2d} = c_4 = 2 * \Delta h / \Delta t = 2 * c'$$

$$c_{3u} = c_{3d} = 4 * \Delta h / \Delta t = 4 * c',$$

where  $c' = \Delta h / \Delta t$ , called apparent velocity, is the slope of the event on the seismogram.

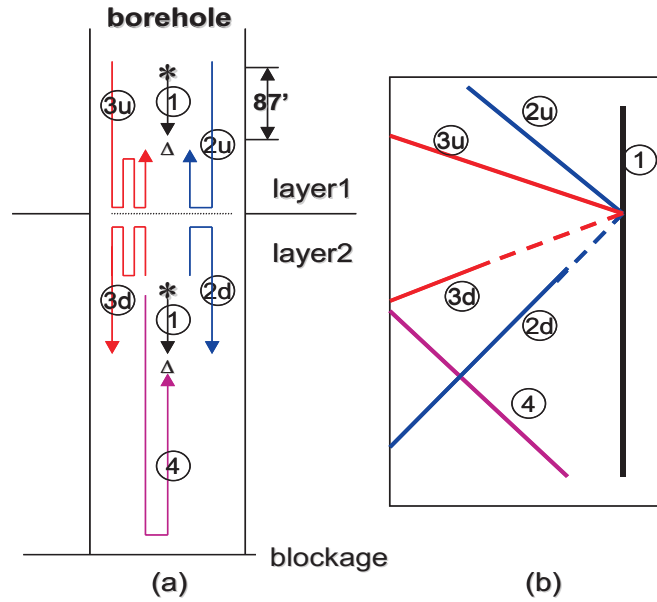


Figure 4-50. Schematic diagram of tube-waves in the single-well survey: (a) Wave paths; (b) Arrivals on the seismogram.

Figure 4-51 shows the apparent and true velocities of the identified events in the field data. We can see these events have almost the same true velocities that confirm they are all tube-waves.

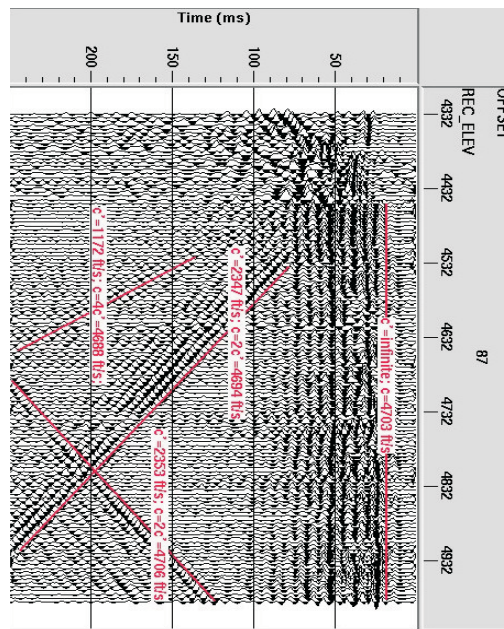


Figure 4-51. The apparent velocity ( $c'$ ) and true velocity  $\text{©}$  of the direct, reflected, and multiple tube-waves in the field data with AGC.

#### 4.4.1 High Amplitude Zone Analysis

In the field seismogram (Figure 4-49), for receiver depths between 4387-4442 ft, the observed direct wave has a very low velocity. True amplitude display (Figure 4-52) shows the event has very high amplitude. The anomalous zone is right above the Menefee shale and is in the Cliffhouse sand. The predicted tube-wave velocity from logs (the 3<sup>rd</sup> panel in Figure 4-49b) for this zone is around 4700 ft/s which is much higher than the velocity of the observed direct wave on the field seismogram (2900 ft/s). Therefore formation properties obtained from logs do not explain the anomaly.

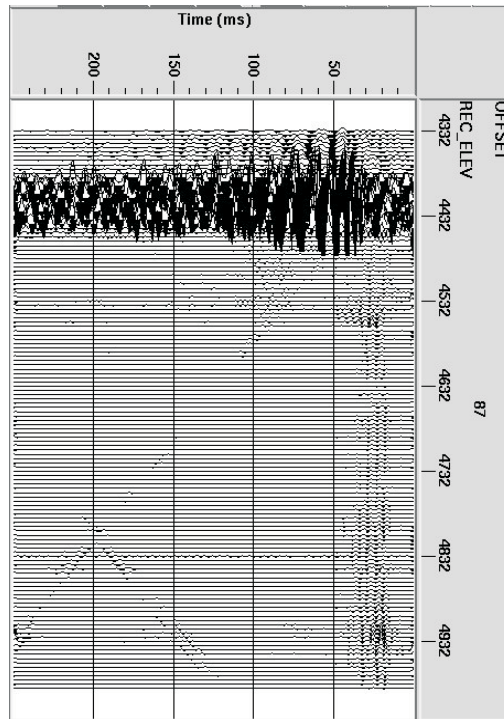


Figure 4-52. True amplitude display of the data: the anomalous zone (4387-4442 ft) with low velocity and high amplitude.

The polarization study (Figure 4-53) shows the anomalous event is horizontally polarized, but the normal tube-wave is vertically polarized. The horizontal polarization is consistent with flexural-waves, but the dispersion relation of flexural-waves (Figure 4-54) indicates that the velocity of the flexural-wave at the single-well frequency (300-400 Hz) cannot be as low as that of the anomalous event in the field observations.

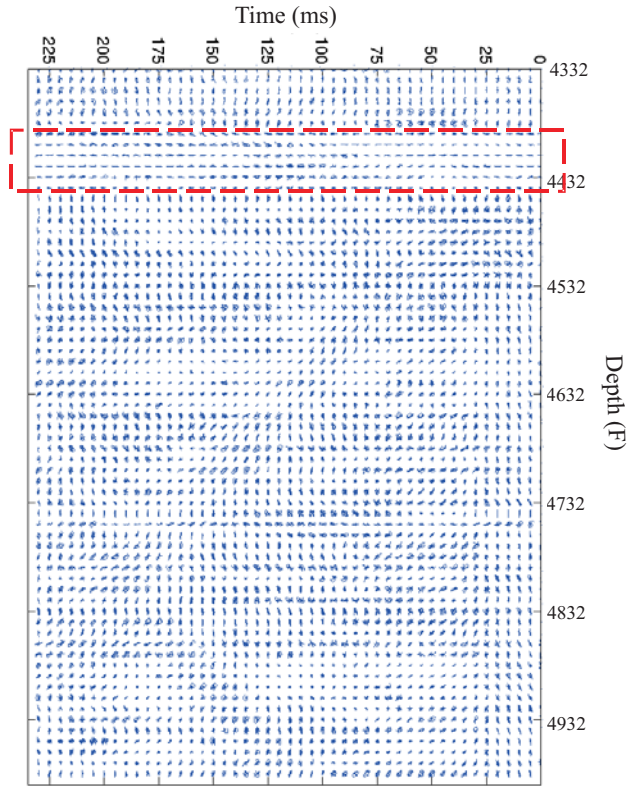


Figure 4-53. Polarization diagram for receiver H2 and V of the source H2. The anomalous zone (in the red box) has horizontal polarization but the rest has vertical polarization.

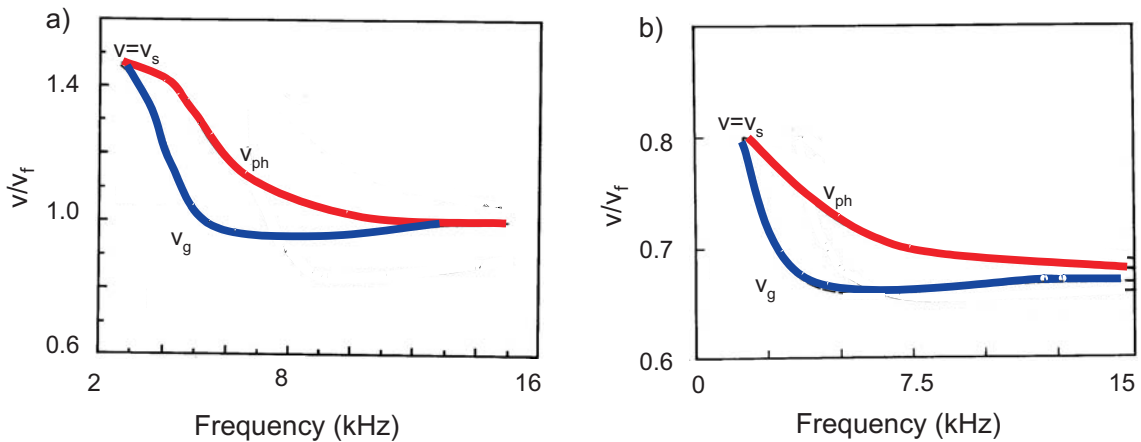


Figure 4-54. Dispersion of flexural waves (Paillet et al. 1991): (a) Sandstone (fast, hard formations  $V_p > V_s > V_f$ ); (b) Shale (slow, soft formations  $V_p > V_f > V_s$ ).  $V_{ph}$  and  $V_g$  are phase and group velocities, respectively.

Comparing the polarization of the four common-offset gathers (offsets 87, 97, 107 and 117 ft) by fixing the source and receiver depth, respectively, we find the anomaly only happens when the source is below 4300 ft and the receiver is above 4442 ft. This indicates that it is not caused by

---

either the source or receiver, but is related to some formation properties not explained by open-hole logs. Out of plane vertical gas-filled fractures can be one possibility.

#### **4.4.2 Modeling study of Single Well Data**

To aid the data analysis, modeling study using a 2-D variable-grid finite-difference parallel code was performed. Figure 4-55a shows the layered model with formation properties from the logs (Figure 4-55b). The water-filled borehole is blocked at 5282 ft. A horizontal direction dipole source is used to excite the model. A small rectangular steel box is placed around the source to represent the tool. A variable grid mesh, which efficiently handles the small tool and the borehole in a large model, is used for the modeling. Simulations performed are based on the field survey: four receivers per shot are placed at offset 87, 97, 107 and 117 ft; the source depth ranges from 4245 to 4900 ft at 5 ft intervals.

Figure 4-56 shows the vertical component of the synthetic common offset gather of channel 1 (Fig. 4-56a) and the blocked fast  $V_s$  log (Figure 4-56b). We can see tube-waves dominate the wavefield though S-waves are visible in some traces. Direct tube-waves (1), up-going and down-going C/M interface reflections (2u and 2d), and well plug reflections (4) observed in the synthetic seismogram confirm the identified events in the field data. The multiple reflections between the tool and C/M interface (3d) observed in the field data is too weak to be seen in the synthetic seismogram since the impedance contrast for the C/M interface in the modeling is not as big as that in the field data.

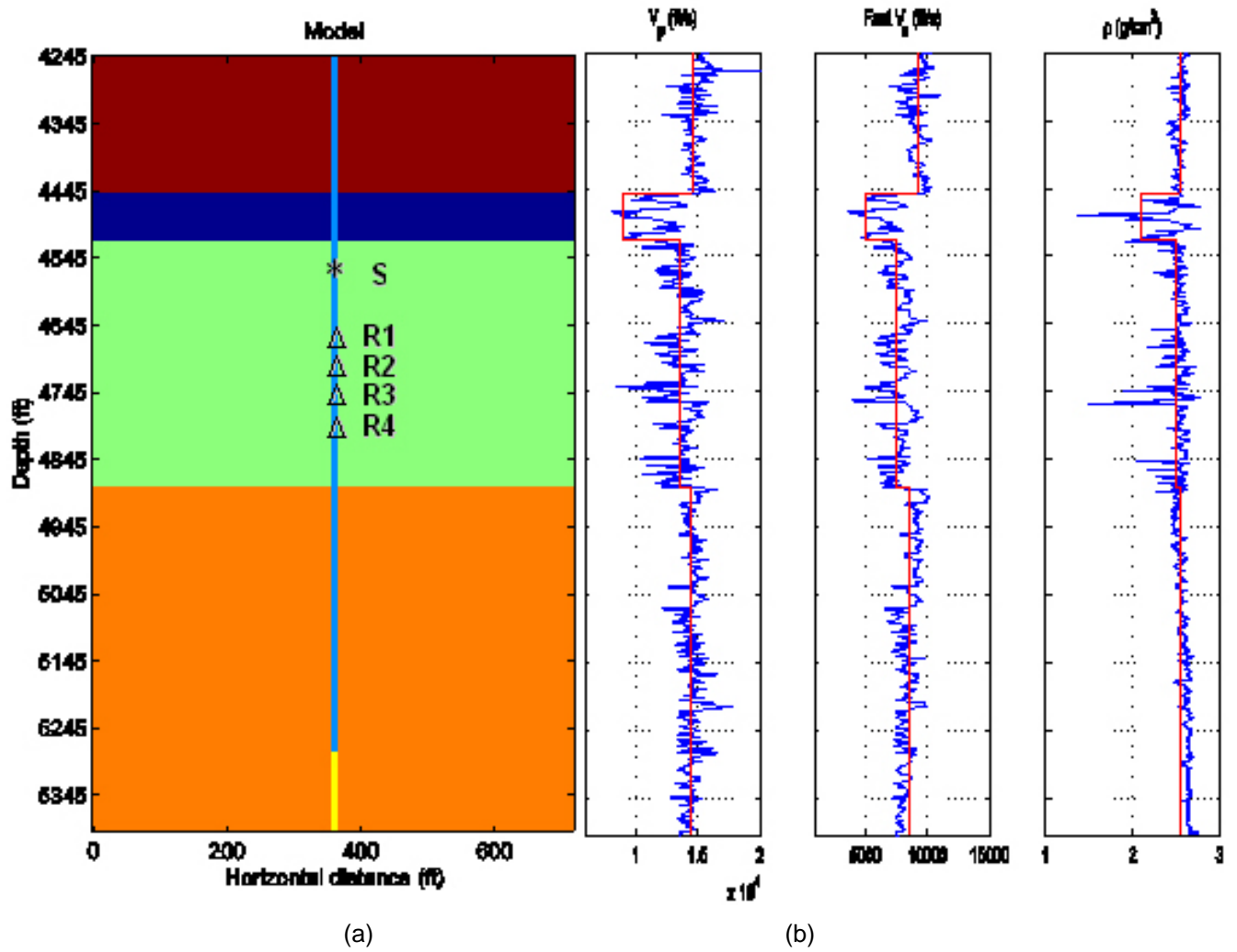


Figure 4-55. (a) Model; (b) Blocked logs.

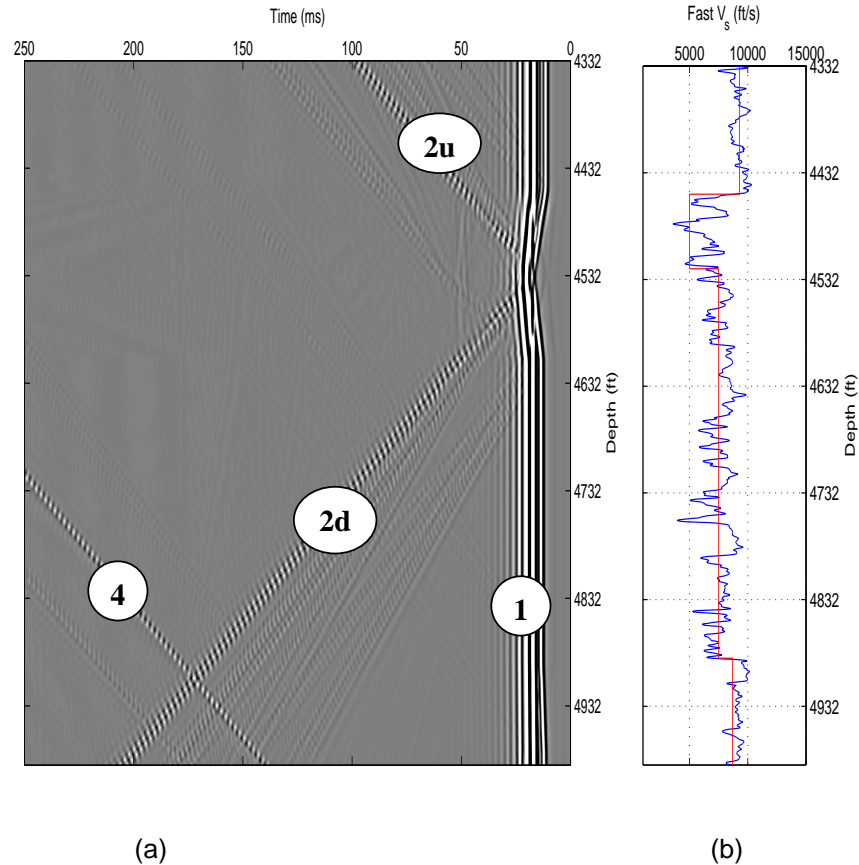


Figure 4-56. (a) Synthetic common-shot gather (vertical component of channel1): marked events are the same as those in the field data (Figure 4-49(a)); (b) Blocked fast  $V_s$  log.

We have conducted single-well acquisition, data analysis and modeling. The data analysis demonstrates that the consistently observable events in the field data are tube-waves. Except an anomalous zone with the low velocity and high amplitude, the direct, reflected and multiple tube-waves can be explained by the formation properties from logs and the survey geometry. Numerical modeling confirms our data analysis.

#### 4.5 WELL LOG ANALYSIS

The following measurements were made during the logging program:

- Acoustic
  - o monopole compressional and shear waveforms
  - o cross-dipole shear waveforms
  - o Stoneley waveforms
- Four-arm caliper
- Gamma-ray
- Resistivity
- Neutron density
- Formation Micro-Imager (FMI)

The raw measurement logs were processed and interpreted to provide petrophysical and lithology logs using Schlumberger’s ELAN software. These lithology logs act as input to the geostatistical work being performed by Virginia Tech for this study.

The FMI images were interpreted to identify natural and drilling induced fractures and were in turn integrated with 4-arm caliper datasets to provide logs of borehole ovality and breakouts. These interpretations in turn indicated the in-situ stress directions. Finally, this information was integrated with the results of acoustic cross-dipole logs processed for anisotropic parameters to provide a characterization of fractures from the sub-millimeter to meter scale.

These individual steps are discussed in the sections below.

#### 4.5.1 Lithology Analysis

Dual Water formation analysis was performed to provide lithology, fluid saturation and estimated production over the entire logged interval. The parameters used for analysis of the Cliff House, Menefee and Point Lookout formations are given in tables 1-3. The permeability and production estimates are based on the San Juan Basin model, developed by Stan Denoo, Product Development Petrophysicist, Schlumberger US Land West, Denver, Colorado.

Table 1. Formation Evaluation Parameters

Formation	Depth (ft)	GRF (api)	GRB (api)	PhiMax (pu)	RWF (ohm)	RWB (ohm)	Model	Vsh	m
Cliff House	4460	30	130	0.21	0.135	0.160	SsLsSh	Gr	2
Menefee	4650	30	130	0.21	0.132	0.167	SsLsSh	Gr	2
Point Lookout	5070	30	130	0.21	0.124	0.150	SsLsSh	Gr	2

**Where** GRF= Gamma Ray Clean (Sandstone or Limestone)

GRB= Gamma Ray Shale

Phi Max= Maximum Porosity (For washed out hole effects)

RWF = connate water resistivity

RWB = shale resistivity

Model = lithology to solve for

Vsh = log for shale volume estimation

m = Archie cementation exponent

Table 2. Permeability Model Parameters  $K^{1/2} = C * \phi_{ie}^4 * ((\phi_{it} - BVI) / BVI)^2$

Formation	Depth (ft)	Model	BVI	PreMultiplier C
Cliff House	4460	San Juan	0.045	30
Menefee	4650	San Juan	0.045	30
Point Lookout	5070	San Juan	0.045	30

Table 3. Production Rate Prediction Parameters (assumes skin=-3 at 168 hours)

Where  $\phi_{ie}$  = effective porosity

$\phi_{it}$  = total porosity

BVI = Bulk Volume Irreducible

Formation	Depth (ft)	Model	Pressure Gradient (psi/ft)	Viscosity (cp)	Temperature (deg F)
Cliff House	4460	San Juan	0.45	0.0138	74
Menefee	4650	San Juan	0.45	0.0138	74
Point Lookout	5070	San Juan	0.45	0.0138	74

Tables 4-6 below list the Formation Evaluation Summary results on the Cliff House, Menefee and Point Lookout formations. See Figures 4-57 to 4-59 for the log analysis graphics displays.

Table 4. Cliff House Formation

Zones (ft)	Ave Porosity (Pu)	Sw Range (%)	Ave. Perm (mD)	Est Production (mcf/day)
4344-4364'	10	40-70	0.042	133 Gas
4378-4387'	9	62-68	0.006	7 Gas
4416-4424'	8	68-75	0.001	3 Gas
4426-4430'	10	37-79	0.023	11 Gas
4439-4445'	8	60-71	0.003	8 Gas

Table 5. Menefee Formation

<b>Zones (ft)</b>	<b>Ave Porosity (Pu)</b>	<b>Sw Range (%)</b>	<b>Ave. Perm (mD)</b>	<b>Est Production (mcf/day)</b>
4472-4480'	8	66-79	0.001	1 Gas
4545-4552'	8	68-71	0.0005	1 Gas
4478-4484'	7	68-75	0.0	0 Gas
4648-4652'	8	80-90	0.0025	2 Gas

Table 6. Point Lookout Formation

<b>Zones (ft)</b>	<b>Ave Porosity (Pu)</b>	<b>Sw Range (%)</b>	<b>Ave. Perm (mD)</b>	<b>Est Production (mcf/day)</b>
4894-4899'	8	28-39	0.0041	4 Gas
4900-4914'	9	24-39	0.0026	9 Gas
4918-4958'	8	25-49	0.0079	56 Gas
4969-4970'	8	26-42	0.0063	13 Gas
4998-5006'	8	30-36	0.0016	4 Gas
5028-5035'	7	36-43	0.0002	1 Gas

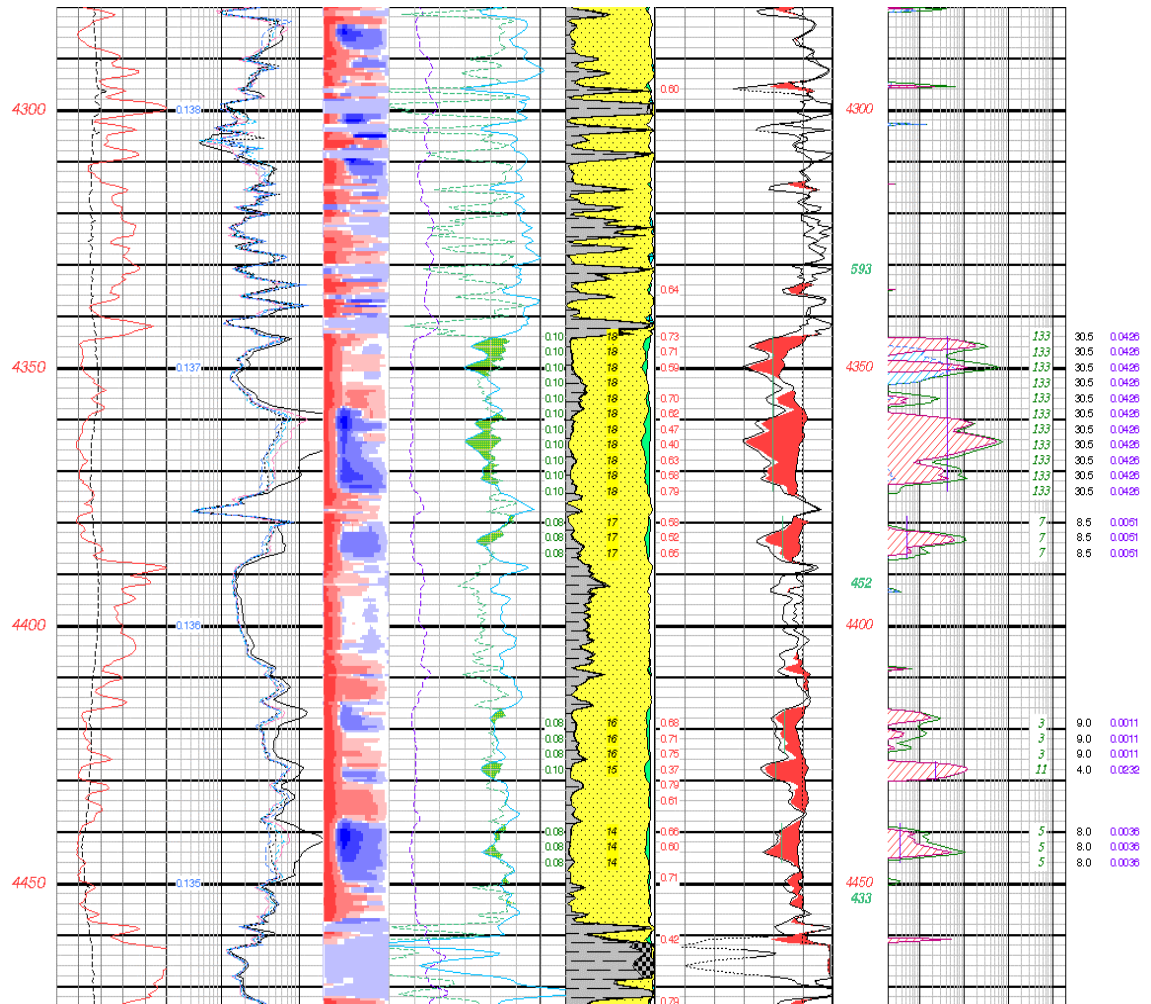
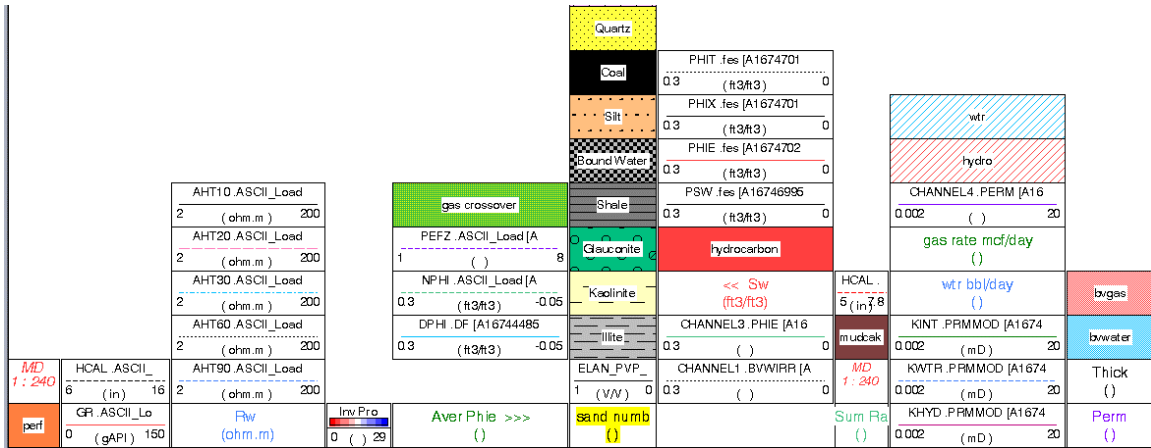


Figure 4-57. Cliff House Formation Evaluation Summary: Track 1, Gamma ray and caliper, Track 2 resistivity arrays and rw value. Track 3, Resistivity Image, Track 4, Density & Neutron Porosity and PEF. Track 5 Lithology and hydrocarbon volumes. Track 6 Relative Permeability and estimated production, Track 7 thickness and average permeability

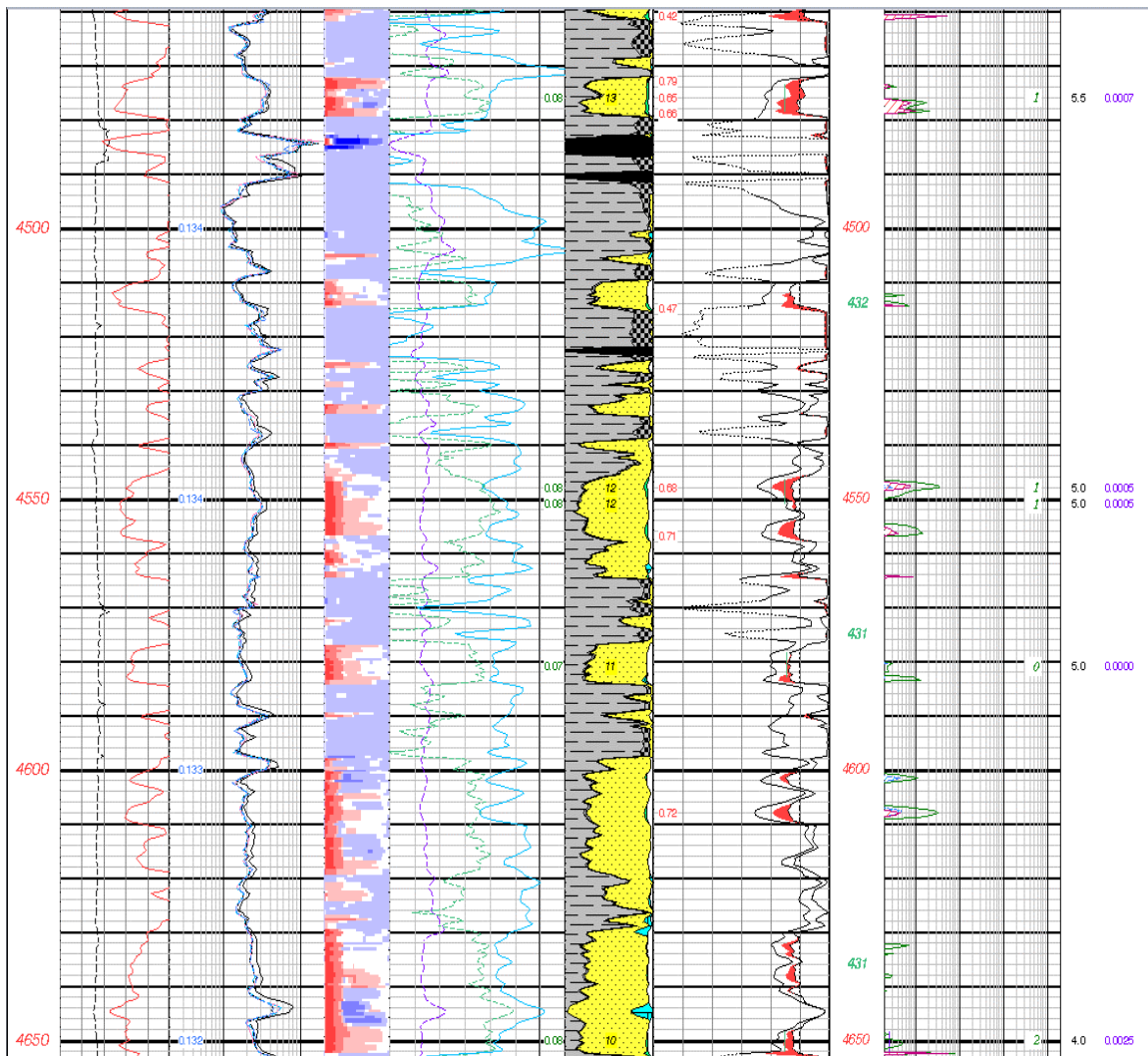
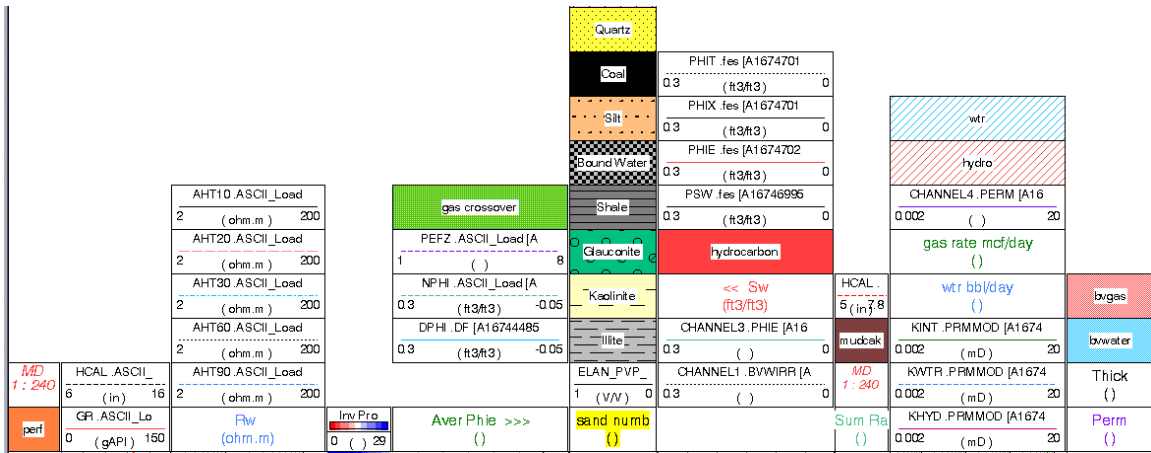


Figure 4-58. Menafee Formation Evaluation Summary: Track 1, Gamma ray and caliper, Track 2 resistivity arrays and rw value. Track 3 Resistivity Image, Track 4, Density & Neutron Porosity and PEF. Track 5 Lithology and hydrocarbon volumes. Track 6 Relative Permeability and estimated production, Track 7 thickness and average permeability

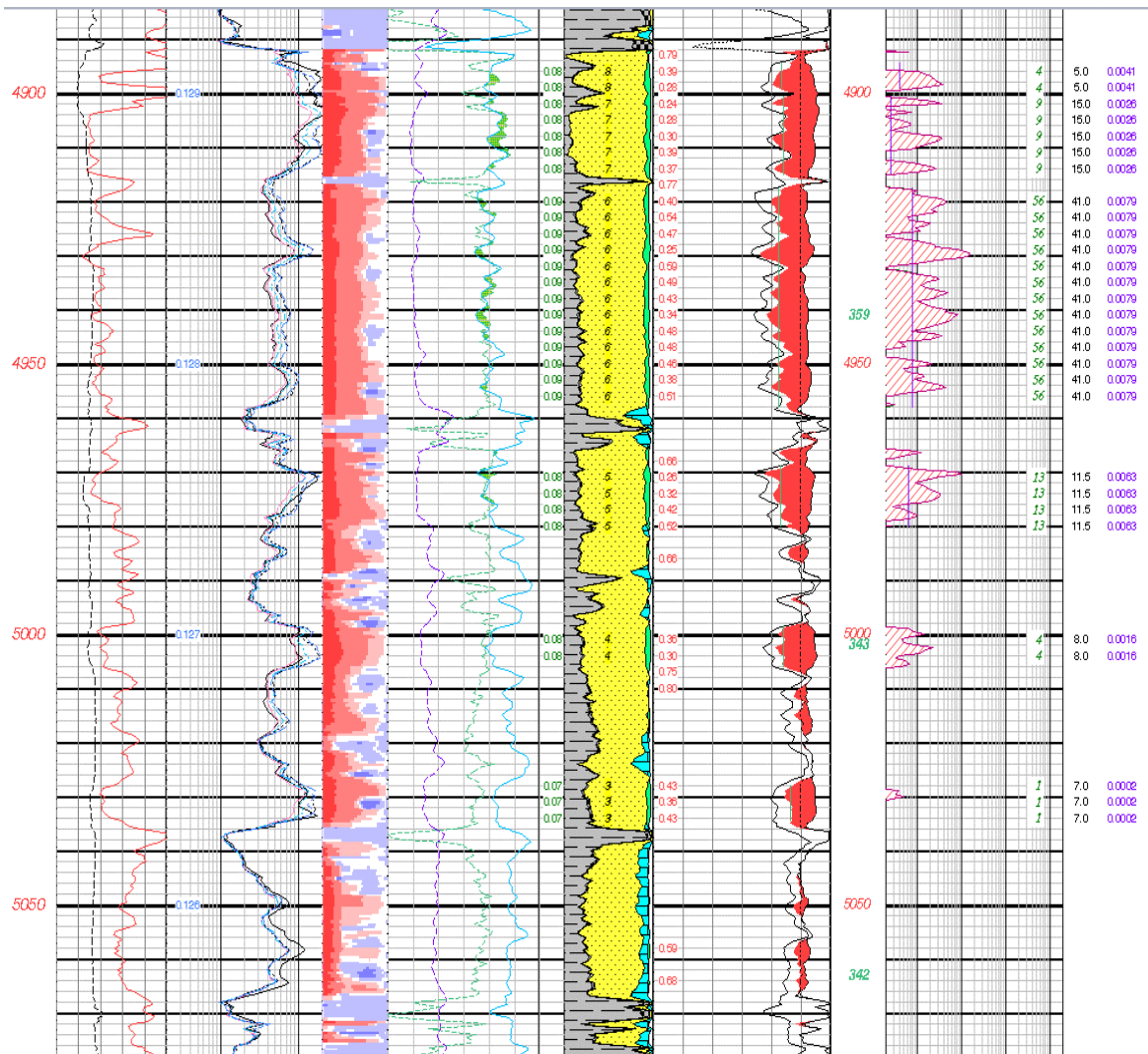
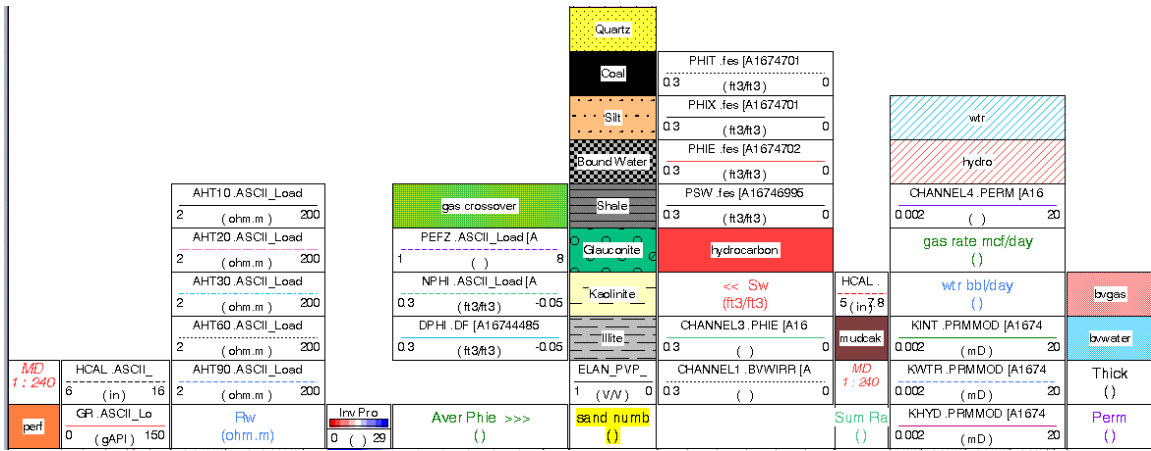


Figure 4-59. Point Lookout Formation Evaluation: Track 1, Gamma ray and caliper, Track 2 resistivity arrays and  $r_w$  value. Track 3 Resistivity Image, Track 4, Density & Neutron Porosity and PEF. Track 5 Lithology and hydrocarbon volumes. Track 6 Relative Permeability and estimated production, Track 7 thickness and average permeability

## 4.5.2 Geology & Geomechanics Analysis

A number of measurements are available to give us information about the fine scale geology, fractures, stress directions and borehole damage. The Formation Micro-Imager (FMI) logs provide the highest resolution (0.2 inch) images of the borehole wall. They are formed using an electromagnetic measurement and provide micro-resistivity images of approximately 80% of the borehole wall circumference. Under ideal conditions bedding planes and open, closed and mineralized fractures can be distinguished and interpreted by a geologist or log analyst. Both natural and drilling induced fractures and breakouts are generally visible in FMI images. The Dipole Sonic Imager (DSI) logs provide two types of information. Run in cross-dipole mode the DSI provides information about anisotropy in a zone of a few feet around the borehole including anisotropy caused by aligned microcracks. Run in Stoneley mode the DSI provides information about borehole caliper enlargements and open fractures conducive to fluid flow. Finally, a simple caliper log can be used to give ovality and breakout directions reflecting the local stress regime.

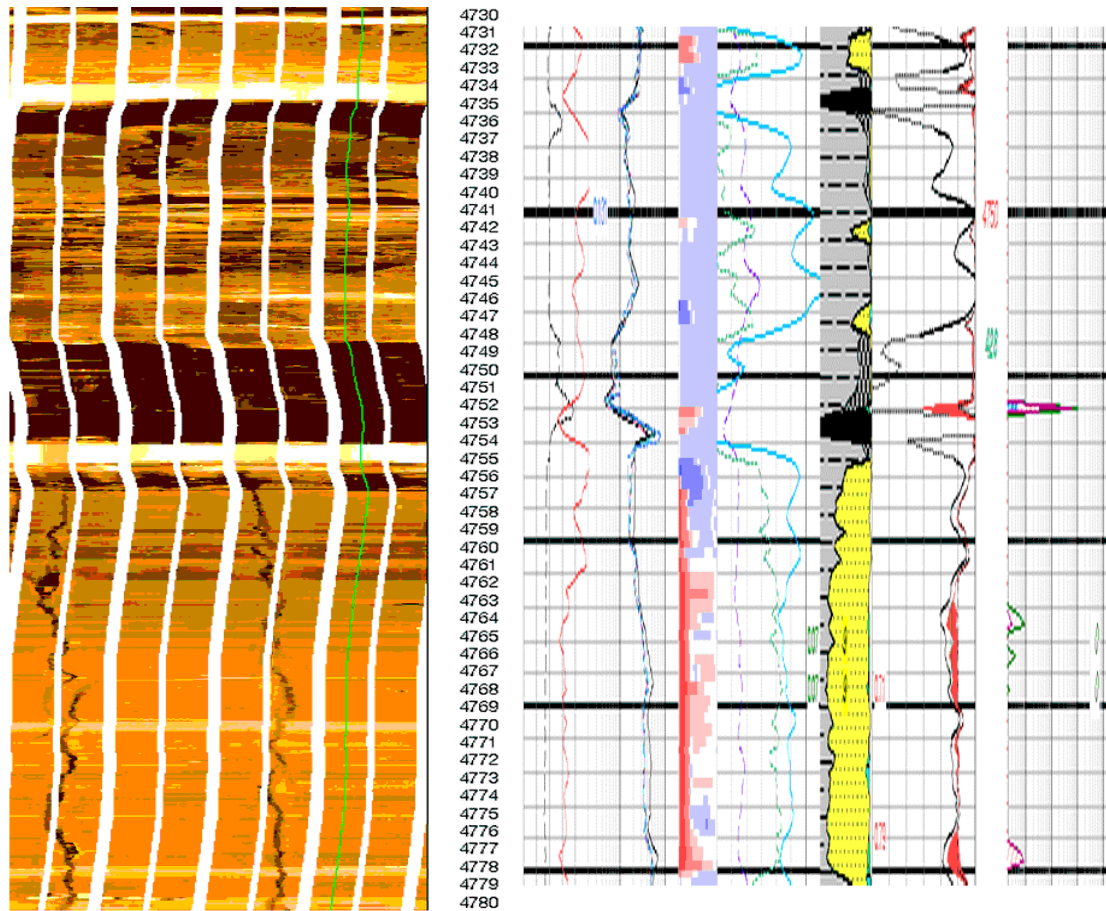


Figure 4-60. Combined FMI and formation evaluation logs for the Newberry well for a segment of the middle Menefee between 4730 and 4780 feet. Bedding is clearly visible on the FMI (left) as lighter (more resistive sands) and darker (less resistive shales and coals). This is reflected in the quartz fraction (yellow) on the lithology log (right). Note the drilling induced fractures running vertically through the in the lower sand.

The two dominant features visible on the FMI logs are bedding planes and drilling induced fractures. Figure 4-60 shows a section of the FMI and formation evaluation logs for the Newberry well in the middle of the Menefee formation. The dominant features of the FMI image are the horizontal bedding that distinguish the quartz rich sands (orange) from the coals and illite rich shales (gray and black). In addition clear vertical fractures are visible in the lower sand between 4756 and 4780 feet. These fractures intersect the borehole over very significant distances, i.e. are essentially vertical. This strongly suggests that they are drilling induced. Their orientation – North-35 degrees -East gives an indication of the maximum stress direction. These drilling induced fractures are present over much of the length of the well. Similar drilling induced fractures are also present in the Moore well with a consistent orientation.

In contrast very few natural fractures could be identified with confidence on the FMI log in the Cliff House, Menefee or Point Lookout formations. A small number of fractures are visible in the Newberry well in the deeper Jurassic (Morrison). One of these fractures, at 7435 feet, is shown in figure 4-61.

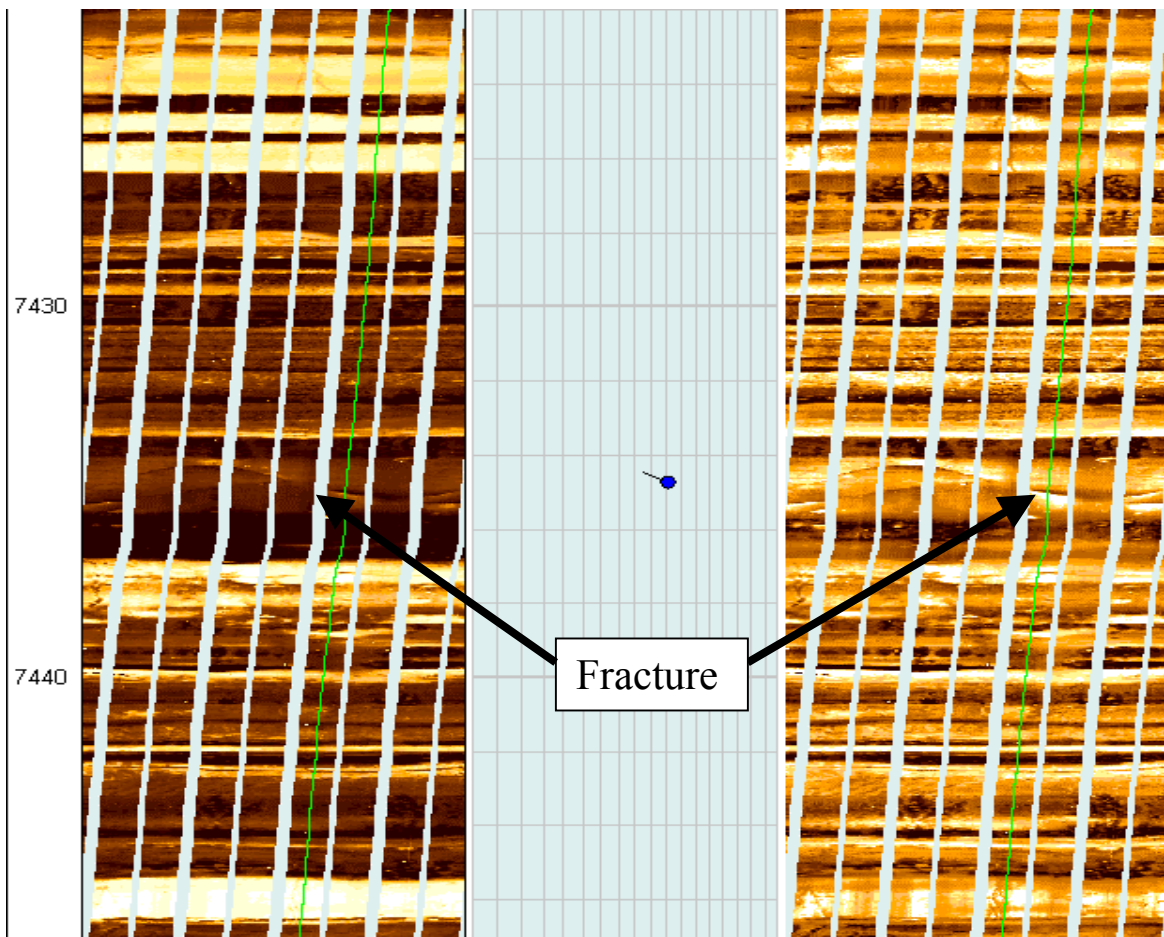


Figure 4-61. An FMI image displayed using static (left) and dynamic scaling (right) of the Dakota sands. An isolated fracture with a dip of approximately 50 degrees and a strike of NNE is visible at 7435 feet as a sinusoid crossing the right image.

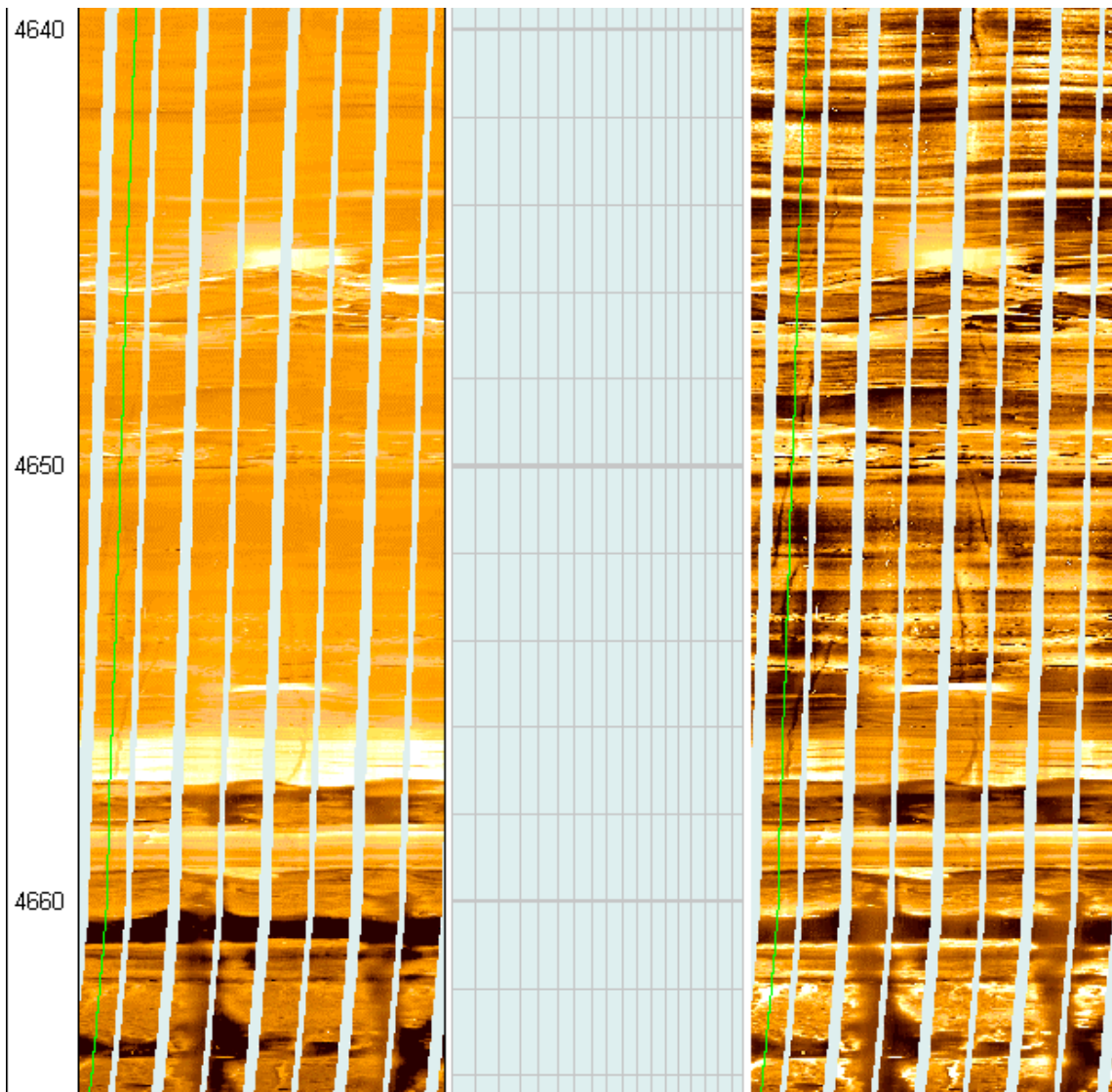


Figure 4-62. An FMI image displayed using static (left) and dynamic scaling (right) of the Menefee sands. Some isolated events, such as the one at 4647 feet may be fractures but are more likely to be depositional features and cross-bedding.

The FMI images of the target sands of interest to this study appear from the logs of both the Newberry and Moore wells to exhibit surprisingly little natural fracturing. In contrast drilling induced fractures are widespread in both wells often extending over tens or hundreds of feet. The orientation of these fractures is consistent with a maximum horizontal stress direction of roughly N35E. The absence of a significant number of fractures intersecting the borehole is consistent with the observation that hydro-fracturing of these formations is a routine procedure to obtain commercial production rates.

The acoustic logs were acquired with the Dipole Sonic Imager™ (DSI). The DSI contains a monopole and two orthogonal dipole sources and the receivers can be configured to record monopole and two orthogonal dipole signals. This allows the tool to record the conventional

---

compressional and shear acoustic velocities using the monopole source and, in addition, flexural waves generated by each of the dipole sources. The monopole source can also be used with a low frequency drive to efficiently generate Stoneley waves.

An example of the processed output from the DSI dipole logs from the middle Menefee is shown in Figure 4-63. A detailed description of each track is included in the caption, however, the key indicators are as follows. The green shaded track at the extreme left is an indication of apparent anisotropy. The left edge of this shaded area should be located close to or at zero if acquisition and processing has been done correctly. A wide shaded band is indicative of apparent anisotropy, however, this may be due to either actual anisotropy or borehole ovality caused by the regional stress field. To distinguish between the two, one must also examine the slownesses of the fast and slow flexural/shear waves shown (red and blue) on the track second from the right. If these slownesses coincide then the apparent anisotropy is likely caused by ovality and not micro-cracks in the formation.

The DSI log exhibits almost no anisotropy above the Cliff House sands. In the Cliff House significant anisotropy is seen with a fast direction oriented North 40 deg East (Figure 4-64). The Menefee, between 4460 and 4900 feet exhibit very little anisotropy (Figure 4-65). This is consistent with the absence of fractures seen on the FMI. The Point Lookout sands between 4900 and 5200 feet again exhibit significant anisotropy with a consistent North 30 deg East orientation (Figure 4-66). Below that, throughout the Mancos shale frequent zones of anisotropy are present with fast directions around North 40 deg East.

The breakout logs (shown in Figures 4-67 through 4-69) show a modest amount of ovalization in the Cliff House with only a single zone of breakout around 4270 ft. This is consistent with the modest amount of anisotropy seen in this zone. In the Menefee breakouts are somewhat more common with a dominant North – 60 deg – West orientation. Since break out occur in the direction of minimal stress this is consistent with a North – 30 deg – East orientation of the maximum stress.

By far the greatest amount of ovalization occurs in the Point Lookout sands. Here breakouts occur over large sections of the formation in an approximately East-West direction. This is consistent with the large amplitude of anisotropy seen in this formation and approximately consistent with the North – 30 deg – East fast direction determined from the cross-dipole anisotropy.

Finally we examine the Stoneley reflection logs. These are shown in Figures 4-70 through 4-72 for the three formations of particular interest. Although all the logs show significant activity on the fracture permeability logs, on closer inspection most if not all of these events are associated with breakouts or lithology changes visible on the FMI and the inference of permeable fractures is most likely an incorrect one caused by an incomplete accounting of breakout and lithology effects in the Stoneley inversion model.

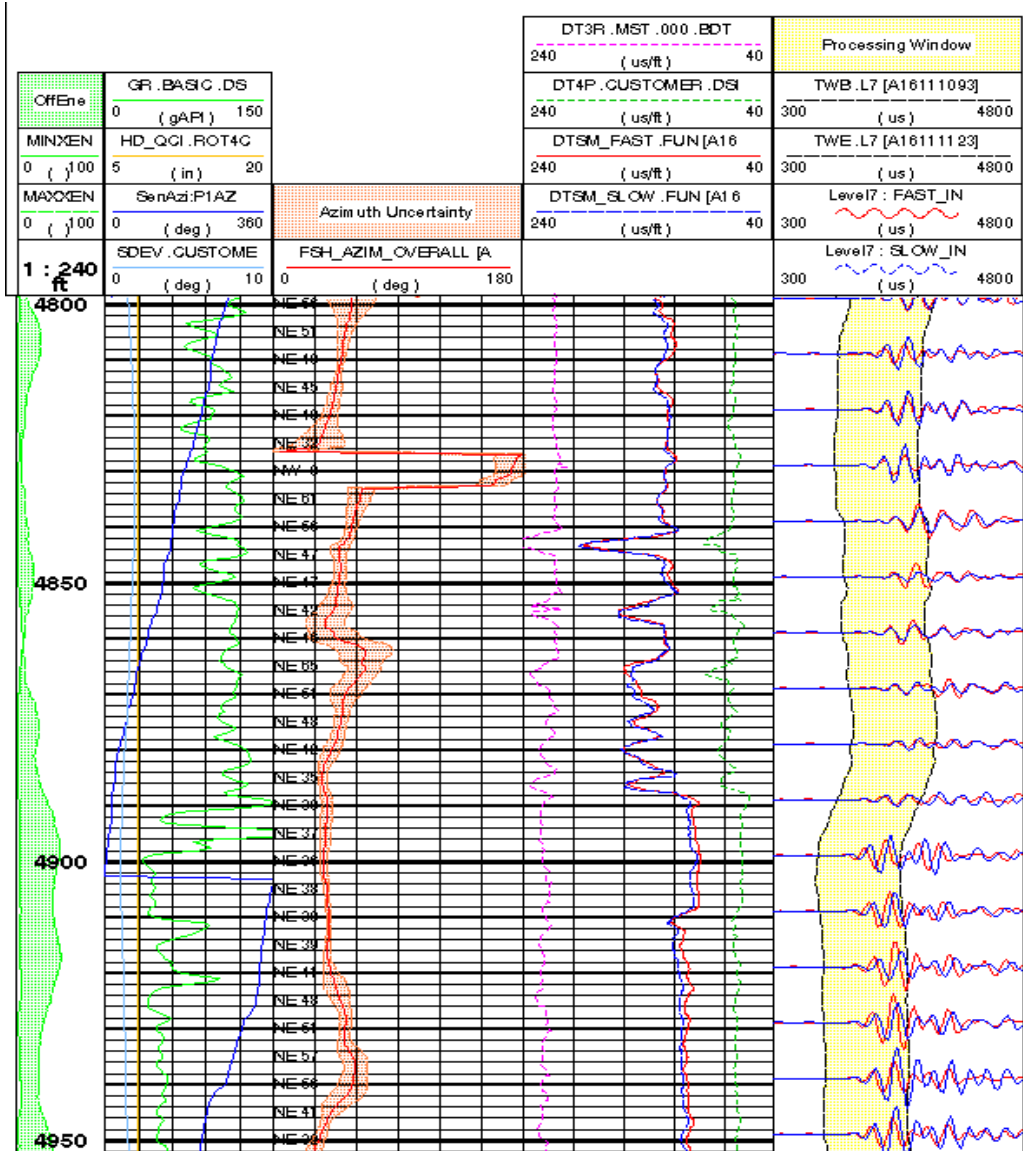


Figure 4-63. A segment of DSI dipole data from the middle Menefee in the Newberry well. The right-most track shows selected waveforms generated as if the dipole source was oriented along the fast axis of the formation anisotropy (red) and slow axis (blue). Above 4900 ft these waveforms overlay well indicating little anisotropy. Between 4900 and 4930 feet there is a significant phase difference indicating the presence of anisotropy. The yellow band indicates the time window used for anisotropy processing. The next track to the right indicates the Stoneley (purple dash), fast and slow flexural (red and blue respectively) and compressional (green dash) slownesses. The center track indicates the azimuth of the fast direction of anisotropy (red line) together with an estimate of its uncertainty (orange shade). The next track to the left shows the gamma ray (green), hole diameter (orange), the azimuthal orientation of the tool (dark blue) and the deviation of the tool from vertical (light blue). Finally the left most track shows the maximum and minimum cross-line energy as the data is rotated. If acquisition and processing has been done correctly the left edge of the green band should always be close to zero. Where no significant apparent anisotropy is present the green band is narrow. Where significant anisotropy is present the green band is wide.

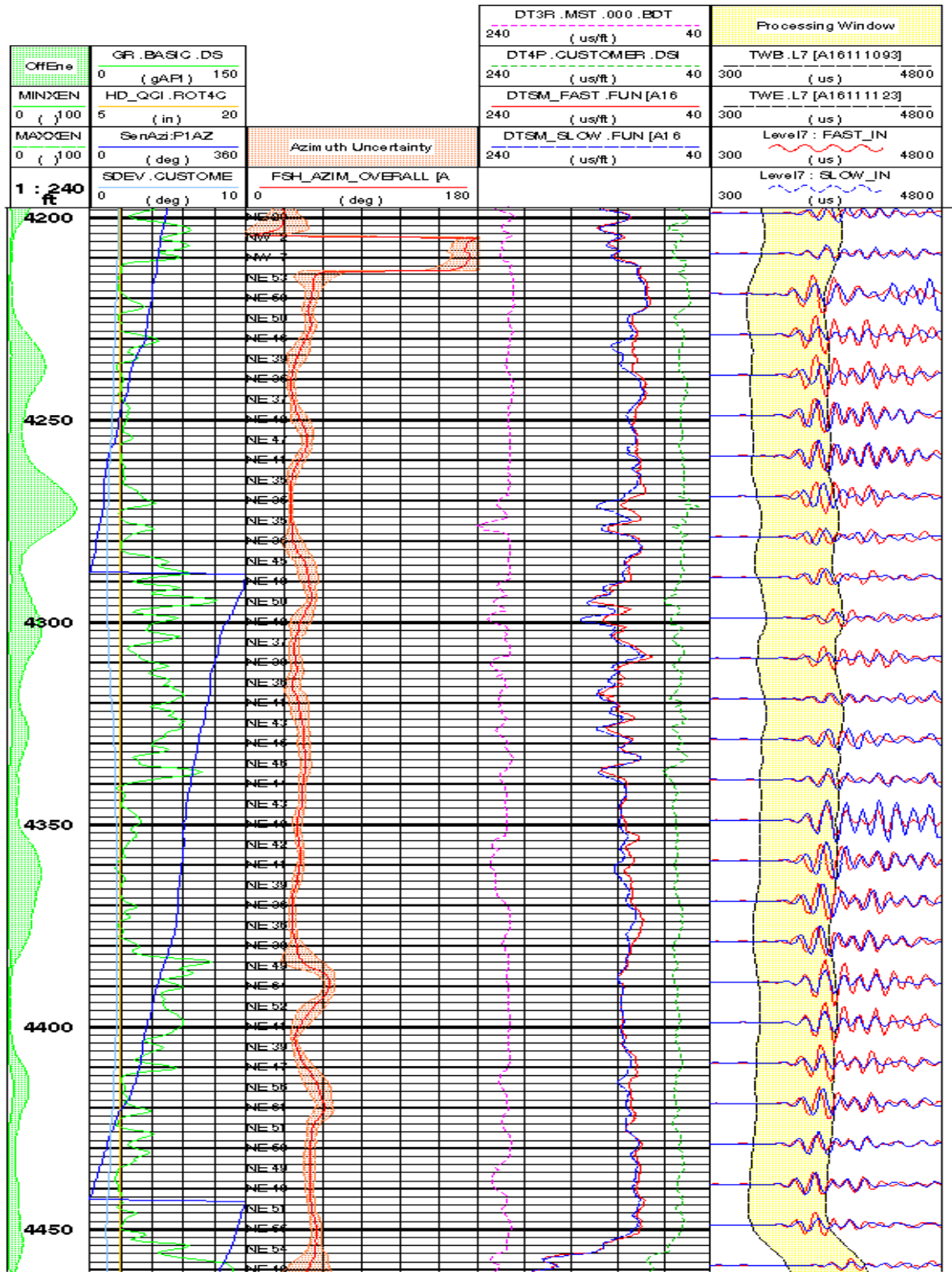


Figure 4-64. The result of the DSI processed for anisotropy over the Cliff House section of the Newberry well. Some anisotropy is present indicating some aligned microcracks are present with a dominant orientation around N40degE.

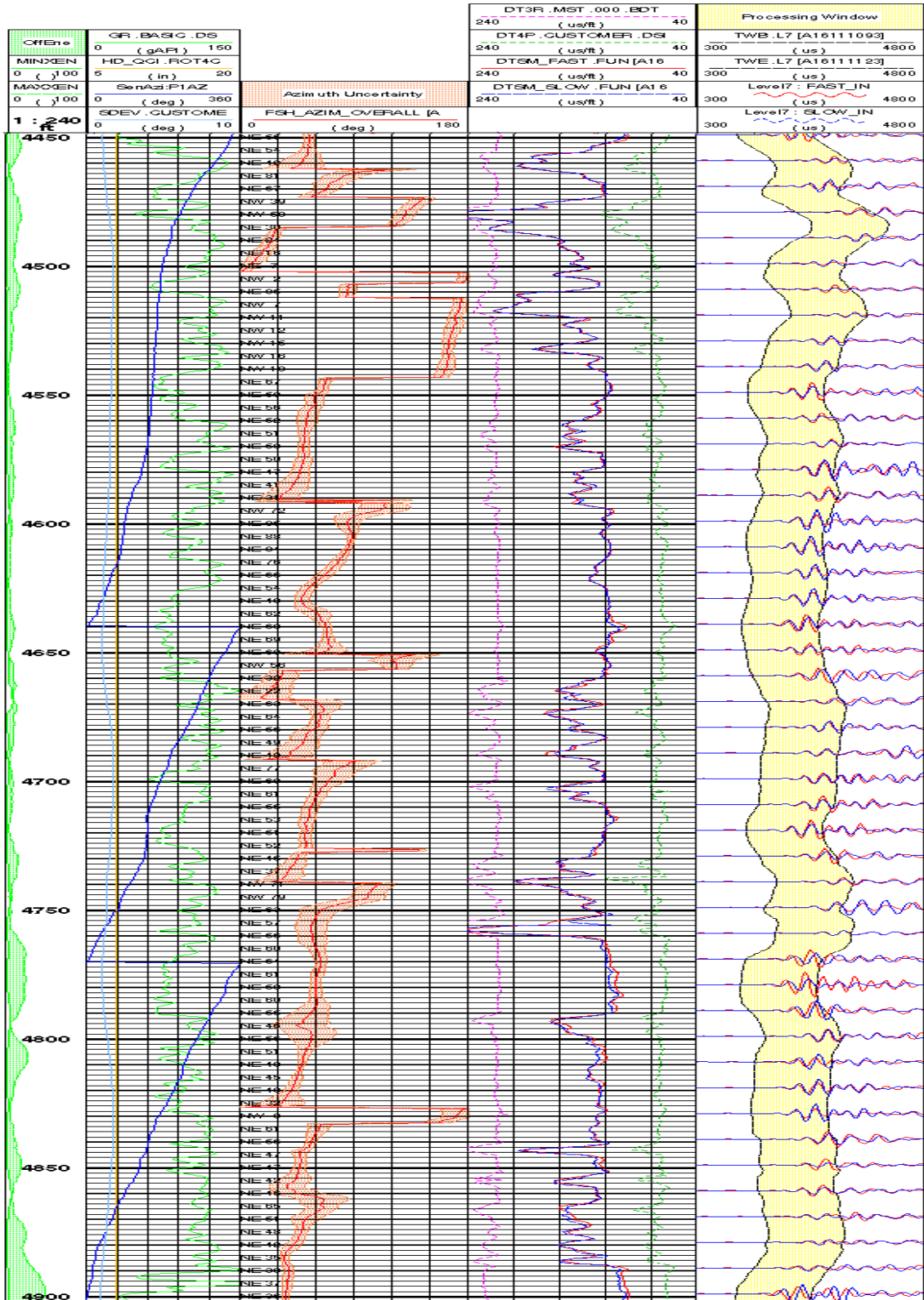


Figure 4-65. The result of the DSI processed for anisotropy over the Menefee section of the Newberry well. Very little anisotropy is present indicating weak or poorly aligned microcracks.

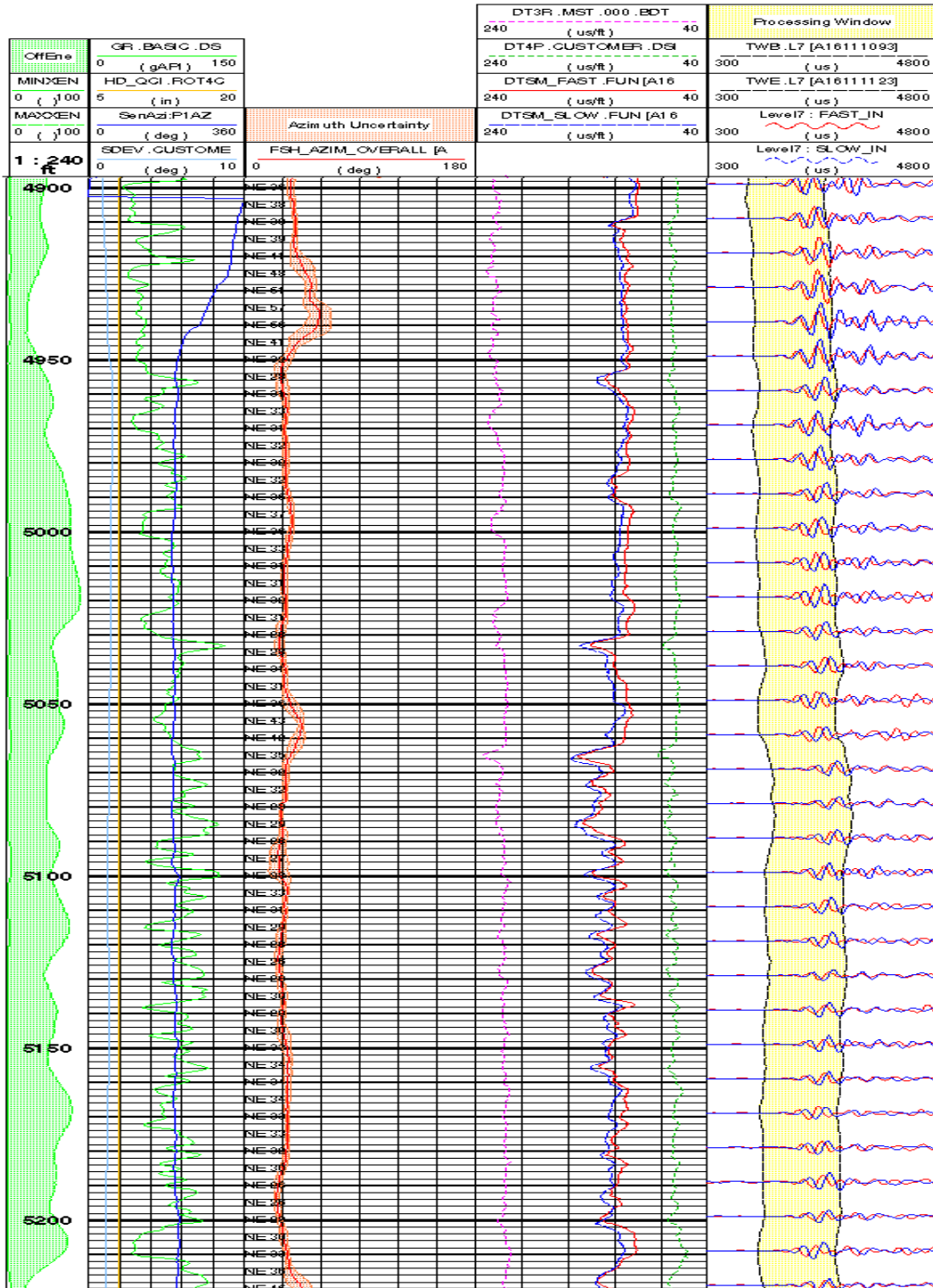


Figure 4-66. The result of the DSI processed for anisotropy over the Point Lookout section of the Newberry well. Significant anisotropy is present with a fast direction around N30degE. This indicating significant well aligned microcracks with a maximum regional stress in the N30degE direction.

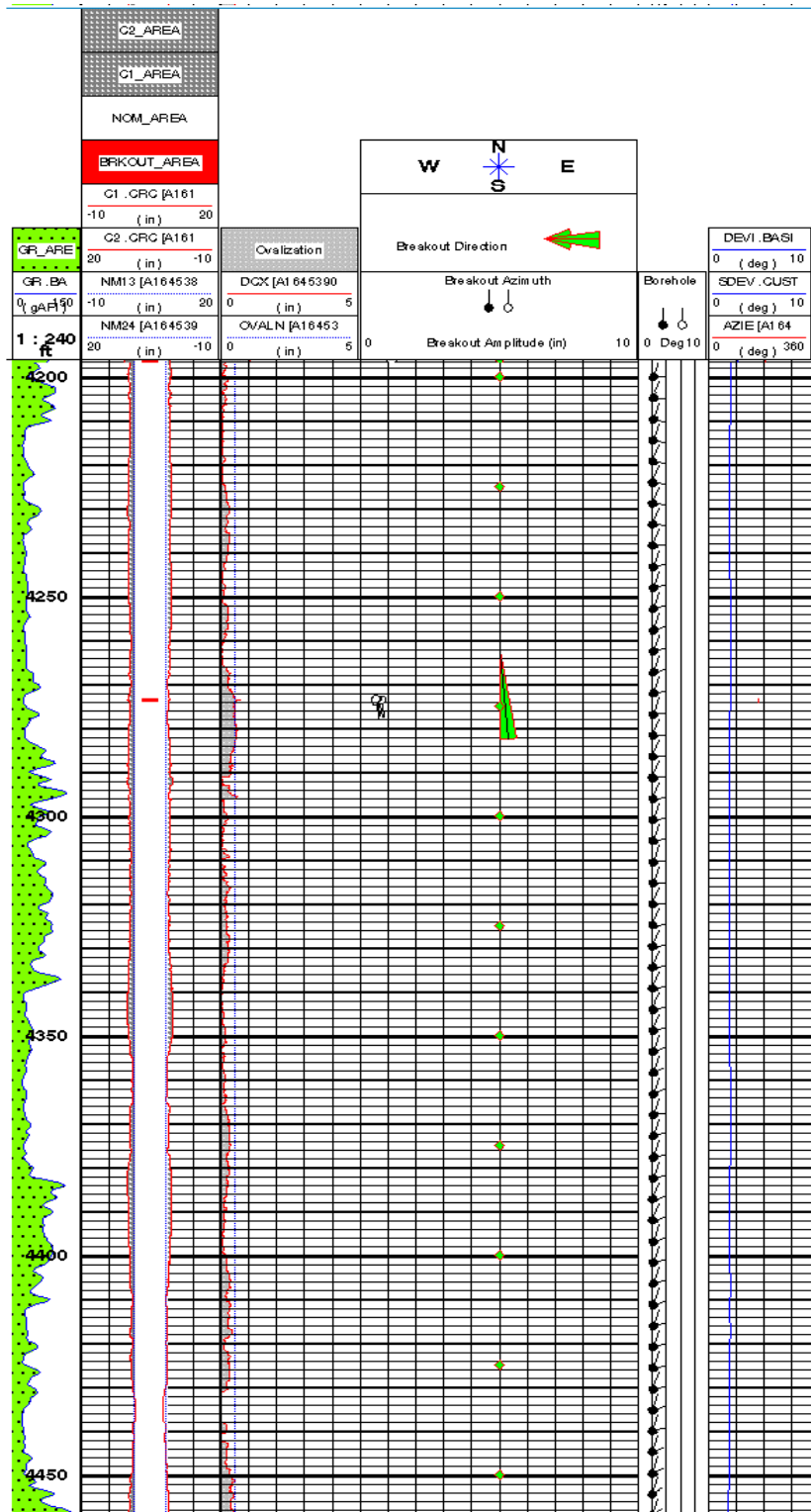


Figure 4-67. Breakout and ovality logs for the Cliff House formation. Track 1 shows the gamma ray. Track 2 shows the two orthogonal caliper measurements together with a red bar where significant breakouts occur. Track 3 shows the borehole ovalization. Track 4 shows individual breakouts in black and summed breakouts over ten foot intervals in green.

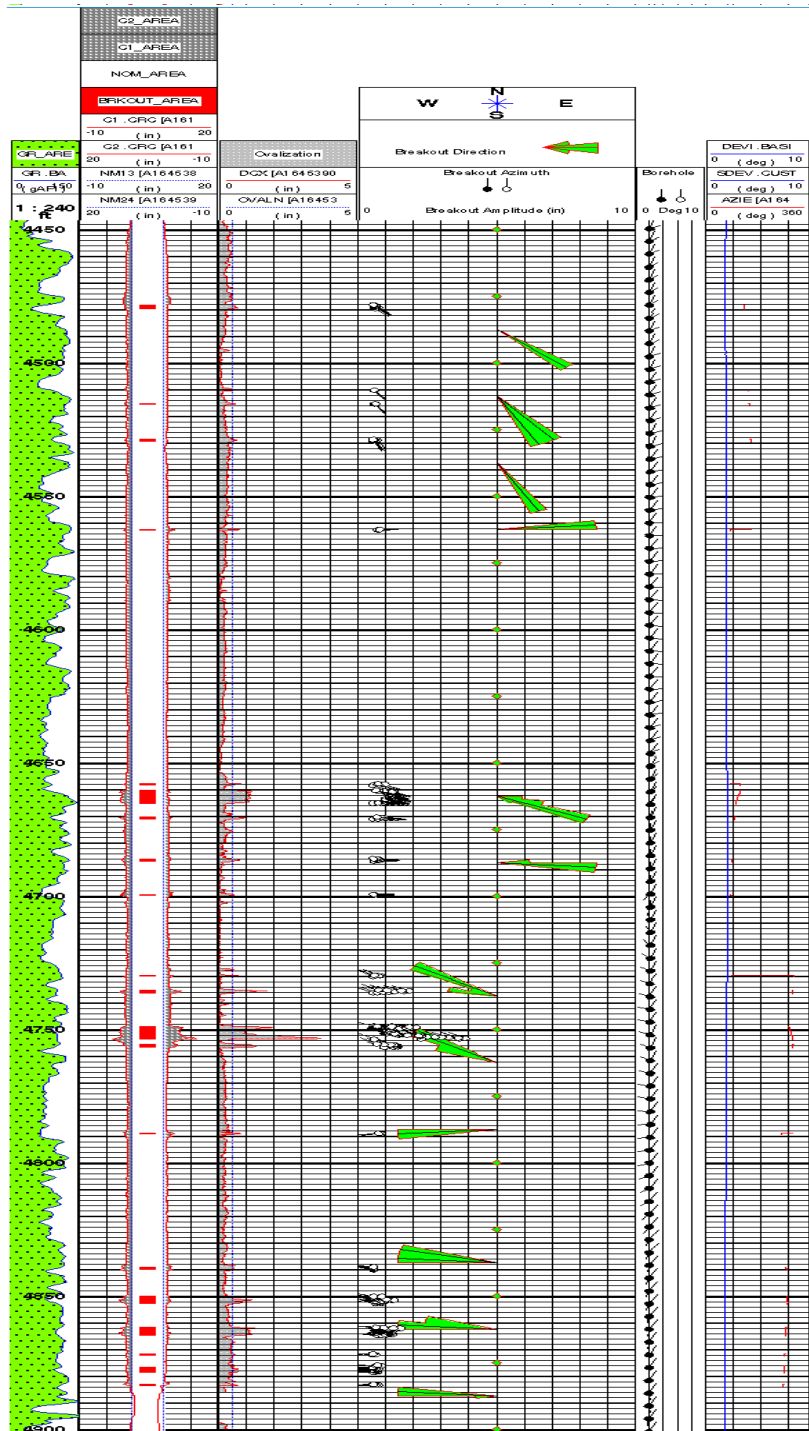


Figure 4-68. Breakout and ovality logs for the Menefee formation. Track 1 shows the gamma ray. Track 2 shows the two orthogonal caliper measurements together with a red bar where significant breakouts occur. Track 3 shows the borehole ovalization. Track 4 shows individual breakouts in black and summed breakouts over ten foot intervals in green.

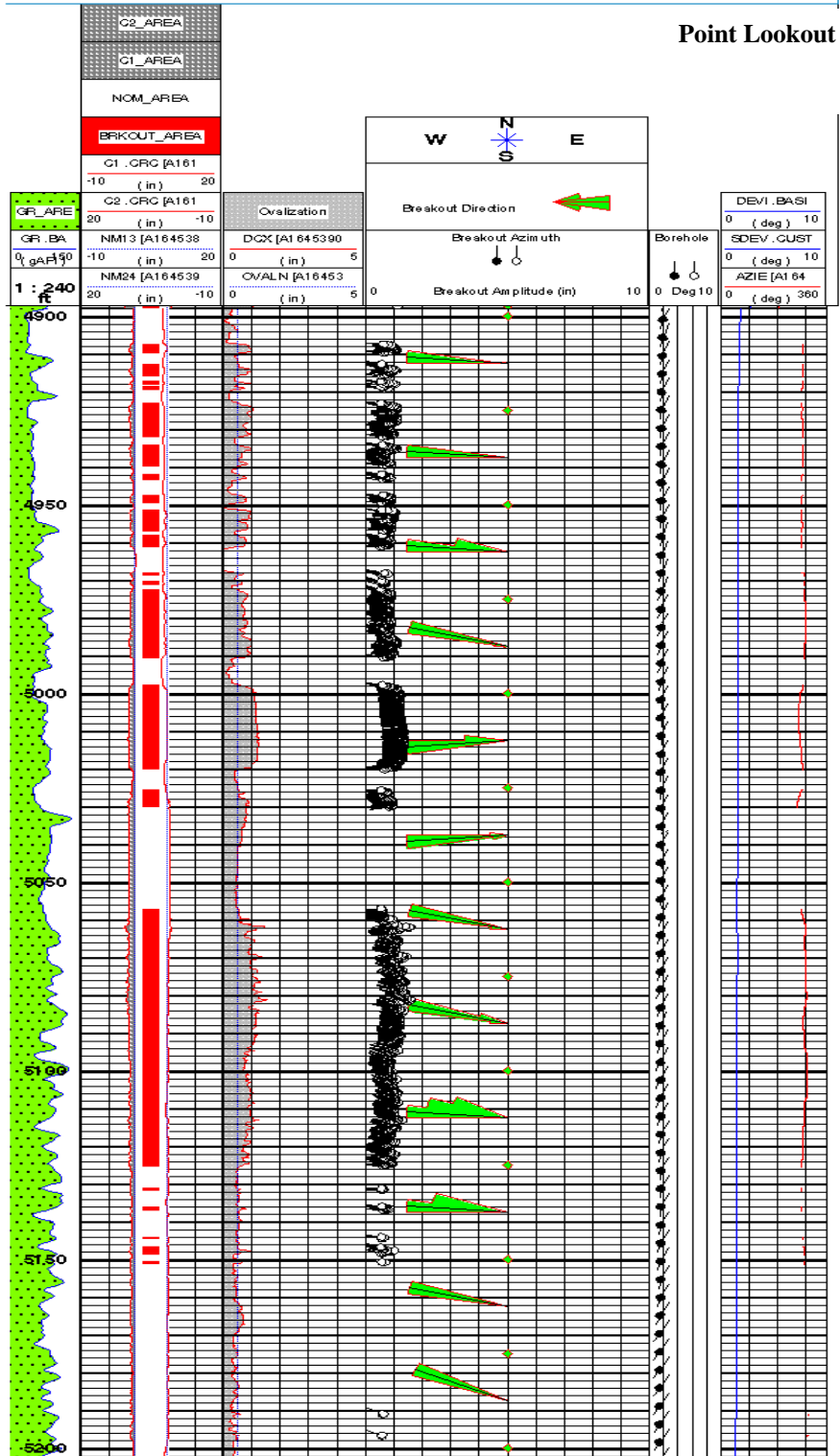


Figure 4-69. Breakout and ovality logs for the Point Lookout formation. Track 1 shows the gamma ray. Track 2 shows the two orthogonal caliper measurements together with a red bar where significant breakouts occur. Track 3 shows the borehole ovalization. Track 4 shows individual breakouts in black and summed breakouts over ten foot intervals in green.

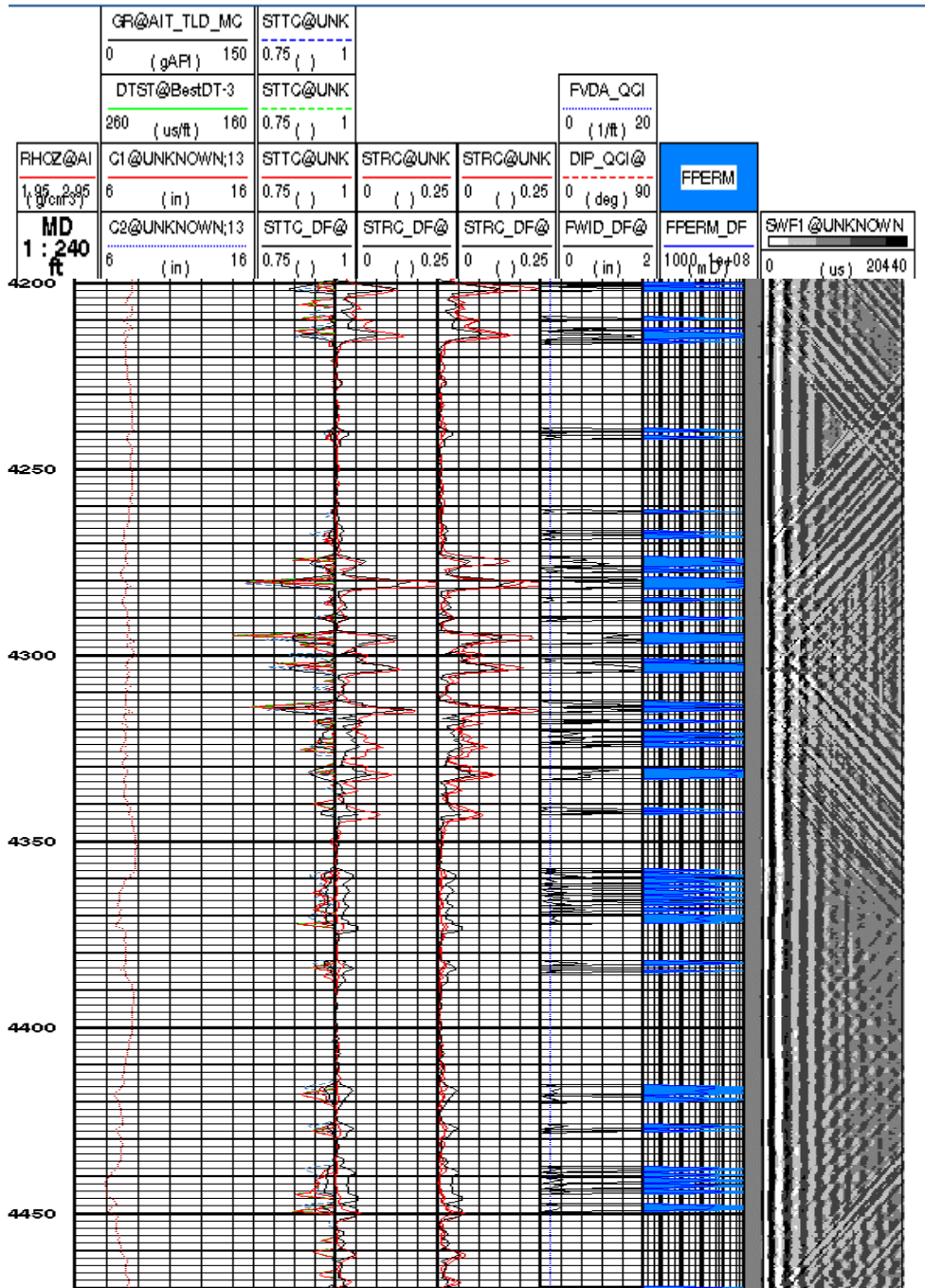


Figure 4-70. Stoneley permeability and fracture aperture logs for the Cliff House formation. Track 1 shows the depth and bulk density. Track 2 shows the gamma ray, Stoneley slowness and two orthogonal caliper measurements. Track 3 shows the up, down and average (red) Stoneley transmission coefficients from the data together with that computed theoretically from the inversion results. Track 4 and 5 show the actual and computed Stoneley reflection coefficients for up and down-going waves respectively. Track 6 shows assumed fracture density, fracture dip and fracture apertures needed for the model. Track 7 shows the computed Stoneley permeability and Track 8 shows the input Stoneley waveforms.

	GR@AIT_TLD_MC 0 (gAPI) 150	STTC@UNK 0.75 ( ) 1						
	DTST@BestDT-3 260 (us/ft) 160	STTC@UNK 0.75 ( ) 1			FVDA_QCI 0 (1/ft) 20			
RHCZ@AI 1.95-2.95 (g/cm <sup>3</sup> )	C1@UNKNOWN;13 6 (in) 16	STTC@UNK 0.75 ( ) 1	STRC@UNK 0 ( ) 0.25	STRC@UNK 0 ( ) 0.25	DIP_QCI@ 0 (deg) 90	FFERM		
<b>MD 1 : 240 ft</b>	C2@UNKNOWN;13 6 (in) 16	STTC_DF@ 0.75 ( ) 1	STRC_DF@ 0 ( ) 0.25	STRC_DF@ 0 ( ) 0.25	FWID_DF@ 0 (in) 2	FFERM_DF 1000 (m) 1008	SWFI@UNKNOWN 0 (us) 20440	

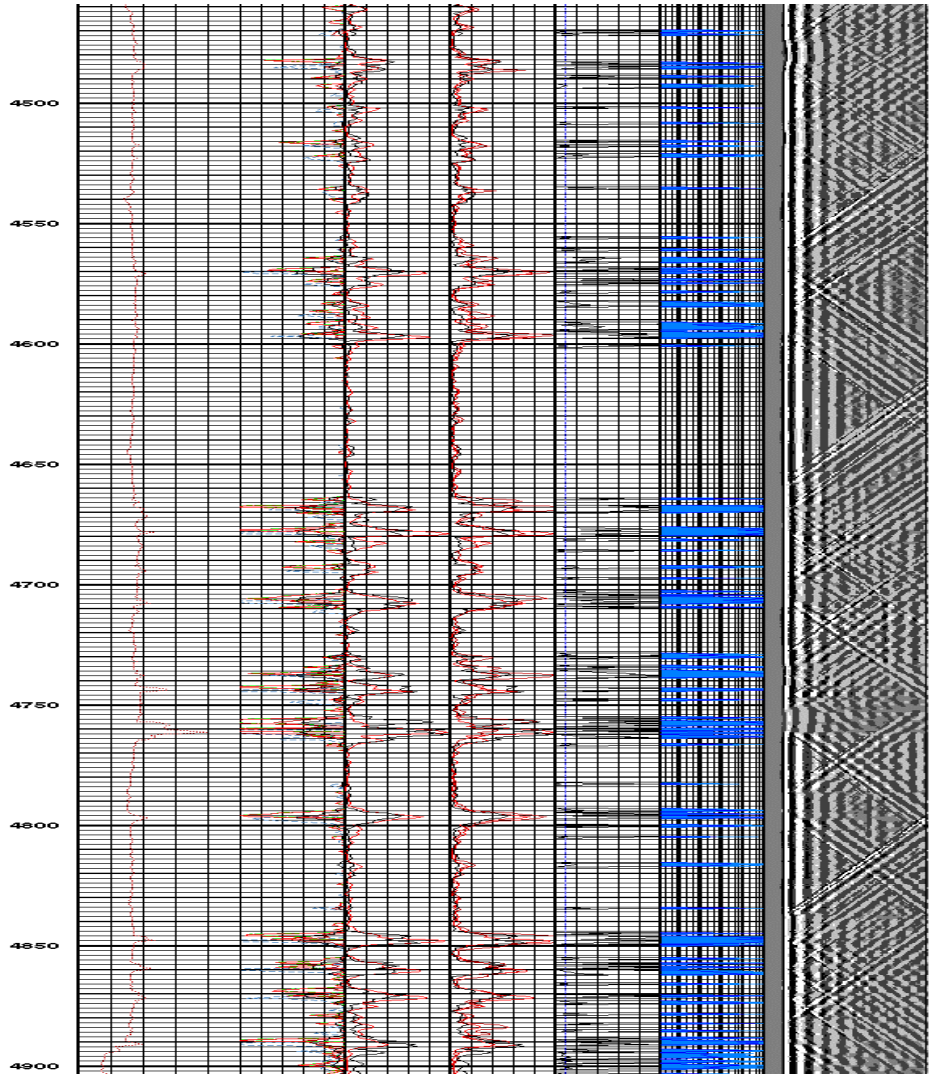


Figure 4-71. Stoneley permeability and fracture aperture logs for the Menefee formation. Track 1 shows the depth and bulk density. Track 2 shows the gamma ray, Stoneley slowness and two orthogonal caliper measurements. Track 3 shows the up, down and average (red) Stoneley transmission coefficients from the data together with that computed theoretically from the inversion results. Track 4 and 5 show the actual and computed Stoneley reflection coefficients for up and down-going waves respectively. Track 6 shows assumed fracture density, fracture dip and fracture apertures needed for the model. Track 7 shows the computed Stoneley permeability and Track 8 shows the input Stoneley waveforms.

	GR@AIT_TLD_MC	STTC@UNK						
	0 (gAPI) 150	0.75 ( ) 1						
	DTST@BestDT-3	STTC@UNK			FVDA_QCI			
	260 (us/ft) 160	0.75 ( ) 1			0 (1/ft) 20			
RHCZ@AI	C1@UNKNOWN;13	STTC@UNK	STRC@UNK	STRC@UNK	DIP_QCI@	FFERM		
1.95 2.95 (g/cm <sup>3</sup> )	6 (in) 16	0.75 ( ) 1	0 ( ) 0.25	0 ( ) 0.25	0 (deg) 90			
<b>MD</b> <b>1 : 240</b> <b>ft</b>	C2@UNKNOWN;13	STTC_DF@	STRC_DF@	STRC_DF@	FWID_DF@	FFERM_DF	SWFI@UNKNOWN	
	6 (in) 16	0.75 ( ) 1	0 ( ) 0.25	0 ( ) 0.25	0 (in) 2	1000 (m) 1e+08	0 (us) 20440	

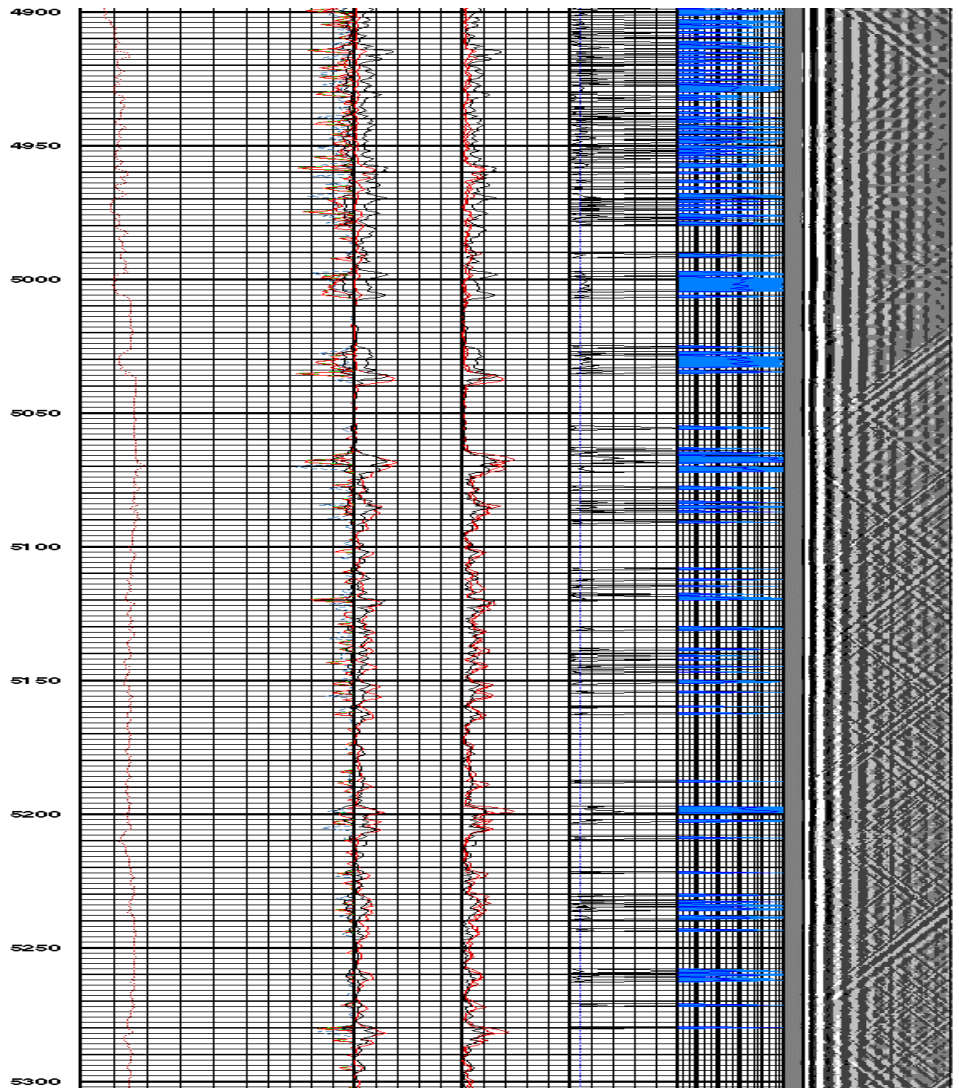


Figure 4-72. Stoneley permeability and fracture aperture logs for the Point Lookout formation. Track 1 shows the depth and bulk density. Track 2 shows the gamma ray, Stoneley slowness and two orthogonal caliper measurements. Track 3 shows the up, down and average (red) Stoneley transmission coefficients from the data together with that computed theoretically from the inversion results. Track 4 and 5 show the actual and computed Stoneley reflection coefficients for up and down-going waves respectively. Track 6 shows assumed fracture density, fracture dip and fracture apertures needed for the model. Track 7 shows the computed Stoneley permeability and Track 8 shows the input Stoneley waveforms.

---

### **4.5.3 Conclusion of well log analysis**

The analysis of the logs run in the Newberry LS #2C and Moore LS #7B wells indicate very little natural fracturing in the Mesaverde formation on a scale visible to the FMI.

Drilling induced fractures are visible over an extensive section of the well including the Mesaverde in an orientation that indicates a dominant stress direction of North-35 degrees-East. The fast direction of anisotropy as determined from the DSI cross-dipole survey confirms this direction and indicates that aligned open micro- fractures are indeed present.

The DSI Stoneley mode indicates a significant number of permeable zones or fractures. However, the high correlation in the location of these zones with lithology changes and/or breakout gives cause to view these permeability results with some skepticism.

---

## 5. MODELING THE EFFECT OF DISCRETE FRACTURES

The ability to model the seismic response of fractures embedded in complex lithologic earth structure and having a wide range of length and aperture scales has been a major road block to quantifying fractures through the use of seismic methods. Such modeling tools are essential in developing insight into the first order fracture response expected from the various seismic acquisition geometries and frequencies available to the geoscientist charged with developing fractured reservoirs. Sophisticated modeling is needed to guide them in selecting the most efficient types of surveys from the many available for the particular fracture problem they expect. Once a survey method is selected, detailed modeling is essential in designing a specific survey that will answer the critical questions facing them. Finally, once data are in hand, modeling is invaluable for interpreting the seismic response for particular fracture quantities affecting the performance of a given reservoir.

To be effective, modeling tools have to satisfy a formidable set of requirements. In order to capture the intricate interaction between seismic waves, fractures, and complex sedimentary structure, both 2-D and full 3-D capability is required. With most seismic surveys covering distances of kilometers, the modeling tools must be capable of extending over similar scales. At the same time, they must be capable of resolving the sub-wavelength features of discrete fractures and their displacement discontinuities on the scale of meters or less. To capture all of the scattering and frequency effects expected from fractures, the modeling must be fully elastic, and ideally, include viscoelastic and poroelastic capabilities. Fractures are known to cover length scales from many meters to microns, and often fractures can be expected below the resolution of any particular seismic method. Additionally, anisotropy due to fine layering and clays is ubiquitous. For these reasons, the modeling must include the capability of modeling the effective elastic anisotropy arising from these two effects. Lastly, the modeling codes must be efficient enough to execute in reasonable times on computers currently available.

While many modeling approaches have been available to model fracture response for a number of years, none have come close to satisfying these stringent requirements. One of the major accomplishments of this project has been the production of a number of codes executing on modern Linux cluster computers which satisfy most of these requirements.

Based on the staggered grid finite difference method, both 2-D and 3-D codes have been written within the framework of the Message Passing Interface (MPI), making them suitable for large cluster computers. They are fully elastic, accounting for discrete fractures with the displacement discontinuity method. They include the capability to model orthonormal anisotropy, accounting for both effective media micro-cracks as well as thin bed anisotropy. Using these codes, models extending over several kilometers have been run with resolutions on the meter scale.

Following a discussion of the displacement discontinuity method, details of the implementation of these codes will be presented. Applications of these codes to the problems of general fracture response, limits of detectability, survey design, and interpretation will then be illustrated.

---

## 5.1 THEORETICAL AND LABORATORY BASIS FOR DISPLACEMENT DISCONTINUITY MODELING

Quite some time ago Kendall and Tabor (1971) recognized that the seismic properties of an *incomplete interface* of zero thickness relative to the wavelength can be described by boundary conditions between two elastic half-spaces in which the seismic stresses are continuous and the displacements are discontinuous

$$\sigma_1 = \sigma_2 \tag{1}$$

$$\mu_2 - \mu_1 = \sigma/K \tag{2}$$

where  $\sigma$  is the stress,  $\mu$  is the particle displacement of the wave,  $K$  is the specific stiffness in units of [Pa/m] which has both normal and shear components, and the subscripts **1** and **2** refer to the elastic media on either sides of the fracture. Collectively, Eq. (1) and (2) are boundary conditions for a non-welded interface which are often referred to as the *slip interface* model (Shoenberg, 1980), the *displacement-discontinuity* model (Pyrak-Nolte et al., 1990a) or the *imperfect interface* model (Rohklin and Wang, 1991). This boundary condition is generalized in the sense that it degenerates to the boundary conditions for a welded interface as the stiffness goes to infinity, and a traction-free interface as it goes to zero. The fracture specific stiffness,  $K$ , depends on the number and distribution of points of contact (i.e., asperities) between the fracture surfaces (Greenwood and Williamson, 1966; Gangi, 1978; Brown and Scholz, 1985, 1986; Hopkins et al., 1987). For example, a fracture with closely spaced asperities will have a higher stiffness than a fracture with a sparse population of asperities.

Shoenberg (1980), Kitsunezaki (1983), and Pyrak-Nolte (1988) derived plane wave transmission and reflection coefficients for P- and S-waves obliquely incident upon a non-welded interface described by Eq. (1) and Eq. (2). Figure 5-1 displays the concept of fracture stiffness interface separating two half-spaces with identical elastic properties. Unlike for a welded interface, the plane wave transmission and reflection coefficients for a displacement-discontinuity interface are functionally dependent on the frequency of the wave. Myer et al. (1985) provided laboratory confirmation of the displacement-discontinuity model by demonstrating that the model matched the low pass filtering characteristics observed in ultrasonic measurements on single artificial fractures of calculable stiffness (Figure 5-2). Pyrak-Nolte et al. (1990a) noted that for causal wave propagation the frequency-dependent transmission properties of a non-welded interface should be accompanied by a frequency-dependent phase delay. They derived frequency-dependent phase and group velocities for a displacement-discontinuity model which satisfy the Kramers-Kronig causality relations (Aid and Richards, 1980) and found that the model predicts an increase in the velocities with frequency (i.e., positive velocity dispersion).

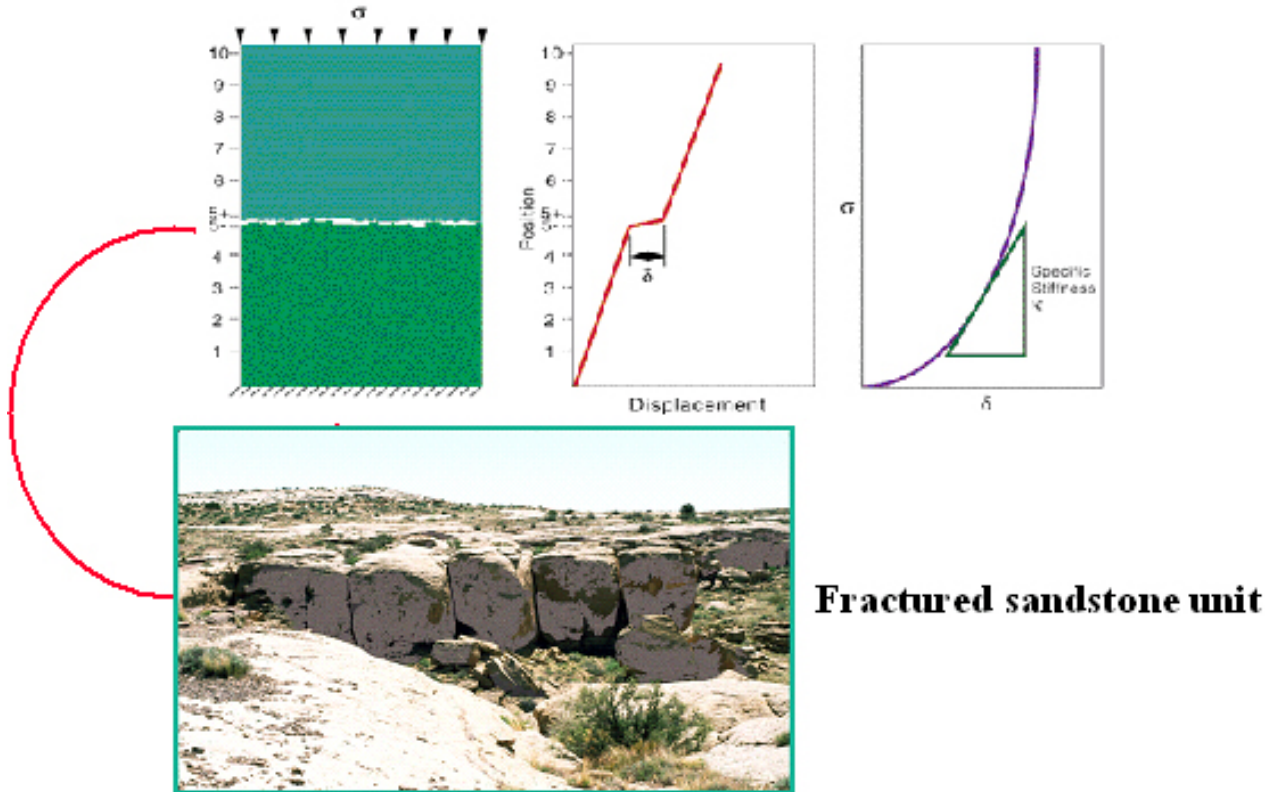


Figure 5-1. Concept of fracture stiffness, the fracture represents a discontinuity in the displacement of the seismic wave across the interface, the more the displacement the less stiff and more attenuative the wave.

Using both measured amplitudes and velocities of P- and S-waves, Pyrak-Nolte (1988, 1990a) was able to directly relate laboratory ultrasonic transmission across a single natural fracture in crystalline rock with the measured mechanical stiffness of the fracture. Both the amplitude and shape of the spectra are well predicted by the displacement-discontinuity model. This work has firmly established the importance and validity of the displacement-discontinuity theory for representing the seismic response of fractures.

Angel and Achenbach (1985) provided a theoretical justification of the displacement-discontinuity model by comparing the reflection and transmission coefficients for the displacement-discontinuity model with the transmission and reflection coefficients for an infinite coplanar array of cracks determined using a dynamic boundary integral equation method. The results for normal angles of incidence demonstrate that the displacement-discontinuity model is capable of accurately modeling the frequency-dependent reflection and transmission coefficients provided that the crack spacing is several times larger than the seismic wavelength. For very short wavelengths, the scattering interaction between the cracks becomes significant and the static specific stiffness that appears in Eq. (2) must be replaced by a frequency-dependent dynamic stiffness (Sotiropoulos, 1990).

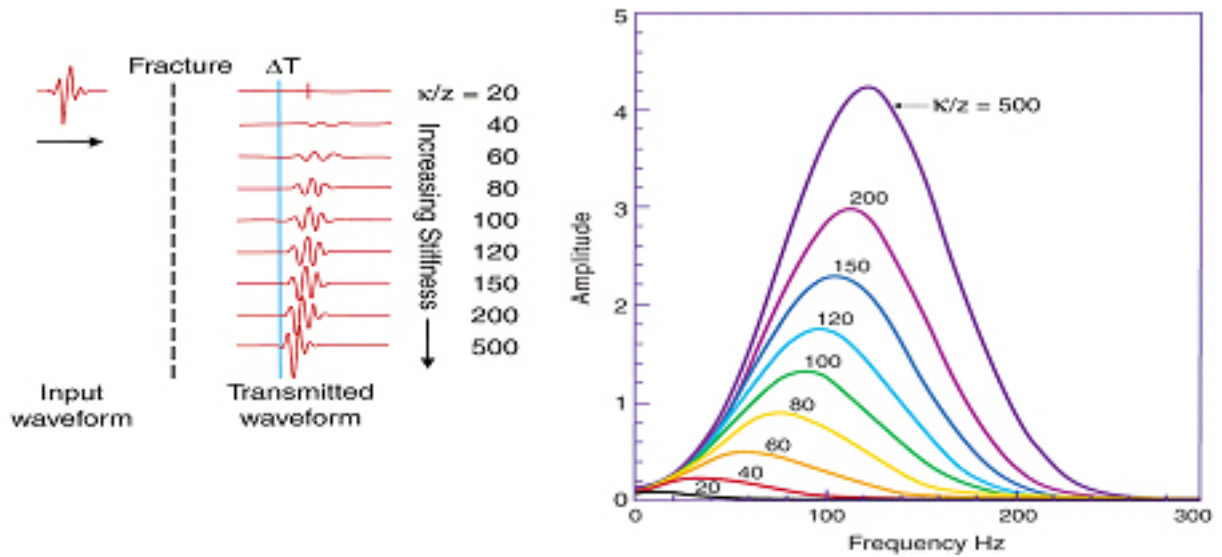


Figure 5-2. Effect of fracture stiffness on the travel time and amplitude of seismic wave as a function of frequency

Extensions of the displacement-discontinuity model have been proposed which include the effects of interface rheology (e.g., Pyrak-Nolte, 1988; Rokhlin and Wang, 1991; Suarez-Rivera, 1992; and others) and anisotropy (Rokhlin and Huang, 1992). If the fracture is filled with a viscous fluid or a thin clay coating, the displacement-discontinuity model described by Eq. (1) and Eq. (2) can be generalized by allowing the stiffness to become a complex quantity. The presence of fluid in a fracture can enhance or attenuate both shear and compressional wave transmission by changing the stiffness of the fracture through adhesional and viscous flow effects. A variety of rheologic models such as the Newton (dashpot), Kelvin-Voight (spring and dashpot in parallel), the Maxwell (spring and dashpot in series), as well as other rheologic models can be modeled explicitly by specifying the appropriate real and imaginary parts of the complex stiffness,  $k = x_i + i \mathbf{K}_i$ . Expressions for the plane wave transmission coefficients for these rheologic models have been derived by Suárez-Rivera (1992) and found to successfully match the measured filtering characteristics observed in S-waves transmitted and reflected from a thin layer of clay saturated with polar and nonpolar fluids.

The displacement-discontinuity model and the various extensions of this model for describing the characteristics of solid state bonds (Nagy and Adler, 1990), adhesive joints and coated and laminated parts (Rokhlin, 1992) have gained widespread acceptance and are currently the subject of many efforts in nondestructive evaluation research. In fact, techniques employing ultrasonic waves have recently been identified as *“the most promising for nondestructive evaluation of imperfect interfaces since they are extremely sensitive to the state of contact on the interface and can be utilized to directly measure interfacial viscoelastic properties”* (Rokhlin, 1992). In the geosciences, however, the displacement-discontinuity model is not widely used in the interpretation of seismic measurements, in part, because of the lack of understanding about the predictions of the model for source-receiver configurations and realistic fracture geometries that are typically encountered in the field. It is likely that two key issues need to be addressed before the model will find widespread use: (1) how does the seismic energy from a source of finite dimension and bandwidth partition between the transmitted, reflected and guided waves for

---

single and multiple fractures and (2) how does spatial heterogeneity in the properties of the fracture modify body waves traveling across the fracture and guided waves traveling along the fracture? Solving these two issues would allow for quantitative interpretation of seismic measurements in fractured rock which are, at present, lacking.

Fractures are not single ones but occur in multiple sets and often occur as nearly parallel groups or sets. A set (or sets) of fractures results in anisotropy in the material properties of the rock mass. Field measurements in fractured rock have been performed by King et al. (1986), Myer and Majer (1984) Majer et al. (1985) and Majer et al. (1997) in jointed rock. In these measurements, transmission perpendicular to the joints resulted in a low pass filtered P-wave which was found to agree with the theoretical predictions of the displacement-discontinuity model for three parallel fractures. Transmission parallel to the joints resulted in very little P-wave attenuation.

Laboratory ultrasonic measurements on synthetic fractures consisting of laminated plates with sand blasted interfaces have been reported by Pyrak-Nolte et al. (1990b) and Hsu and Shoenberg (1990) for P- and S-wave propagation parallel and perpendicular to the fractures. In the study by Hsu and Shoenberg, the wavelengths used were over ten times the thickness of the plates, and the P- and S-wave velocities were reported to show favorable agreement with Shoenberg and Douma's (1988) static effective moduli theory for a series of parallel displacement-discontinuity interfaces.

In the study by Pyrak-Nolte et al. (1990b), velocities and amplitudes for waves traveling perpendicular to the fractures were found to agree well with the theoretical transmission coefficients for a series of parallel displacement-discontinuity interfaces derived under the assumption that there is no multiple scattering between interfaces. However, for an SV-wave propagating parallel to the fractures, they observed a reduction in amplitude and frequency content and which did not agree with the plane wave transmission coefficients for the displacement-discontinuity model. This study concluded that the discrepancy between theory and measurement was most likely caused by the conversion of body waves into interface waves which is not accounted for in the plane wave theory. The theoretical curves for the P-P, SV-SV, and SH-SH plane wave transmission coefficients for 30 parallel fractures (ignoring multiple scattering between fractures) are shown in Figure 1-6 as a function of the angle of incidence. The peaks in the SV-wave transmission coefficients may be in fact the angles of incidence where an SV-wave couples energy into guided waves which travel along the fracture (Nagy et al., 1990).

A pitfall of the plane wave analysis is that it does not provide information about the partitioning of body wave energy into guided waves since these waves are generated by curved wavefronts (Aki and Richards, 1980) which are generated by a source of finite dimensions. This issue of energy partitioning is particularly important in rock with multiple fractures since body waves may generate channel waves which travel in the layer between by two parallel fractures in addition to the (fast and slow) interface waves which travel along the fracture.

Numerical techniques can be used to compute the full wave field for a finite source and arbitrary angles of incidence. Numerical propagator matrix schemes for computing wave propagation in multiple, parallel non-welded interfaces have been proposed by Mal (1988), Shoenberg (1983), Frazer (1990) and Ju and Datta (1992). These schemes provide exact numerical solutions for a

---

point impulse source which include body waves, multiply reflected waves and guided waves. As Frazer points out, the numerical theory in itself does not reveal any of the physics of wave propagation. Rather, insight into the physics of wave propagation in fractured rock can only be developed through numerical simulations. Before this work there was very limited numerical simulations of wave propagation through multiple, parallel fractures modeled as displacement-discontinuity interfaces to investigate the partitioning of seismic energy into body waves and guided waves from an impulsive source of finite size. Such simulations were necessary to provide the range of angles of incidence for which plane wave transmission and coefficients are valid and to generate energy partitioning curves for the various wave types.

The term *guided wave* refers to a class of elastic waves which propagate within thin layers or along interfaces between two media. In many cases, the energy of the guided wave is localized within a zone which may extend only a few wavelengths outside of the interface or layer. As a consequence of this localization of wave energy, geometrical spreading is two dimensional rather than three, allowing these waves to travel extensive distances while suffering very little amplitude reduction. These waves have potential for characterizing the properties of fractures since they primarily sample the elastic and viscoelastic properties of the fracture.

It is becoming recognized that non-welded interfaces, such as fractures, occur frequently in nature and that these features can have a significant effect on propagating waves (Ferrazzini and Aki, 1987; ). Murty (1975) examined the conditions for existence for a non-welded interface with a discontinuity in the shear displacements across the thickness of the interface. Pyrak-Nolte and Cook (1987) extended Murty's analysis to the case where both normal and shear displacements are discontinuous across the thickness of the interface. Non-welded interfaces, such as a fracture, can support a fast (symmetric) wave and a slow (antisymmetric) wave which propagate with phase velocities between the Rayleigh and shear wave velocities and are dispersive. The velocities of the fast and slow interface waves are each dependent on only one fracture stiffnesses and, consequently. Each wave carries separate information about the fracture properties. Nagy and Adler (1989, 1991) describe techniques for exciting and detecting these waves with finite radius P- and S-wave ultrasonic transducers for nondestructive evaluation of bonds and adhesives. Laboratory measurements by Pyrak, Xu, and Haley (1992b) have confirmed the existence of both the fast and slow interface waves in a synthetic fracture in aluminum. Very good agreement was found between the measured and predicted group velocities of the fast and slow interface waves. It should be noted that non-welded interface waves are likely to be more detectable in the field than Stoneley waves because their conditions for existence are less restrictive. For example, the slow interface wave can in principle always exist for many ranges of stiffnesses (Pyrak and Cook, 1987b) even when the elastic properties on either side of the fracture are identical.

In the field of nondestructive evaluation, the displacement-discontinuity model has been used to approximate thin elastic adhesive bonds (e.g., Rokhlin, 1984; Xu and Datta, 1990). In these models, the shear displacements across the thin bond are discontinuous by an amount that is inversely proportional to the shear stiffness of the bond, while the normal displacements are continuous. Interface waves have also been demonstrated to exist on very thin viscoelastic layers (Rokhlin et al., 1981; Murty and Kumar, 1991). Rokhlin et al. have demonstrated theoretically and experimentally that a dispersive guided interface wave can always exist when the shear modulus of the thin viscoelastic layer is lower than the two bounding identical, elastic half-

---

spaces. Using a theoretical expression they demonstrated that it is possible to deduce the complex shear modulus of the viscoelastic layer from measurements of velocity and attenuation of the interface wave for layer thicknesses less than .005 the wavelength of the interface wave. It is likely that the models used in nondestructive testing for describing the interfacial properties of bonds and adhesive joints may not be directly applicable for modeling the properties of fractures in rock. For example, theoretical and experimental work on fractures shows that displacements across the fracture are discontinuous in both the normal and tangential directions (Brown and Scholz, 1986; Yoshioka and Scholz, 1989). If the normal stiffness is discounted, as in the study of Murty and Kumar (1991), only one interface wave exists. Therefore, models which include discontinuities in both the normal and tangential displacement and velocities may prove to be an accurate description of fractures with complex rheology such as thin clay-filled fractures and melange.

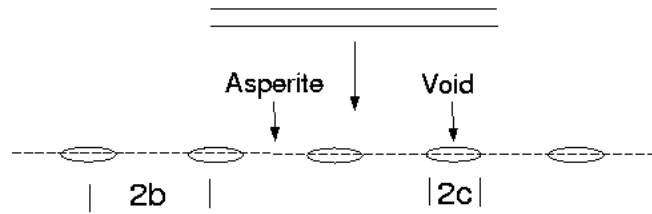
Critical in the development of seismic techniques for imaging fractures is our understanding of the interaction of P- and S-waves with a fracture. If a fracture does not generate a strong scattered wave field, techniques such as diffraction tomography (Wu and Toksöz, 1987; Tura et al., 1992) may suffer from poor resolution. It is therefore imperative to have an understanding of how heterogeneity in the mechanical stiffness and fluid saturation of a fracture influences the magnitudes and frequency characteristics of body waves, interface waves, and scattered waves.

Nihei (1989) performed simulations of seismic wave transmission across a fracture modeled as a displacement-discontinuity interface with spatially varying fracture stiffness using the elastic Kirchhoff method. The variable stiffness fractures were generated by first assigning each point on the fracture a random value of the fracture stiffness chosen from a uniform distribution. Spatial correlation was introduced by filtering the random stiffness fracture with a Gaussian correlation function. Synthetic seismograms were computed for three different correlation lengths. It was found that the i-component of particle displacement shows a small reduction in the amplitude of the transmitted P-wave for the two random stiffness surfaces with  $a=0.2$  and  $0.5$  m, as compared to the constant stiffness ( $a=\text{constant}$ ) surface, and very little scattered energy. If the plot is magnified by 150 times as was done for the y-component of displacement, the scattered waves generated by variations in the specific stiffness become visible. Although the amplitudes of the scattered waves increases as the correlation length decreases and begins to approach the seismic wavelength, they are still very small relative to the amplitude of the direct P-wave and, for this particular example, are likely to be too small to be detectable in the field. However, scattering may be stronger if the magnitude of the variations in specific stiffness is significantly larger than the value used in this simulation (10%). Since the Kirchhoff method is an approximate technique which neglects scattering between different points on the fracture, further analysis of this problem using the boundary integral equation method, which is an exact numerical technique, will provide information.

### **5.1.1 Conceptual Model of Displacement Discontinuity**

Discrete fractures can be characterized by a displacement discontinuity. In turn, displacement discontinuities are fully determined by their shear and compressional specific stiffness. The following example illustrates the physical interpretation of the stiffness parameters in terms of a specific conceptual fracture model. As shown in the figure below, we have a linear arrangement of elliptical voids.

### Field Scale Conceptual Fracture Model



$$\frac{1}{\kappa} = \frac{\bar{\delta}}{\sigma}$$

$$\bar{\delta} = \frac{-8\sigma b(1-\nu^2)[\ln \cos(\pi c/2b)]}{\pi E}$$

For a constant contact area of 30%,  
 $(1 - c/b) = 0.3$

For  $c = 0.25$  m,  $k = 9 \times 10^9$  Pa/m

$\kappa$  = stiffness  
 $\delta$  = extra displacement  
 $\sigma$  = stress  
 $E$  = Young's Modulus  
 $\nu$  = Poisson's Ratio

Figure 5-3. Conceptual fracture model of displacement discontinuity stiffness

These voids have a spacing of  $b$ , and a length of  $c$ . Inspection of the above equations shows that the specific stiffness is determined by three parameters: the elastic constants of the background material (Young's Modulus); the percentage of contact area; and the length  $c$  of the voids. For a fixed length of void, the specific stiffness decreases as the contact area decreases. Correspondingly, for a fixed contact area, the specific stiffness decreases as the voids become larger. Such conceptual models allow for the potential quantification of fractures from specific stiffness parameters interpreted from seismic measurements.

#### 5.1.2 Development of Finite Difference Modeling for Geoscience Application

The finite difference methods are a very attractive approach for modeling the seismic response to complex earth models. They differ from asymptotic methods such as ray tracing in that they incorporate the full wave equation. Because of this, they include such effects as channel and various other guided waves, mode conversions, multiply scattered waves, and waves propagating in shadow zones. One of the earliest applications of these methods to exploration seismic is described by Kelly et al., (1976).

---

A variation of the finite difference method called staggered grid has been developed (Virieux, 1986; Levander, 1988; Robertsson et al., 1994; Igel et al., 1995). The staggered grid method overcomes many of the instabilities associated with high contrasts in Poisson ratio encountered with standard finite difference, and also allows the inclusion of anisotropic elastic constants. Because it solves for velocities on one grid and at one time step and stresses at a staggered time step and on a staggered grid, it is suitable for implementation on large cluster computers. In order to include discrete fractures, Coates and Schoenberg (1995) developed a stable method for including displacement discontinuities in the staggered grid scheme by computing the equivalent anisotropic elastic constants for single grid cells containing displacement discontinuities.

To meet the modeling objectives of this project, both 2-D and 3-D staggered grid finite difference codes were developed. These codes were then adapted to Linux cluster computers by implementing them under MPI. These codes are able to include anisotropic elastic constants, and in the case of the 3-D code, anisotropic symmetries up to orthonormal can be used. This allows the modeling of small scale cracks parallel to the grids, as well as thin bed anisotropy. Discrete cracks can also be included using the Coates and Schoenberg (1995) scheme. In order to minimize the effects of reflections from the grid boundaries, the absorbing boundary conditions described by Cerjan et al. (1985) have been used.

### **5.1.3 Development of Matrix Geologic Model**

In order to have a realistic geologic model to compare to the fracture model we examined 40 wells within the 20 square mile study area and found that we could separate the Mesaverde interval into a sequence of regression phases, a channel dominated sequence, and a sequence of transgressive phases. Correlating these phases, we identified six regression surfaces and eight transgression surfaces that bound the Mesaverde. Picking the depths of these surfaces from the 40 wells allowed construction of a basic model using the Roxar's RMS software, which is an industry standard program for geostatistical reservoir modeling. Its output can either be formatted as an ECLIPSE file which is a standard file format for fluid-flow simulators, or as regular cartesian grids which would allow use in third-party finite-difference programs to simulate wave propagation in complex media. Unfortunately there was not enough data on the seismic velocities so we could not derive a velocity model. Figure 5-4 shows the model surfaces derived .

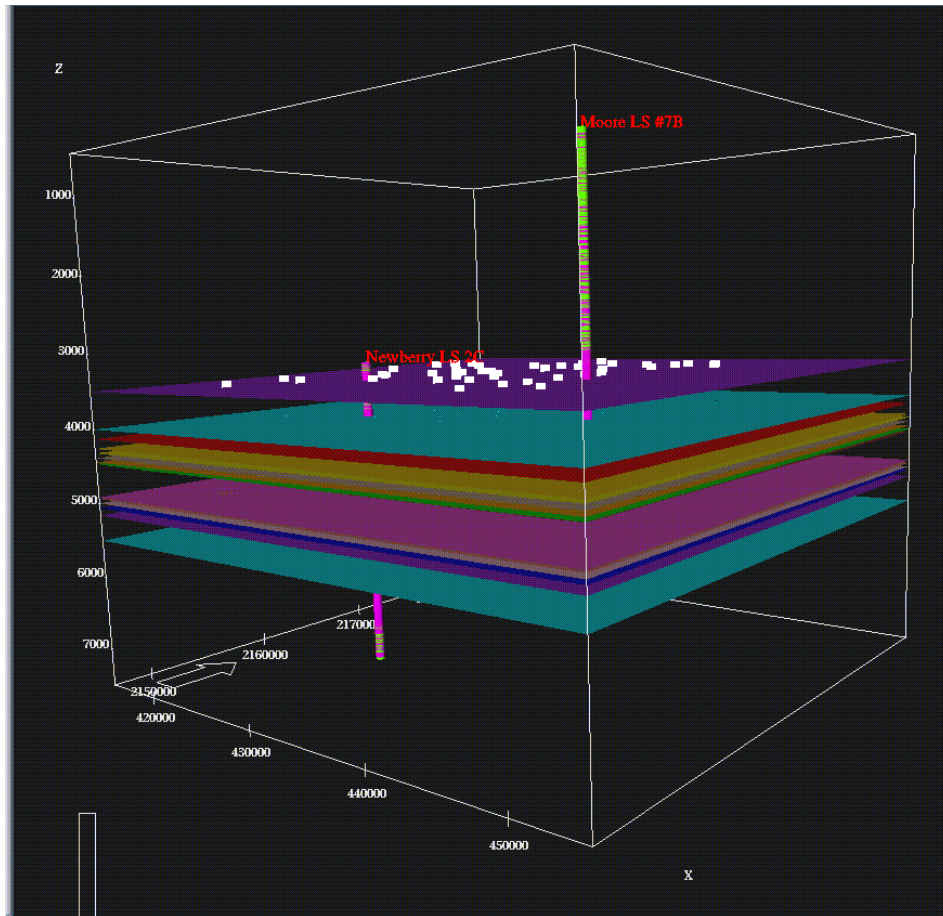


Figure 5-4. Model surfaces. The purple to green surfaces bound transgressive intervals, while the pink to blue surfaces bound regressive sequences. The thicker interval between the green and pink surfaces is the central Mesaverde. The white dots mark the location of the 40 wells used to construct these surfaces. Also shown are the blocked Newberry and Moore wells.

We populated each interval with facies or with lithologies. For the facies model, we assigned the following facies using a geostatistical method: marine, offshore, foreshore, barrier, floodplane, and channels.

The regressive intervals were populated with a facies sequence ranging from marine, offshore, foreshore, barrier, to floodplane. In each interval, this sequence is shifted a little bit more offshore yielding the stair-stepping look observable in Figure 5.5. The transgressive sequences were generated in a similar manner, but the sequences are shifted onshore instead of offshore. The central Mesaverde was modeled by as a floodplane with embedded channels. The geometry parameters for the channels, e.g., width, were estimated from modern analogues. Channel thickness and density was estimated from the wireline data.

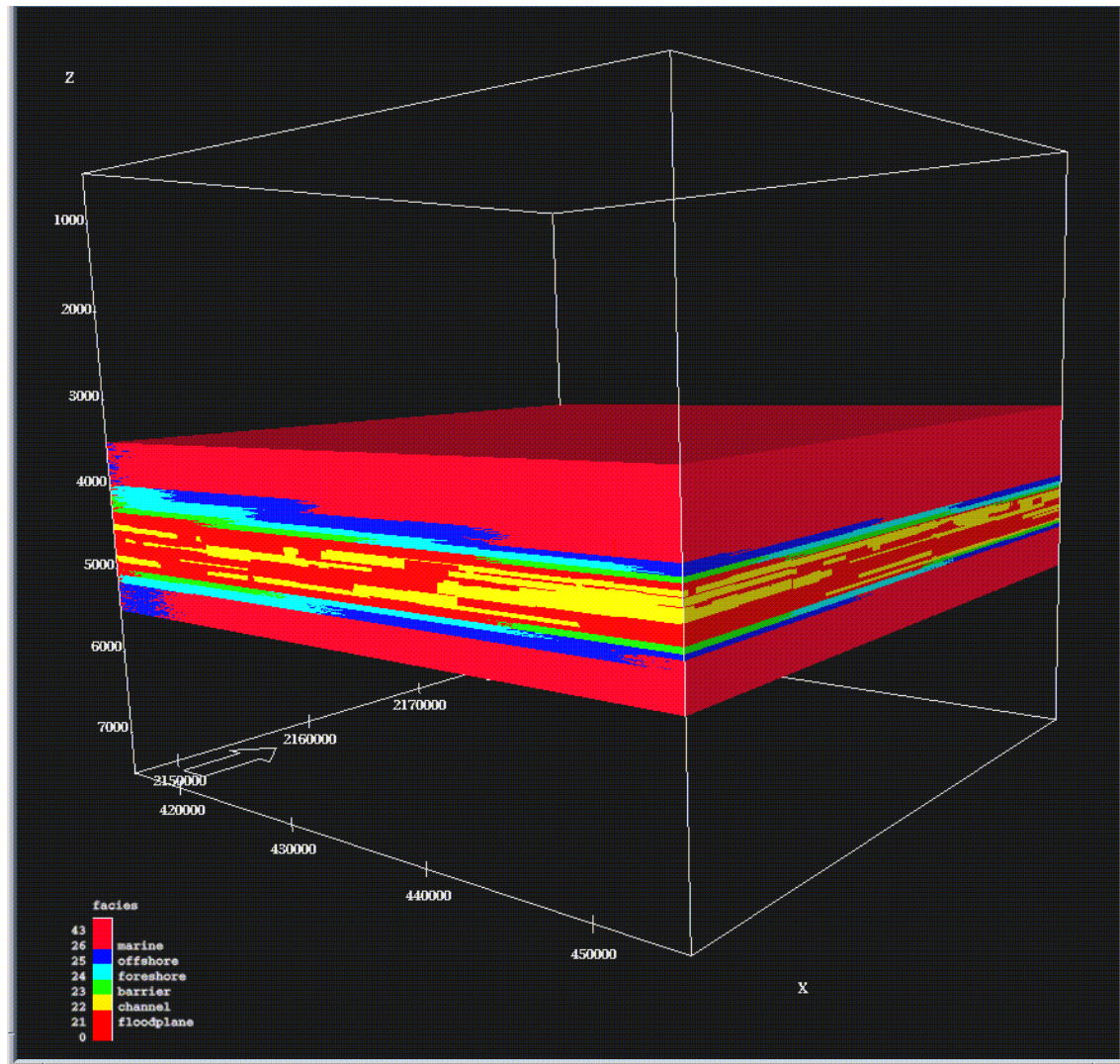


Figure 5-5. Geostatistical facies model. The facies range from marine, offshore, foreshore, barrier, to floodplane with channels.

For numerical simulation of fluid flow or wave propagation, models of lithology (sand versus shale) may be more useful than models of facies (marine to channel). Hence, we also constructed a geostatistical lithology model where the marine facies is shale dominated while the barrier facies is sand dominated. Inbetween, the sand proportion increases steadily. Sand bodies were modeled as thin, extended sheets. The floodplane was assumed to be shale dominated, while channels were considered rich in sand.

The availability of gamma logs for the Moore and Newberry wells allowed conditioning of these simulations. The gamma logs were blocked in one foot intervals to yield a pseudo log indicating sand or shale (Figure 5-6). These logs were then used during the geostatistical simulation of sand bodies. During simulation, a sandbody which erroneously intersects a sand-free section of the wells is removed again. Simulation was continued until all sand intervals in the wells are matched with a sandbody and the specified sand/shale is reached.

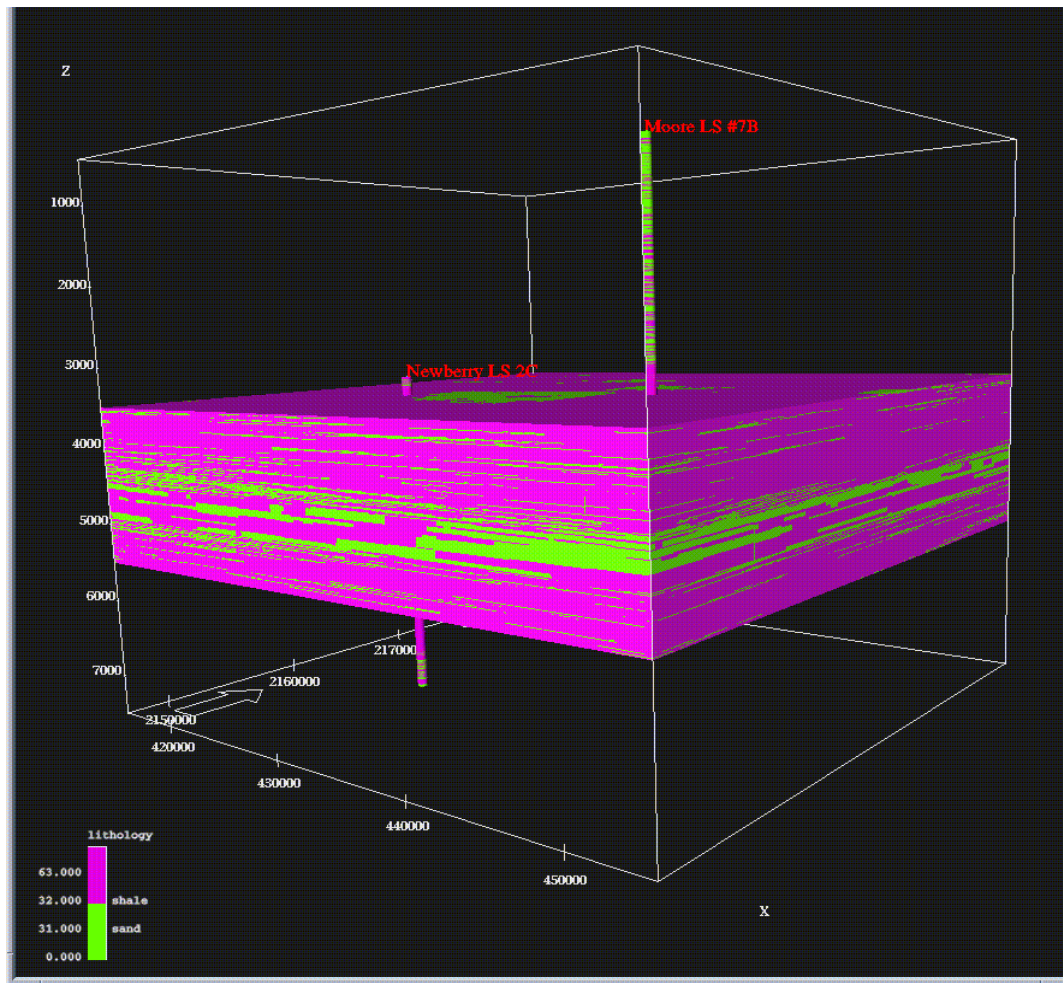


Figure 5-6. Geostatistical lithology model (sand and shale). Each facies in Figure 5-5 was modeled as shale with a facies-dependent amount of sand. The blocked sand-shale pseudologs derived from the gamma logs at the Newberry and Moore wells was used to condition the simulation.

#### 5.1.4 Basic Features of Seismic Fracture Response.

With sophisticated modeling tools and geologic model in hand, the basic features of the seismic response to fractures of various scales and stiffnesses can be investigated. Initially, a simple earth model containing two scales of fractures will be examined in 2-D. This model consists of five layers. It is representative of the Mesa Verde section encountered in the San Juan Basin study area. The velocities for each of these layers were estimated from well logs from near the study area. This model is shown in Figure 5-7 below. This 2-D model covers a vertical area of 2250 m<sup>2</sup>. The source is a point source characteristic of an explosion source, and the applied source wavelet is a 50 Hz Ricker wavelet. The receiver spacing is 60 m (approximately 200 ft), which is typical for surface reflection data in the San Juan Basin. The smaller scale fractures are spaced every 21 m, and are confined to the Cliffhouse Sand section. They have specific stiffness of  $8 \times 10^9$  Pa/m for both shear and compressional stiffness, appropriate for gas filled fractures. The larger scale fractures extending through the Mesa Verde section are spaced every 650 m.

## Basic Model (P-Velocity)

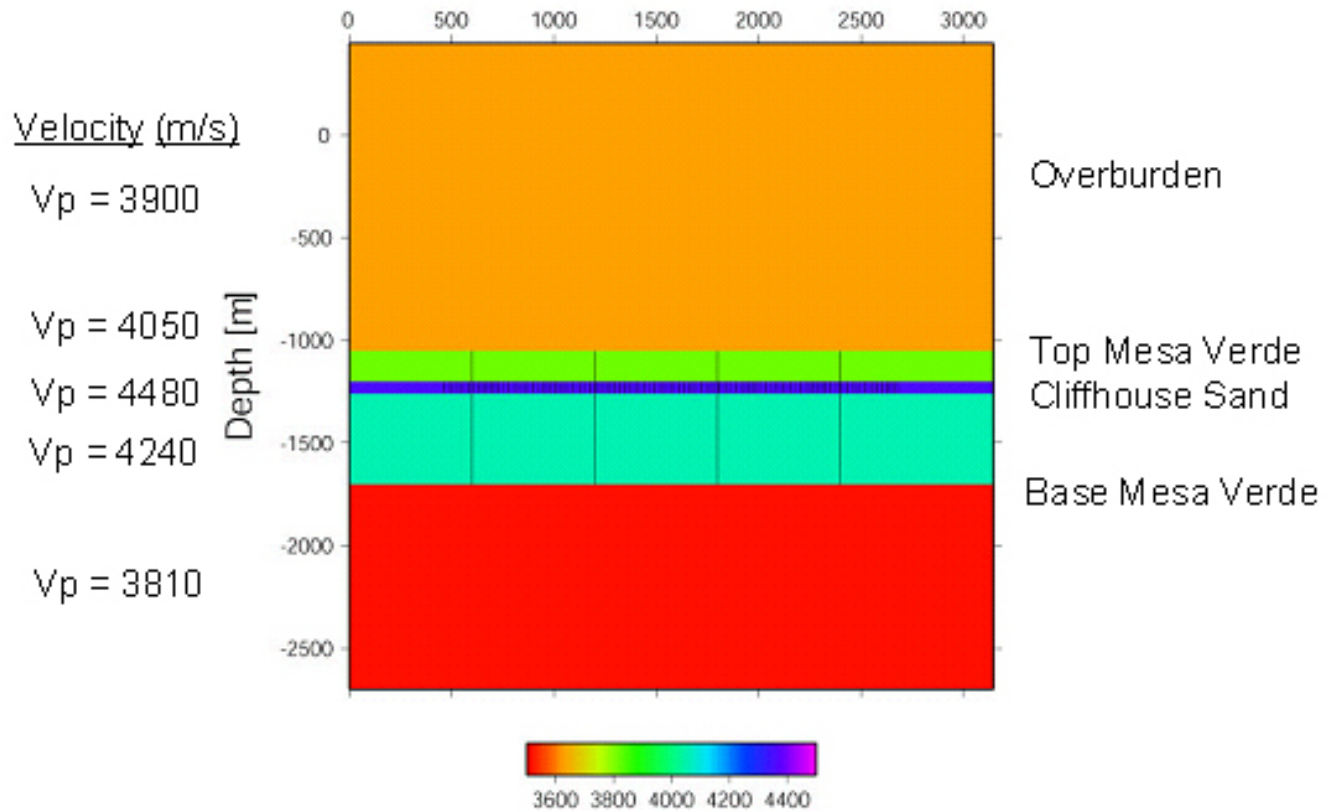


Figure 5-7. Simple 5 layer model with small fractures in the Cliffhouse Sand, and larger scale fractures extending through the Mesa Verde section

## Fractures in Model

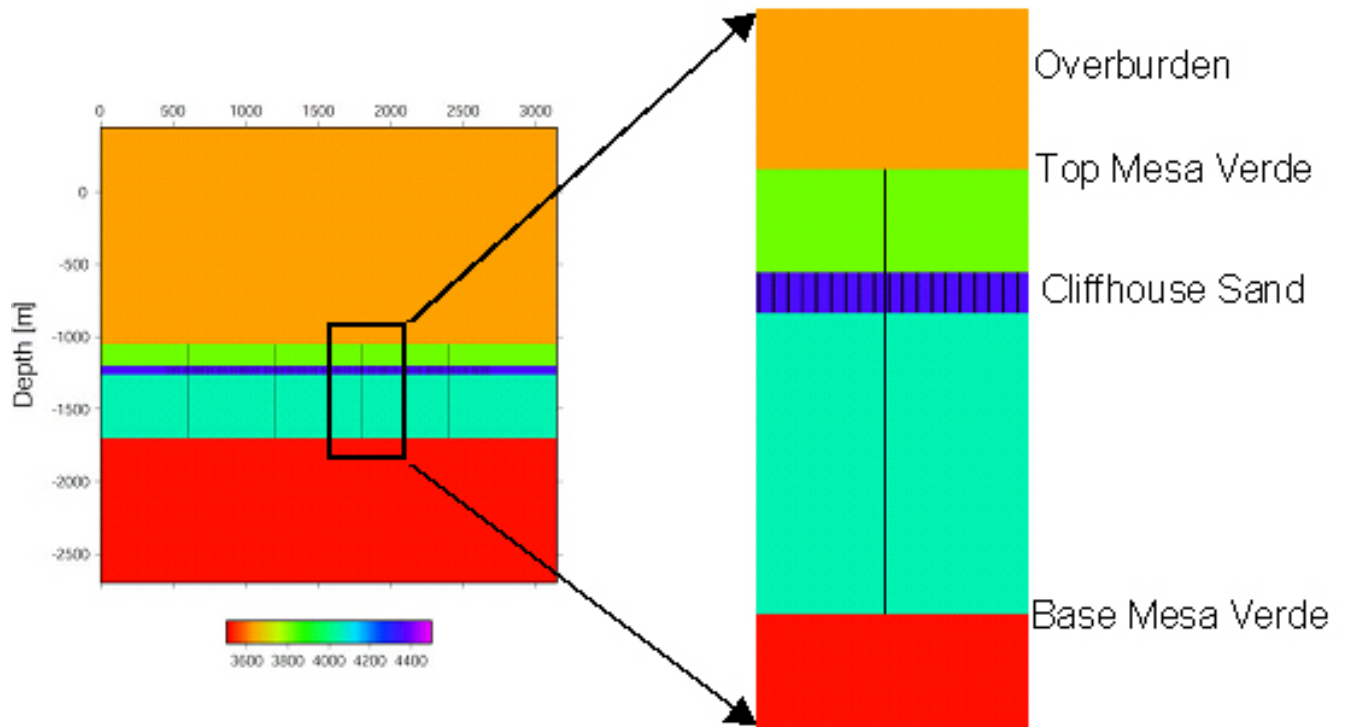


Figure 5-8. Details of the simple model showing details of small scale fracturing in the Cliffhouse Sand

They have both shear and compressional specific stiffnesses of  $8 \times 10^8$  Pa/m, again appropriate for gas filled fractures.

To examine the effects of small-scale fractures, the model was initially run with no fractures. Then it was run a second time with only the small-scale fractures included. Figures 5-9 and 5-10 show snapshots of the wave fields generated by these two models.

## Wave field – No Fractures

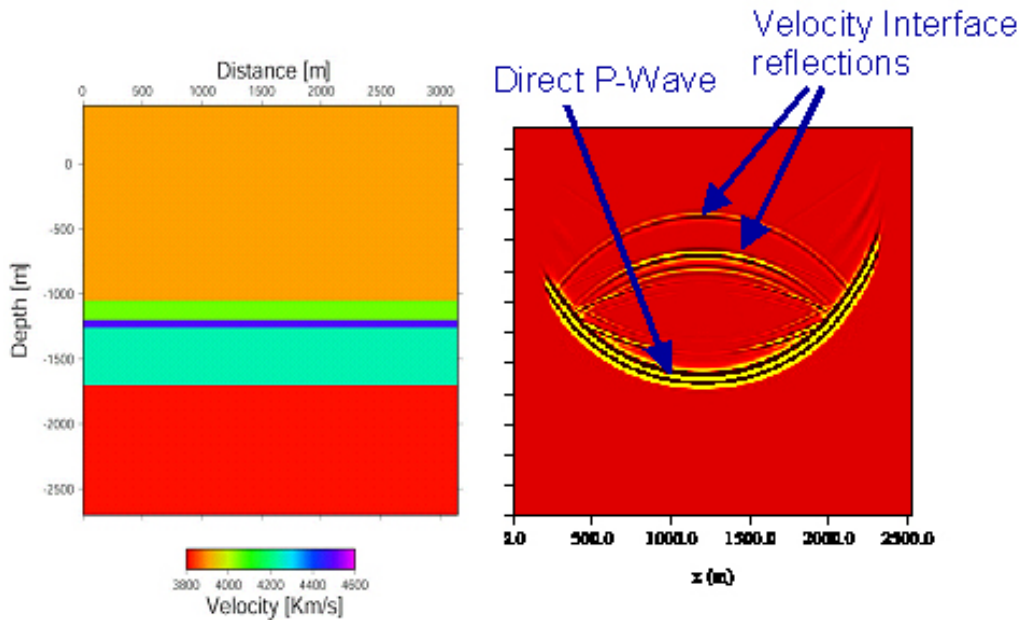


Figure 5-9. Wave field snapshot for the model without any fractures

## Wave field – Small Fractures Only

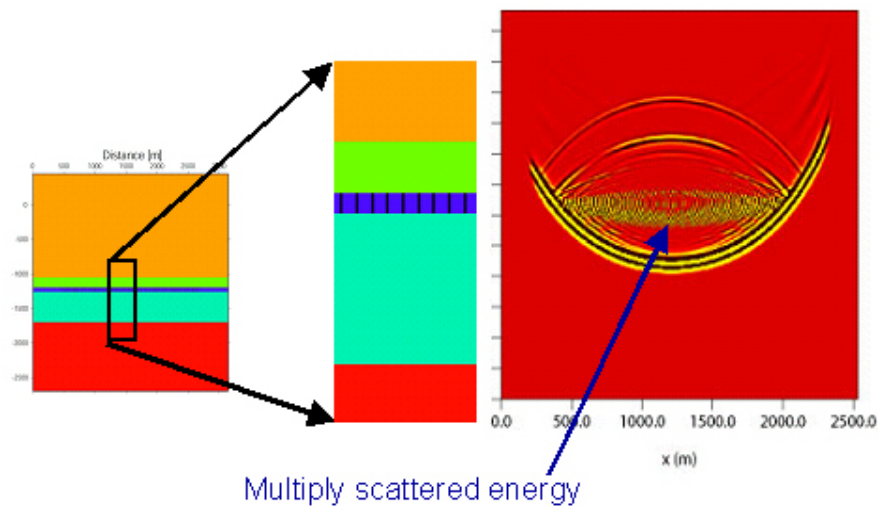


Figure 5-10. Wave field snapshot for model including small scale fractures

Comparison of the two snapshots from Figures 5-9 and 5-10 shows that the major effect of the small-scale fractures is to generate a rather diffuse and chaotic zone of scattered energy. This scattered energy would generally be treated as noise in standard seismic processing. While not

as obvious from the figures, the small-scale fractures also impart a slight delay to both the transmitted and reflected wave fronts. This is the same effect predicted by the equivalent anisotropic medium treatment of fractures. Thus, the intuitive expectation that small-scale fractures can be treated as equivalent anisotropic media is born out by this simulation.

Figure 5-11 shows a snapshot of the wave field with both sets of fractures present.

## Wave field – All Fractures

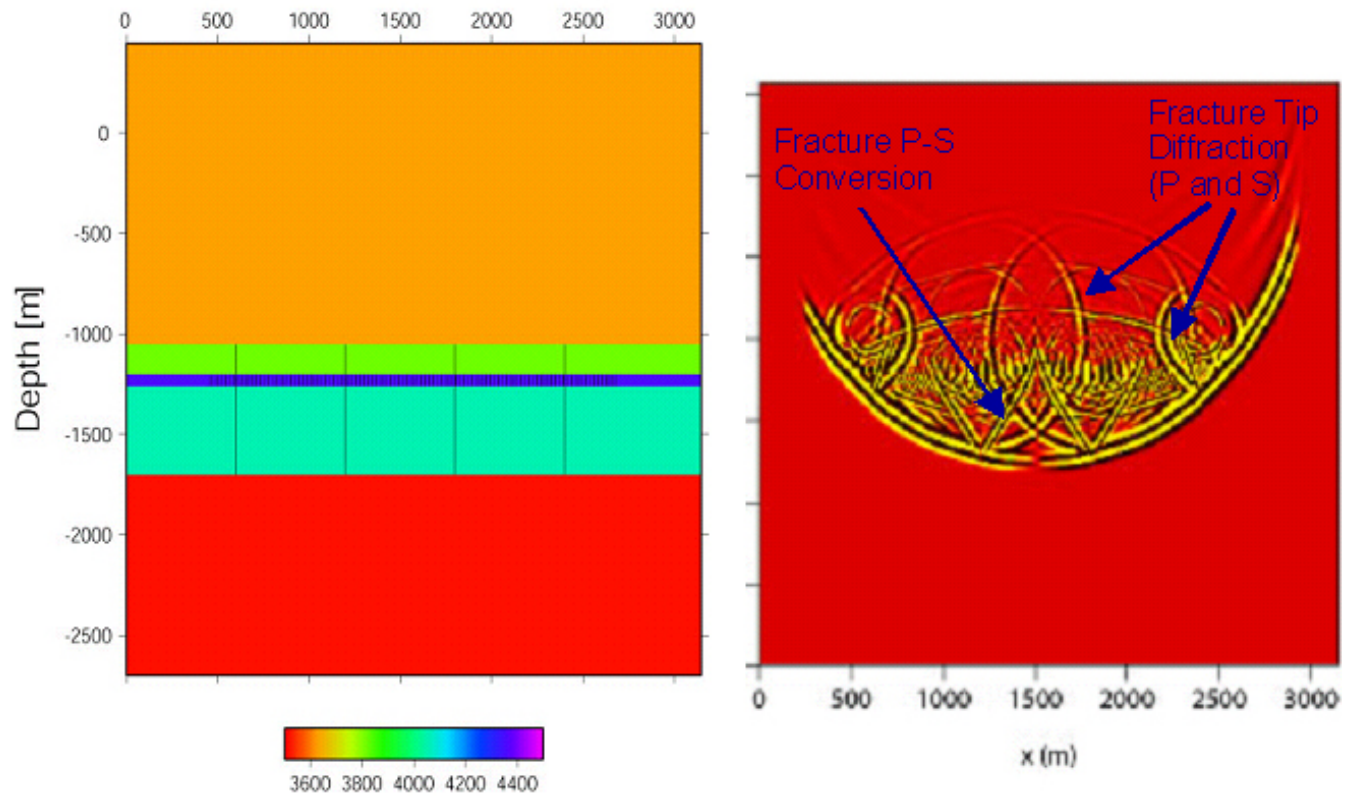


Figure 5-11 Snapshot of the wave field with both large and small scale fractures

Comparison of Figure 5-11 with Figure 5-9 shows that there are distinct effects generated by including the large scale fractures. Strong diffractions generated by the fracture tips are prominent. Somewhat unexpected, significant P-S mode conversions are also clearly visible. Standard seismic imaging methods such as Kirchhoff migration would properly collapse the P-wave diffractions to images of the fracture tips. However, such methods would not deal correctly with the strong S-wave diffractions. They would also not collapse the P-S mode conversions, which are one of the most prominent features arising from the displacement discontinuities. Instead of imaging these events, standard migrations would smear them, resulting in a distorted image.

Figure 5-12 shows how these events will appear on a typical shot gather from receivers placed along the surface.

## Shot Gathers

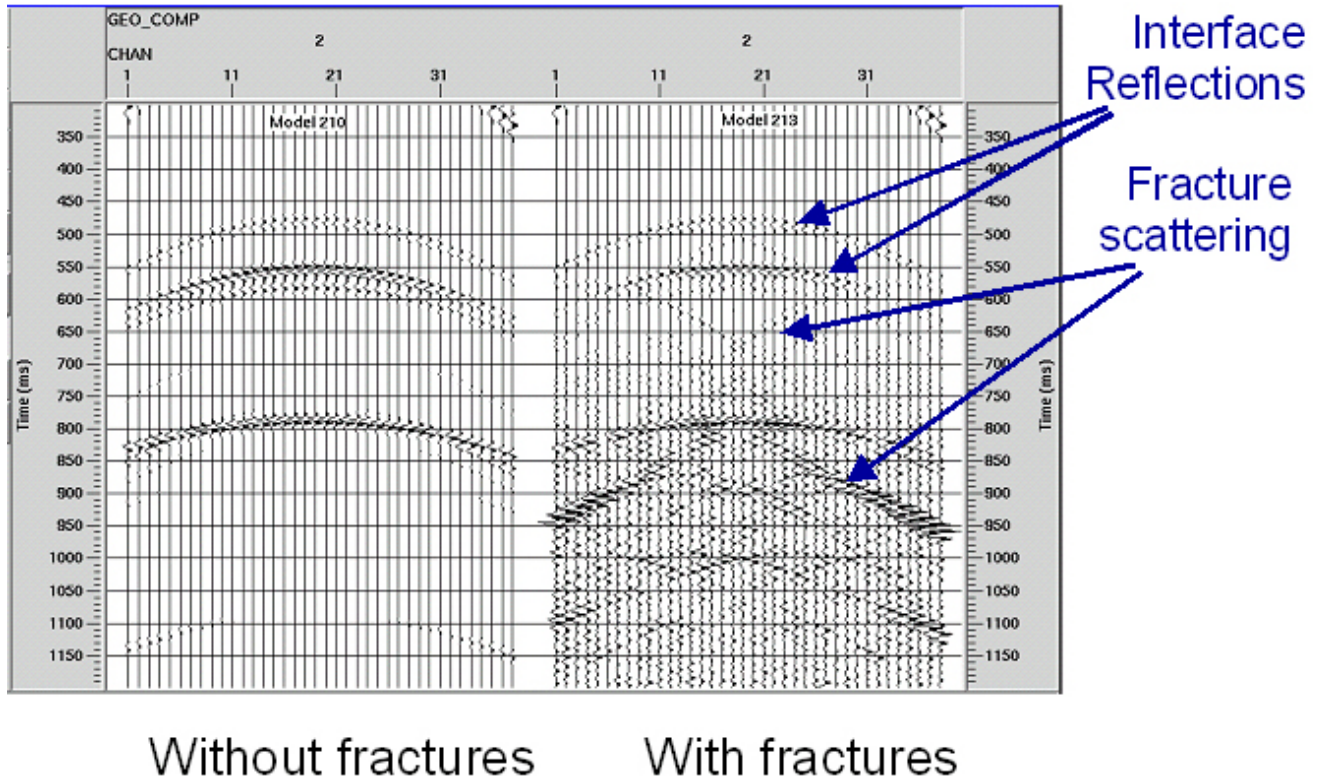


Figure 5-12. Synthetic shot gather seismograms for simulated receivers deployed along the surface of the model. Seismograms on the left are for a model with no fractures, while seismograms on the right are for a model with both sets of fractures

The figure on the left in Figure 5-12 is for a model with no fractures. The events show the typical hyperbolas expected for reflection events from horizontal layers. The figure on the right shows the same events, as well as the various diffractions and mode conversions arising from the fractures.

The next figure illustrates the effect of spatial sampling. The figure on the right shows a shot gather simulated over a model containing both sets of fractures, with a receiver spacing of 60 m. This is a common receiver spacing used in seismic acquisition. The figure on the right shows a shot gather over the same model, but in this case, the receiver spacing is a much finer 3 m. A number of the scattered events generated by the fractures, particularly the small-scale fractures, have very short spatial wavelengths in the horizontal direction. These events are severely aliased at the coarser 60 m spacing typically used in acquiring reflection seismic data. These results

suggest that much finer spatial sampling be considered when attempting to detect effects of discrete fractures.

## Spatial Sampling

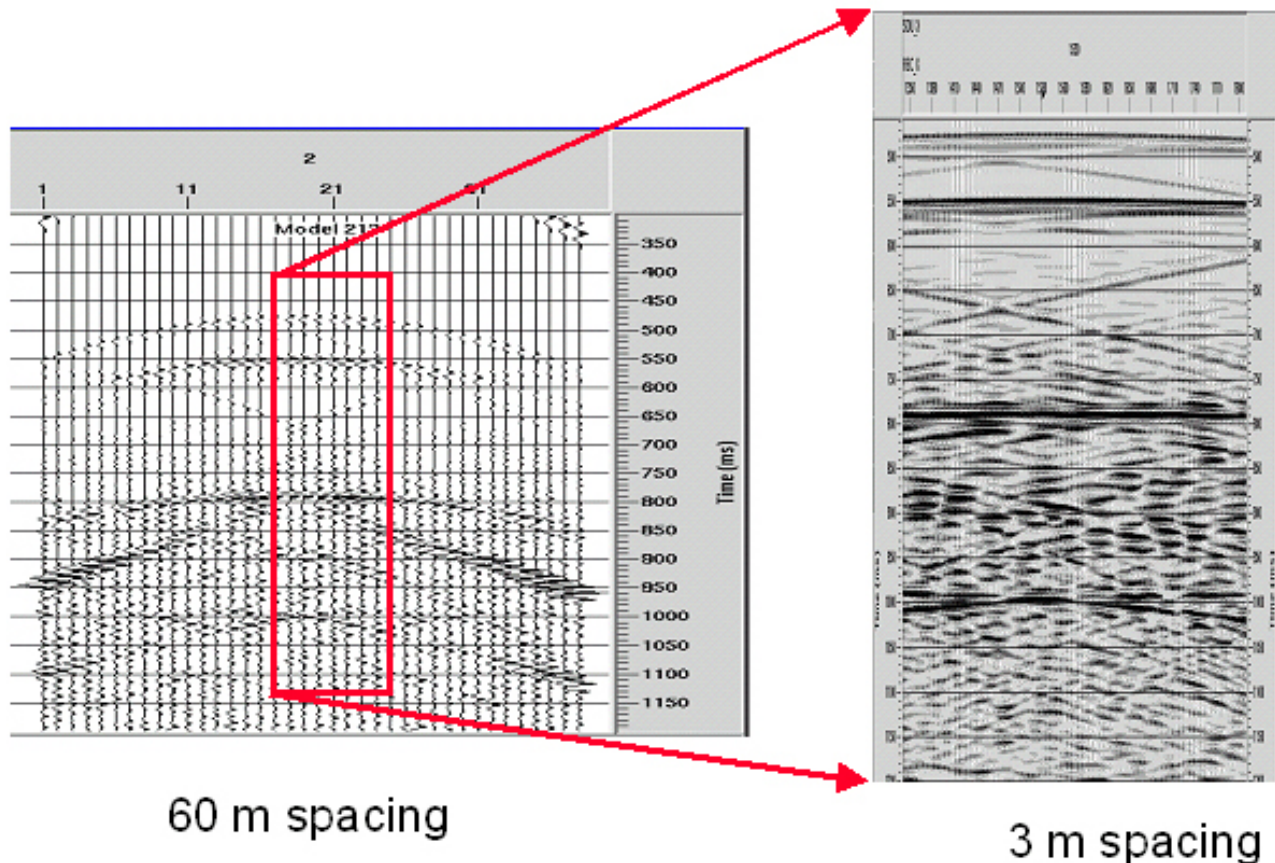


Figure 5-13. Effect of spatial sampling. Events arising from discrete fractures are aliased at typical receiver spacings.

One of the major questions in detecting the effects of discrete fractures is the sensitivity of seismic data to the various fracture stiffnesses. How soft do the displacement discontinuities have to be in order to generate a convincing seismic signature? To answer this question, a series of models were run, each with different fracture stiffness. In these models, the fracture stiffness was varied from  $8 \times 10^8$  Pa/m to  $8 \times 10^9$  Pa/m. The results of these simulations are shown in the next figure. For softer fractures with a stiffness of  $8 \times 10^8$  Pa/m, the scattered events are clearly visible in the shot gathers. However, for stiffer fractures with a stiffness of  $8 \times 10^9$  Pa/m, the scattered events are barely visible. This suggests that fractures significantly stiffer than  $8 \times 10^9$  Pa/m will not be visible on surface reflection data.

## Variable fracture stiffness

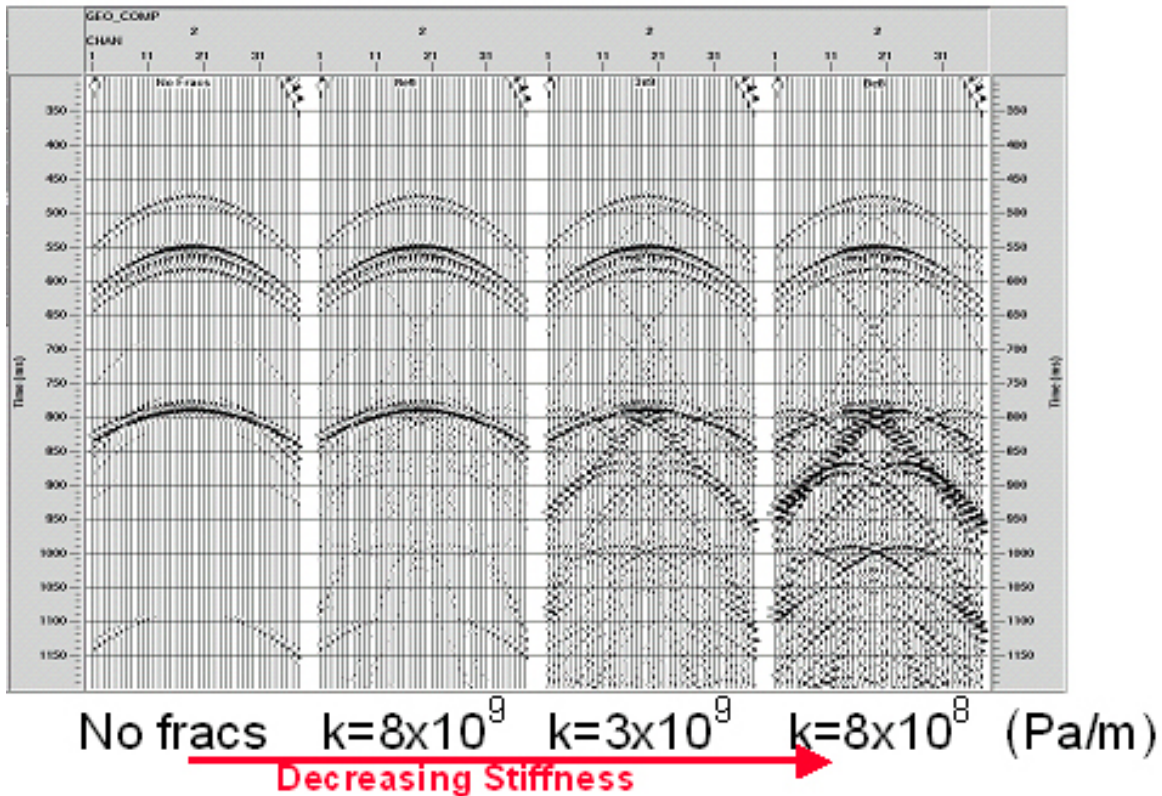


Figure 5-14. Effects of varying the fracture stiffness on the visibility of fracture generated scattered events

This simple five-layer model has illustrated a number of aspects to be considered when modeling, acquiring, and processing surface seismic reflection data over fractured reservoirs. In modeling, very small scale fractures can be treated as equivalent anisotropic media. Larger scale fractures, which often dominate productivity, should be treated as discrete features through approaches such as displacement discontinuity. To adequately characterize the scattered events generated by discrete fractures, much finer spatial sampling than is typically used should be considered. Properly imaging data which contain scattered events from fractures will require the development of more sophisticated imaging algorithms. The algorithms will need to include effects of mode conversions and guided waves. Finally, this simple model suggests that discrete fractures significantly stiffer than  $10^{10}$  Pa/m will not generate detectable scattered events.

### 5.1.5 Discrete Fracture Example in 2-D

This next example illustrates some of the features of the seismic response expected from clusters of discrete fractures which have formed about a fault. In this 2-D model, the fractures are embedded in a much more complex layered earth. The velocities, density and depths for these layers have been derived through blocking of the velocity logs from the Ludwick 13B well,

located near to the study area. A total of 45 layers are contained in this model, and they capture some of the details of thin-bedded sands and shales within each of the major Mesa Verde units.

The two faults are represented in the model as vertical displacement discontinuities each with a specific stiffness of  $8 \times 10^8$  Pa/m. Surrounding each fault is a cluster of discrete vertical fractures which are vertically discontinuous. They extend through the sandstones, but do not continue through the shales. The fractures are characterized by a specific stiffness of  $8 \times 10^9$  Pa/m, an order of magnitude greater than their associated faults.

This model allows us to see the interaction between the seismic events scattered from the fractures and faults, and the realistic layering encountered in the study area. The simulated source is an explosion source, and the source wavelet is a 30 Hz Ricker wavelet. The figure below shows a snap shot of the horizontal component of the wave field 0.150 s after the initiation of the source, overlaid on the P-wave velocity model. The source is located at the “surface” at a depth of 0 m and at the horizontal coordinate of -1250 m.

## Basic 2-D Model

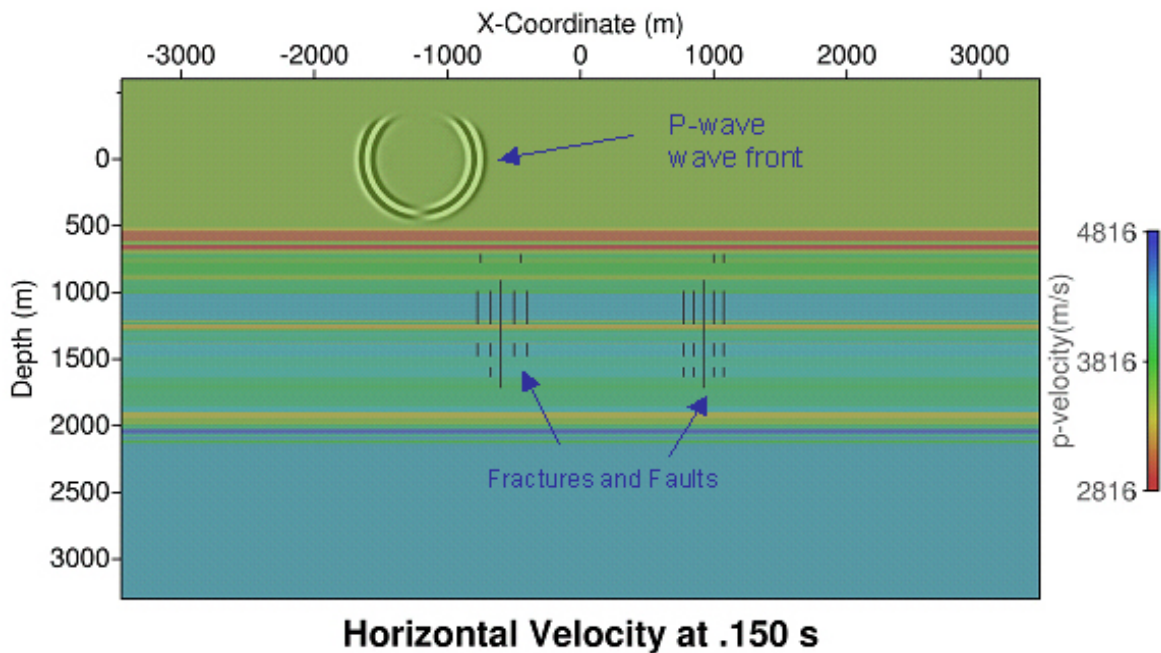


Figure 5-15. Snapshot of the horizontal component of the wave field overlaid on the P-wave velocity model

At this time, the P-wave wave front is circular, and is about to impinge on the first significant reflecting boundary, which is the Lewis shale. The attenuation of the wave front near the top of the model is due to the absorbing boundary conditions on the edges of the model.

The next figure shows the wave field shortly after it has crossed the Lewis shale at 0.250 s. A P-wave reflection and a mode converted S-wave reflection generated at the top of the boundary are visible. It is also apparent that even at these shallow depths, a complex wave field is beginning to develop. This complexity is caused by multiple reflections and transmissions through the fine bedding in the model.

## Wave Field Shortly After Crossing First Significant Boundary

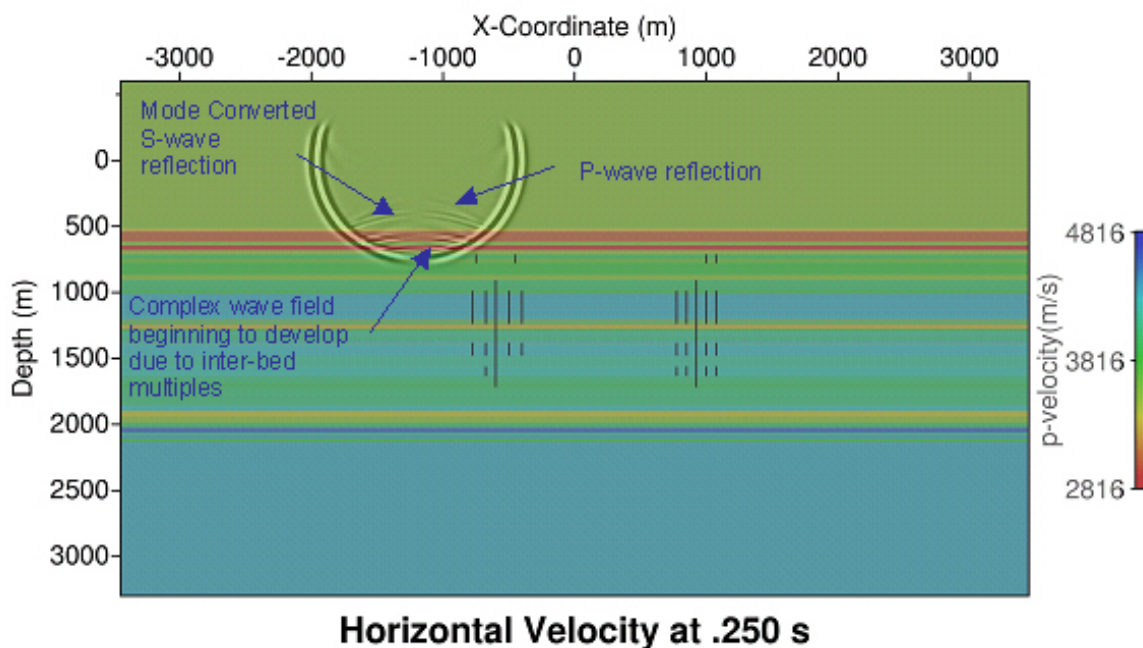


Figure 5-16. Wave field shortly after crossing the Lewis shale boundary

At 0.450 s, as shown in the next figure, the wave field is just crossing the fractures nearest to the source, on the left. A complex series of scattered events is generated by this cluster of fractures, with the largest event being the mode conversion that has moved about halfway down the “fault”. For surface reflection seismic, an array of receivers would be deployed along the “surface” at a depth of 0 m. Reflections from the Lewis shale are just crossing this depth at the time of the snapshot. Accordingly, these reflections will appear at times of around 0.45 s on simulated shot gathers. The fracture events are still relatively deep, and would only be recorded by an array of VSP receivers in a well at a horizontal coordinate of approximately -750 to -1000 m at this time. To be recorded on a surface array of receivers such as those used in reflection seismic, these fracture events will have to propagate back up to the surface through the complex layering.

## Wave Field as Front Crosses Fractures Nearest to Source

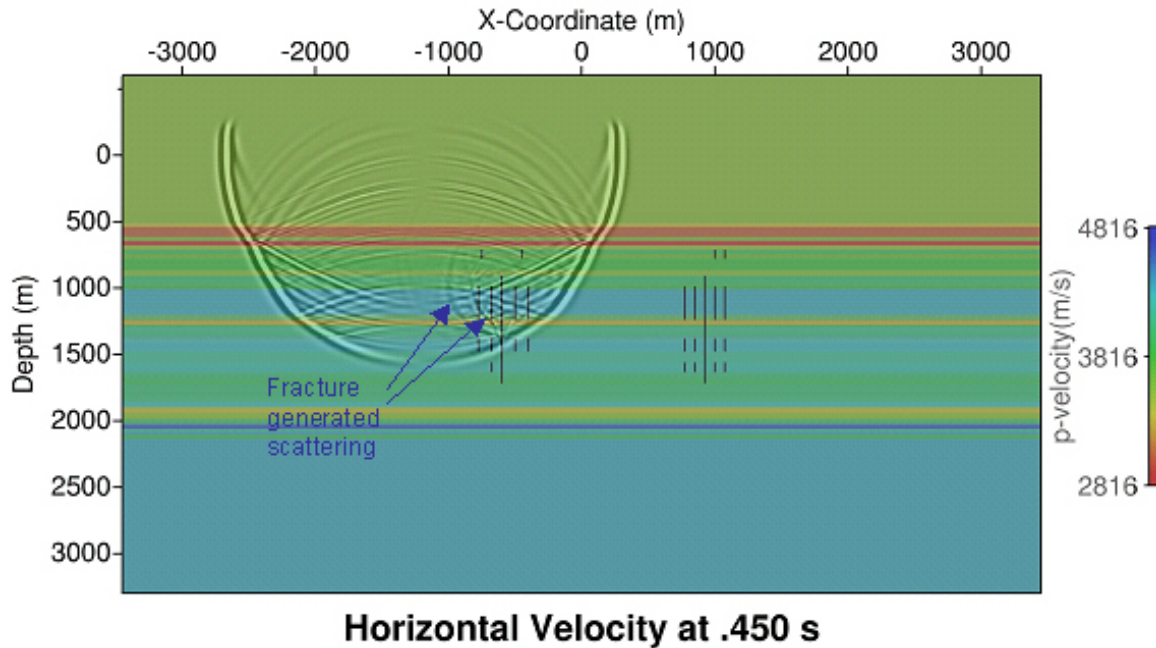


Figure 5-17. Wave field shortly after the wave front crosses the cluster of fractures and the fault nearest to the source

The wave front reaches the far offset fractures at a time of approximately 0.725 s, as shown in the next figure. At this time, as can be seen in the figure, the events generated by the near offset fractures are just reaching the surface. However, they have been significantly weakened by passing through the layering, and would be barely visible on a surface array of geophones. Comparison of Figures 5-17 and 5-18 shows that the events generated by the far offset fractures are significantly stronger than those generated when the wave front passed through the near offset fractures. This is because the wave front is more nearly parallel to the fractures when it reaches the far offset cluster. This suggests that in general, stronger events will be generated by farther offset surface sources. Alternatively, stronger fracture events will be generated by sources which are placed at the same depth as the fractures, as would be the case when using downhole sources.

## Wave Field as Front Crosses Fractures Far from Source

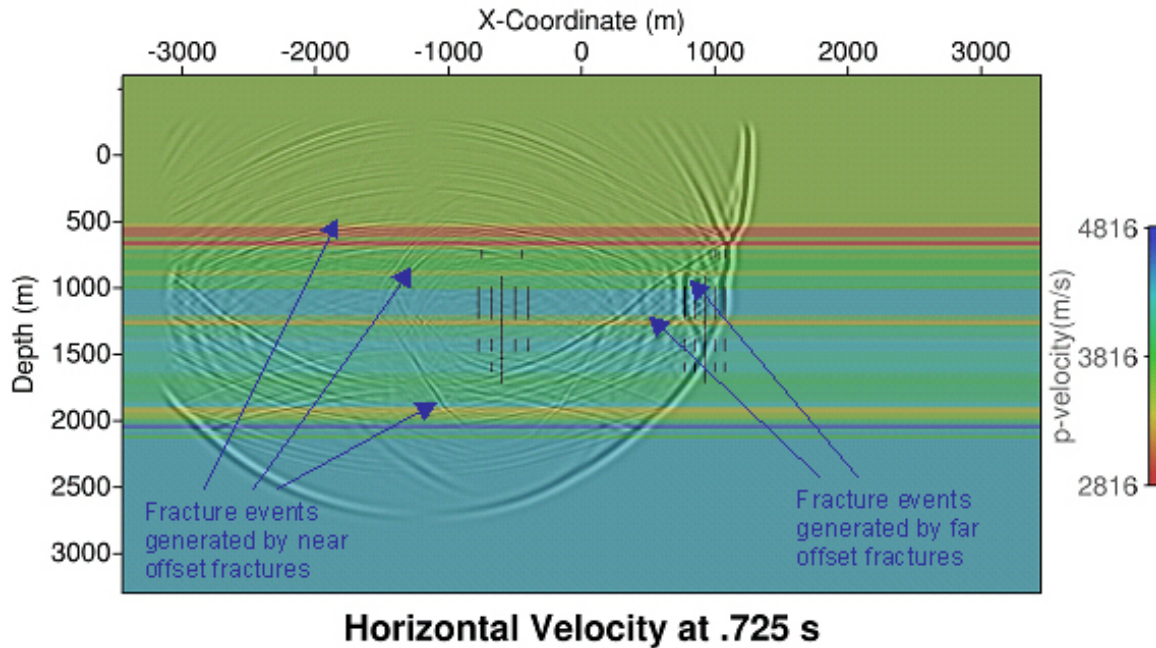


Figure 5-18. Wave field shortly after the wave front crosses the cluster of fractures and the fault farthest from the source

The propagation of the major event generated by the far offset fractures is shown in the next figure. Shown are a series of snapshots as time increases. This event is a mode converted shear wave, and propagates at near the shear velocity. At 0.800 s, it is seen to be propagating primarily in the horizontal direction and is moving to the left. Some vertical growth is taking place, but the event is mostly channeling across the Mesa Verde. By 0.875 s, the event has finally reached the shallower Lewis shale. At 1.025 s, the event can be seen refracting along the Lewis shale. Some weak energy can be seen to be reaching the surface depth (0 m) at a horizontal coordinate of approximately 0 m where it will begin to be recorded on a surface array. It will be recorded on geophones nearly a kilometer to the left of the cluster. At 1.175 s, the higher amplitude part of this event finally reaches the surface and will begin to be recorded on geophones at a coordinate of approximately -500 m. At 1.325 s, the event is seen to continue to refract along the Lewis shale, propagating to the surface as a fairly high amplitude event and moving to the left.

By the time this event reaches the surface where it can be recorded by a reflection seismic array, it has been seriously corrupted by its interaction with the velocity layering, particularly the low velocity Lewis shale. This once again underscores the need to have very sophisticated imaging algorithms if such events are to be properly imaged. Proper imaging will also require a very precise knowledge of the layer velocities in order to back propagate the fracture events to their source.

Examination of the snapshots for 0.800 s and 0.875 s shows that if a vertical array of receivers were placed at a horizontal location corresponding to a coordinate of between 0 and 500 m, this fracture event would have been recorded relatively uncorrupted.

### Wave Field as Front Crosses Fractures Far from Source

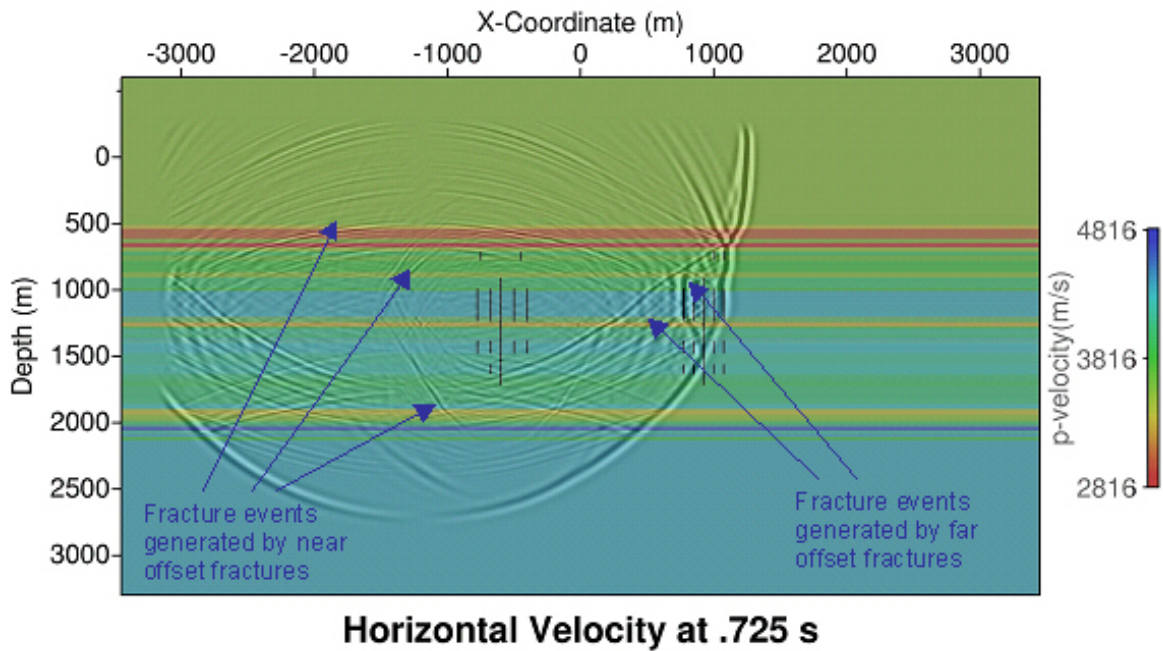


Figure 5-19. Propagation with time of major fracture event from far offset fractures to the surface

Overall, this suggests that VSP and single well measurements are much more suitable for interpreting specific fracture quantities than are surface reflection measurements. Unfortunately, one of the limitations of such borehole methods is significantly smaller areal coverage.

A shot gather from this simulation for a source located at -1250 m is shown in the next figure. Coordinates shown in this figure are offsets from the source in m, so the far offset fractures are at an offset of approximately 2000 m from the source. The major fracture event tracked in Figure 5-19 is highlighted by the blue arrow in Figure 5-20. As discussed, this event begins to appear at a source offset of approximately 1 km, nearly a kilometer to the left of the fractures which generated the event. The linear moveout of this event is also characteristic of a refraction event. Again, very sophisticated imaging algorithms and a very detailed knowledge of the velocity field would be required to properly image the fractures generating these events.

## 45 Layer Model Shot Gather

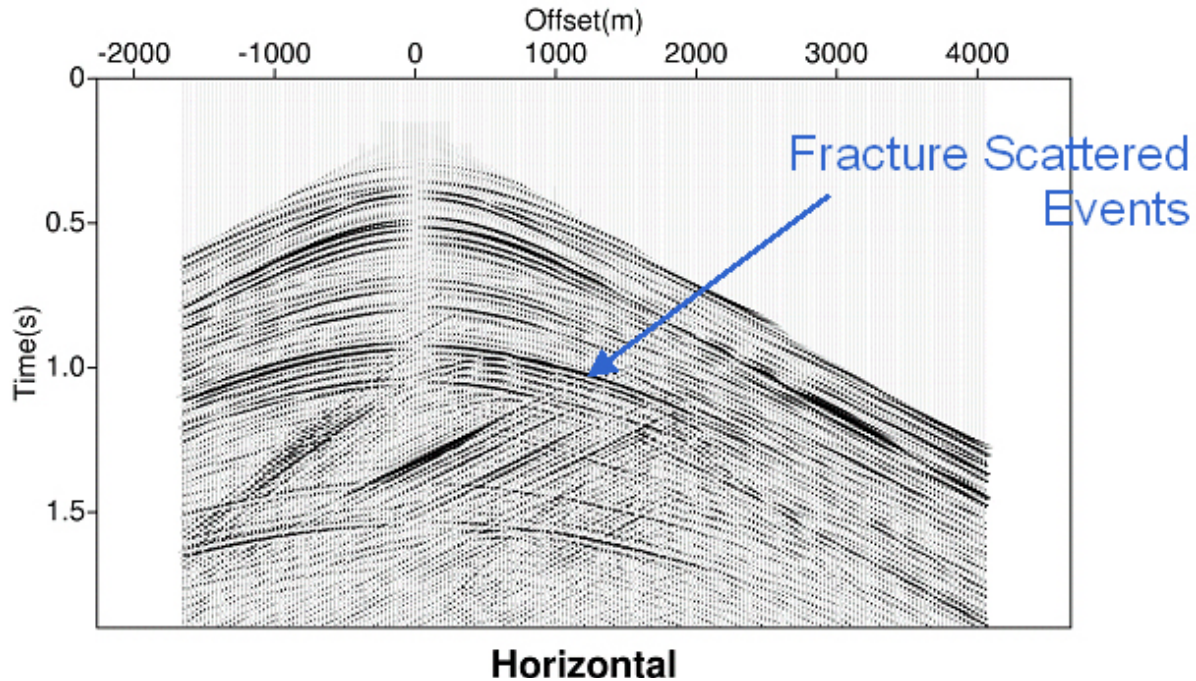


Figure 5-20. Shot gather for a source located at -1250 m. The fracture event tracked in Figure 5-19 is arrowed.

### 5.1.6 VSP Modeling in 3-D

The previous discussion suggests that quantifying fracture properties will be more straightforward with VSP. With this in mind, a series of full 3-D models simulating VSP geometries were run. The first 3-D model used the 45 layer blocked well log model from the Ludwick 13 B well. This is the same layered model used in the 2-D modeling discussed above.

As with the 2-D model, two faults were placed in the model surrounded by a cluster of fractures. The two faults are represented in the model as vertical displacement discontinuities each with a specific stiffness of  $8 \times 10^8$  Pa/m. Surrounding each fault is a cluster of discrete vertical fractures which are vertically discontinuous. They extend through the sandstones, but do not continue through the shales. The fractures are characterized by a specific stiffness of  $8 \times 10^9$  Pa/m, an order of magnitude greater than their associated faults. This model also contains numerous small-scale fractures in the Fruitland Coal section, again characterized by a specific stiffness of  $8 \times 10^9$  Pa/m.

Figure 5-21 shows an X-Z plane snapshot at 0.550 s from one of these simulations. Here, a vertical source typical of a surface P-wave vibratory source is placed in the center of the model at X and Y coordinates of 1500 m. The applied source wavelet is again a 30 Hz Ricker wavelet.

## 3-D Finite Difference Modeling

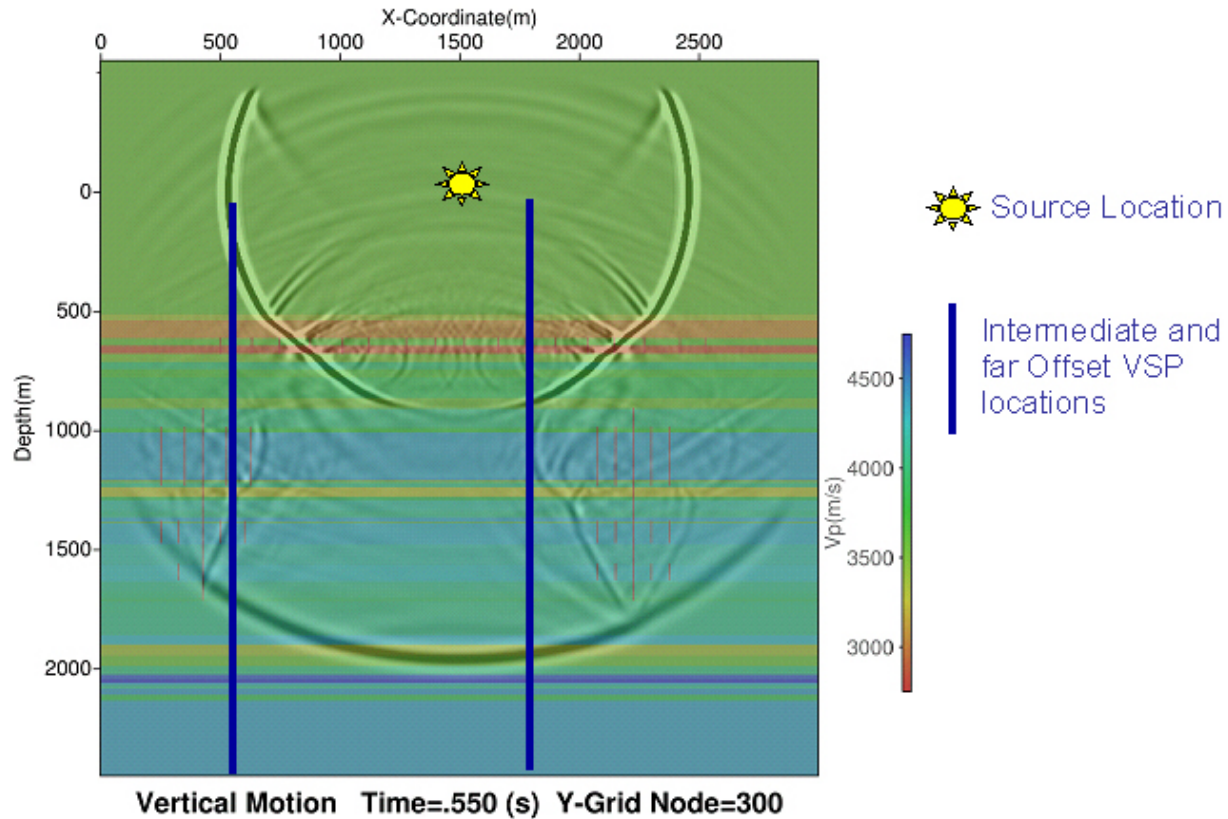
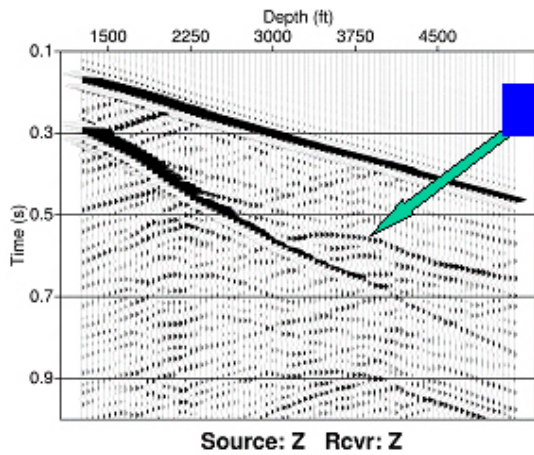


Figure 5-21. X-Z plane snapshot from the 3-D model at 0.550 s. The blue lines show the locations of intermediate and far offset VSP wells where seismic traces were generated

As with the 2-D simulations, strong mode converted events have been generated by the fractures. At the time shown (0.550 s), the strong mode converted event from the fractures on the right are seen to be just arriving at the intermediate offset well at a depth of approximately 1100 m. A strong mode converted event from the fractures on the left is crossing the far offset well. At this time, it is being “recorded” by geophones at a depth of approximately 1250 m. This event will show up at slightly earlier times on the shallower geophones for the far offset well, and slightly later times for the deeper geophones.

Figure 5-22 shows the simulated VSP traces from the intermediate offset well. The strong mode converted event is arrowed. The shape (moveout) of this event is quite distinct. Its apparent velocity at its earliest times is quite high, and is faster than the downgoing P-Wave events. Such high apparent velocities are characteristic of events generated by vertical features such as

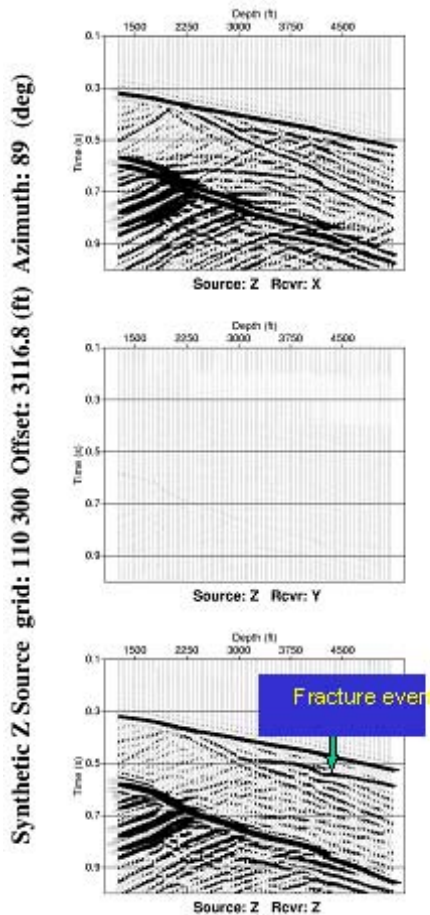
fractures and faults. The overall shape of this event gives insight into the type of events to be looked for in actual VSP field data.



**Synthetic  
Data for  
Intermediate  
Offset**

**Z-Z  
Component**

Figure 5-22. Simulated VSP vertical geophone traces for the intermediate offset well



**Synthetic  
Data for Far  
Offset VSP  
Well**

Figure 5-23. Simulated VSP vertical and horizontal geophone traces for the far offset well

---

Simulated traces for the far offset well are shown in Figure 5-23. The fracture generated events are again quite distinct, showing very fast moveout. The X and Z trace displays of Figures 5-22 and 5-23 are plotted with each trace amplitude normalized in order to make the deeper traces visible. However, the relative amplitude of two events at the same depth can be compared. At the far offset, the fracture generated event is seen to have an amplitude comparable with the direct arrival. The fracture event in the intermediate offset example has an amplitude somewhat less than the direct arrivals. This is consistent with the previous observation from the 2-D modeling that wave fronts which are more parallel to the vertical fractures generate stronger fracture scattered events.

The predictions of this 3-D model simulation give a great deal of insight into the type of events to be expected from discrete fractures in an actual VSP measurement. These results were very useful in searching for fracture related events in the 3-D 9-C VSP data collected as part of this project. However, detailed comparison of arrivals in the field data with predictions of the model showed significant differences even in the relative amplitudes of the first arrivals. These differences were attributed to the fact that the VSP data were acquired about the Newberry LS 2C well, while the model was built using velocities from the Ludwick 13 B well.

To begin to investigate these differences, a detailed velocity and density model was built from data from the Newberry LS 2C well. As part of this project, detailed P- and S-wave logs were acquired over the Mesa Verde section of this well. These well logs were then blocked to give a detailed layered velocity and density model for the deeper part of the section covered by the VSP. One of the major differences between the area around the Newberry LS 2C well and that around the Ludwick 13 B well was the presence of a very low velocity near surface around the former. A shallow VSP data set acquired in the Newberry LS 2C well was analyzed for the near surface velocities. These velocities were then used with the deeper blocked well log results to form an overall layered earth model.

The resulting model is shown in the next figure. The Figure shows an X-Z plane cut through the source location from the 3-D model. The source is a vertical point force with a 30 Hz Ricker wavelet. The model is overlain by a snapshot of the vertical particle motion for a time of 0.520 s. A number of interesting events can be seen. The direct P-wave arrival has moved to near the bottom of the model by this time, and numerous P-wave reflections are apparent. A strong mode converted event is also visible, having reached a depth of approximately 600 m by this time. The absorbing boundary conditions of Cerjan et al. 1985 are used in this model. These absorbing boundary conditions have been seen to be quite effective at damping out direct reflections of waves incident on the grid boundaries. However, very strong waves such as the direct P-wave arrival do generate weak refractions when they reach the grid edges, and are not completely damped by these absorbing boundary conditions. Two such events are arrowed in the figure.

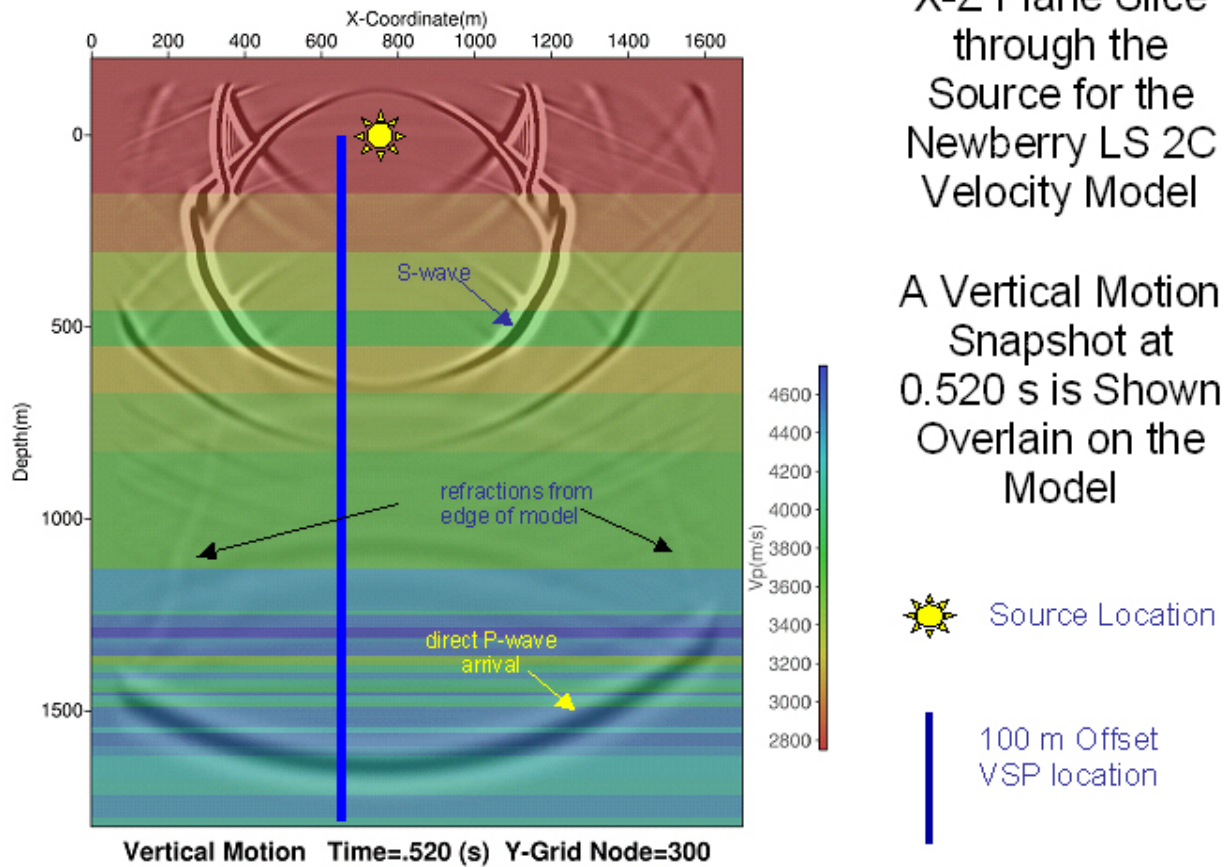


Figure 5-24. Newberry LS 2C P-wave velocity model overlain by a vertical motion snapshot at 0.520 s

Also shown in Figure 5-24 is the location of a simulated VSP well. This well is at an X offset of 100 m from the source, and has the same Y coordinate as the source. Figure 5-25 shows the simulated vertical traces from this VSP well. The direct P-wave arrival is quite apparent, and is arrowed on the figure. Also shown is the down going mode converted S-wave event visible in the snapshot. Numerous P-wave reflection events have also been highlighted. One of the refraction events generated by the interaction of the direct P-wave arrival with the edge of the grid is also highlighted. This event looks very similar to the fracture events highlighted in the simulated traces of Figure 5-22, though its amplitude is quite a bit lower. This underscores the need to look at all the details of such simulations before interpreting anomalous events.

The traces from this simulation have been passed on for processing with the same flow used in processing the actual VSP data acquired about the Newberry LS 2C well. These synthetics will also be used to examine relative amplitudes between  $S_h$  and  $S_v$  waves for far offset sources related to layer refractions. Ultimately, fractures and faults will be included in the models. This will help answer questions about which faults and fractures should be visible in the field data.

## Vertical Traces from the Simulated 100 m Offset VSP Newberry LS 2C 3-D Velocity Model

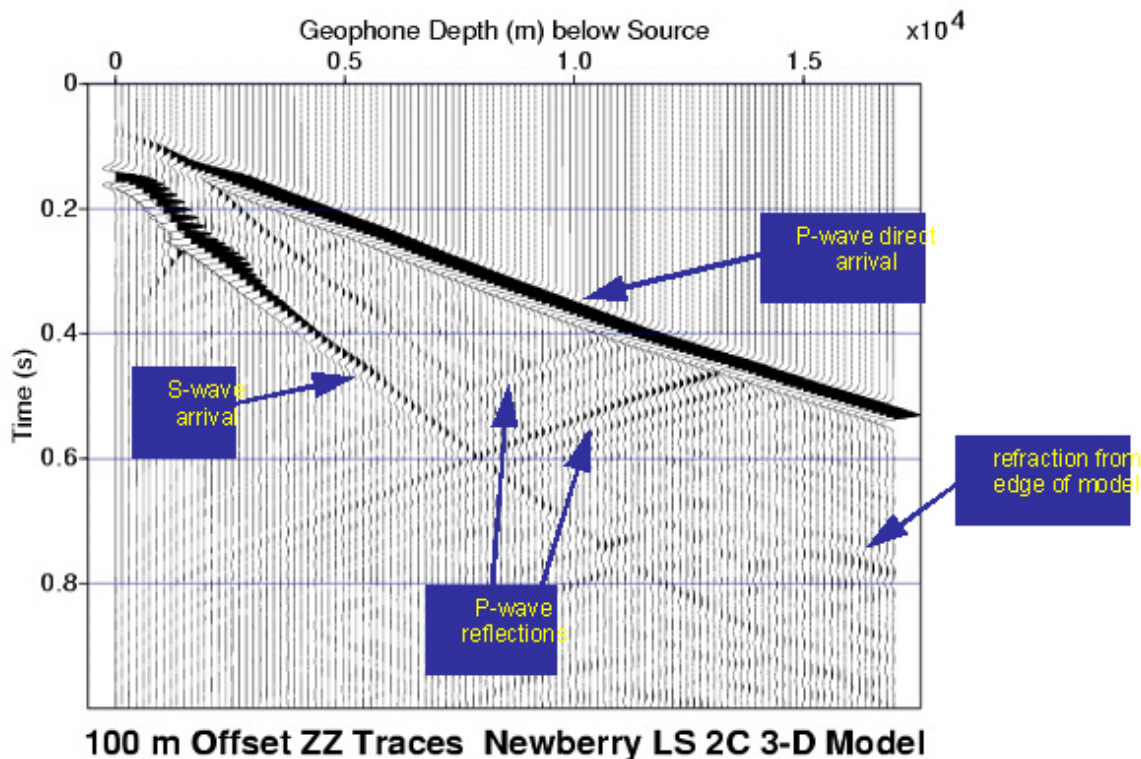


Figure 5-25. Synthetic vertical traces from the Newberry LS 2C 3-D velocity model

Finite difference modeling based on the displacement discontinuity formalism has been found to be valuable in a number of applications. Fundamental insight into the nature of discrete fracture response has been gained. Of particular interest are the mode converted events generated by discrete fractures and the need for finer scale sampling. In order to image these events with surface reflection seismic data, advanced imaging algorithms need to be developed and applied. The limit of specific fracture stiffness detectable in surface reflection measurements has been estimated at  $10^{10}$  Pa/m. Realistic earth models have revealed the complex interaction between fracture scattered seismic events and detailed layering. In attempting to apply sophisticated imaging methods to surface reflection data imaging discrete fractures, the velocity structure of the earth must be known in detail. Borehole seismic methods such as VSP and single well are seen to be more direct measurements of the fracture events. Finally, the use of full 3-D modeling to process and interpret 3-D 9-C VSP data has been illustrated. Overall, sophisticated modeling capability is found to be a critical component in quantifying fractures through seismic data.

---

## 6. SYNTHESIS OF THE RESULTS

To make the most use of the individual results it is desired to combine the various results from the different studies at a variety of scales. At the small scale (centimeter to meter) we have core studies and well logs. At the next larger scales we have the single well (meter to 10's of meters), then the VSP (100s of meters to kilometers) and finally the surface seismic (kilometer to 100's of kilometers). The primary question addressed at the beginning of this work was at which scale do we need to measure to improve our chances of successful well placement in the San Juan basin. Again it must be emphasized that our study was effectively one data point in a very large volume, and it was in an area that was quite complex.

A cornerstone of this work was characterizing fractures as discrete targets (or groups of fractures) that at some scale could be imaged with seismic methods. A considerable effort was carried out to accurately model the effect of fractures on seismic wave propagation. This was necessary to accurately interpret the results of the different scales of seismic data. Therefore the synthesis included this modeling effort.

The primary question addressed at the beginning of this work was at which scale do we need to investigate in order to improve our chances of successful well placement in the San Juan basin. Again it must be emphasized that our study was effectively one data point in a very large volume, and it was in an area that was quite complex.

### 6.1 CORRELATION OF SEISMIC DATA WITH HISTORICAL PRODUCTION DATA

From looking at the results of the surface seismic it is clear that on a large volume the data were useful. Reprocessing of the data for specific purposes aided in the understanding of the overall fault and lithology in the study area. Figure 6-1 shows the 20 square mile study area and the cumulative production for the first year contoured. The figure was produced by taking all of the available production data from each well's first year of production and contouring it.

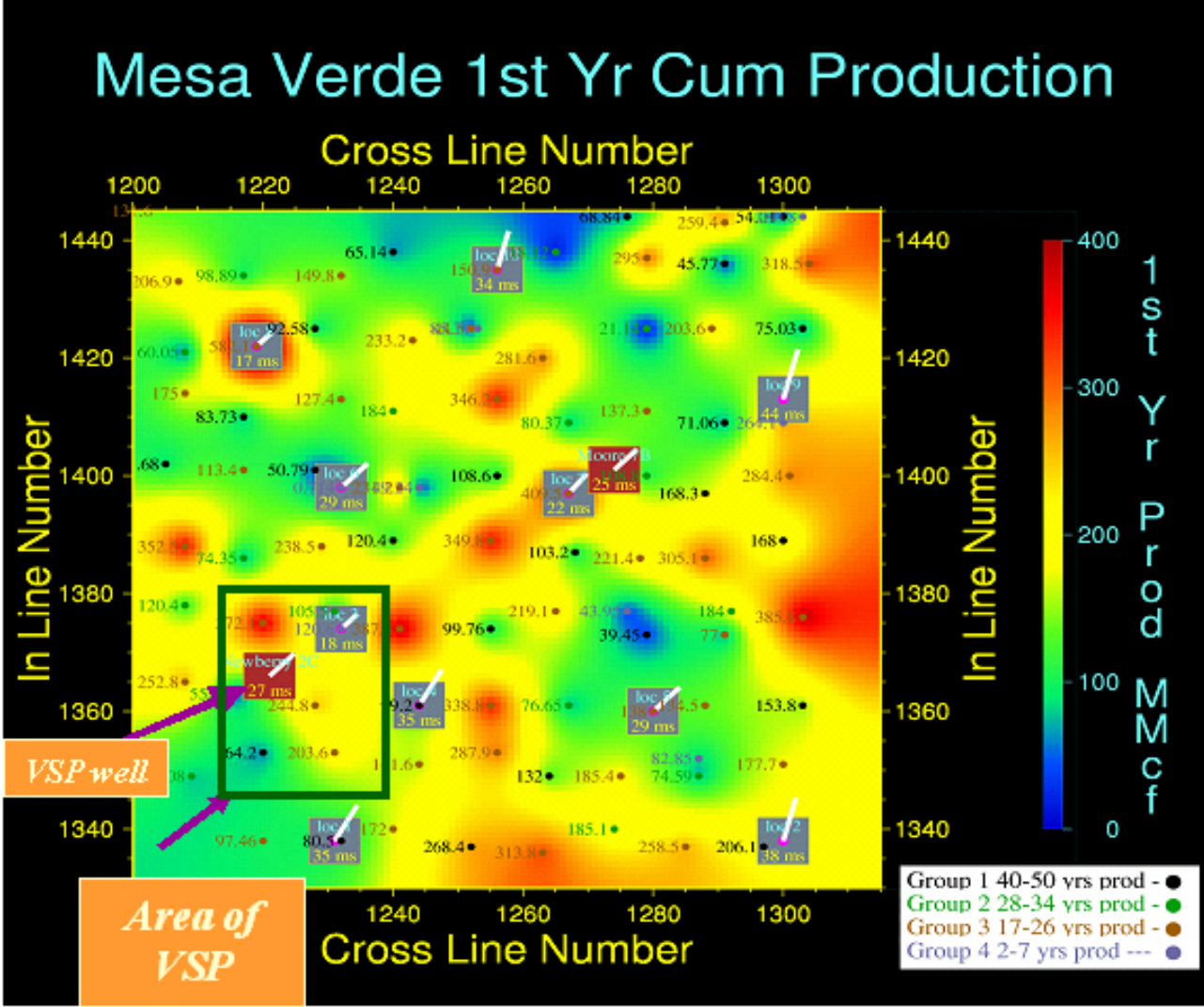


Figure 6-1. The first year production from each well contoured over the 20 square mile study area.

If one takes the result of the fault mapping using azimuth of the Point Lookout using method A picking of the surface seismic and over lay on Figure 6-1 the result is Figure 6-2.

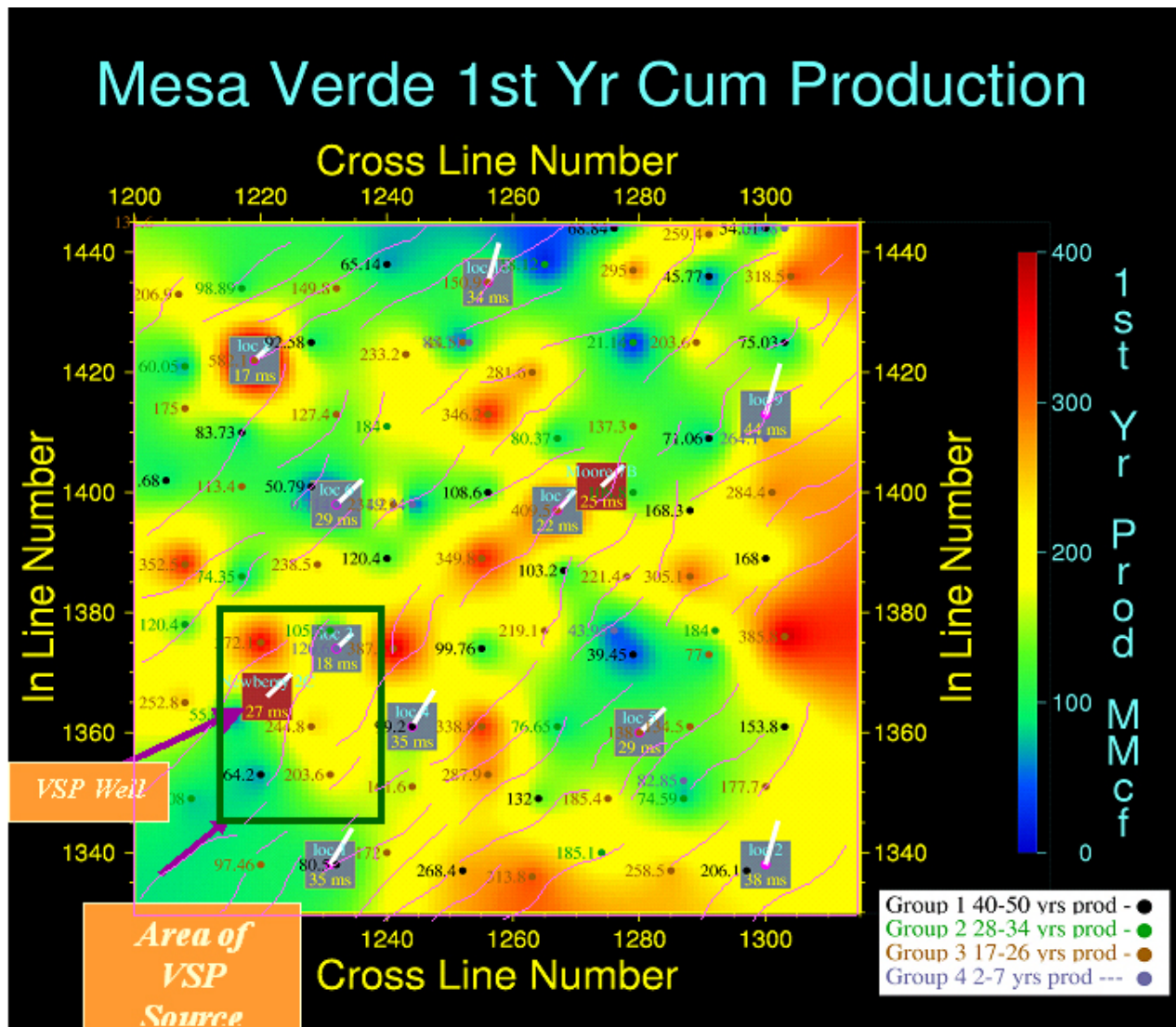


Figure 6-2. The faults picked using method A and using the azimuth direction in the Point Lookout plotted on top of the contoured production.

If one takes the faults picked by looking at the azimuth directions in the Menefee and overlying the production the result is Figure 6-3.

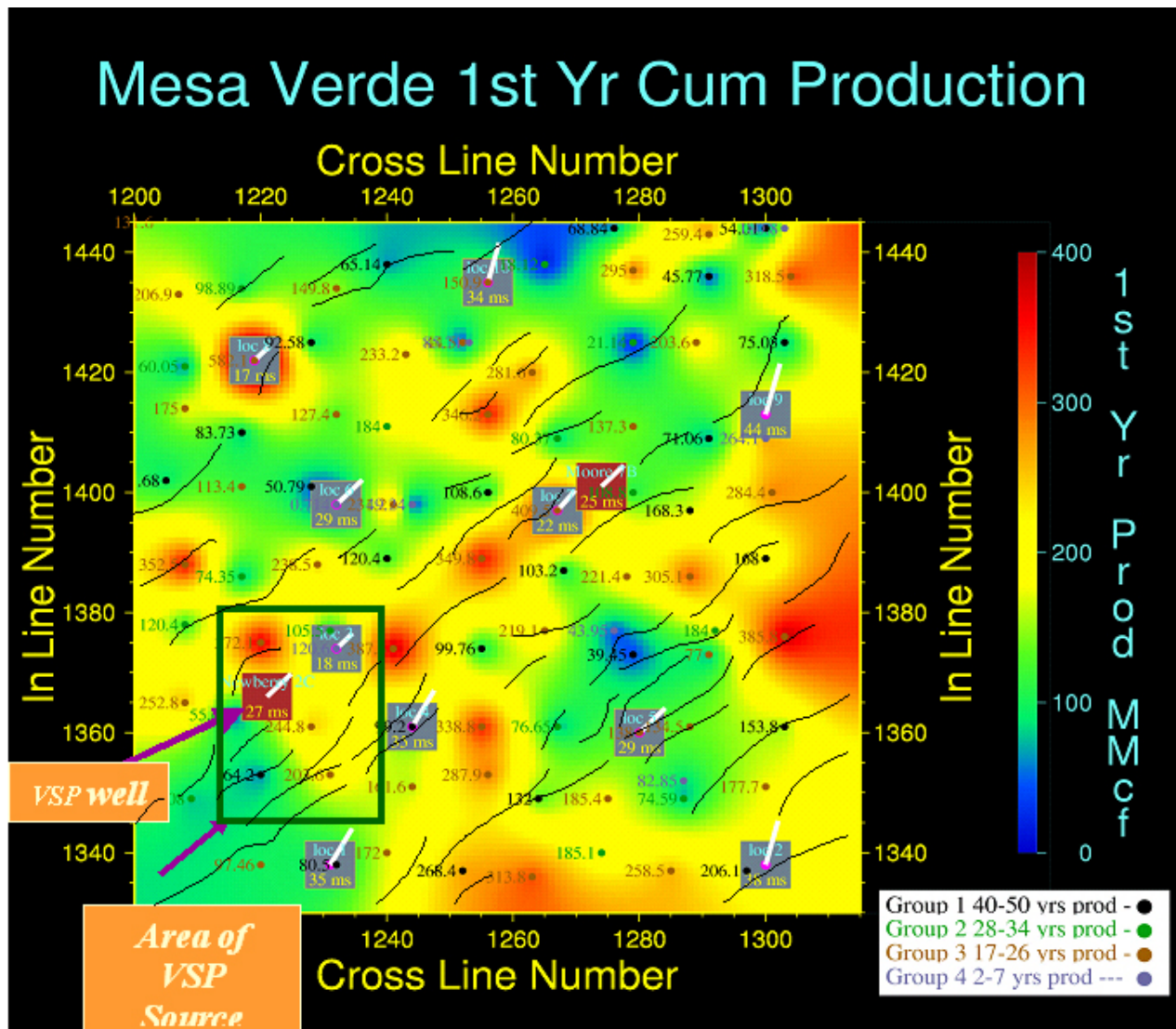


Figure 6-3. The faults picked using method A on the Menefee azimuth directions.

If one takes the summary of the faults picked with Methods A and B and over lay the production the result is Figure 6-4.

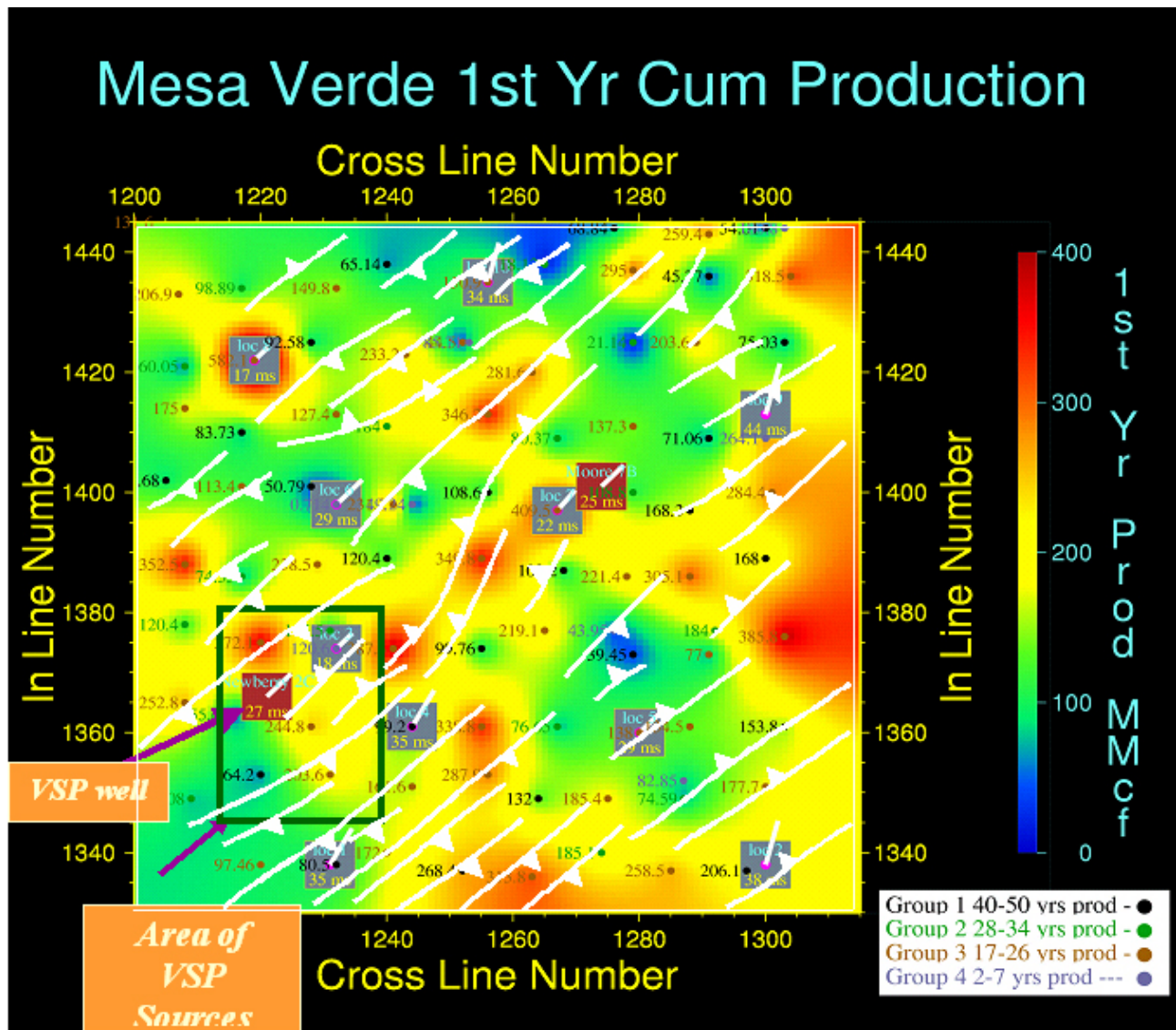


Figure 6-4. The results of taking the summary of fault picking using methods A and B and overlying the production data.

Finally if one takes the results of using method A and over lay the production data Figure 6-5 is produced.

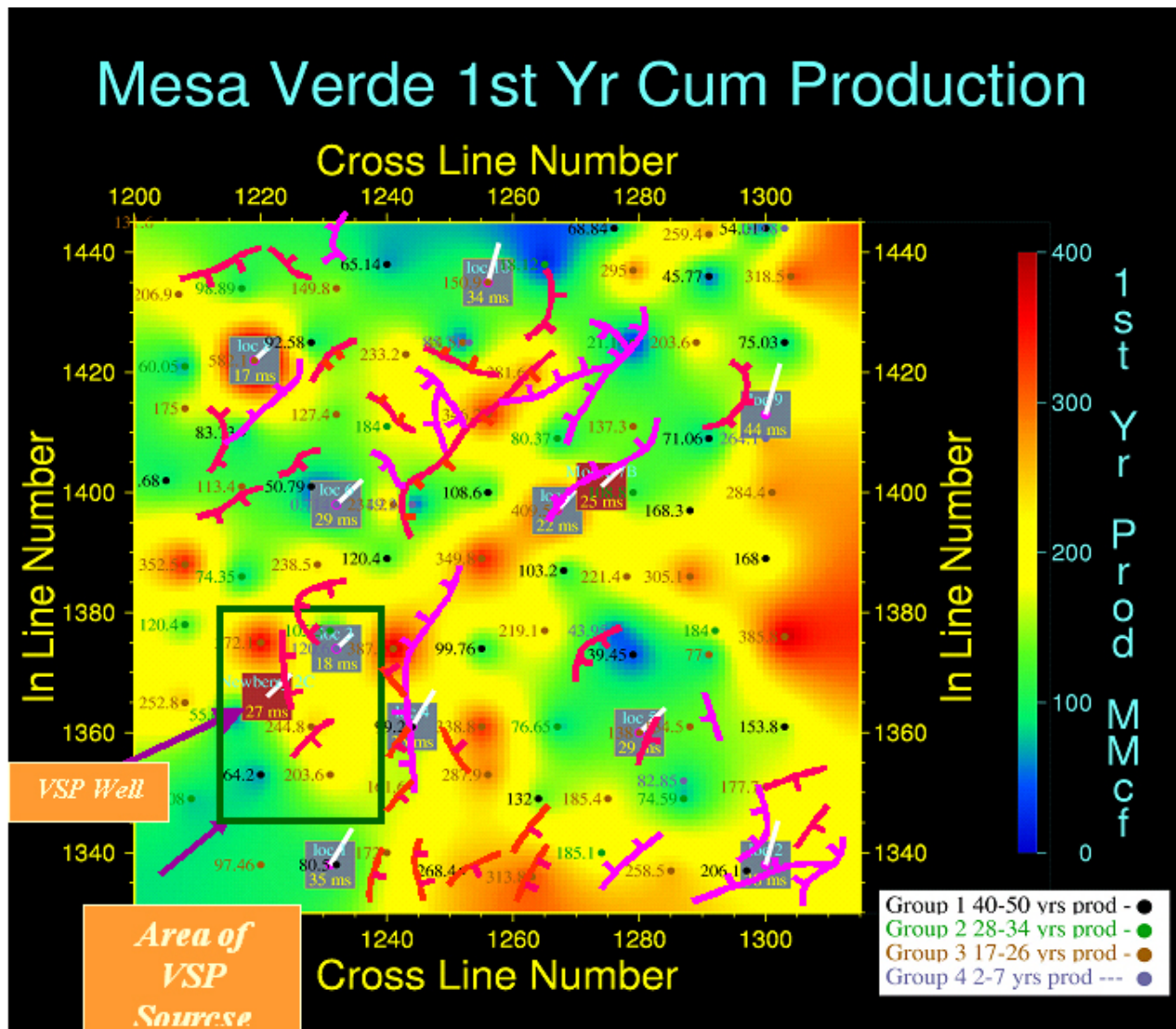


Figure 6-5. The result of over laying the final result of the method “A” fault picking.

Shown in figures 6-1 through 6-5 are also the directions of anisotropy picked at 10 well locations using the surface seismic. The “tadpoles” are the direction of P-wave velocity anisotropy and the values listed in the squares are the amount of anisotropy in milliseconds. There is little correlation between these values and the well production, in fact there is a reverse correlation in some cases. As was stated in the VSP analysis the shear wave anisotropy studies indicated that the observed shear wave splitting was not solely explained by one simple type of anisotropy. In the reservoir, the shear-wave splitting data do not provide sufficient constraints against a model of lower symmetry than orthorhombic, so that the existence of more than one fracture set cannot be excluded. VTI anisotropy in the Lewis shale, however, is well defined by a shear-wave line singularity.

## 6.2 INFORMATION ON FRACTURING FROM GEOLOGIC AND GEOMECHANICAL ANALYSIS

### Geologic Evidence of Fracturing

Figure 6-6 shows the stress directions and expected fracture/fault patterns in the San Juan area and the 20 square mile study area.

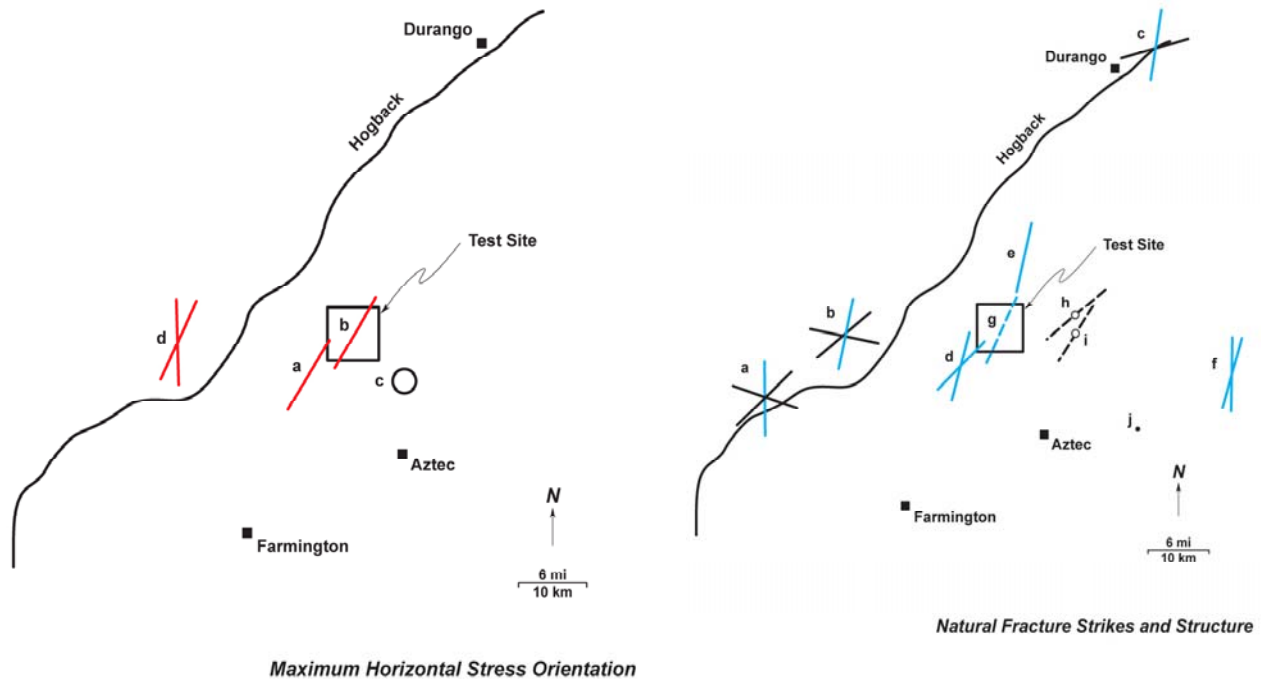


Figure 6-6. The maximum horizontal stress orientation derived from several different analysis and the natural fracture directions. The box shows the 20 square mile study area.

To derive the patterns in Figure 6-6 natural fracture orientations and characteristics from several wells and outcrops in the vicinity of the seismic test site were obtained and assessed during the course of this study. The well data consisted of cores and well bore image logs from the Mesaverde and Dakota formations. The cores are not oriented but give indications of millimeter to meter scale fracture characteristics such as mineralization and surface roughness that cannot be obtained from image logs. The image logs provided invaluable orientation data and covered much broader intervals of the formations of interest, but they are still an extremely limited, one-dimensional sampling of the reservoirs. The fracture data are keyed to the map in Figure 6-6 and are divided into outcrop data (a, b, and c on the map), image data (d, e, f, and g), core data (e and j), and structural data (h, and i). The blue lines in Figure 6-6 indicate major fracture strikes, black lines indicate secondary fracture strikes. Dots and dashed lines are locations and other structural trends discussed in the text.

---

Outcrop data from nearby sites provided complementary information on the lateral characteristics of the fracture systems and allowed a much broader view of the fractures, including estimates of fracture spacing and lengths that are difficult to obtain from vertical, subsurface data. However, outcrop data must be filtered in order to eliminate those fractures that may have been created in the strata by the uplift and exposure process, and that are not, therefore, present in the subsurface. The cores and image logs provided invaluable information on the in situ fracture characteristics that can be used to filter the outcrop data. The data presented below consist of images, cores, and outcrops, some of which are proprietary company data and which therefore cannot be completely described. In addition, several data points were obtained that bear on the larger, kilometer-scale fault systems in the basin and their effects on production.

Outcrop data were obtained from the Mesaverde Formation that forms the Hogback rimming the edge of the basin. The Waterflow pavement (location “a” on Figure 6-6; and the fracture map, Figure 6-7) show that three sets of natural fractures are present in the Mesaverde sandstones that crop out along the Hogback north of Waterflow, NM. When the strata are rotated from their present dip back to horizontal, these fracture sets strike approximately north-south, northeast-southwest, and southeast-northwest. Abutting relationships indicate that the north-south fractures are the oldest (see Figure 6-7) even though they are not as numerous as fractures of the other sets. Because of this relationship, and because the image and core data indicate that the younger fracture orientations are not present in the subsurface, the fractures of the older, north-south striking set are the ones most likely to be characteristic of the Mesaverde reservoirs.

These fractures are sub-parallel and have spacing that ranges from somewhat less than a meter to several meters. Their surfaces are weathered and therefore do not retain either mineralization that affects fracture permeability or the ornamentations that indicate their mode of origin, but parallelism between adjacent fractures and the lack of offset across fracture faces suggest that the fractures originated in extension. Fracture lengths are typically at least as long as the outcrops, i.e., they extend tens and probably hundreds of meters. These fractures contrast with the shorter, more closely spaced extension fractures typically found in outcrops of the more quartz-rich Dakota Sandstone.

Another example can be found on the Hogback closest to the test site that is located on lands belonging to the Southern Ute Indian tribe and therefore off limits without special tribal permission. It has low relief and does not form the best outcrops, so permission to visit these outcrops was not pursued. Better and more accessible outcrops occur both north and south of the area, and the outcrop data that were obtained are consistent, thus we are comfortable that the fracture characteristics reported here, though not immediately adjacent to the test site, are representative of fractures at the site. The location is marked a “b” in Figure 6-6. Ute Dome is an indentation in the Hogback where a basement-cored uplift has elevated Mesaverde and underlying strata to the surface and several hundreds of meters higher than equivalent strata along the Hogback. Despite the fact that it has been subjected to a different tectonic deformation history than the Mesaverde strata exposed on the Hogback described above, the three dominant fracture sets at Ute Dome have orientations similar to those found at the Hogback exposure. The north-south fracture set is again the oldest, and it is the most likely to be found in the subsurface. Fracture spacing on the orders of half a meter to a few meters are the norm except where closer spacing have been created along fault zones. Such fault zones may in fact dominate flow in

subsurface reservoirs where they exist, as documented below. The rose diagram derived from the fracture orientations is shown in Figure 6-8.

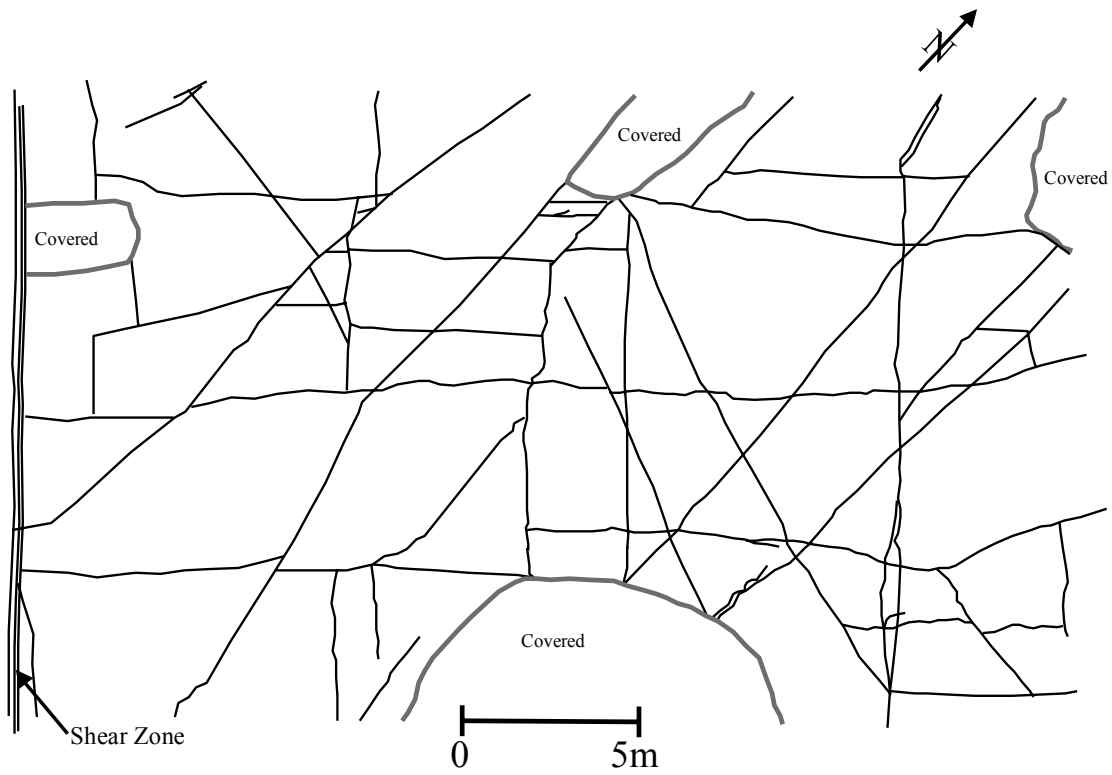


Figure 6-7. Sketch of fractures on a bedding surface of Mesaverde sandstones on the Hogback north of Waterflow, New Mexico (location "a" on Figure 6-6).

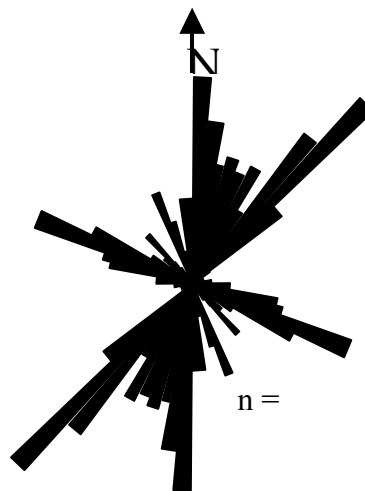


Figure 6-8. Rose diagram showing the strikes of 259 fractures measured on Ute Dome.

---

Several studies of fractures along the Hogback near Durango (among them Condon, 1997, Lorenz and Cooper, 2001). Location “c”, have documented an oldest north-south striking fracture set and a younger cross-fracture set in both the Mesaverde and the older, underlying Dakota sandstones. Condon noted that the main fractures in Mesaverde strata have an average strike of N15°E, consistent with the fracture orientations measured in both the Dakota sandstones and Mesaverde strata measured by Lorenz and Cooper. The younger, cross fractures are somewhat different between the two formations, however, Condon reports an average strike of N74°E in Mesaverde sandstones, whereas an irregular cross fracture strike, averaging about E-W, is present in the Dakota strata.

Several wellbore-image logs were run and several unoriented Mesaverde cores taken from wells near the seismic test site were studied. The logs corroborate the dominant north-south fracture set seen in outcrop but suggest that fractures of other orientations are largely absent in the subsurface. The cores confirm that the fractures are natural, rather than induced fractures, and that they are extension fractures with open, in situ aperture.

Image logs and cores (locations d, e, f, g, and j, Figure 6-6) and the FMI/image log data for the Moore and Newberry wells (location g, Figure 6-6), suggests that natural fracturing at the seismic test site is not pervasive. However, the probability of hitting vertical fractures with 8-inch diameter wellbores is actually fairly low (i.e., only 50% even if the fractures have an average, very close spacing of 16 inches), thus an absence of fractures in a wellbore does not definitively indicate that a reservoir is not fractured, whereas the presence of *any* fractures in a wellbore strongly suggests the presence of a subsurface fracture system (e.g., Lorenz, 1992). Regardless, the few fractures sampled by image logs at the test site have a north-northeast strike, consistent with both the oldest set of outcrop fractures and with the subsurface strikes of natural fractures in adjacent wells.

Other image logs from nearby locations (d, e, and f, Figure 6-6) recorded more pervasive natural fracturing in both the Mesaverde and Dakota intervals than observed in the Moore and Newberry wells at the test site, and the orientations are consistent, with local hints of two, conjugate fracture sets (locations d and f).

The well at location “e” was also cored through the Dakota interval, with fractures resembling those reported from the Dakota sandstones in an earlier memo. Horizontal shear fractures, vertical extension fractures, and vertical conjugate shear fractures are present in this core. Most of the natural fractures are extension fractures but there are suggestions of conjugate fracturing as well. Another class of horizontal shear fractures is present, locally abundant, in the #238R core. Natural fractures are most common in the well sorted, well cemented sandstones and seemingly non-existent in the poorly sorted, high porosity sandstones and conglomerates.

Location “j” plots the position of the Sunray H well that is the well closest to the test site for which Mesaverde core is available. The fractures in this core were above: they consist of a single set of parallel-striking, vertical extension fractures in sandstones, striking parallel to the present-day maximum horizontal compressive in situ stress. Fifteen percent of the total core length contains fractures, and 26% of the fracture-prone sandstones and siltstones are fractured. A fracture family is present in 68% of the thickest (25-ft thick) sandstone. Fractures in this principle reservoir consist of multi-stranded fracture families that extend top to base of the

---

reservoirs. These observations suggest that the reservoir strata contain significant numbers of sub-parallel fractures.

In terms of structure analysis (locations h and i, Figure 6-6) significant interference between well pairs aligned along north-northeast/south-southwest axes has been reported in two areas east of the test site. Significant interference between well pairs aligned along north-northeast/south-southwest axes has been reported in two areas east of the test site. Typically such interference is caused by a high-conductivity pathway that connects the two wells, usually assumed to be fracture-enhanced permeability associated with faulting. The first area, location “h” in Figure 6-6, Pasternak, (Pers. Comm., Amoco geologist responsible for this part of Amoco’s San Juan basin holdings several years ago) reports that production declined rapidly in one well after a second well was drilled about 1.5 miles to the southwest. By itself, this report would not be much to rely on, but it is corroborated by a more scientifically constrained study in the same area. Tom Engler (head of the Petroleum Engineering Department at New Mexico Tech) and Bruce Hart (formerly at Tech but now at McGill University) have been analyzing a 3D seismic shoot in this area and have reported marked production interference between three wells aligned along a north-northeast-south-southwest trend at location “i” on Figure 6-6. This trend is marked in the seismic survey by a distinct linear anomaly in strike curvature properties of the survey, which links the three wells. The wells and seismic trends are shown in Figure 6-9.

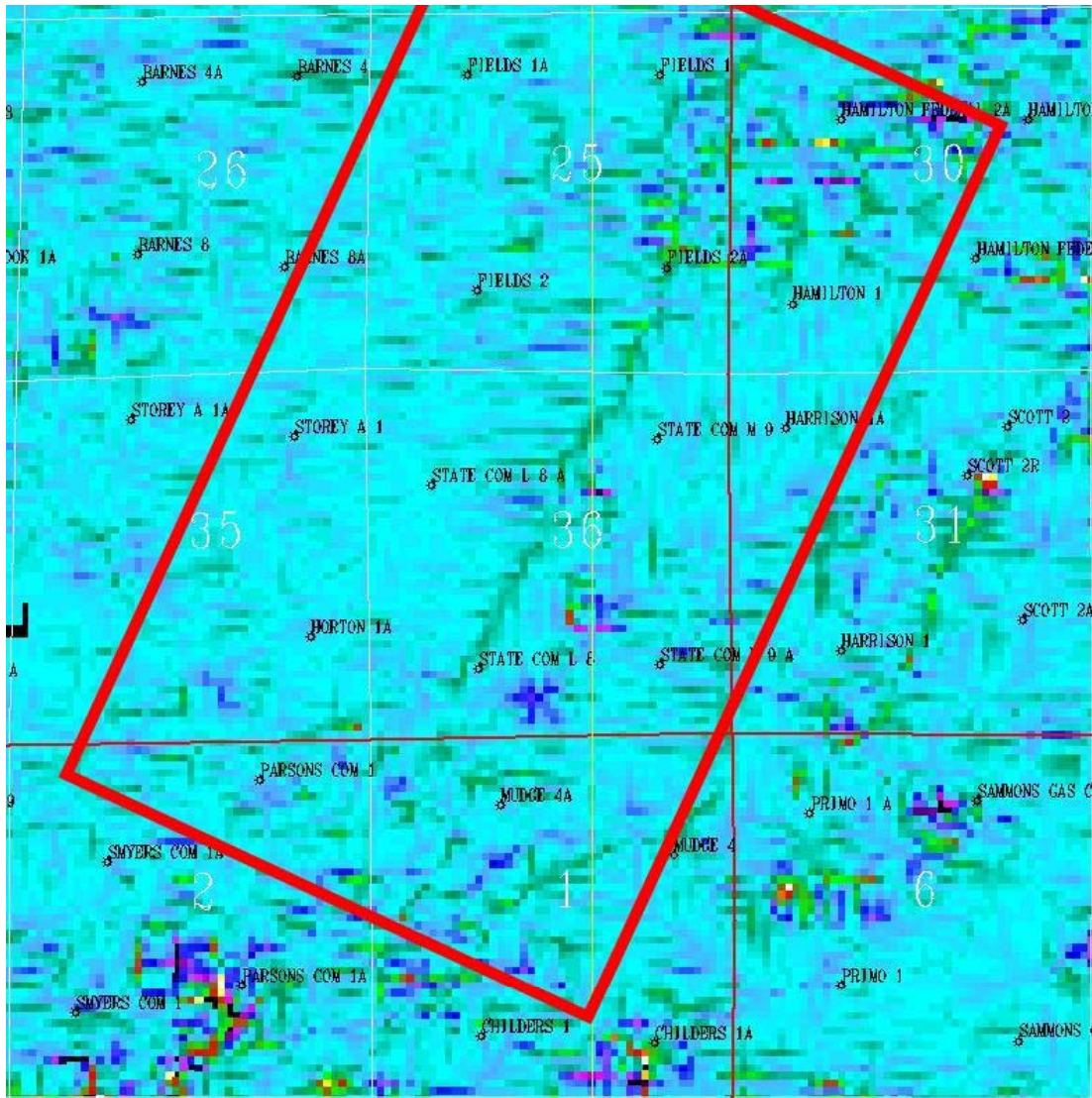


Figure 6-9. Strike curvature anomalies on the 3D seismic survey at location “i”. The green lines mark probable fault zones that have created fracture-enhanced permeability connecting three wells. Courtesy Bruce Hart, McGill University (see Hart et al., 2000.)

Therefore, using the geologic data from outcrops and other sources would imply that natural fractures in the subsurface at the seismic test site trend north-northeast/south-southwest. Data from nearby outcrops, cores, and wellbore image logs suggest that natural fractures are probably numerous in the subsurface reservoirs at this site despite the apparent dearth of fracturing in the Newberry and Moore wells. Estimated fracture spacing is on the order of one to five meters in Mesaverde sandstones, less in Dakota sandstones. Fractures are also more frequent along fault zones, which in nearby areas trend between north-northeast/south-southwest and northeast-southwest and are probably spaced a mile or two apart. They create pathways of permeability enhancement and allow anomalous interference between wells. The maximum, in situ, horizontal, compressive stress in the vicinity of the seismic test site trends approximately north-northeast/south-southwest. The data are few but they are consistent.

---

## Stress Measurements and Analysis

Turning now to stress measurements, there are fewer data points that record the orientation of the present maximum in situ compressive stress than there are that have measured fracture orientations at or near the seismic test site. Most of the data on stress orientation have been derived from coring-induced fracturing and wellbore breakouts seen in wellbore image logs. There are no measurements, published or otherwise, that we are aware of reporting the in situ stress magnitudes. All of the stress orientation data are considered to be proprietary by the various companies that took the measurements, and they can only be reported in general terms.

The FMI logs have been run in a number of wells across the basin, typically recording a north-south to north-northeast/south-southwest orientation for the maximum horizontal compressive stress. The well bore breakout data in the Newberry LS 2C well indicate a variable maximum horizontal compressive stress orientation, varying by depth/formation but with a limited range between north-south to N40°E. This is consistent with well bore breakout data from a well drilled to the southwest (location “a”, Figure 6-6).

Also, three FMI’s run in wells in the Ute Dome field farther to the west (location “d”) have recorded maximum horizontal compressive stress orientations ranging from north-south to northeast-southwest, but with a north-northeast/south-southwest trend dominating. These measurements confirm that some variability exists within in the local stress system but are generally consistent with the previous two data points. Variability is probably related to depth of burial, proximity to larger structures, and the different mechanical properties of the different formations. Finally, a tiltmeter/hydraulic fracture monitoring test ( location “c”, Figure 6-7) was run in the township immediately southeast of the seismic test site. This fracture test provides reliable data that are consistent with the above trends for the orientation of the maximum horizontal compressive stress. However, the stress orientation is not exactly parallel to that provided by the two data points to the west. These data are proprietary and cannot be presented here.

To further address the issues of potential fracturing geomechanical modeling was performed to infer possible subsidiary faulting or fracturing. Figure 6-10 shows the result of boundary element modeling that assumed NW-SE stress of 6 Mpa, SW-NE stress of 10 Mpa on the fault model in Figure 6-5.

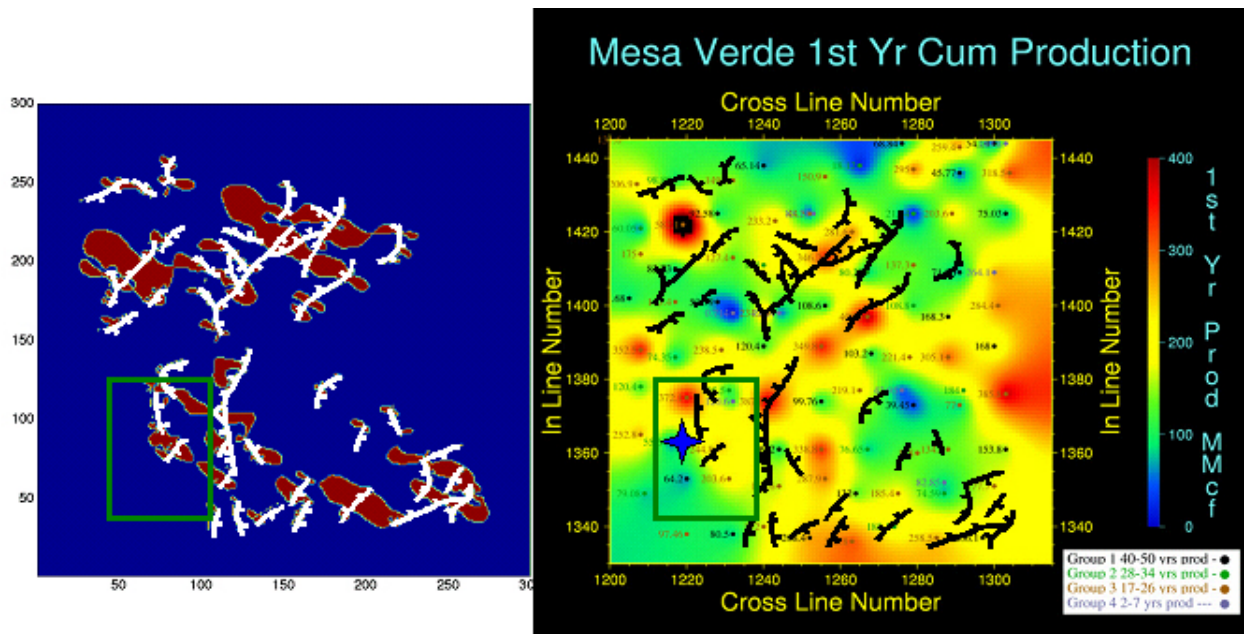


Figure 6-10. The results of the boundary element stress analysis compared to the production and fault map derived from the surface seismic data analysis. The green square is the zone of the VSP sources and the blue star is the well used for the VSP. The red zones on the left figure are the zones where the critical stress is 0.8 of failure. These are the zones in the model where the fractures may either may initiate or start to open.

A Young's modulus of 50Gpa , Poisson's ratio of 0.25 and a fault compliance of 10GPa/meter was used for the model. A simple Mohr-Coulomb envelope was used as a failure criteria. Figure 6-10 shows the stress values where the critical value (failure) is 0.8 next to the fault map superimposed on top of the production map.

The obvious question to ask is, is there a good correlation between the stress pattern produced by the faults and the production. To us there is a fair correlation but not a good correlation. If one were to have no production data and just the stress picture and sited wells on the high stress zones would the production be improved? In some cases yes, but in many cases it does not correlate well.

Three dimensional geomechanical modeling was carried out to determine if this would improve the understanding of the fault and fracture system. The surface seismic was interpreted again, this time at a much finer scale in the vicinity of the VSP well to derive a higher resolution fault model in the vicinity of the VSP.

Figure 6-11 shows a typical result of the 3-D geomechanical modeling of 15 of the faults. Poly 3D that was developed by David Pollard at Stanford was used to carry out this modeling. The purpose was to further understand if significant fracturing could be anticipated between the faults picked from the surface seismic data. Displayed in Figure 6-11 is the maximum tensile stress pattern expected around the faults picked in the vicinity of the VSP Newberry well. As can be seen using the best guess on the stress direction and magnitude (John Lorenz and Peter D'Onfro, personnel communication) the direction is generally consistent with the mapped fractures from the outcrop and core data as well as from the well logs, but the resulting stress pattern in Figure

6-11 infers a possibility of more complicated faulting which may develop between the fault tips. Figure 6-12 shows the Coulomb stress calculated.

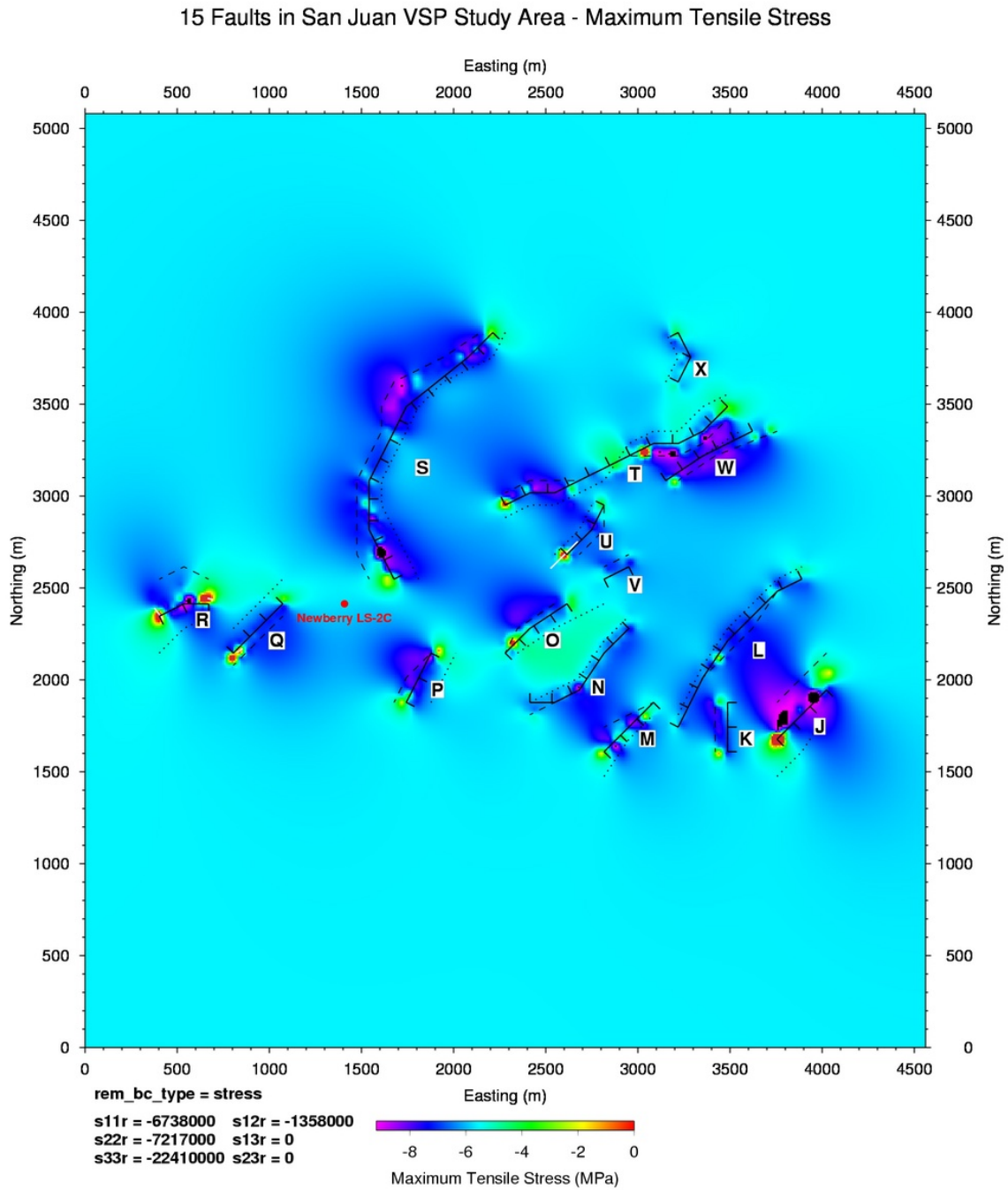


Figure 6-11. The maximum tensile principle stress model as calculated from Poly 3D for the 15 faults mapped from the surface seismic in the vicinity of the VSP well . The objective was to determine if one could anticipate subseismic faulting from the observed fault and stress directions.

### 15 Faults in San Juan VSP Study Area - Maximum Coulomb Stress

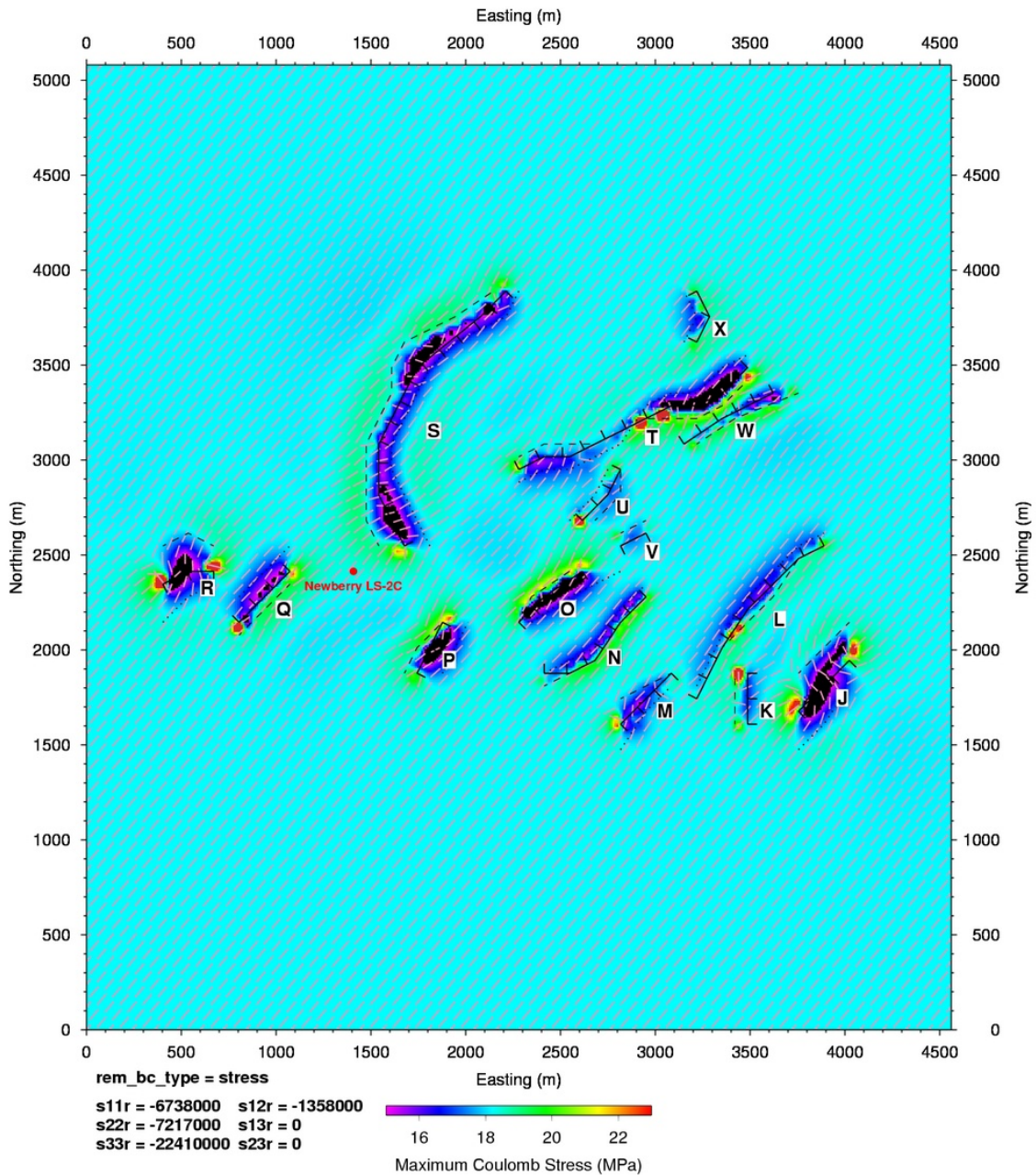


Figure 6-12. The maximum Coulomb stress model as calculated from Poly 3D for the 15 faults mapped from the surface seismic in the vicinity of the VSP well . The objective was to determine if one could anticipate sub-seismic faulting from the observed fault and stress directions.

The orientation of the maximum horizontal stress directions used was SSE 35 degrees, this was chosen to be consistent with the results of the core studies and the well logging. This was somewhat different from the shear-wave splitting results which concluded that SSE 55 degrees was the fracture direction in the vicinity of the VSP well. Many different model runs were

performed at varying angles but unless the angle was at radically different directions there was not much difference in the results. As can be seen in Figures 6-11 and 6-12 the stress accumulates at the tips and at the curvature of the faults, thus this is where one would expect the fractures or small faults to form.

The next obvious question is, does the P-wave anisotropy add information to the fault and fracture picture, or is it even consistent with the well log and modeling data? As seen in the analysis of the P-wave anisotropy studies of the surface seismic there were weak indications of P-wave anisotropy in the data. After a considerable analysis of the data there was some evidence that the data did have indications of anisotropy in time and amplitude. As discussed earlier a random set of fractures can give an appearance of no anisotropy, which would of course be the wrong conclusion for this area. If one compares the results of the surface P-wave anisotropy studies (for example Figures 4-20 through 4-28) to the contours of the production history (Figure 6-1) there is little correlation. If production is changing the stress distribution in the reservoir the direction of open fractures may also be changing. Thus the integrated production map would not be expected to be correlated with the seismic data. Last but not least an alternative conclusion is that the surface seismic is not detecting the fractures controlling the production. Although a negative conclusion it is important to note so that other data sets with higher resolution can be pursued.

### Integration of VSP Data

Next to consider is the VSP data. From the modeling we would expect to see scattered energy in the VSP (as well as the single well data). Therefore a search for the scattered energy was undertaken to identify any scatters. The procedure was to begin with ZZ and YY data, remove direct and multiple down going events, remove up going reflections and multiples. As seen in the modeling the YY data has the clearest signature of scattered events from nearly vertical features. The objective of the processing was to remove the direct and reflected arrivals and end up with the scattered energy, i.e., the energy that is usually processed away, see Figure 6-13

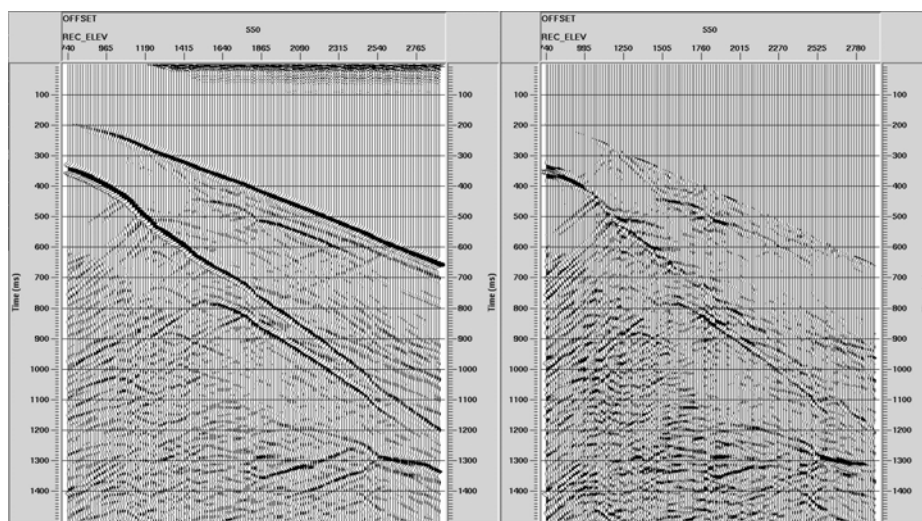


Figure 6-13. Example of data processed to show scattered energy, left side shows data before the down going and up going data are removed

Figure 6-13 shows a modeling example of scattered energy before the primary down going energy is removed (left hand side) and after the down going energy is removed (right hand side). Figures 6-14 shows the sites where the scattering analysis was carried out, both near and far sites were processed. Figures 6-15 show the sites where scattering was observed.

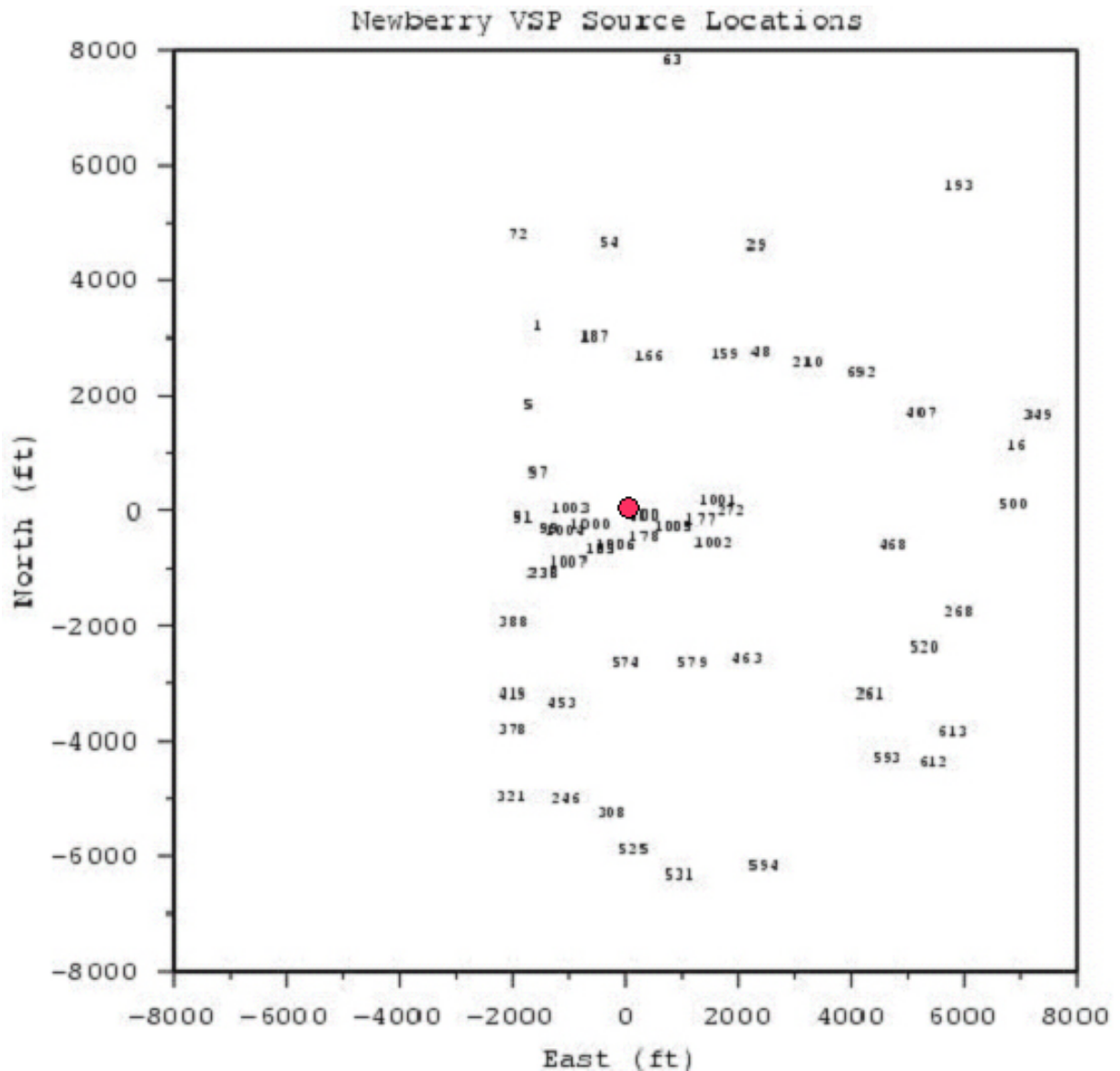


Figure 6-14. The sites where the scattering analysis was performed.

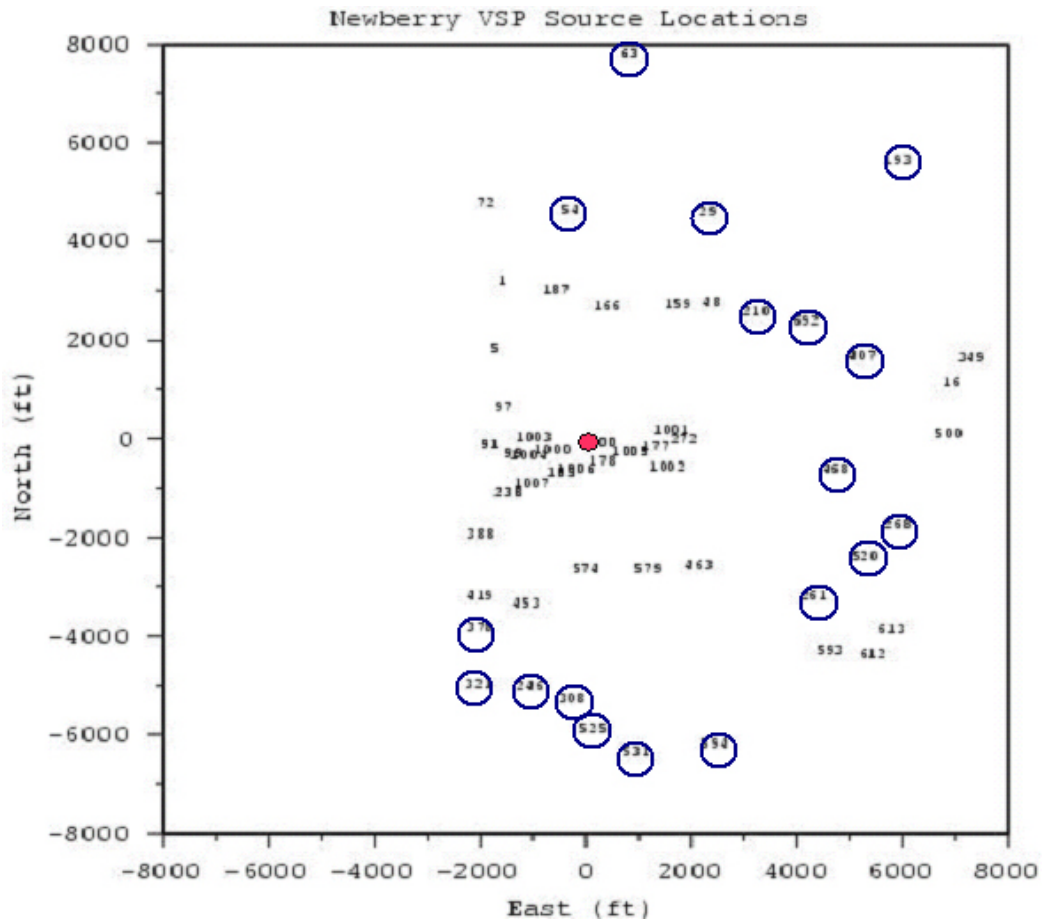


Figure 6-15. Sites where scattering was observed.

As can be seen from Figure 6-15 only the far offset sites show significant scattering. This may be due also to horizontally propagating energy as well as scattering.

Another important feature we wanted to investigate was the high amplitude zone seen in the single well data. The VSP were examined for reflections in the data at this point in the well. A good reflector was observed at this point (see Figure 6-16).

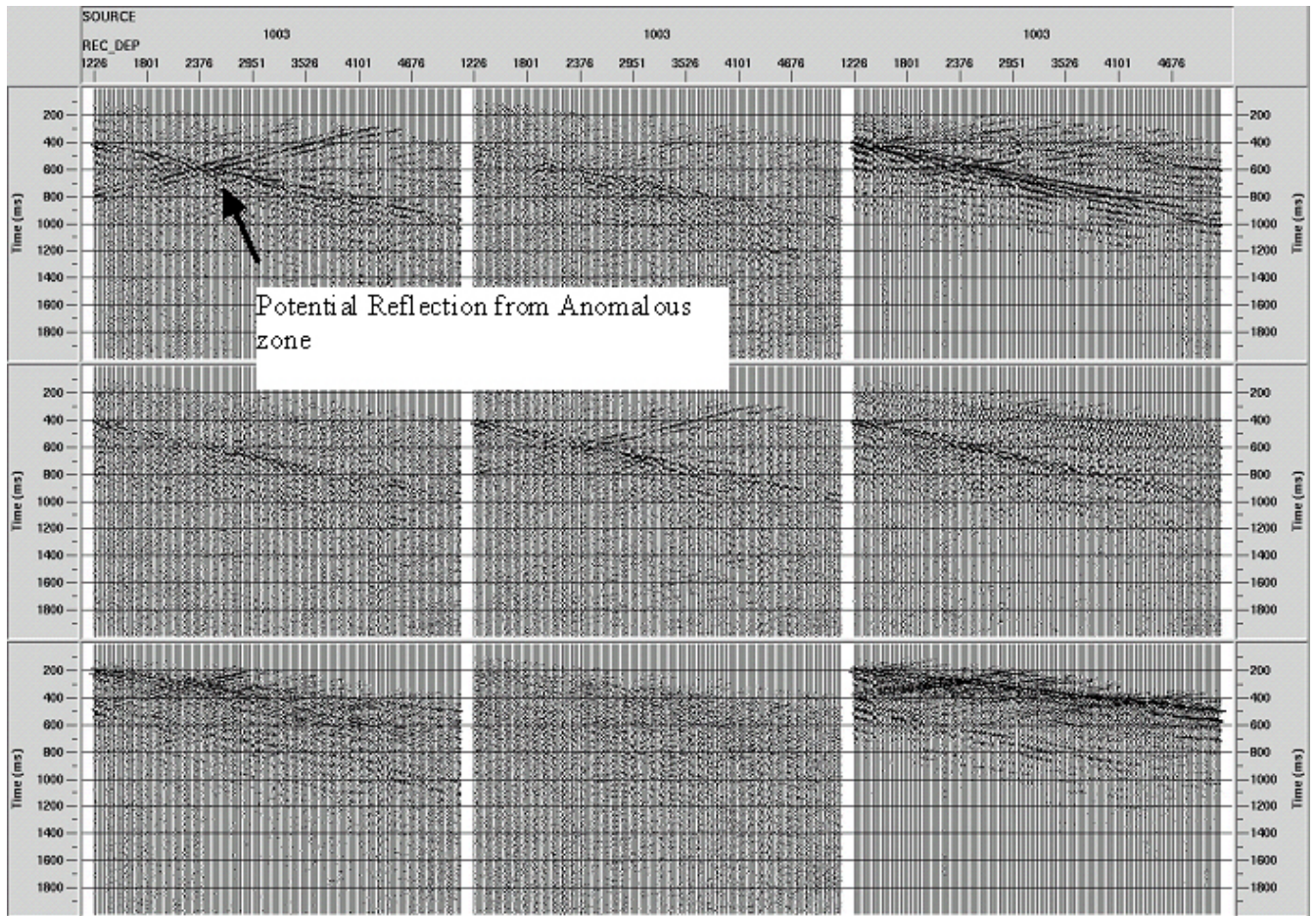


Figure 6-16. An example of the reflection observed in the VSP data at sites close to the VSP well.

Several sites next to the well had this reflection in the data. Figure 6-17 shows the sites where this reflector was observed.

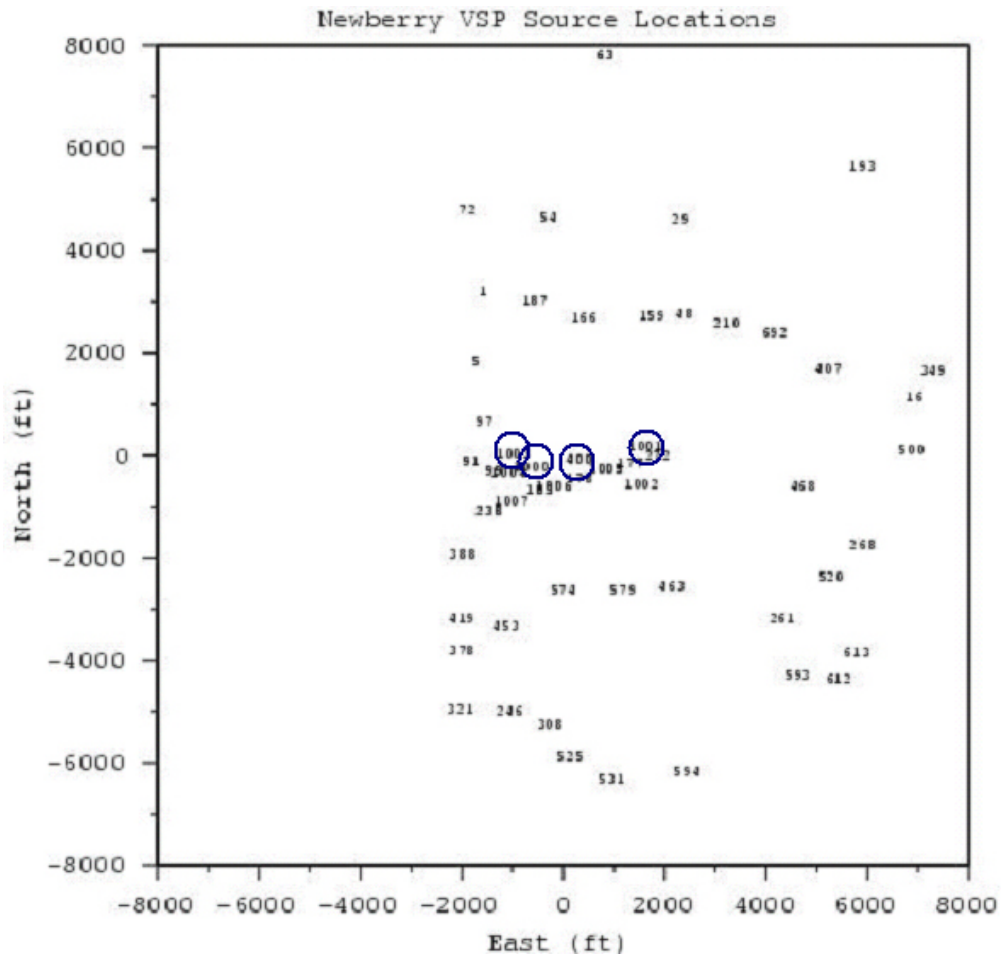


Figure 6-17. Sites where the VSP data showed a reflection from the zone where the single well data showed the high amplitude data.

Last but not least we consider the CDP data from the VSP. Figure 6-18 shows the locations of the VSP shots plotted relative to the projections of the faults mapped with the surface seismic in the vicinity of the VSP well. Figure 6-19 shows the data plotted in 6-18 with the production data superimposed. We wanted to determine if the VSP data could map the faults detected by the surface seismic, and/or pick up faults or evidence for faulting that was not detected by the surface seismic. In order to do this we examined various different VSP data sets that we thought may intersect not only the faults mapped with the surface seismic but zones of higher production. It should be noted that all of the VSP data were processed for CDP imaging. Ray tracing was done on the model to determine which VSP points would intersect the reservoir horizon and /or mapped faults. Space does not allow the display of all of the CDP plots, but example plots will be shown.

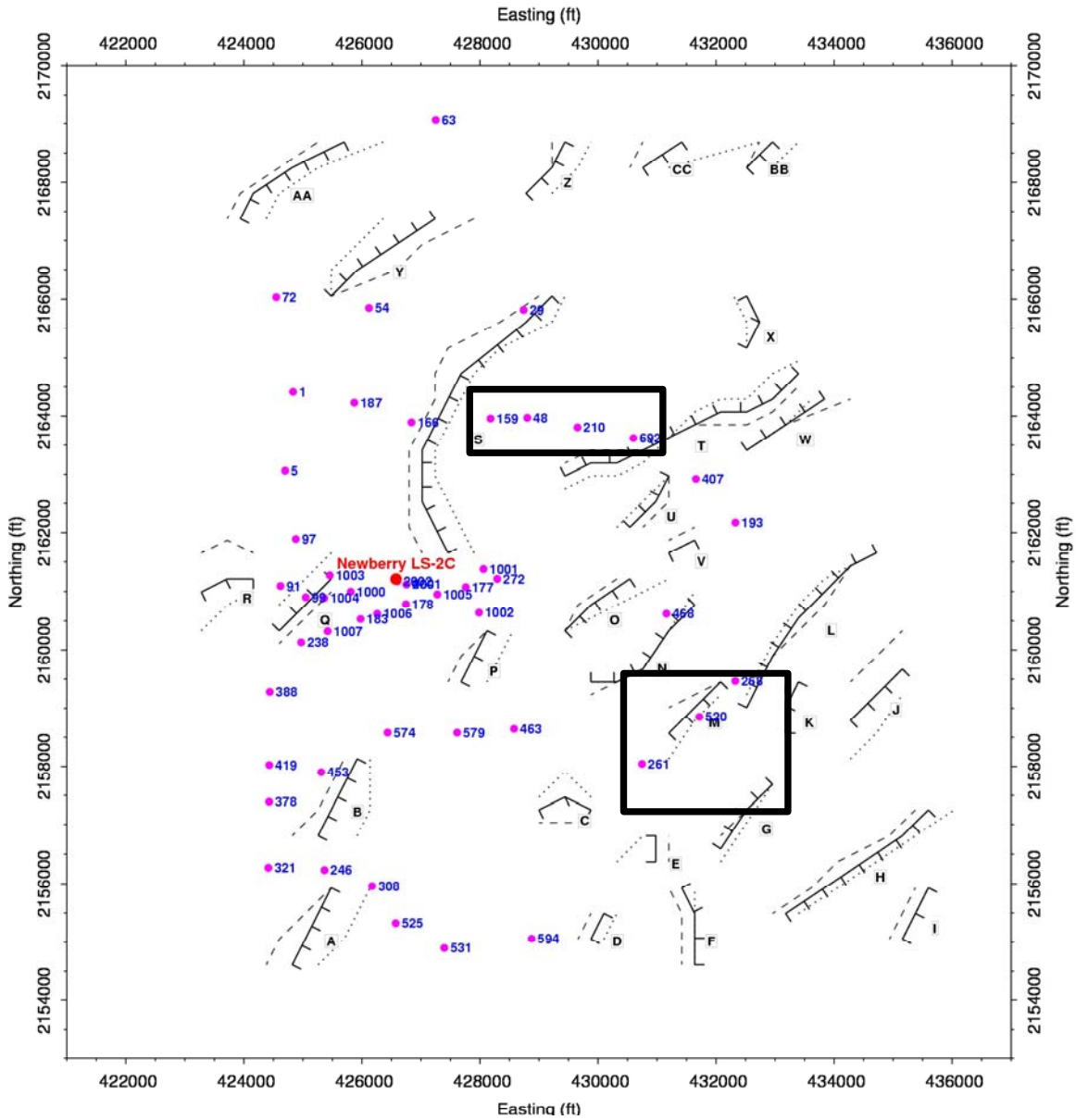


Figure 6-18. Location of the VSP shots with respect to the faults mapped with the surface seismic. The black boxes show the CDP VSP shot locations of the CDP results shown in Figure 6-20 and 6-21.

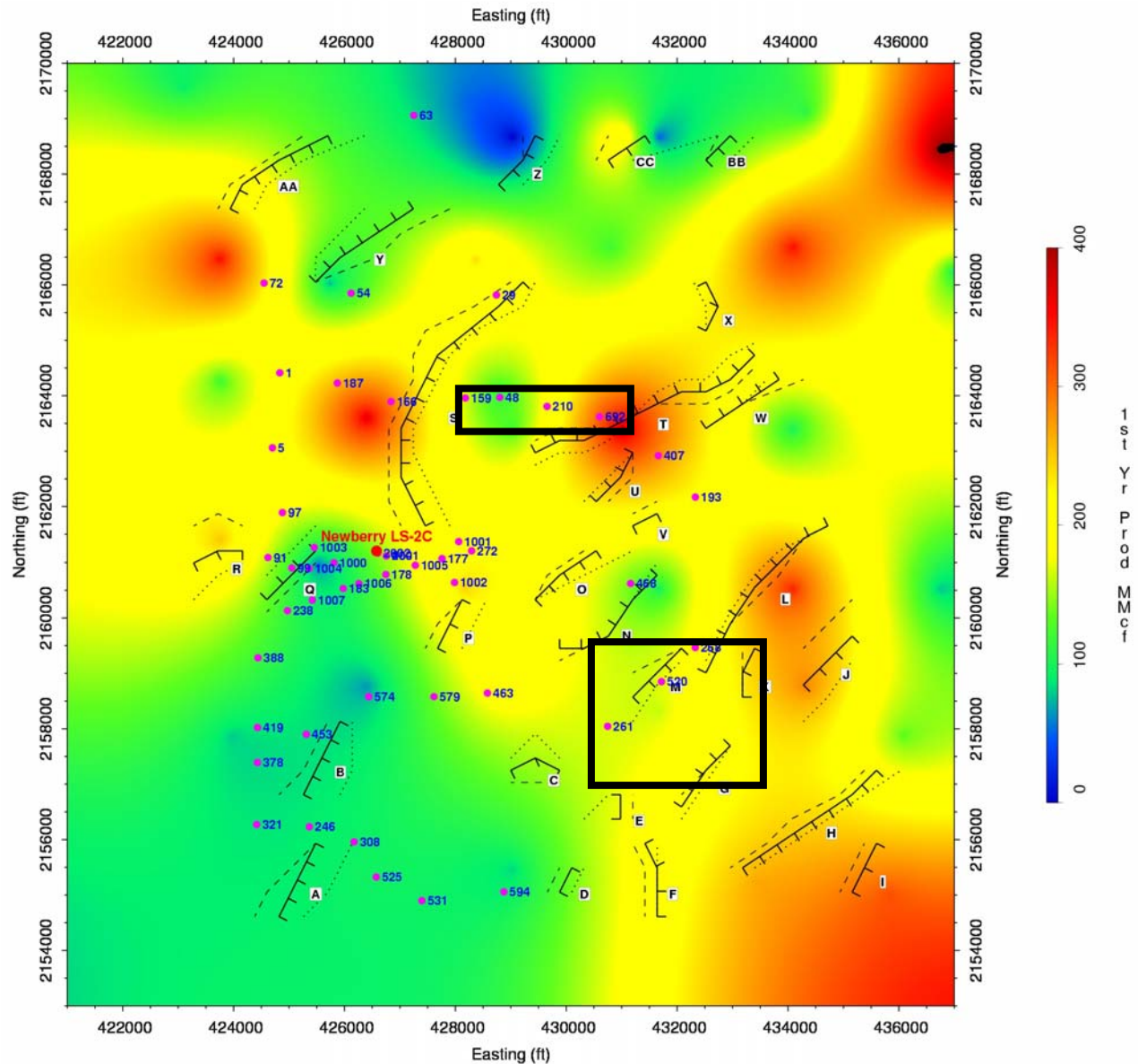


Figure 6-19. The Production data plotted with the VSP shot locations and the faults inferred from the surface seismic. The black box shows the CDP VSP shot locations of the CDP results shown in Figure 6-20 and 6-21.

Shown in Figure 6-20 are the final CDP stacks from the four shots in the top black box in Figures 6-18 and 6-19, i.e., shots 159, 48, 210 and 692. Also marked are interpreted faults/offsets that may indicate faulting. Figure 6-21 shows the CDP data from shots in the bottom black box in Figures 6-18 and 6-19.

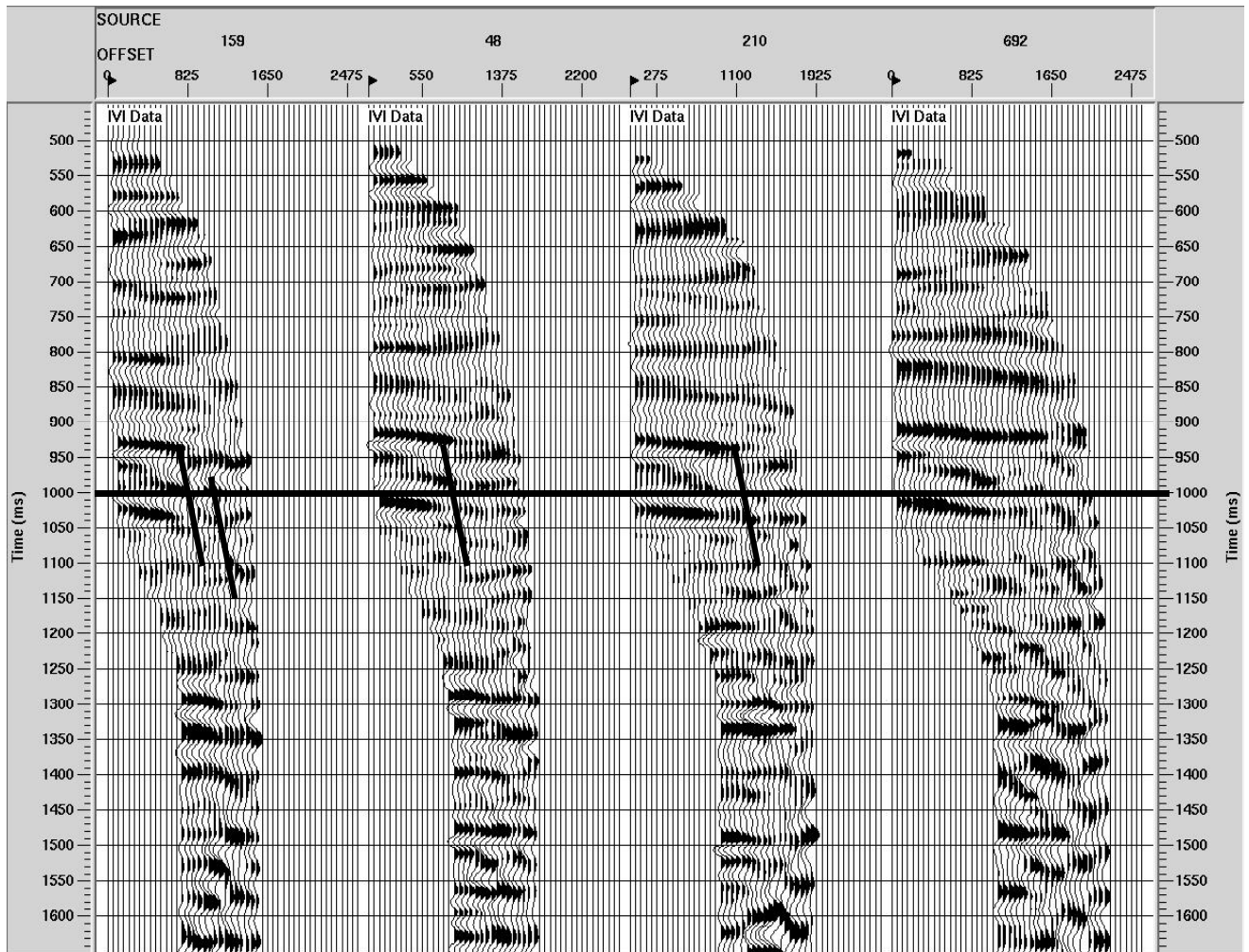


Figure 6-20. CDP images from shots from 159, 48, 210, and 692, the shots in the top black box in Figures 6-18 and 6-19. The data have been interpreted for faults.

The faults interpreted in Figure 6-20 are not inconsistent with the faulting interpreted in Figure 6-18 and 6-19. The VSP data were not as dense as the surface seismic, but as can be seen from these 2-D slices there is considerable offsets in the reflections. Figure 6-21 shows data from a different direction, the lower black box in Figures 6-18 and 6-19. (It should be noted that several of the shots shown in figure 6-21a and 6-21b are not plotted in the black box.)

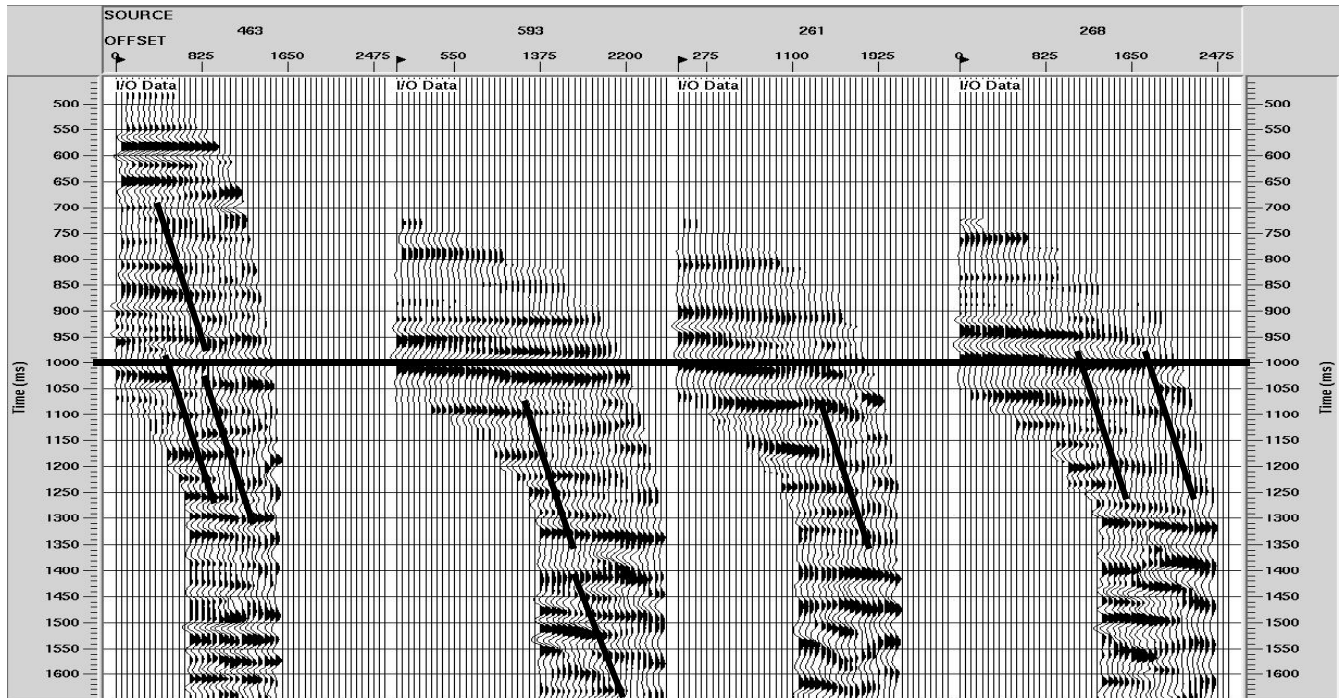


Figure 6-21a. CDP images from the lower black box in Figures 6-18 and 6-19, interpreted for faults.

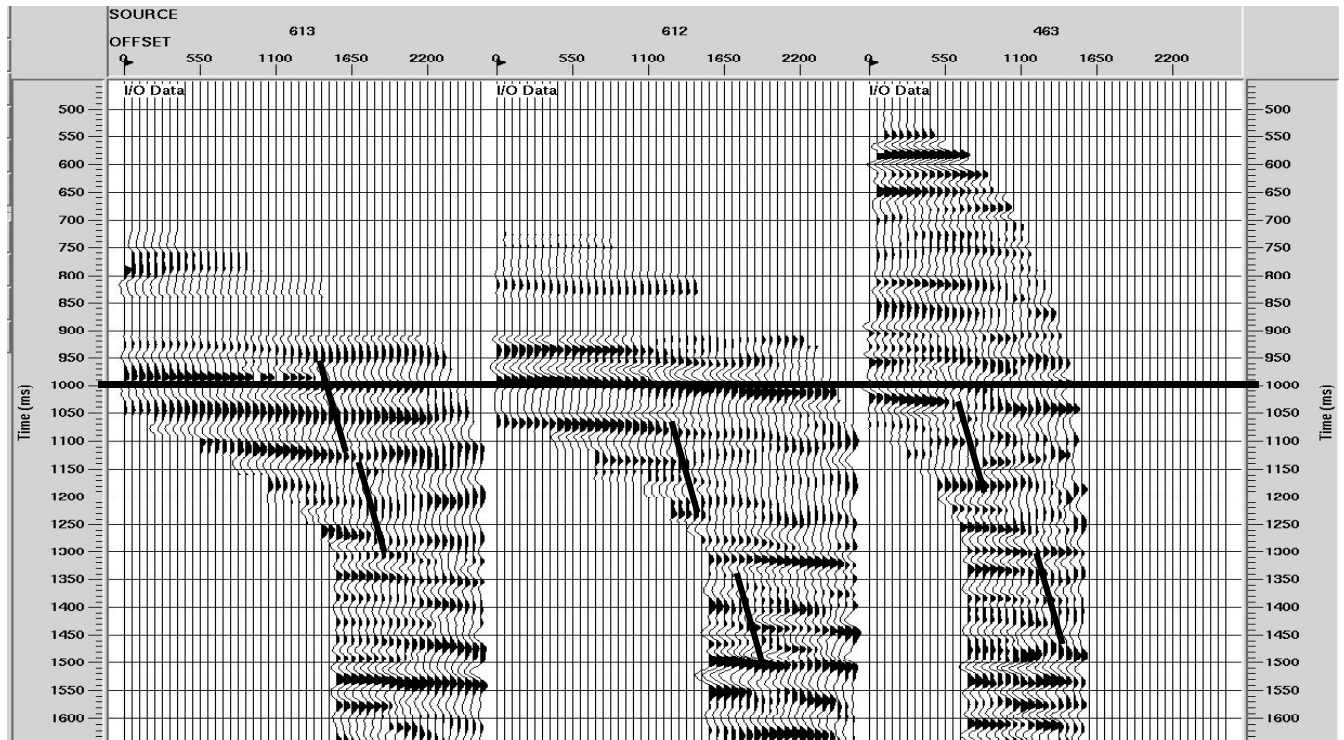


Figure 6-21b. CDP images from the lower black box in Figures 6-18 and 6-19, interpreted for faults.

As can be seen from Figures 6-20 and 6-21 there is considerable opportunity to pick heterogeneity in the data. Shown in Figure 6-22 is the tensile stress modeled with Poly 3-D from 15 faults in the vicinity of the VSP well.

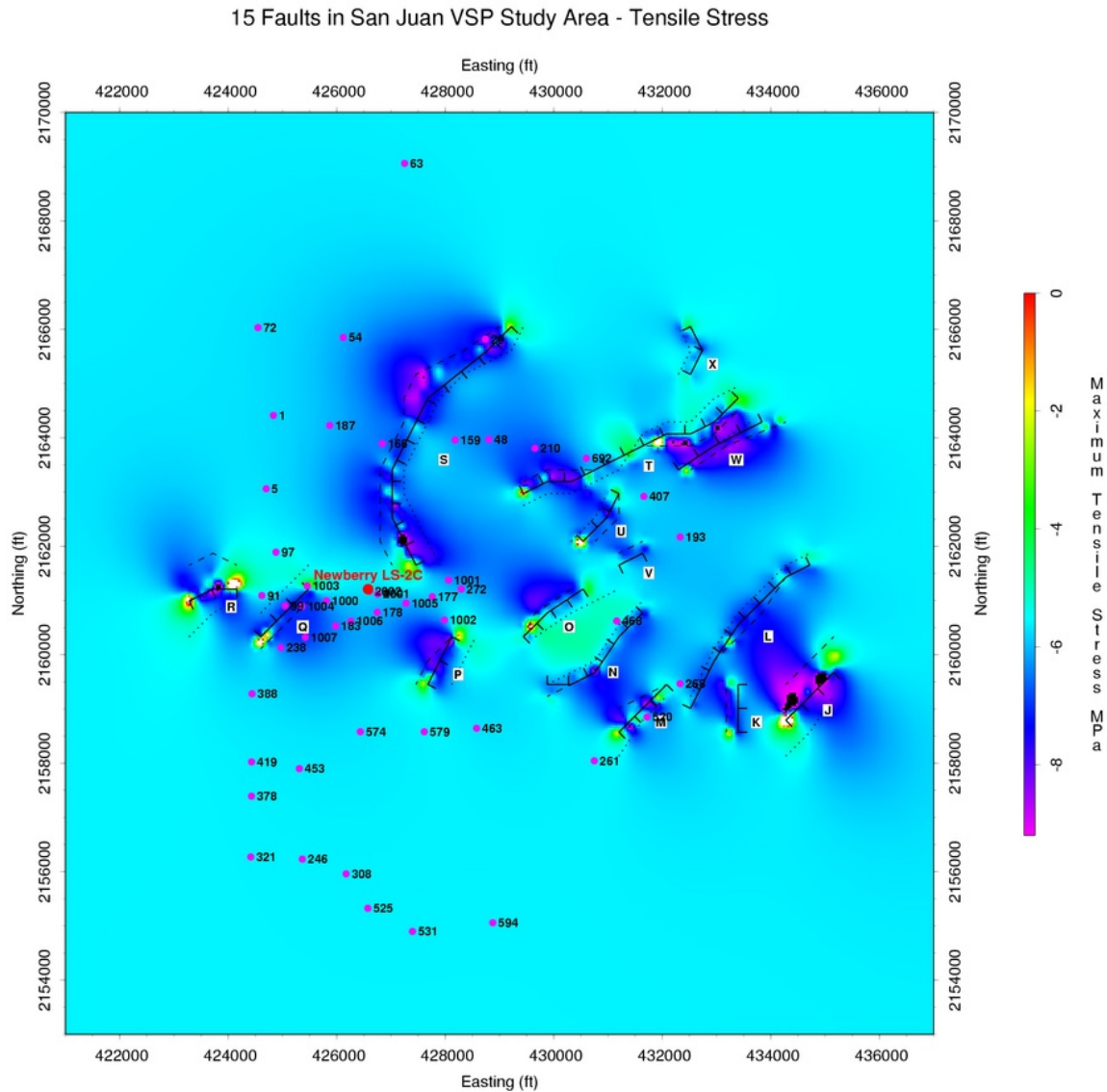


Figure 6-22. The tensile stress model from 15 faults in the vicinity of the VSP well.

The yellow and reds are the lower tensile stress, which if fractures were present would tend to open the fractures and possibly provide higher permeability. Figure 6-23 is the combination of the tensile stress, shot points and the production in the area of the VSP well.

15 Faults in San Juan VSP Study Area - Tensile Stress + Production

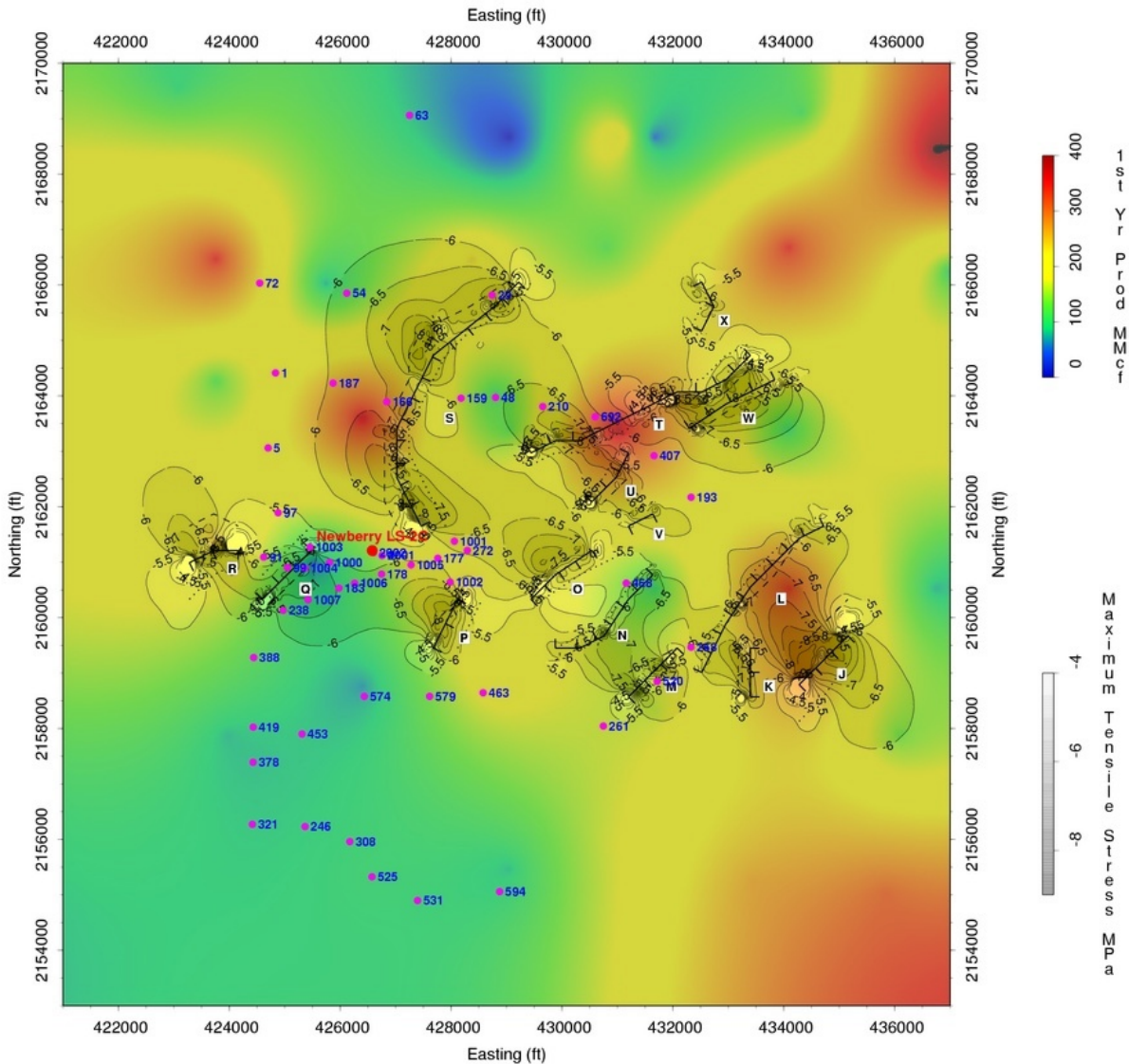


Figure 6-23. The tensile stress model from 15 faults plotted with the production data in the vicinity of the VSP well.

As can be seen it is a rather complex stress model. If we considered all the faults found by VSP it would undoubtedly be even more complex. From looking at the stress analysis a possible well target would be between faults N and O in Figure 6-23.

From the above analysis of the VSP data there is no one single indication of fractures, however, taken together the reflections, the shear wave splitting, the tomography analysis and the scattering results all point to a fractured complex system.

The only validation we have at this point is the production data from the Newberry LS 2C well. Shown in Figure 6-24 is the first month's production of the well. The well came on production

just a few weeks after the VSP was completed. The well was a very good producer, indicating high permeability and possibly a well connected fracture set. This was somewhat contradictory to the seismic data.

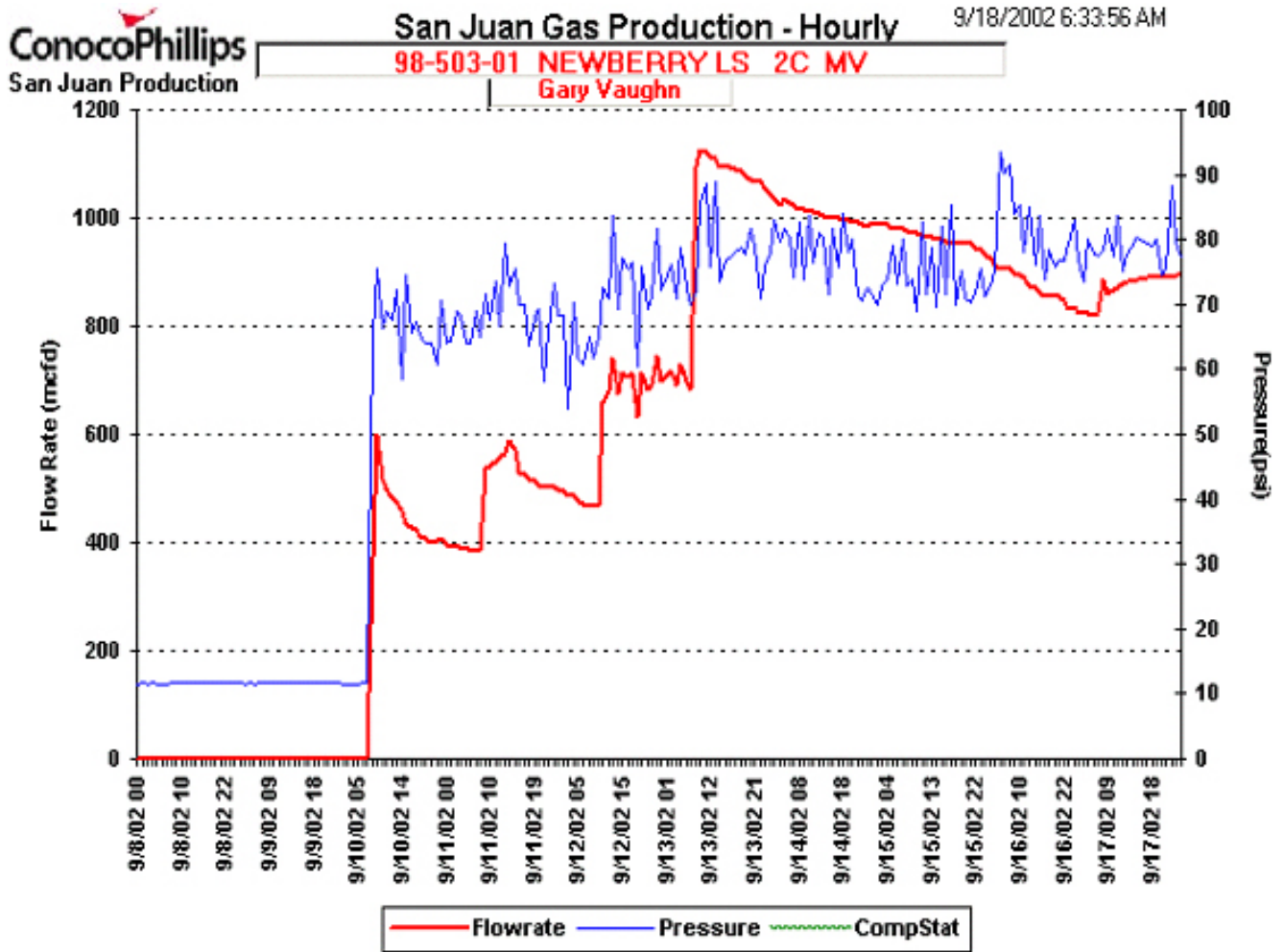


Figure 6-24. First month's gas production from the Newberry LS 2C well.

All of the seismic data, especially the well logs and the surface seismic, indicated that this well was not in a fractured or faulted zone and the fractures were relatively sparse. On the other hand the single well data (the high amplitude data) and the local VSP data indicate that locally there may be fractures. If one examines the production data after a year, however, a picture more consistent with the seismic emerges. Figure 6-25 shows the gas production for one year after the well was drilled. As can be seen the well soon started to decline in production and turned out to be a somewhat average well. This is more consistent with the seismic data in that if the well were drilled in a volume local fractures (as the VSP and single well suggested), hydrofracturing the well would possibly connect those fractures and produce very well for a short period, which was observed. It would be expected that the production would taper off to a lower value as observed if a larger volume was not fractured.



# San Juan Gas Production - 365 Day

1/21/2004 5:17:49 PM

San Juan Production

98-503-01 NEWBERRY LS 2C MV  
Gary Vaughn

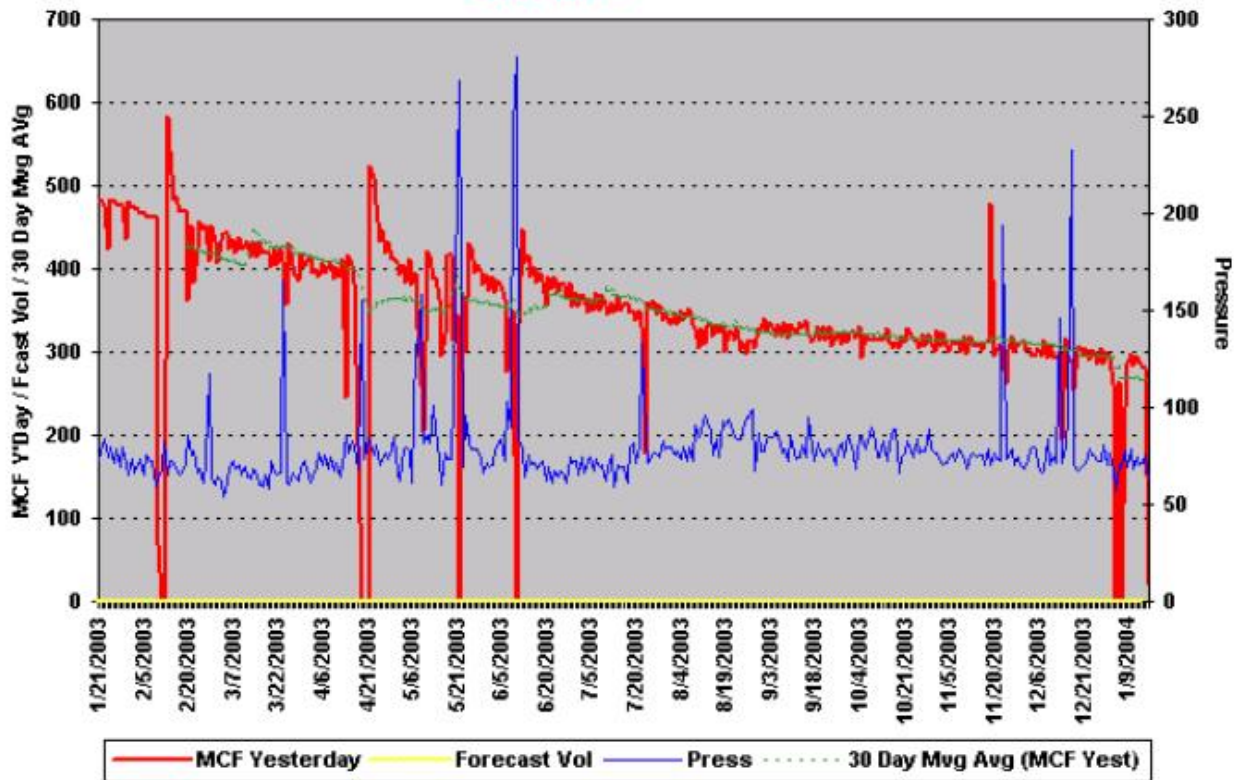


Figure 6-25. The last part of a full year's production from the Newberry LS 2C well.

In summary, by combining the seismic data from multiple scales has yielded a picture consistent with the production and known geology of the study area.

---

## 7. CONCLUSIONS AND RECOMMENDATIONS

This work focused on deriving the most efficient way to use seismic methods for characterizing fractures that are controlling production in fractured gas reservoirs in the San Juan Basin. It must be observed that this study was not over the entire San Juan basin but over a relatively small volume. It was in an area that is a complex zone with a variety of different structures and lithology. Overall, the conclusions and recommendations are:

1. While an analysis of the surface P-wave seismic data has not been able in this study to define reservoir scale fractures it has been of sufficient quality to image and orient regional to local scale faults. As such it can likely yield valuable information about the sub-seismic fracturing. In future work it would be recommended that higher fold, high frequency data be acquired prior to performing the interpretation outlined earlier. Specifically, interpretation should include the following practices, 1) an analysis of every line or every other line (and cross-line) – method A. If small scale reservoir fracturing (in the 10's to 100's of meters) is expected or present in the subsurface, then one should interpret seismic lines on the same physical scale. While every 10<sup>th</sup> line is sufficient in the Gulf of Mexico where line spacing is 12 meters, that same interpretation spacing is woefully insufficient in the San Juan Basin study area where the line spacing is almost 75 meters. 2) Time slices over the target horizons should be interpreted for faults (method B) but arbitrary line analysis should be undertaken with caution due to the possibility of bin jumping in displays. 3) Seismic volume and horizons based attributes should be analyzed for use with particular concentration on horizon azimuth. Surface seismic is meant for mapping large volumes of the subsurface at a resolution that can map controlling faults, but not faults that can be reliably correlated to production. 3-D P-wave surface reflection is useful for mapping broad anisotropy trends but not for fracture sets that are relatively discrete. 3-D seismic in general does give higher definition of faults and structure, which can be used to infer stress and fracture patterns, but not productivity. It should be noted that 3-D 3-Component surface seismic was not employed in this work. Thus it could not be evaluated. It has the potential to be of much greater benefit than P-wave, especially if combined with 9-C VSP.
2. After a considerable analysis of the surface seismic data for P-wave anisotropy there was some evidence that the data did have indications of anisotropy in time and amplitude. We of course have no absolute ground truth that this was due to fractures other than inference from core and well log data. On the other hand as we have seen from the interpretation of the surface seismic and cores the study area was in a very complicated stress zone and fault zone. If one compares the results of the surface P-wave anisotropy studies (for example Figures 4-22, 4-23 and 4-24) to the contours of the production history there is little correlation. A possible explanation is that the production history map covers both the Dakota and Mesaverde zones and is thus an integrated result. In contrast, Figures 4-22 to 4-24 are specific to different horizons and one would have a direct correlation if the production from each of these specific horizons could be compared. Another explanation is that the seismic is a snapshot in time of the reservoir. The production diagram is an

---

integration of the first year production over 50 years. If production is changing the stress distribution in the reservoir the direction of open fractures may also be changing. Thus the integrated production map would not be expected to correlate with the seismic data. Last but not least an alternative conclusion is that the surface seismic is not responding to the complex fractures controlling the highest production. The fractures in the study area are known to be heterogeneous and complex. It is possible that there are three distinct regimes in the study area: areas with no fractures; regions with a single fracture orientation in the NNE direction, and highly fractured zones with multiple fracture orientations due to the interaction of the regional stress field with the faulting. Wells drilled into areas with no fractures would have low production, and the surface seismic would also show low anisotropy. Wells in regions with a single fracture orientation would have intermediate production levels. Surface seismic measurements over such regions would show high anisotropy. Finally, wells drilled and hydrofracture treated in the highly fractured zones would have the highest production. In contrast, as discussed earlier, the effective anisotropy in such zones of multiple fracture orientations is low. Correspondingly, the surface seismic would show very little P-wave anisotropy. If indeed these three regimes of fracturing are present in the study area, the relationship between surface seismic anisotropy and production would be complex. The surface seismic P-wave anisotropy would still be useful. Zones of low anisotropy could be indicative of low productivity or high productivity. Low anisotropy zones could be prospective if they could be qualified by some of the many other methods discussed in this project.

3. The analysis of data from the 9-C VSP has given insight into the anisotropy structure with depth around the borehole. We can explain the observed shear-wave characteristics by a model composed of VTI and orthorhombic layers. The model is consistent with other information from borehole and surface seismic data, where available. In the reservoir, the shear-wave splitting data do not provide sufficient constraints against a model of lower symmetry than orthorhombic, so that the existence of more than one fracture set cannot be excluded. VTI anisotropy in the Lewis shale, however, is well defined by a shear-wave line singularity. Even for shots with low signal-to-noise ratio this singularity can be clearly observed. Effects of anisotropy are commonly studied in VSP data to gain insight into lithological properties of reservoirs, such as fracturing. In addition, the characterization of anisotropy from shear-wave splitting as demonstrated in this study could provide useful information for the processing of surface seismic data, where incorporating an appropriate anisotropic model in the overburden and the reservoir may improve the final image considerably. Furthermore, P-wave travel times from 3D VSP data are often inverted to obtain a detailed velocity field around the borehole. In this study where the data points are relatively sparse, the results of the shear-wave splitting analysis could provide necessary constraints for a more detailed inversion of travel times. Because of the relative sparseness of the VSP data the CDP mapping and the tomographic studies were limited in fracture detection. Although it was demonstrated that VTI and orthorhombic symmetry can be well defined from field data by analyzing shear-wave splitting patterns, a more detailed analysis would require more data. Especially the detection of shear-wave singularities provides clear constraints to distinguish between different symmetry systems. Therefore our prime recommendation for VSP is to employ number offsets comparable to the density of surface seismic with receivers also

---

comparable to surface seismic. The 9-C VSP has the potential to be of the highest value in terms of bridging different scales of application. From the above analysis of the VSP data there is no one single indication of fractures, however, taken together the reflections, the shear wave splitting, the tomography analysis and the scattering results all point to a fractured complex system. It was clear that the VSP methods could detect smaller scale features than the surface seismic (10's of meters) but to be effective they should be deployed at denser spacing than used in this study, i.e. source spacing on the order of surface seismic. Technology is now available to deploy large VSPs at relatively low costs. One would not cover the same volume as a surface seismic, but in selected areas to more fully understand and scale up to the surface seismic results.

4. The well logging had its traditional use in imaging the fractures and properties at the well bore. Breakouts and natural fracturing at the centimeter scale were detectable, similar to examining a core. While useful in a traditional sense, because of the sparse application of the fracture logs, they gave little understanding by themselves of the broad fracture trends, however, used with the other data they were the only ground truth we had in this study and used more extensively would have great value.
5. The single well data were limited and thus of limited value. The method has the potential to map fractures from the sub meter to the 10's of meters and thus bridge the gap between well logs and VSP. It also has the potential to map volumes from 10's of meters to several hundred meters away from the well in an open hole environment, thus providing information as the well is being drilled to provide information to target "sweet spots" in the reservoir. As a developing technique it may hold great potential. As processing and hardware capability advance it may be more widely deployed. There are no commercial vendors at the present time, but Schlumberger and P/GSI are developing the capability. It must be noted that it was the only method that directly correlated to gas content and production in the different well zones.
6. Last but not least the integration and interpretation of the methods depended heavily upon modeling of the data. In commercial application either no modeling or limited modeling is carried out. This leads to ambiguous interpretations and/or a lack of understanding of the potential of a data set. Finite difference modeling based on the displacement discontinuity formalism has been found to be valuable in a number of applications. Fundamental insight into the nature of discrete fracture response has been gained. Of particular interest are the mode converted events generated by discrete fractures and the need for finer scale sampling. In order to image these events with surface reflection seismic data, advanced imaging algorithms need to be developed and applied. The limit of specific fracture stiffness detectable in surface reflection measurements has been estimated at  $10^{10}$  Pa/m. The stiffness of a fracture controls the "detectability". The stiffer the fracture the more difficult it is to detect, thus higher frequencies must be used which implies borehole methods. Realistic earth models have revealed the complex interaction between fracture scattered seismic events and detailed layering. In attempting to apply sophisticated imaging methods to surface reflection data imaging discrete fractures, the velocity structure of the earth must be known in detail. Borehole seismic methods such as VSP and single well are seen to be more direct measurements of the fracture events. Finally, the use of full 3-D elastic modeling to process and interpret 3-D 9-C VSP data

---

has been illustrated. The geomechanical modeling linked with the geologic information provided valuable information to infer subsurface fracture patterns. Overall, sophisticated modeling capability is found to be a critical component in quantifying fractures through seismic data.

It is obvious that no one method can be used to map all the “productive” fractures. Each method has its strengths and weaknesses. One of the methods not tried in addition to 9-C surface seismic was crosswell. It also has the capability to bridge the resolution gap between VSP and well logging/small scale single well imaging. If wells are available it may be of great use in the San Juan Basin. It appears that surface seismic was not able to resolve the fractures on a scale of the proper dimension. The other methods (single well and well logging) were at too fine a scale. All of these methods depend upon cost, well availability, and commercial availability.

Overall, if we were to repeat our efforts in the most efficient way, the method of choice would be dense 9-C VSP coverage. Today’s commercial systems may prohibit such a venture, but as vendors offer more and more levels of VSP coverage it may become cost effective. Looking further to the future, if drilling becomes more cost effective multiple VSP surveys would be very cost effective, linked with multiple receiver strings and source points. This would also allow the crosshole and higher resolution methods such as single well to be applied as well as time lapse studies to infer fracture response, probably the most reliable and powerful method of quantifying fractured reservoirs.

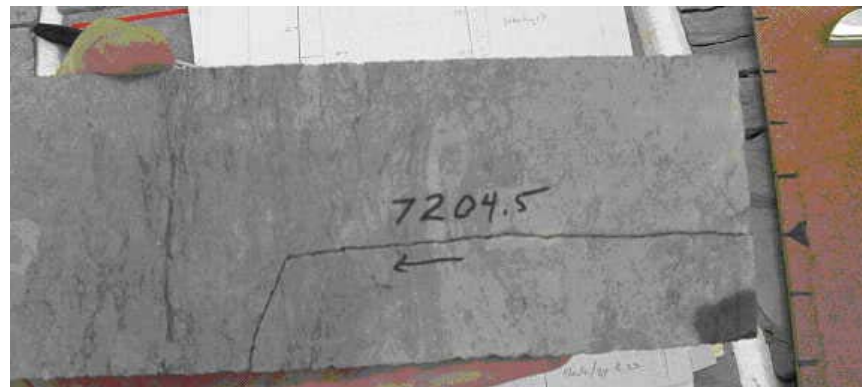
---

**APPENDIX I—CORE FROM PICTURES FROM 28-7 #225E AND THE MERIDIAN  
SUNRAY H COMM 6 WELLS**

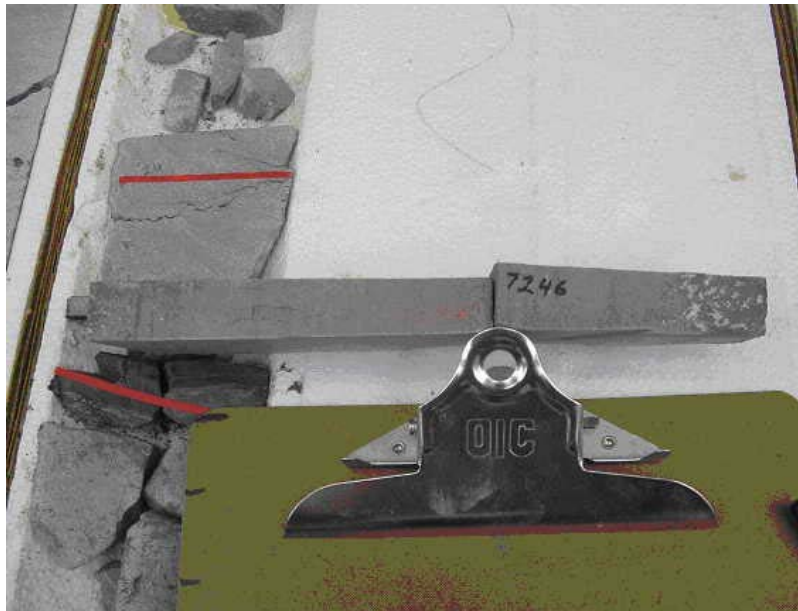
**A.1 CORE FROM THE 28-7 #225E WELL, DAKOTA SECTION**



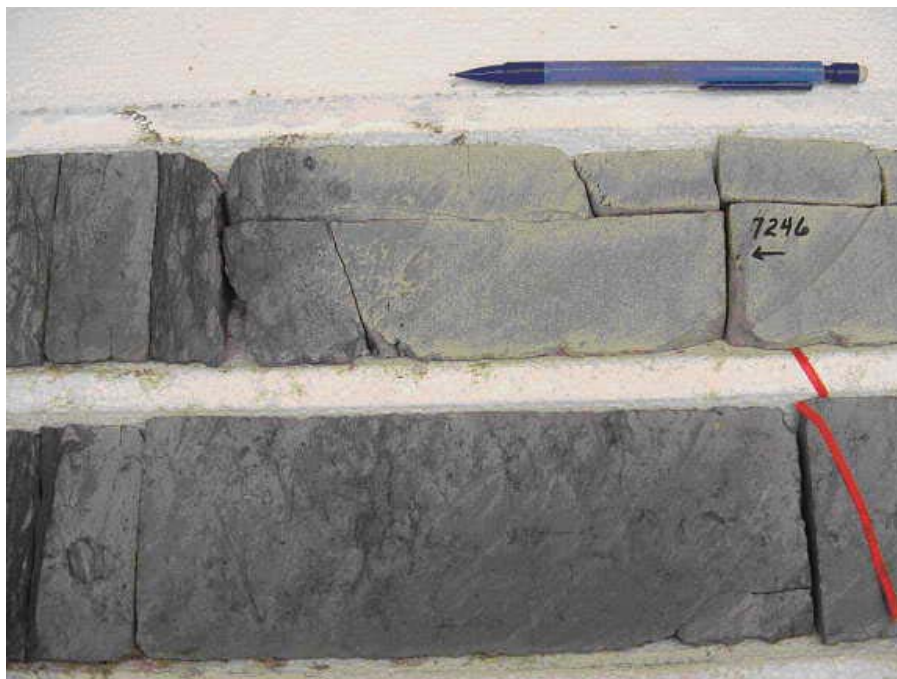
Parallel petal fractures (outlined in dotted black lines) and an inclined un-mineralized fracture, San Juan 28-7 #225E.



Vertical natural fracture in the San Juan 28-7 #225E core. Surface of this fracture is coated with patchy iron-rich dolomite rather than the more common calcite and it is one of the few fractures that is not parallel to petal fractures, suggesting it represents a subordinate fracture set. Arrow points uphole. (The oblique splay off of the fracture at the upper termination is where the core broke during handling and is not part of the fracture.)



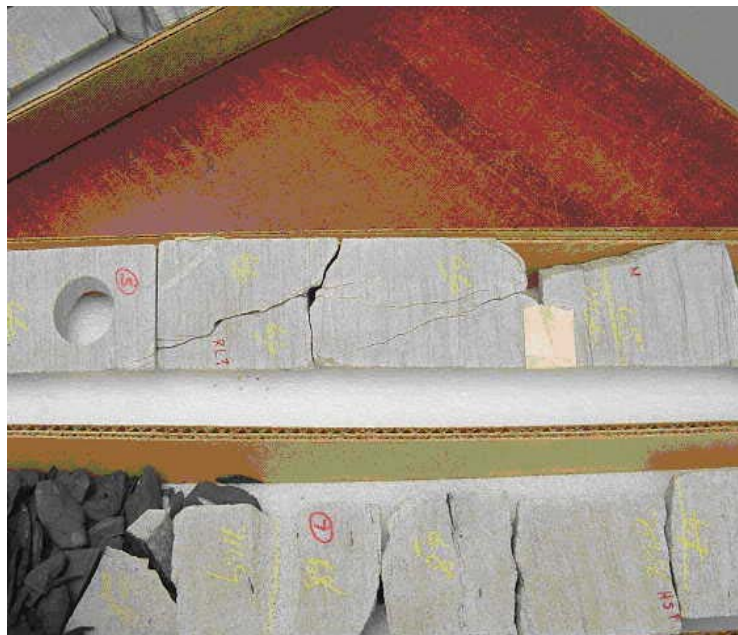
Patchy calcite mineralization at the right side of the photo coats only the face of the fracture where it narrowed before terminating in the overlying silty lithology. San Juan 28-7 #225E.



Same fracture as above showing the natural fracture expression on the slabbed face of the core.



Same interval as previous two photos, showing the parallel relationship between the strike of the natural fracture (“N,” with the depth marking printed on the fracture face) and the strike of the coring-induced petal fracture (“P”).



Inclined fractures, possibly from a conjugate set, cutting obliquely across the core in the San Juan 28-7 #238R well.



Scribe line, marked in yellow, that has imparted sufficient strain to the core to crack it. The induced fracture on the slabbed face resembles a natural fracture. San Juan 28-7 #238R



Inclined fracture (above pencil), stylolite (at pencil point) and horizontal shear planes ("HS") in the San Juan 28-238R core.



Intersection between two natural fracture faces (upper right to lower left, and a very short top-to-bottom, as highlighted in magic marker) and the slabbed surface of the core (against the palm of the hand). San Juan 28-7 #238R

**A-2 CORE FROM THE MERIDIAN SUNRAY H COMM 6 WELLS, MESAVERDE SECTION**



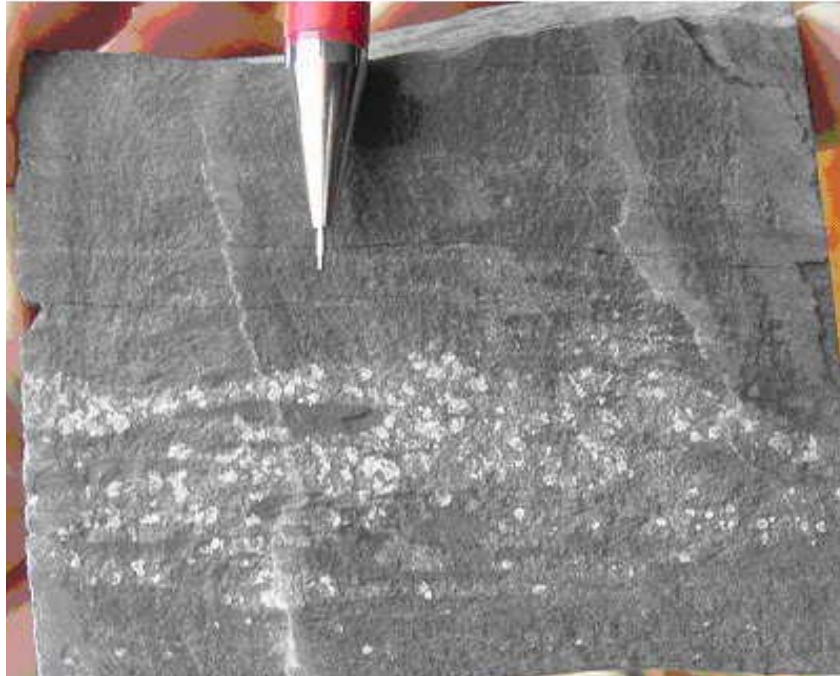
Short vertical extension fracture, terminating top and bottom at bounding lithologies.



Opposing faces of a horizontal shear fracture



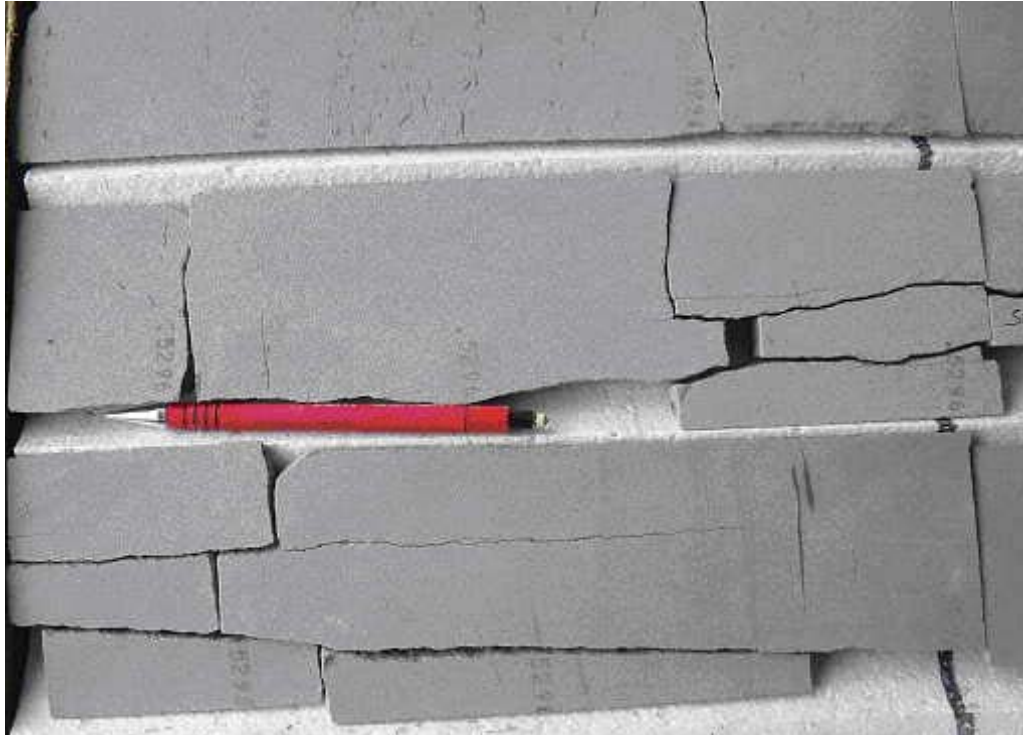
Two parallel vertical extension fractures. Apparent irregularity of the fracture plane is an artifact, accentuated by the narrow angle between the fracture plane and the plane of the slabbed face.



Millimeter-scale patches of calcite cement on a fracture face, concentrated along the gray, fine-grained sandstone layers in a darker siltstone bed near the top of the largest fracture noted in the core.



Open fracture aperture along the largest fracture noted in the core.



Multiple parallel fracture planes in a thick sandstone



Plume structure on an unmineralized fracture face, indicating that the fracture formed in extension, not shear. The axis of the plume is horizontal (stratigraphic up is to the right), indicating that the fracture is natural.

---

## REFERENCES

- Aid, K. and P. O. Richards (1980). *Quantitative Seismology*, v. 1, W. H. Freeman and Co., New York.
- Alford, R. M., 1986, Shear data in the presence of azimuthal anisotropy: Dilley, Texas, 56<sup>th</sup> Ann. Internat. Mtg., Soc. of Expl. Geophys., Session S9.6.
- Angel, Y. C. and I. D. Achenbach (1985). Reflection and transmission of elastic waves by a periodic array of cracks, *J. Appi. Mech.*, 52, 33-41.
- Baltz, E. H., 1967, Stratigraphy and regional tectonic implications of part of Upper Cretaceous and Tertiary rocks, east-central San Juan basin, New Mexico, Geological Survey Professional Paper 552: Washington, U.S. government printing office, 101 p.
- Baltz, E. H., 1978, Resume of Rio Grande depression in north-central New Mexico, Guidebook to the Rio Grande rift in New Mexico and Colorado, New Mexico Geological Society, p. 210-228.
- Bat J.-M. and R. B. Thompson (1984). Ultrasonic scattering from imperfect interfaces: A quasi-static model, *I. Nondestr. Eva!*, 4(3/4), 177-196.
- Brown, S. R. and C. H. Scholz (1985). Closure of random surfaces in contact, *J. Geophys. Res.*, 90, 5531.
- Brown, S. R. and C. H. Scholz (1986). Closure of rock joints, *J. Geophys. Res.*, 91, 4939.
- Budreck, D. E. and J. D. Achenbach (1988). Scattering from three-dimensional planar cracks by the boundary integral equation method, *J. AppI. Mech.*, 55, 405-412.
- Bush, I. and Crampin, S., 1991, Paris Basin VSPs: case history establishing combinations of fine-layer (or lithologic) anisotropy and crack anisotropy from modelling shear wavefields near point singularities: *Geophys. J. Int.*, **107**, 433-447.
- Cather, S.M., 1989, Post-Laramide tectonic and volcanic transition in west-central New Mexico, *in* Anderson, O.J., Lucas, S.G., Love, D.W., and Cather, S.M., eds., *Southeastern Colorado Plateau*, New Mexico Geological Society 40th Field Conference Guidebook, p. 91-97.
- Cerjan, C., D. Kosloff, R. Kosloff, and M. Reshef (1985). A nonreflecting boundary condition for discrete acoustic-wave and elastic-wave equations. *Geophysics*, 50, 705-708.
- Chapin, C.E., and Cather, S.M., 1981, Eocene tectonics and sedimentation in the Colorado Plateau-Rocky Mountain area, *in* Dickinson, W.R., and Payne, M.D., eds., *Relations of tectonics to ore deposits in the southern Cordillera: Arizona Geological Society Digest*, Volume 14, p. 173-198.

- 
- Coates, R. T., and M. Schoenberg (1995). Finite-difference modeling of faults and fractures, *Geophysics*, 60, 1514-1526
- Condon, S. M., 1997, Geologic mapping and fracture studies of the Upper Cretaceous Pictured Cliffs sandstone and Fruitland Formation in selected parts of La Plata county, Colorado: USGS Open-File report 97-59.
- Corbitt, L.L., and Woodward, L.A., 1973, Tectonic framework of Cordilleran foldbelt in southwestern New Mexico: *American Association of Petroleum Geologists Bulletin*, v. 57, p. 2207-2216.
- Crampin, S. and Yedlin, M., 1981, Shear-wave singularities of wave propagation in anisotropic media: *J. Geophys.*, **49**, 43-46.
- Crampin, S. and Lovell, J., 1991, A decade of shear-wave splitting in the Earth's crust: What does it mean? What use can we make of it? And what should we do next?: *Geophys. J. Int.*, **107**, 387-40.
- Crampin, S. (1984). Effective anisotropic elastic constants for wave propagation through cracked solids, *Geophys. J. Roy. Astr. Soc.*, 76, 133- 145.
- Daley, T.M. and Cox, D., 2001, Orbital vibrator seismic source for simultaneous P- and S-wave crosswell acquisition, *Geophysics*, 66, 1471-1480.
- Daley, Thomas M., Ernest L. Majer, Roland Gritto and Jerry M. Harris, 2000b, Progress and Issues in Single Well Imaging, Society of Exploration Geophysicist Annual Meeting, August 2000, LBNL #45230.
- Daley, T.M., R. Gritto, and E.L. Majer, Single-well seismic imaging of a gas-filled hydrofracture, Berkeley, California, 2003. Berkeley Lab Report LBNL-53601.
- Daley, T.M., Majer, E.L., Gritto, R., 2000a, Single well seismic imaging – Status Report, Lawrence Berkeley National Laboratory Report LBNL-45342, Berkeley, Ca, March 2000.
- Daley, T.M., Gritto, R., Majer, E.L., West, P., 2003, Tube-wave suppression in single-well acquisition, *Geophysics*, 68, p863-869.
- Fassett, J.E., 2002: The Oil and Gas Reservoirs of the San Juan Basin, New Mexico and Colorado
- Fehler, M. and C. Pearson (1984). Crosshole seismic surveys: Applications for studying subsurface fracture systems at a hot dry rock geothermal site, *Geophys.*, 49, 37-45.
- Ferrazzini, V. and K. Aki (1987). Slow waves trapped in a fluid-filled infinite crack: Implications for volcanic tremor, *J. Geophys. Res.*, 92(B9), 92 15-9223.
- Frazer, L. N. (1990). Dynamic elasticity of microbedded and fractured rocks, I. *Geophys. Res.*, 95(B4), 4821-4831.

- 
- Gangi, A. F. (1978). Variation of whole- and fractured-porous-rock permeability with confining pressure, *Int. J. Rock Mech. Mi Sci. & Geomech. Absr.*, 15, 249-257.
- Greenwood, J. A. and J. B. P. Williamson (1966). Contact of nominally flat surfaces, *Proc. Roy. Soc. Lon., Ser. A*, 300-319.
- Grimm, R.E., Lynn, H.B., Bates, C.R., Phillips, D.R., Simon, K.M., Beckham, W.E., 1999, Detection and analysis of naturally fractured gas reservoirs; multi-azimuth seismic surveys in the Wind River Basin, *Geophysics*, **64**, 1277-1292.
- Grimm, R.E., and Lynn, H.B., 1997, Effects of acquisition geometry, large-scale structure and regional anisotropy on AVOA: an example from the Wind River basin, *67<sup>th</sup> Ann. SEG Mtg., Exp. Abstr.*, 1997-2000.
- Gritto, R., T.M. Daley, and L.R. Myer, 2004, Joint cross well and single well seismic studies at Lost Hills, California. *Geophysical Prospecting*, 52, p323-339.
- Hale, B.W., S. Roth, L. Daniel: The Mesaverde Formation of the San Juan Basin, New Mexico and Colorado - A 50 Year Old Gas Field with Significant Remaining Productivity
- Hamilton, W.B., 1981, Plate-tectonic mechanism of Laramide deformation: University of Wyoming Contributions to Geology, v. 19, p. 87-92.
- Hamilton, W.B., 1988, Laramide crustal shortening, *in* Schmidt, C.J., and Perry, W.J., eds., Interaction of the Rocky Mountain foreland and Cordilleran thrust belt: Geological Society of America Memoir 171, p. 27-39.
- Harris, J. M. (1988). Cross-well seismic measurements in sedimentary rocks, Expanded Abstracts, v.1, Soc. Expi. Geophys. 58th Annual Meeting, Anaheim, 147-150.
- Hart, B., et al., 2000, Horizon attributes and fracture-swarm sweet spots in low-permeability gas reservoirs, SPE 63207, SPE ATCE, Dallas, October 1-4, 2000.
- Hopkins, D. L., N. O. W. Cook, and L. R. Myer (1987). Fracture stiffness and aperture as a function of applied stress and contact geometry, *Proc. 28th US Symp. Rock Mech.*, 673-680.
- Hsu, C.-J. and M. Shoenberg (1990). Characterization of anisotropic elastic wave behavior in media with parallel fractures, Expanded Abstracts, v.2, Soc. Expl. Geophys. 60th Annual Meeting, San Francisco, 1410-1412.
- Hudson, J. A. (1981). Wave speeds and attenuation of elastic waves in material containing cracks, *Geophys. J. Roy. Astr. Soc.*, 64, 133-150.
- Igel, H., Mora, P., and Rioulet, B. (1995). Anisotropic wave propagation through finite difference grids, *Geophysics*, 60, 1203-1216.

- 
- Jilek, P., Hornby, B. and Ray, A., 2003, Inversion of 3D VSP P-wave data for local anisotropy: A case study, 73<sup>rd</sup> Ann. Internat. Mtg., Soc. of Expl. Geophys., 1322-1325.
- Ju, T. H. and S. K. Datta (1992). Dynamics of a laminated composite plate with interface layers, *in Special issue: Modeling and ultrasonic characterization of interfaces*, S. I. Rokhlin (ed), J. Nondestr. Eval., 11(3/4), 227-235.
- Kelley, V.C., 1957, Tectonics of the San Juan basin and surrounding areas, *in* Little, C.J., ed., *Geology of the San Juan Basin: Second Field Conference*, Four Corners Geological Society, p. 44-52.
- Kelly, K. R., Ward, R. W., Treitel, S., and Alford, R. M. (1976). Synthetic seismograms: A finite-difference approach, *Geophysics*, 41, 2-27.
- Kendall, K. and D. Tabor (1971). An ultrasonic study of the area of contact between stationary and sliding surfaces, *Proc. Roy. Soc. London, A*, 323, 321-340.
- King, M. S., L. R. Myer, and I. J. Rezowalli (1986). Experimental studies of elastic wave propagation in a columnar-jointed rock mass, *Geophys. Prosp.*, 34(8), 1185-1199.
- Kitsunozaki, C. (1983). Behavior of plane waves across a plane crack, *J. Mining Coll. Akita Univ.*, A, 6(3), 173-187.
- Kleinberg, R. L., E. Y. Chow, T. J. Plona, M. Orton, and W. J. Canady (1982). Sensitivity and reliability of fracture detection techniques for borehole application, *J. Petr. Tech.*, 34(4), 657-663.
- Levander, A. R. (1988). Fourth-order finite-difference P-SV seismograms, *Geophysics*, 53, 1425-1436.
- Li, X. -Y. and Crampin, S., 1993, Linear-transform techniques for processing shear-wave anisotropy in four-component seismic data: *Geophysics*, **58**, 240-256.
- Liu, E., Crampin, S., Queen, J. H. and Rizer, W. D., 1993, Behaviour of shear waves in rocks with two sets of parallel cracks: *Geophys. J. Int.*, **113**, 509-517.
- Lorenz, J.C., 1992, Well-bore geometries of optimum fracture characterization and drainage, *West Texas Geological Society Bulletin*, v. 32, p. 5-8.
- Lorenz, J.C., and Cooper, S.P., 2001, Tectonic setting and characteristics of natural fractures in Mesaverde and Dakota reservoirs of the San Juan Basin, New Mexico and Colorado: Sandia National Laboratories company report (in press), 72 p.
- Lorenz, J.C., and S.P. Cooper, 2001, Tectonic setting and characteristics of natural fractures in Mesaverde and Dakota reservoirs of the San Juan basin, New Mexico and Colorado, Sandia National Laboratories Report SAND2001-0054, 75 pages.

- 
- Lorenz, J.C. and Cooper, S. P., 2003, Tectonic setting and characteristics of natural fractures in Mesaverde and Dakota reservoirs of the San Juan basin, new Mexico Geology, V25, No.1, p. 3-15.
- Lorenz, J.C., and Cooper, S.P., 2002, Tectonic setting and characteristics of natural fractures in Mesaverde and Dakota reservoirs of the San Juan basin, New Mexico and Colorado: SAND report SAND2001-0054, 73 p.
- Lynn, H. B., Beckham, W. E., Simon, K. M., Bates, C. R., Layman, M. and Jones, M., 1999, P-wave and S-wave azimuthal anisotropy at a naturally fractured gas reservoir, Bluebell-Altamont Field, Utah: Geophysics, **64**, 1312-1328.
- Lynn, H.B., Compagna, D., Simon, K.M., Beckham, W.E., 1999b. Relationship of P-wave seismic attributes, azimuthal anisotropy, and commercial gas pay in 3-D P-wave multiazimuth data, Rulison Field, Piceance Basin, Colorado, Geophysics, **64**, 1293-1311.
- MacBeth, C., 1991, Inversion for subsurface anisotropy using estimates of shear-wave splitting: Geophys. J. Int., **107**, 585-595.
- Majer, E.L., Peterson, J.E., Daley, T.M., Kaelin, B., Queen, J., D'Onfro, P., and Rizer, W., Fracture Detection using Crosswell and Single Well Surveys, Geophysics, v62, n2, 1997
- Majer, E. L., Queen, J. H., Daley, T. M., Murphy, J., Fortuna, M., Lynn, H., Coates, R., Eike, P., Sinton, J., Cox, D., Myer, L., Nihei, K. and Nakagowa, S., 2002, Scaling between logs, single well, VSP and surface seismic for fracture quantification in naturally fractured gas reservoirs: 72<sup>nd</sup> Ann. Internat. Mtg., Salt Lake City, Soc. of Expl. Geophys., 2381-2384.
- Mal, A. K. (1988). Guided waves in layered solids with interface zones, *tnt. J. Engng. Sci.*, 26(8), 873-88 1.
- Medlin, W. L. and L. Marsi (1984). Laboratory experiments in fracture propagation, *Soc. Petr. Engr. J.*, 256-268.
- Moreland, L. W. (1974). Elastic response of regularly jointed media, *Geophys. J. Roy. Astr. Soc.*, 37, 435-446.
- Morris, R. L., D. R. Grine, and T. E. Arkfeld (1964). Using compressional and shear acoustic amplitude for the location of fractures, *J. Petr. Tech.*, 16(6), 623-632.
- Murty, O. S. (1975). A theoretical model for the attenuation and dispersion of Stoneley waves at the loosely bonded interface of elastic half spaces. *Phys. Earth Plan. Inter.*, 11, 65-79.
- Murty, O. S. and V. Kumar (1991). Elastic wave propagation with kinematic discontinuity along a non-ideal interface between two isotropic elastic half-spaces, *J. Nondestr. Eval.*, 10(2), 39-53.
- Myer, L. R., D. Hopkins, and N. G. W. Cook (1985). Effects of contact area of an interface on acoustic wave transmission characteristics, 26th U.S. Rock Mech. Symp., 1, 565-572.

- 
- Myer, L. R. and E. L. Majer (1984). Evaluation of technology for detection of anomalies during repository excavation at the BWIP site, Basalt Waste Isolation Project, Hanford, WA, SD-BWI-Tm-262.
- Nagy, P. B. and L. Adler (1989). Guided wave generation by direct excitation, I. *Acoust. Soc. Am.*, Suppl. 1, 86, S94.
- Nagy, P. B. and L. Adler (1990). New ultrasonic techniques to evaluate interfaces, in *Elastic Waves and Ultrasonic Nondestructive Evaluation*, S. K. Datta, J. D. Achenbach, and Y. S. Rajapakse (eds), 229-239.
- Nagy, P. B., D. V. Rypien, and L. Adler (1990). Dispersive properties of leaky interface waves in adhesive layers, in *Review of Progress in Quantitative Nondestructive Evaluation*, D. O. Tompson and D. E. Chimenti (eds), 9, 1247-1254.
- Nagy, P. B. and L. Adler (1991). A novel technique for interface wave generation, in *Physical Acoustics*, 0. Leroy and M. A. Breazeale (eds), Plenum Press, New York.
- Nihei, K. T. (1989). *Modeling Elastic Waves in Fractured Rock with the Kirchhoff Method*, MS Thesis, University of California at Berkeley.
- Nur, A. (1971). Effects of stress on velocity anisotropy in rocks with cracks, *J. Geophys. Res.*, 76(8), 2022-2034.
- O'Connell, R. J. and B. Budiansky (1977). Viscoelastic properties of fluid-saturated cracked solids, *J. Geophys. Res.*, 82(36), 57 19-5736.
- Pyrak-Nolte, L. J. (1988). *Seismic Visibility of Fractures*, PhD Thesis, University of California at Berkeley.
- Pyrak-Nolte, L. J. and N. G. W. Cook (1987b). Elastic interface waves along a fracture, *Geophys. Res. Lett.*, 14, 1107-1110.
- Pyrak-Nolte, L. J., N. O. W. Cook, and D. D. Nolte (1988). fluid percolation through single fractures, *Geophys. Res. Lett.*, 15, 1247-1450.
- Pyrak-Nolte, L. J., L. R. Myer, and N G. W. Cook (1990a). Transmission of seismic waves across natural fractures, *J. Geophys. Res.*, 95, 8617-8638.
- Pyrak-Nolte, L. J., L. R. Myer, and N G. W. Cook (199Db). Anisotropy in seismic velocities and amplitudes from multiple parallel fractures, *J. Geophys. Res.*, 95, 11345-11358.
- Pyrak-Nolte, L. J., J. Xu, and O. M. Haley (1992b). Elastic interface waves propagating in a fracture, *Phys. Rev. Lett.*, 68, 3650-3653.
- Queen, J. H. and Rizer, W. D., 1990, An integrated study of seismic anisotropy and the natural fracture system at the Conoco borehole test facility, Kay county, Oklahoma: *J. Geophys. Res.*, 95, 11255-11273.

- 
- Robertsson, J. A., Blanch, J. O., and Symes, W. W. (1994). Viscoelastic finite difference modeling, *Geophysics*, 59, 1444-1456.
- Rokhlin, S. I. (1984). Adhesive joint characterization by ultrasonic surface and interface waves, in *Adhesive Joints*, K. L. Mittal (ed), Plenum Press, New York, 307-345.
- Rokhlin, S. I., M. Hefets, and M. Rosen (1981). An ultrasonic interface-wave method for predicting the strength of adhesive bonds, *J. Appl. Phys.*, 52(4), 2847-2851.
- Rokhlin, S. I. and Y. I. Wang (1991). Analysis of boundary conditions for elastic wave interaction with an interface between two solids, *J. Acoust. Soc. Am.*, 89(2), 503-515.
- Rokhlin, S. I. and W. Huang (1992). Ultrasonic wave interaction with a thin anisotropic layer between two anisotropic solids: Exact and asymptotic-boundary condition methods, *J. Acoust. Soc. Am.*, 92(3), 1729-1742.
- Rokhlin, S. I. (1992). *Special issue: Modeling and ultrasonic characterization of interfaces*, *J. Nondestr. Eval.*, S. I. Rokhlin (ed), 11(3/4), Preface.
- Shoenberg, M. (1980). Elastic wave behavior across linear slip interfaces, *J. Acoust. Soc. Am.*, 68(5), 1516-1521.
- Shoenberg, M. (1983). Reflection of elastic waves from periodically stratified media with interfacial slip, *Geophys. Prosp.*, 31, 265-292.
- Shoenberg, M. and J. Douma (1988). Elastic wave propagation in media with parallel fractures and aligned cracks, *Geophys. Prosp.*, 36, 571-590.
- Sotiropoulos, D. A. (1990). Dynamic stiffness of cracked interfaces, *Trans. ASME*, 57, 476-478.
- Suárez-Rivera, R. (1992). *The Influence of Thin Clay Layers Containing Liquids on the Propagation of Shear Waves*, PhD Thesis, University of California at Berkeley. Tang, X. M., C. H. Cheng, and F. L. Paillet (1991). Modeling borehole Stoneley wave propagation in a permeable in situ fracture, *Soc. Prof. Well Log. Analys. 32nd Ann. Symp.*, Midland, Tx, Trans., GG1-GG25.
- Taylor, D.J., and Huffman, A.C., Jr., 1998, Map showing inferred and mapped basement faults, San Juan basin and vicinity, New Mexico and Colorado, United States Geological Survey Investigation Series I-2641.
- Thomsen, L., 1986, Weak elastic anisotropy: *Geophysics*, **51**, 1954-1966.
- Tsvankin, I., 1997, Reflection moveout and parameter estimation for horizontal transverse isotropy, *Geophysics*, **60**, 1409-1425.
- Tura, M. A. C., L. R. Johnson, E. L. Majer, and J. E. Peterson (1992). Application of diffraction tomography to fracture detection, *Geophys.*, 57(2), 245-257.

- 
- Virieux, J. (1986). Velocity-stress finite-difference method, *Geophysics*, 51, 889-901.
- Wang, Z., 2002, Seismic anisotropy in sedimentary rocks, part 2: Laboratory data: *Geophysics*, **67**, 1423-1440.
- Wild, P. and Crampin, S., 1991, The range of effects of azimuthal isotropy and EDA anisotropy in sedimentary basins: *Geophys. J. Int.*, **107**, 513-529
- White, J. E., Martineau-Nicoletis, and Monash, C., 1983, Measured anisotropy in Pierre Shale: *Geophys. Prosp.*, **31**, 709-725.
- White, J. E. (1983). *Underground Sound*, Elsevier, New York.
- Winterstein, D. F. and Meadows, M. A., 1991, Shear-wave polarizations and subsurface stress directions at Lost Hills field: *Geophysics*, **56**, 1331-1348.
- Winterstein, D. F. and Meadows, M. A., 1991, Changes in shear-wave polarization azimuth with depth in Cymric and Railroad Gap oil fields: *Geophysics*, **56**, 1349-1364.
- Winterstein, D. F. and De, G.S., 2001, VTI documented: *Geophysics*, **66**, 237-245.
- Winterstein, D. F., De, G. S. and Meadows, M.A., 2001, Twelve years of vertical birefringence in nine-component VSP data: *Geophysics*, **66**, 582-597.
- Woodward, L.A., Kaufman, W.H., and Anderson, J.B., 1972, Nacimiento fault and related structures, northern New Mexico: *Geological Society of America Bulletin*, v. 83, p. 2383-2396.
- Woodward, L.A., Hultgren, M.C., Crouse, D.L., and Merrick, M.A., 1992, Geometry of Nacimiento-Gallina fault system, northern New Mexico, *in* Lucas, S.G., Kues, B.S., Williamson, T.E., and Hunt, A.P., eds., *San Juan Basin IV*, New Mexico Geological Society Guidebook, 43rd Field Conference, p. 103-108.
- Woodward, L.E., and Callender, J.F., 1977, Tectonic framework of the San Juan Basin, *in* Fassett, J.E., ed., *San Juan Basin III*, New Mexico Geological Society, 28th Field Conference, p. 209-212.
- Wu, R.-S. and M. N. ToksOz (1987). Diffraction tomography and multisource holography applied to seismic imaging, *Geophys.*, 52(1), 11-25.
- Xu, P.-C. and S. K. Datta (1990). Guided waves in a bonded plate: A parametric study, *J. Appl. Phys.*, 67(11), 6779-6786.
- Yoshioka, N. and C. H. Scholz (1989). Elastic properties of contacting surfaces under normal and shear loads 2. Comparison of theory with experiment, *J. Geophys. Res.*, 94, 1769 1-
- Zimmerman, R. W. (1991). *Compressibility of Sandstones*, Developments in Petroleum Science 29, Elsevier, Amsterdam.